UNIVERSIDADE FEDERAL DO PARÁ
INSTITUTO DE GEOCIÊNCIAS
PROGRAMA DE PÓS-GRADUAÇÃO EM GEOLOGIA E GEOQUÍMICA

TESE DE DOUTORADO Nº 186

PETROGÊNESE DA SUÍTE IGARAPÉ GELADO: IMPLICAÇÕES PARA O MAGMATISMO NEOARQUEANO DA PROVÍNCIA CARAJÁS, CRÁTON AMAZÔNICO

Tese apresentada por:
CAIO JOSÉ SOARES MESQUITA
Orientador: Roberto Dall'Agnol (UFPA)

BELÉM – PARÁ
2025

Dados Internacionais de Catalogação na Publicação (CIP) de acordo com ISBD Sistema de Bibliotecas da Universidade Federal do Pará

Gerada automaticamente pelo módulo Ficat, mediante os dados fornecidos pelo(a) autor(a)

M578p Mesquita, Caio José Soares.

Petrogênese da Suíte Igarapé Gelado: implicações para o magmatismo neoarqueano da Província Carajás, Cráton Amazônico / Caio José Soares Mesquita. — 2025.
xxii, 193 f. : il. color.

Orientador(a): Prof. Dr. Roberto Dall'Agnol
Tese (Doutorado) - Universidade Federal do Pará, Instituto de Geociências, Programa de Pós-Graduação em Geologia e Geoquímica, Belém, 2025.

1. Geoquímica-Pará. 2. Petrologia. 3. Granitoides. 4. Província Carajás. 5. Arqueano. I. Título.

CDD: 551.9098115

Universidade Federal do Pará
Instituto de Geociências
Programa de Pós-Graduação em Geologia e Geoquímica

PETROGÊNESE DA SUÍTE IGARAPÉ GELADO: IMPLICAÇÕES PARA O MAGMATISMO NEOARQUEANO DA PROVÍNCIA CARAJÁS, CRÁTON AMAZÔNICO

TESE APRESENTADA POR:

CAIO JOSÉ SOARES MESQUITA

Como requisito parcial à obtenção do Grau de Doutor em Ciências na Área de GEOQUÍMICA E PETROLOGIA, linha de pesquisa EVOLUÇÃO CRUSTAL E METALOGÊNESE.

Data de Aprovação: 30 / 04 / 2025

Banca Examinadora:

Prof. Dr. Roberto Dall'Agnol (Orientador – UFPA)

Documento assinado digitalmente
gov.br VALDECIR DE ASSIS JANASI
Data: 05/05/2025 09:28:30-0300
Verifique em https://validar.iti.gov.br

Prof. Dr. Valdecir de Assis Janasi (Membro-USP)

Documento assinado digitalmente
gov.br CARLOS EDUARDO DE MESQUITA BARROS
Data: 06/05/2025 13:32:00-0300
Verifique em https://validar.iti.gov.br

Prof. Dr. Carlos Eduardo de Mesquita Barros (Membro-UFPR)

Documento assinado digitalmente
gov.br FERNANDO FERNANDES DA SILVA
Data: 02/05/2025 11:26:37-0300
Verifique em https://validar.iti.gov.br

Prof. Dr. Fernando Fernandes da Silva (Membro-UNIFESSPA)

Documento assinado digitalmente
gov.br JEAN MICHEL LAFON
Data: 01/05/2025 13:36:48-0300
Verifique em https://validar.iti.gov.br

Prof. Dr. Jean Michel Lafon (Membro-UFPA)

Dedico aos meus pais, irmãs e esposa.

AGRADECIMENTOS

O desenvolvimento desta tese de doutorado só foi possível devido ao auxílio e suporte dado por diversas pessoas e entidades, as quais destaco meus sinceros agradecimentos em especial:

- Ao Programa de Pós-Graduação de Geologia e Geoquímica (PPGG) do Instituto de Geociências da UFPA pela infraestrutura de laboratórios e salas de estudos cedidas;
- À Coordenação de Aperfeiçoamento de Pessoal de Nível Superior Brasil (CAPES) pela concessão de bolsa de estudo – Código de financiamento 001;
- Ao Conselho Nacional de Desenvolvimento Científico e Tecnológico (CNPq) pela concessão de taxa de bancada em nome de meu orientador, Roberto Dall'Agnol (Processo 3006767/2019–8);
- Ao Instituto Nacional de Ciência e Tecnologia de Geociências da Amazônia/Geociam (Processo N°573733/2008-2) pelo apoio financeiro nas etapas iniciais dessa pesquisa, em especial, às atividades de campo realizadas na Província Carajás;
- Laboratório de Geologia Isotópica (Pará-Iso) da UFPA, em nome do professor Marco Antonio Galarza pelo suporte na aquisição e tratamento dos dados de Lu-Hf LA-MC-ICP-MS;
- Ao Laboratório de Microanálises do IG-UFPA, em especial ao professor Cláudio Nery Lamarão e às técnicas Gisele Marques e Ana Paula Correa, pelas contribuições analíticas no microscópio eletrônico de varredura (MEV) e microssonda eletrônica;
- Ao Laboratório de Geocronologia de Alta Resolução da Universidade de São Paulo (GeoLab/USP), em especial ao corpo técnico Dr. Kei Sato e Dr. Maurício Borba, além da secretária Silvana Macedo, pelo grande auxílio prestado durante as etapas de aquisição de dados U-Pb e ETR SHRIMP;
- Ao Laboratório de Estudos Geodinâmicos, Geocronológicos e Ambientais da Universidade Brasília, em nome do prof. Dr. Elton Dantas que prestou auxílio na aquisição das análises Sm-Nd;
- Ao serviço Geológico Brasileiro (SGB) pela concessão de amostras e em especial à geóloga e amiga Junny Kyley que deu todo suporte nessa etapa de aquisição de dados;
- Aos geólogos Sergio Huhn (VALE S.A.), Clovis Wagner Maurity e Alessandro Sabá Leite (ITV DS) pelo suporte na primeira campanha de campo e aos geólogos Dr. José de Arimatéia (PPGG-UFPA) e Diwhemerson Barbosa que me acompanharam na segunda campanha;

- Às funcionárias da secretaria do PPGG, Cleida e Joyce que estiveram sempre dispostas a auxiliar nas questões burocráticas;
- Aos amigos e técnicos da oficina de laminação do IG-UFPA, Joelma e Bruno, pela agilidade na confecção das lâminas utilizadas nessa pesquisa;
- Ao orientador Roberto Dall'Agnol pelo incentivo, oportunidades, conhecimento compartilhado, por ter acreditado no meu potencial para escrever esta tese e acima de tudo me ensinou a ter resiliência na pesquisa;
- Ao Grupo de Pesquisa Petrologia de Granitoides (GPPG) do Instituto de Geociências (IG-UFPA), em especial aos integrantes do Laboratório de Petrologia Magnética, Luan Martins, Ingrid Cunha, Mayara Fraeda e Arthur Neri pela amizade "granítica" que construímos durante estes anos;
- Aos professores do PPGG, pelo conhecimento transmitido;
- Aos meus familiares, em especial aos meus pais e irmãs que sempre estiveram na torcida durante toda esta etapa;
- À minha amada esposa Rafaela Oya que sempre me deu força durante a confecção desta tese doutorado, mas que vem me apoiando desde o início dessa caminhada quando eu ainda "engatinhava" na pesquisa ao escrever meu primeiro relatório de iniciação científica;
- Por fim, agradeço a todos que contribuíram direta ou indiretamente para a elaboração desse trabalho. Meus sinceros agradecimentos a todos.

Mesmo que na vida fatos CISALHANTES abalem suas ESTRUTURAS, e nos machucados sangue quente FLUA, não desista, pois, NADA É POR ACASO e quando o sangue esfriar algo RARO e VALIOSO você pode conquistar!
Caio Mesquita

RESUMO

A Suíte Igarapé Gelado (SIG) localiza-se próximo à fronteira norte da Província Carajás, quase no limite com o Domínio Bacajá, ao longo do lineamento Cinzento. É intrusiva em rochas metamáficas e formações ferríferas bandadas. A porção centro-leste da SIG compreende quatro variedades de rochas: tonalito a granodiorito com teores variados de biotita e anfibólio, (1) com clinopiroxênio e / ou ortopiroxênio (PBHTnGd) ou (2) desprovido de piroxênios (BHTnGd); e monzogranitos que exibem conteúdo variável de biotita e anfibólio, e podem ser (3) moderadamente (BHMzG) ou (4) fortemente reduzidos (BHMzGR). O PBHTnGd contém ferrosilita e/ou augita com hedenbergita subordinada. Os anfibólios são K-hastingsita e, subordinadamente, Fe-Tschermakita em monzogranitos. As biotitas são ferrosas, e em granitos reduzidos apresentam #Fe > 0,90. Essas micas são afins daquelas de rochas alcalinas a subalcalinas e composicionalmente semelhantes às biotitas magmáticas primárias. Plagioclásio é oligoclásio. A integração dos resultados da termobarometria e da modelagem termodinâmica e sua comparação com a paragênese presente nas rochas naturais permitiu aprimorar a estimativa dos parâmetros de cristalização (T, P, fO_2, X_{H2O}) e da evolução magmática. Assim, os granitos da SIG cristalizaram a pressões de 550 ± 100 MPa, superiores às atribuídas a outros granitos neoarqueanos em Carajás. A temperatura *liquidus* estimada para a variedade com piroxênio é de ~ 1000±50° C. Os BHTnGd e BHMzG se formaram dentro de uma faixa de temperatura semelhante ao PBHTnGd, enquanto o BHMzGR teve temperaturas líquidas mais baixas (≤900 ° C). Foram estimadas temperaturas *solidus* de cerca de ~ 660 ° C para as quatro variedades da SIG. O magma do BHMzG evoluiu em condições de baixa fO_2, ligeiramente acima ou abaixo do tampão FMQ (FMQ±0,5), como os da Suíte Planalto e dos granitos reduzidos das suítes Vila Jussara e Vila União da Província de Carajás. Nos magmas das variedades PBHTnGd e BHTnGd a fugacidade do oxigênio atingiu FMQ+0,5. O BHMzGR cristalizou sob condições fortemente reduzidas equivalentes a FMQ-0,5 a FMQ-1. Os magmas das variedades monzograníticas evoluíram com alto teor de H_2O (≥4% em peso), atingindo 7% no caso dos monzogranitos reduzidos. Isso é comparável ou ligeiramente superior aos níveis geralmente atribuídos aos granitos neoarqueanos de Carajás (>4%). Em contraste, a variedade com piroxênio tem um teor de água (~4%), tal como os do Enderbiro Café e do Charnoquito Rio Seco da Província Carajás, e do Pluton Matok do Cinturão do Limpopo. Com base na composição química, as rochas do SIG são ferrosas, reduzidas a oxidadas e com composição similar a granitos tipo A, semelhantes a outras suítes graníticas neoarqueanas da Província de Carajás. As idades da SIG são mais jovens do que as idades de 2,76-2,73 Ga atribuídas aos

granitos neoarqueanos da Província Carajás. Uma idade concordante de cristalização de ~2,68 Ga foi obtida por U-Pb SHRIMP em zircão para a variedade BHMzGR, e idades de intercepto superior semelhantes foram fornecidas pelas outras variedades da SIG, exceto aquelas de ~2,5 Ga que se assemelham às idades do depósito IOCG Salobo associadas à reativação do Lineamento Cinzento. As zonas de cisalhamento associadas a este lineamento são responsáveis pela deformação das rochas da SIG, que moldou corpos alongados com foliação variada. Essas zonas facilitaram a migração e causaram deformação dos magmas desde o estágio final da cristalização até seu resfriamento completo, caracterizando um processo sintectônico. O sintectonismo destes granitos está associado à inversão da Bacia Carajás, e a idade de cristalização mais jovem dessas rochas indica que a inversão ocorreu até 2,68 Ga, estendendo o intervalo estimado anteriormente (2,76–2,73 Ga). A SIG exibe valores negativos a ligeiramente positivos de $\varepsilon Nd(t)_{(-2,86\ a\ 0,18)}$ e $\varepsilon Hf(t)_{(-3,3\ a\ 0,1),}$ e idades TDM do Paleoarqueano ao Mesoarqueano [Nd-$T_{DM(2,98-2,84)}$ e Hf-$T_{DM}^{C}{}_{(3,27-3,12)}$]. Os valores positivos de εNd(t) e εHf(t) para a variedade BHMzGR, sugerem possível contribuição juvenil ou contaminação na fonte de seu magma. As rochas da SIG foram geradas por fusão de 19% (PBHTnGd) e 14% (BHTnGd) de granulito máfico contaminado e por fusão de 9% (BHMzG) e 7% (BHMzGR) de um granulito máfico toleítico. A área de ocorrência da SIG é marcada por hidrotermalismo que modificou localmente a composição de rochas e minerais, permitindo a lixiviação de ETR e Y que fez com que algumas amostras de BHMzG fujam do padrão dominante e apresentem características geoquímicas de granitos do subtipo A1. Além disso, esses processos foram responsáveis pela transformação do zircão, que resultou em grãos com enriquecimento em U, Th e ETRL, e aspecto maciço, que apresentam idades U-Pb de intercepto superior, ao contrário dos cristais de zircão da variedade BHMzGR que preservaram características primárias e apresentam idades Concordia.

Palavras-chave: geoquímica-Pará; química mineral; parâmetros de cristalização; modelamento termodinâmico; geocronologia; geoquímica; isótopos; zircão; granito tipo A; arqueano; Carajás; Cráton Amazônico.

ABSTRACT

The Igarapé Gelado suite (IGS) is located near the northern border of the Carajás Province, almost at its boundary with the Bacajá Domain, along the Cinzento lineament, and is intrusive in metavolcanic mafic rocks and banded iron formations. The central-eastern portion of the IGS comprises four rock varieties: tonalite to granodiorite with varying contents of biotite and amphibole, (1) with associated clinopyroxene and/or orthopyroxene (PBHTnGd) or (2) devoid of pyroxenes (BHTnGd); and monzogranites that exhibit variable biotite and amphibole content and can be (3) moderately (BHMzG) or (4) strongly (RBHMzG) reduced. The PBHTnGd shows ferrosilite and/or augite with subordinate hedenbergite. The amphiboles are K-hastingsite and, subordinately, Fe-Tschermakite in monzogranites. Biotites are ferroan, and in reduced granites show #Fe > 0.90. These micas are similar to those of alkaline to subalkaline rocks and compositionally akin of primary magmatic biotites. Plagioclase is oligoclase. The integration of thermineral chemistry;mobarometry results and thermodynamic modeling and their comparison with the paragenesis present in natural rocks improved the estimation of crystallization parameters (T, P, fO_2, H_2O), and allowed a better interpretation of magmatic evolution. The IGS granites crystallized at pressures of 550 ± 100 MPa, higher than those attributed to other Neoarchean granites in Carajás provinve. The estimated *liquidus* temperature for the IGS pyroxene variety is ~1000±50°C. BHTnGd and BHMzG formed within a similar temperature range to PBHTnGd, while RBHMzG had lower liquidus temperatures (≤900°C). Solidus temperatures of around ~660 °C were estimated for the four IGS varieties. The BHMzG magma evolved under conditions of low fO_2, slightly above or below the FMQ buffer (FMQ±0.5), like those of the Planalto suite and the reduced granites of the Vila Jussara and Vila União suites of Carajás province. In the magmas of the PBHTnGd and BHTnGd varieties the oxygen fugacity attained FMQ+0.5. The RBHMzG crystallized under strongly reduced conditions equivalent to FMQ-0.5 to FMQ-1. The magmas of the monzogranitic varieties evolved with a H_2O content of ≥4 wt%, attaining 7 wt% in the case of the reduced monzogranites. This is comparable to, or slightly exceeding, the levels typically attributed to the Neoarchean granites of Carajás province (≥ 4% wt%). In contrast, the variety with pyroxene has a water content (~4 wt%) like that of Café enderbite and Rio Seco charnockite from Carajás province, and Matok Pluton from Limpopo belt. Based on the chemical composition, the rocks from IGS are ferroan, reduced to oxidized A-type-like granites, akin to other Neoarchean granite suites from the Carajás province. The IGS are younger than the 2.76-2.73 Ga Neoarchean granites from the Carajás province. A crystallization concordia age of ~2.68 Ga was obtained by U-Pb

SHRIMP in zircon for the RBHMzG variety, and similar upper intercept ages were furnished by the other IGS varieties, except for ages of ~2.5 Ga that resemble the ages of the IOCG Salobo deposits associated with reactivation of the Cinzento Lineament. Tmineral chemistry;he deformation of the IGS rocks was influenced by shear zones linked to that lineament, forming elongated bodies with varied foliation. These zones facilitated the migration and deformation of magmas from the final crystallization stages until their complete cooling, characterizing a syntectonic process. This syntectonicity is associated with the inversion of the Carajás Basin, and the younger crystallization age of these rocks indicates that the inversion occurred up to 2.68 Ga, extending the previously estimated interval (2.76–2.73 Ga). The IGS displays negative to slightly positive values of $\varepsilon_{Nd}(t)_{(-2.86\ to\ 0.18)}$ and $\varepsilon_{Hf}(t)_{(-3.3\ to\ 0.1)}$, and Paleoarchean to Mesoarchean T_{DM} ages [Nd-$T_{DM(2.98-2.84)}$ and Hf-$T_{DM}^{C}{}_{(3.27-3.12)}$]. The positive values of $\varepsilon_{Nd}(t)$ and $\varepsilon_{Hf}(t)$ for the RBHMzG variety, suggest possible juvenile contribution or contamination in the source of its magma. The IGS rocks come from the melting of 19% (PBHTnGd) or 14% (BHTnGd) of contaminated mafic granulite, - and from melting of 9% (BHMzG) and 7% (RBHMzG) of a tholeiitic mafic granulite. The area of occurrence of the IGS is marked by hydrothermalism and mineralizations that locally modified the composition of rocks and minerals, allowing the leaching of REE and Y that changed the composition of some samples of BHMzG approaching them of (false) A1-subtype granites. In addition, these processes were responsible for zircon alteration, which resulted in grains showing enrichment of U, Th, and LREE, and massive textures, that furnished upper intercept U-Pb ages, contrarily to the zircon crystals of the RBHMzG variety that preserved primary characteristics and presented Concordia ages.

Key-words: Pará-geochemistry; mineral chemistry; crystallization parameters; thermodynamic modeling; geochronology; geochemistry; isotopes; zircon; A-type Granite; archean; Carajás; Amazonian Craton.

LISTA DE ILUSTRAÇÕES

CAPÍTULO 1

CAPÍTULO 2

CAPÍTULO 3

LISTA DE TABELAS

CAPÍTULO 1

CAPÍTULO 2

CAPÍTULO 3

SUMÁRIO

CAPÍTULO 1: INTRODUÇÃO

1.1 APRESENTAÇÃO

No final do arqueano (3.0-2.5 Ga) ocorreram importantes mudanças nos processos de diferenciação da crosta continental, relacionadas com a mudança no estilo de tectônica vertical para horizontal (Dhuime *et al*. 2011, 2012, 2015, 2017, Laurent *et al*. 2014, Tang *et al*. 2016, Moyen *et al*. 2016, Brown *et al*. 2020, Ribeiro-Silva *et al*. 2022), que se estenderam até o início do Paleoproterozoico e favoreceram a diversificação do magmatismo granitoide com surgimento comum em muitos crátons de rochas progressivamente mais ricas em K formando as suítes sanukitoides caracterizadas pelo caráter magnesiano (Halla *et al*. 2009, Heilimo *et al*. 2010, Oliveira *et al*. 2011, Ribeiro-Silva *et al*. 2022, 2023), assim como suítes leucogranodioríticas a leucograníticas de caráter cálcico alcalino (Dey *et al*. 2012, Feio & Dall'Agnol, 2012, Almeida *et al*. 2013, Feio *et al*. 2013, Rodrigues *et al*. 2014, Leite-Santos & Oliveira, 2016, Batuk Joshi *et al*. 2017, Kaur *et al*. 2019, Jayananda *et al*. 2006, 2020, Joshi *et al*. 2022) ou mesmo de suítes com afinidade com granitos ferrosos do tipo A (Barros *et al*. 2009, Feio & Dall'Agnol 2012, Cunha *et al*. 2016, Dall'Agnol *et al*. 2017, Topno *et al*. 2018, Marangoanha *et al*. 2020, Silva *et al*. 2020). Suas assinaturas geoquímicas podem indicar diferentes processos de formação e fontes de magmas (Chappell & White 1974, 1992, King *et al*. 1997, Frost *et al*. 2001, Dall'Agnol *et al*. 2005, Laurent *et al*. 2014, Moyen & Laurent, 2018) e ambiente tectônico (Pearce *et al*. 1984, Harris *et al*. 1986, Pearce 1996, Moyen *et al*. 2016, Whalen & Hildebrand 2019). Portanto, é clara a importância do estudo de associações granitoides, porque elas fornecem informações-chave para o entendimento da evolução da crosta ao longo do tempo.

Diante disso, vem sendo alvo de estudos nos últimos 30 anos o expressivo evento magmático granítico neoarqueano (~2,75 – 2,73 Ga) que ocorreu nas porções central e norte da Província Carajás (PC), (Barros *et al.* 1997, 2001, 2009, Huhn *et al*. 1999, Sardinha *et al*. 2006, Feio *et al.* 2013, 2012, Cunha *et al.* 2016, Dall'Agnol *et al.* 2017, Oliveira *et al.* 2018a, Marangoanha *et al.* 2020, 2019a, 2019b, Sousa *et al.* 2022, Toledo *et al.* 2023). Este magmatismo é constituído por batólitos e stocks intensamente deformados, alongados nas direções WNW-ESE a E-W, (Fig. 3c), sendo representado por Complexo Estrela, Granito Serra do Rabo e suítes Planalto, Vila União, Vila Jussara e Igarapé Gelado (Barros *et al*. 1997, 2001, 2009, Huhn *et al*. 1999, Sardinha *et al*. 2006, Feio *et al*. 2013, 2012, Cunha *et al*. 2016, Dall'Agnol *et al*. 2017, Oliveira *et al*. 2018a, Marangoanha *et al*. 2019a, Felix *et al*. 2020, Silva *et al*. 2020, 2025). Esses granitos são metaluminosos a levemente peraluminosos e possuem afinidade com granitos tipo A ferrosos reduzidos (Barros *et al*. 1997, 2001, 2009,

Sardinha *et al*. 2006, Feio *et al*. 2012, 2013, Cunha *et al*. 2016) , exceto aqueles da Suíte Igarapé Gelado (Barbosa 2004, Barros *et al*. 2009, Melo *et al*. 2016, Toledo *et al*. 2023), que apresentam também granitos ferrosos oxidados e dos granitoides da Suíte Vila Jussara (Dall'Agnol *et al*. 2017, Silva *et al*. 2020, Sousa *et al*. 2022, Silva *et al.* 2025) e dos granitos da Suíte Vila União (Marangoanha *et al*. 2019a), que incluem igualmente granitoides ferrosos oxidados e até mesmo magnesianos.

A Suíte Igarapé Gelado (SIG) forma um corpo com dimensões batolíticas (80 x 15 km), intrusivo em formações ferríferas bandadas e rochas metabásicas do Supergrupo Itacaiúnas, localizado na porção norte da Bacia Carajás (Fig. 2c), próximo do limite da PC com o Domínio Bacajá (Barbosa 2004, Barros *et al*. 2001, 1997, 2009). Em estudos prévios, foi feita a caracterização preliminar desse magmatismo e a definição de sua idade neoarqueana (Barbosa 2004, Barros *et al.* 2009, Melo *et al.* 2016, Tavares *et al.* 2021, Toledo *et al.* 2023). Entretanto, persistiam lacunas expressivas no conhecimento desta suíte plutônica e, em função disso, foram desenvolvidas pesquisas na porção centro-leste do batólito para refinar o conhecimento disponível e preencher estas lacunas acerca da petrogênese deste expressivo magmatismo. A partir deste quadro, se torna necessário caracterizar as variedades de granitoides presentes no batólito granítico, determinar as suas idades de cristalização e elucidar, assim, se ele é formado por rochas contemporâneas, os processos envolvidos na evolução magmática e as condições de cristalização das rochas que o constituem, caracterizar e definir qual seria(m) a(as) fonte(s) de seu(s) magma(s) e seu ambiente de formação, assim como entender o papel da tectônica transcorrente durante a colocação dos mesmos. Além disso, elucidar até que ponto os eventos hidrotermais recorrentes na área afetaram as rochas da SIG. Para atingir estes objetivos foi realizada petrografia associada a observações (micro) estruturais, estudos geoquímicos, químico-mineralógicos e isotópicos, Sm-Nd em rocha total, U-Pb/Lu-Hf e ETR em zircão, bem como, testes de modelagem geoquímica para identificar possíveis fontes e processos geradores de seu(s) magma(s), e de modelagem termodinâmica associada a termobarometria para determinar com maior exatidão os parâmetros de cristalização. Estas informações permitiram estabelecer comparações com outros granitos neoarqueanos de Carajás e de outros crátons. O que permitiu gerar uma contribuição significativa para a compreensão do magmatismo neoarqueano da Província Carajás e de outros crátons arqueanos, em particular, dos granitoides afins de granitos tipo A.

A presente tese de doutorado faz parte das contribuições do Grupo de Pesquisa Petrologia de Granitoides (GPPG) e está vinculada à área de Geoquímica (linha de pesquisa Evolução Crustal e Metalogênese) do Programa de Pós-Graduação em Geologia e

Geoquímica (PPGG) da Universidade Federal do Pará (UFPA). Os resultados apresentados nessa pesquisa foram financiados pelo Conselho Nacional de Desenvolvimento Científico e Tecnológico (CNPq) pela concessão de taxa de bancada (R. Dall'Agnol; processo:3006767/2019-8) e Coordenação de Aperfeiçoamento de Pessoal de Nível Superior – Brasil (CAPES) pela concessão da bolsa de estudo (C. J. S. Mesquita; processo: 88882.347890/2019-01) com código de financiamento 001.

A compartimentação deste documento inclui o Capítulo 1 de caráter introdutório abordando a apresentação, localização da área de estudo e contexto geológico regional da Província Carajás, com destaque as associações litológicas do Terrenos Sapucaia, Canaã dos Carajás e Bacia Carajás. Além da apresentação da problemática de estudo, objetivos a serem alcançados e metodologias aplicadas. Os capítulos 2 e 3 apresentam os resultados alcançados nessa tese na forma de artigos científicos publicados e/ou submetidos a periódicos internacionais com Qualis A1 e A2. No capítulo 4 são discutidas as feições microestruturais e suas implicações para a colocação da Suíte Igarapé Gelado. Por fim, o capítulo 5, sumariza as discussões e apresenta as conclusões finais da tese de doutorado.

Os artigos serão apresentados na seguinte ordem:

CAPÍTULO 2: Crystallization parameters and thermodynamic modeling of the Igarapé Gelado suite: Implications for the Neoarchean magmatism of the Carajás province, Brazil. Publicado na revista *Journal of South America Earth Science*. Este artigo apresenta os resultados de geologia, petrografia, química mineral e modelamento termodinâmico da Suíte Igarapé Gelado. Esse estudo permitiu caracterizar as variedades faciológicas desta suíte. Além disso, nesta pesquisa fica evidente que a integração dos resultados de termobarometria e de modelamento termodinâmico e sua comparação com as paragêneses presentes nas rochas naturais permitem compreender melhor a evolução magmática da suíte e refinar a estimativa dos seus parâmetros de cristalização (T, P, fO_2, XH_2O).

CAPÍTULO 3: Petrogenesis, U-Pb SHRIMP geochronology, and zircon composition of Neoarchean granitoids of the Igarapé Gelado suite, Carajás province, Amazonian craton

Submetido para publicação à revista *Geoscience Frontiers*. Neste artigo foram discutidos aspectos petrogenéticos envolvidos na geração das variedades da Suíte Igarapé Gelado, com base em dados de campo, geoquímicos, geocronológicos (U-Pb-SHRIMP) e isotópicos (Lu-Hf/Sm-Nd e ETR), além de modelamento geoquímico de elementos maiores e traço. Os resultados permitiram comparar esta suíte com outros granitoides neoarqueanos de

Carajás, determinar idades para esta suíte, discutir o papel de uma fonte granulítica máfica na geração dos seus magmas, bem como elucidar a influência da alteração hidrotermal nestas rochas.

CAPÍTULO 4: Aspectos (micro) estruturais e geocronológicos da Suíte Igarapé Gelado: implicações para colocação dos granitos tipo-A sintectônicos da Província Carajás.

Neste capítulo são discutidos os principais aspectos meso-estrurais e micro-estruturais, associado as novas datações obtidas para SIG. Os resultados permitiram inferir a trajetória e intensidade da deformação, confirmar a temperatura *solidus* com base em microestruturas, bem como discutir a hipótese de sintectonismo dos granitos neoarqueanos tipo-A de Carajás. Com base na geocronologia também foi possível inferir um maior intervalo de duração do evento de inversão da Bacia Carajás.

1.2 LOCALIZAÇÃO E ACESSO

A área de estudo está localizada na porção noroeste do município de Parauapebas e no sudoeste de Marabá, ambos no sudeste do estado do Pará e abrange as folhas SB.22-X-C-IV, SB.22-X-C-V e SB.22-X-C-VI (Fig. 1a). Na porção sul da área de estudo está localizada a Área de Proteção Ambiental do Igarapé Gelado que se estende para oeste até os limites da Floresta Nacional do Tapirapé-Aquiri (Fig. 1b). Esta última compreende toda porção oeste da SIG, na qual não existem acessos trafegáveis, impossibilitando o estudo nesta região. Portanto, a pesquisa se concentrou na porção centro-leste da SIG. Partindo de Belém, o acesso à área pode ser feito por via terrestre ou aérea até as cidades de Marabá ou Parauapebas (Núcleo urbano de Carajás). Saindo de Marabá, o acesso terrestre à área de trabalho pode ser feito pela PA-150 (BR-155), até Eldorado dos Carajás, e, a seguir, pela PA-275 até a cidade de Parauapebas (Fig. 1b). O principal acesso para o interior da área se faz pela estrada pavimentada que conduz à mina de cobre do Salobo (estrada Paulo Fonteles) que secciona a área de estudo no sentido Leste-Oeste. Além dessa via principal, a área é cortada a partir dela por diversas estradas vicinais não pavimentadas e por caminhos trafegáveis (Fig. 2).

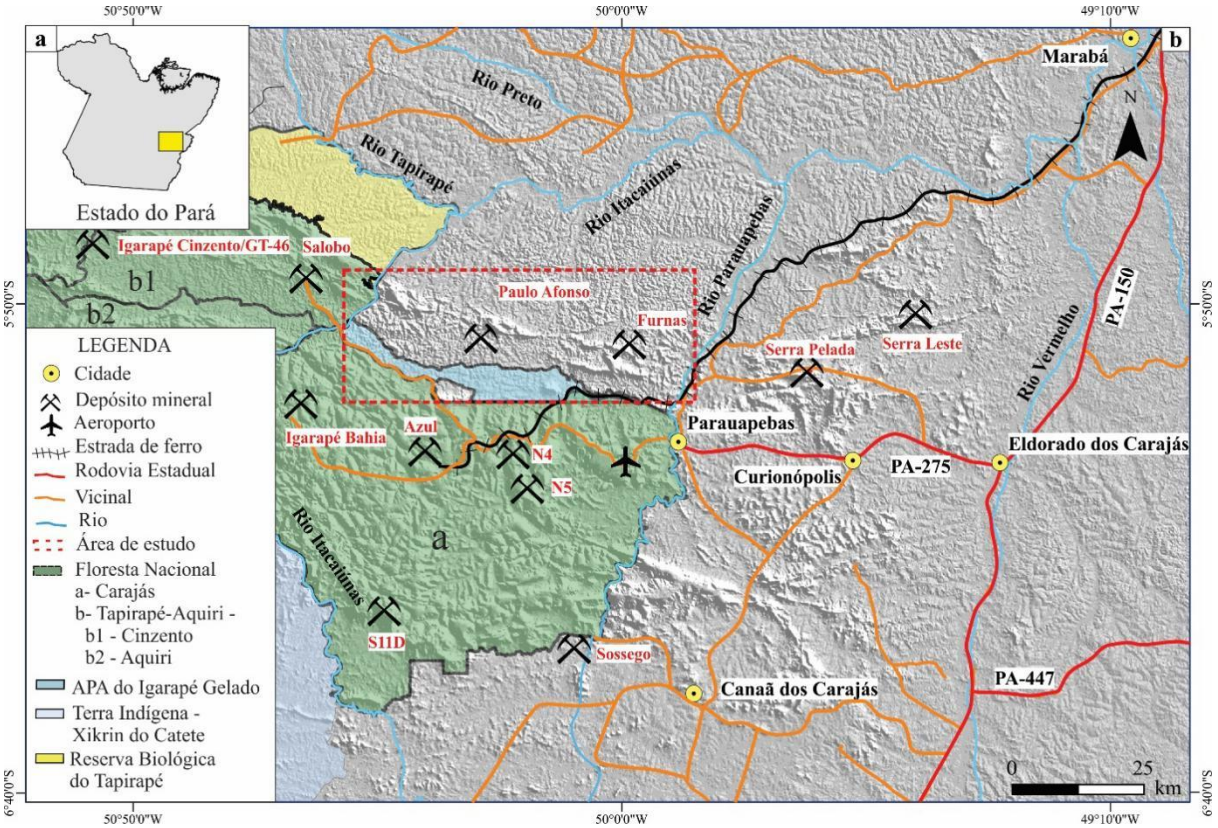

Figura 1- a) Localização da região estudada no estado do Pará; b) Mapa de localização com relevo ao fundo (SRTM) e ênfase para as principais cidades, rodovias e depósitos minerais próximos à área de estudo. Em destaque as unidades de conservação ambiental.

1.3 CONTEXTO GEOLÓGICO REGIONAL

A Província Carajás (PC) está situada na porção sul-oriental do Cráton Amazônico, sudeste do estado do Pará (Fig. 2 a, b). É delimitada a norte pelo Domínio Bacajá, o qual ocorre no extremo sul da província Transamazonas (Santos *et al.* 2006) ou Maroni-Itacaiúnas (Tassinari & Macambira 2004); a sul faz fronteira com o Domínio Santana do Araguaia (Santos *et al.* 2006); a leste é cavalgada pelo Cinturão Araguaia; e a oeste limita-se com a Província Amazônia Central (Santos *et al*. 2006). Ao longo das últimas décadas a PC tem sido alvo de estudos geológicos, geofísicos e estruturais, principalmente devido à sua importância metalogenética. Estes estudos embasaram várias propostas de compartimentação da PC em segmentos crustais tectonicamente distintos (Costa *et al.*1995, Souza *et al.* 1996a, Althoff *et al.* 2000, Vasquez & Rosa-Costa *et al.* 2008, Dall'Agnol *et al.* 2006, 2013, Costa *et al*. 2020b). Souza *et al.* (1996a) e Althoff *et al.* (2000) dividiram a PC em dois blocos, Terreno Granito-*Greenstone* de Rio Maria (TGGRM) a sul e Bloco Carajás a norte. O TGGRM seria formado por rochas mais antigas e de características ígneas preservadas, ao passo que a porção norte compreenderia um embasamento mesoarqueano, afetado por eventos

tectonotermais de idade neoarqueana, que inclui uma vasta sequência vulcanossedimentar e granitoides sintectônicos. Posteriormente, Santos (2003) propôs a divisão da província em dois domínios tectônicos distintos: Domínio Rio Maria (DRM) de idade mesoarqueana (2.98 – 2,85 Ga) e Domínio Carajás (DC), formado por rochas mesoarqueanas e neoarqueanas (3,0 – 2,76 Ga) (Fig. 2c, subdivisão em vermelho). No entanto, com avanço dos estudos o DC foi subdivido em Bacia Carajás (BC), a norte, e Subdomínio de Transição (SDT), a sul, o qual, inicialmente foi interpretado como um possível prolongamento do DRM afetado pelos eventos neoarqueanos que moldaram a BC (Dall'Agnol *et al.* 2006). Porém, estudos realizados mais recentemente, levaram Dall'Agnol *et al.* (2013) a propor que o SDT corresponderia a dois domínios geológica e tectonicamente distintos, denominados de Domínio Sapucaia (DS) a sul e Domínio Canaã dos Carajás (DCC) a norte. O primeiro apresenta fortes analogias litológicas com o DRM, no entanto, diferencia-se dele por apresentar rochas intensamente recristalizadas afetadas por eventos de migmatização no final do Mesoarqueano (Suíte Migmatítica Caracol) e por magmatismo do Neoarqueano (Suíte Vila Jussara) (Teixeira *et al.* 2013, Sousa *et al.* 2013, Gabriel & Oliveira 2014, Silva *et al.* 2014, Leite-Santos & Oliveira 2014, 2016, Souza *et al.* 2017, Dall'Agnol *et al.* 2017, Santos *et al.* 2018, Silva *et al.* 2020, 2025). O DCC apresenta características peculiares, sendo o provável embasamento da BC e seria geologicamente distinto dos demais domínios por apresentar dominância de granitos *stricto sensu* e possuir associações charnoquíticas, migmatitos, granulitos, com raras ocorrências de TTG e *greenstone belts* (Pidgeon *et al.* 2000, Feio *et al.* 2012, 2013, Rodrigues *et al.* 2014, Marangoanha *et al.* 2019a, 2019b, 2020, Felix *et al.* 2020, Silva-Silva *et al.* 2020, 2025, Silva *et al.* 2021). Oliveira *et al*. 2023 e Ribeiro-Silva *et al*. (2022) seguem em linhas gerais a proposta de Dall'Agnol *et al*. (2013), mas adotam as denominações de Terreno gnáissico migmatítico Sapucaia e Terreno granítico-granulítico Canaã dos Carajás (Fig. 2c, linhas tracejadas em preto). A nomenclatura das unidades que compõem estes terrenos foi simplificada por esses autores e serão as adotadas neste trabalho. A BC a norte compreende sequências metavulcanossedimentares neoarqueanas com idade mínima de 2,76 Ga, intrudido por magmatismo bimodal (rochas máfico-ultramáficas e granitos subalcalinos) (Docegeo 1988, Machado *et al.* 1991, Barros *et al.* 2009, Martins *et al.* 2017, Tavares *et al.* 2018).

Atualmente, vêm sendo desenvolvidos trabalhos baseados em imagens aerogeofísicas associadas a dados gravitacionais (Oliveira *et al.* 2018c; Costa *et al*. 2020b), os quais sugerem que durante o Mesoarqueano no Domínio Rio Maria predominou a arquitetura em domos e quilhas, resultado de regime de tectônica vertical. Contudo, com a diminuição progressiva do

gradiente geotérmico, este regime evoluiu gradativamente para condição similar à da tectônica moderna, envolvendo tectônica de placas e processos de subducção. Tais autores admitem que esta transição ocorreu entre 3.0 a 2.5 Ga. Neste contexto, os TTGs mesoarqueanos que ocorrem a sul do antigo Domínio Carajás também teriam sido formados em regime de tectônica vertical, porém foram afetados por eventos neoarqueanos, caracterizados por intrusões sintectônicas (~2,75 Ga) com zonas de cisalhamento associadas (Costa *et al*. 2020b), ao passo que a granitogênese neoarqueana e paleoproterozoica da Bacia Carajás já se adequaria melhor ao estilo da moderna tectônica de placas.

1.3.1 Terreno granito-*greenstone* Rio Maria

O Terreno granito-greenstone Rio Maria (TGGRM) está localizado na porção sul da Província Carajás e corresponde a uma crosta essencialmente mesoarqueana (Fig. 2c) (Macambira & Lafon 1995, Macambira & Lancelot 1996, Dall'Agnol *et al.* 2006, Vasquez & Rosa-Costa *et al.* 2008; Oliveira *et al*. 2011, Almeida *et al*. 2011, 2013). É formado por *greenstone belts* (3,0 a 2,9 Ga; Macambira & Lancelot 1991, Araújo & Maia 1991, Pimentel & Machado 1994; Avelar 1996; Lafon *et al.* 2000; Rolando & Macambira 2003) e por suítes de granitoides diversos, similares àqueles caracterizados nos terrenos arqueanos clássicos.

Greenstone belts: De acordo com Silva *et al.* (2021) os *greenstone belts* do TGGRM são subdivididos nos grupos **Tucumã-Gradaús e Andorinhas** que incluem as formações Babaçu, Lagoa Seca e Tucumã. Souza *et al.* (2001) descreveram em detalhe o *greenstone belt* Identidade, o qual faz parte do Grupo Babaçu e encontra-se exposto a sul de Xinguara.

Magmatismo máfico ultramáfico: no TGGRM é representado pelos **complexos mesoarqueanos Guara-Pará** e **Serra Azul** (~2.97 Ga, Pimentel & Machado 1994, Vasquez & Rosa-Costa. 2008, Santos-Silva *et al*. 2021).

Associações TTG: Suíte Mogno composta pelo **Trondhjemito Mogno** (2,97–2,92 Ga; Docegeo 1988, Almeida *et al.* 2011), **Tonalito Arco Verde** (2,98–2,92 Ga; Althoff *et al.* 1994, Almeida *et al.* 2011), **Tonalito Carapanã** (~2,92 Ga; Oliveira *et al.* 2023) e **Tonalito Mariazinha** que também aflora subordinadamente no Terreno Sapucaia (~2,92 Ga; Guimarães *et al.* 2010, Almeida *et al.* 2011).

Sanukitoides: Suíte Rio Maria (Oliveira M.A. *et al.* 2011, Oliveira D.C. *et al.* 2023), composta pelo **Granodiorito Rio Maria** (2,88–2,85 Ga; Dall´Agnol *et al.* 1986, Docegeo 1998, Avelar *et al.* 1999, Vasquez & Rosa-Costa 2008, Oliveira M.A. *et al.* 2009, 2010, 2011, Santos & Oliveira *et al.* 2016) e rochas intermediárias associadas (2.88-2.87 Ga; Oliveira *et al.* 2011). Além do **Granito Rancho de Deus** (~2,89 Ga; Dias S.B. 2009,

Almeida *et al.* 2013), **Quartzo-Diorito Parazônia** (2,87–2,85 Ga; Pimentel & Machado 1994, Guimarães *et al.* 2010) e **Granodiorito Cumaru** (2,81 Ga; Lafon & Scheller 1994). Um pequeno corpo do Granodiorito Rio Maria aflora dentro do Terreno Sapucaia, próximo ao limite do TGGRM.

Leucogranitoides com alto Ba e Sr: Suíte Guarantã (Almeida *et al*. 2013, Oliveira *et al*. 2023), composta pelo **Granito Guarantã** (2,87–2,86 Ga; Almeida *et al*. 2013), **Granodiorito Trairão** (~2,87 Ga; Almeida *et al*. 2013), **Granodiorito Azulona** (não datado; Almeida *et al.* 2013) e **Granodiorito Grotão (**2,94 Ga; Machado *et al*. 2023, Guimarães *et al*. 2010) que aflora essencialmente no TGGRM, mas possui um pequeno corpo dentro dos limites do Terreno Sapucaia.

Suíte Tucumã (Oliveira *et al*. 2023, Ribeiro-Silva *et al*. 2022): é caracterizada por altos conteúdos de TiO_2 e HFSE e é composta por **pequenos plútons** (2,86–2,84 Ga; Souza D.B. 2018) que ocorrem intimamente relacionados ao Granito Manelão aflorante a oeste de Tucumã e incluído na Suíte Granítica Xinguara (Oliveira *et al*. 2023) e ao Granito Boa Sorte incluído na Suíte Granítica Canaã dos Carajás que faz parte do Terreno homônimo (Ribeiro-Silva *et al*. 2022)

Suíte Xinguara (Almeida *et al*. 2013): ocorre nos terrenos Rio Maria e Sapucaia e é composta pelo **Granito Xinguara** (~2,86 Ga; Leite *et al*. 2004), **Granito Mata Surrão** (2,88–2,87 Ga; Althoff *et al*. 1998, Rolando & Macambira 2003) e **Granito Manelão** (~2,90 Ga; Oliveira *et al*. 2023).

Granitos anorogênicos paleoproterozoicos: são representados pelos corpos **Seringa** (Paiva Jr. *et al.* 2011) e **São João** (Lima *et al.* 2014) da Suíte Serra dos Carajás e **Velho Guilherme** pertencente a suíte homônima (Teixeira *et al*. 2002), além dos granitos da Suíte Jamon, que incluem os **granitos Musa, Jamon, Gradaús, Marajoara, Manda Saia, Bannach** e **Redenção**, associados a diques félsicos a máficos (Rivalenti *et al.*1998, Dall'Agnol *et al.* 2005, Silva *et al.* 2016, Teixeira *et al.* 2018; Santos *et al*. 2023).

Coberturas sedimentares paleoproterozóicas: são representadas pelas sequências do **grupos Rio Fresco** e **Gemaque** (Santos & Pena Filho 2000) sucedidas por conglomerados da **Formação Gorotire** (Barbosa *et al*. 1966, Vasquez & Rosa-Costa 2008, Santos-Silva *et al*. 2021). Essas sequências são compostas por conglomerados e arenitos na base e pelitos carbonáticos no topo (Marinho *et al*. 1977, Cunha *et al*. 1984, Ramos *et al*. 1984, Macambira *et al*. 1986, Santos & Pena Filho 2000, Santos-Silva *et al*. 2021).

1.3.2 Terreno gnáissico migmatítico Sapucaia

Este é um segmento crustal com geometria e trama de direção E-W, com

predominância de suítes TTG, similar ao TGGRM, e conforme discutido anteriormente, foi afetado por eventos de migmatização no Mesoarqueano e magmatismo no Neoarqueano. A seguir serão apresentadas as principais unidades do Terreno Sapucaia, com exceção daquelas que também ocorrem no TGGRM, citadas anteriormente.

Greenstone belts: Representados pelo **Grupo Sapucaia**, que compreende metamafitos, metaultramafitos e rochas metassedimentares, com paragênese de fácies xisto verde a anfibolito (Araújo & Maia 1991, Docegeo 1988, Costa *et al.* 1994, Oliveira D.C *et al.* 2010, Feio *et al.* 2013, Sousa *et al.* 2013, Marangoanha & Oliveira 2014, Souza *et al.*2017).

Complexo Caracol: compõe o embasamento TTG do Terreno Sapucaia (Oliveira *et al.* 2023) e é composto por cinco unidades litoestratigráficas denominadas **Ortognaisse Caracol** (2,94–2,93 Ga; Almeida *et al*. 2011), **Ortognaisse Água Azul** (2,93 Ga; Santos *et al*. 2018, Oliveira *et al*. 2023), **Ortognaisse Colorado** (2,94-2,93 Ga; antes denominado como Trondhjemito Colorado; Santos *et al.* 2013a, Silva *et al.* 2014, Nascimento *et al*. 2023); **ortognaisse Bom Jesus** (Ribeiro-Silva *et al*. 2023) que ocorre no Terreno Canaã dos Carajás
e Ortognaisse São Carlos (2.94-2,93 Ga; Silva *et al.* 2014, Guimarães F.V. não-publicado, Oliveira *et al*. 2023, Nascimento *et al.* 2023)

Suíte Água Limpa (Oliveira *et al.* 2023; Nascimento *et al*. 2024): Agrupa rochas sanukitoides e é composta pelos batólitos do **Granodiorito Água Limpa** (~2,87 Ga; Gabriel & Oliveira 2014) e **Granodiorito Água Azul** (~2,87 Ga; Gabriel & Oliveira 2014).

Suíte Nova Canadá (Oliveira *et al.* 2023): tem afinidade com os TTG transicionais (Leite-Santos & Oliveira 2016, Leite-Santos 2016, Machado *et al.* 2021) e é composta pelos granodioritos **Bonito** (~2,87 Ga; Silva & Oliveira 2013, Leite-Santos 2016) e **Carapanãzinho** (2,85–2,84 Ga; Silva-Silva *et al.* 2020, Silva-Silva em preparação) que ocorrem no Domínio Rio Maria, e pelos granodioritos **Nova Canadá** (2,89–2,87 Ga; Leite-Santos & Oliveira 2016, Leite-Santos 2016) e **Pantanal** (~2.87(?); Teixeira *et al.* 2013, Leite-Santos *et al*. 2023) que afloram no Terreno Sapucaia.

Magmatismo máfico e ultramáfico: é representado pelo **anfibolito Surucucu** do Mesoarqueano (Souza *et al*. 2017) e **Peridotito Fafá,** recentemente datado com idade de cristalização de 2,75 Ga e de recristalização 2,72 Ga (Santos-Silva *et al*. 2023)

Suíte Vila Jussara: Foi inserida na Supersuíte Planalto e é formada por granitoides com afinidade com granitos tipo A associados a stocks enderbíticos da Suíte Pium (Teixeira *et al*. 2013, Dall Agnol *et al*. 2017). Informações mais detalhadas acerca desta unidade são apresentadas a seguir no tópico sobre o conjuntos dos granitos neoarqueanos da Província

Carajás.

Granito anorogênico paleoproterozoico: é prepresentado pelo **granito Gogó da Onça** (Teixeira *et al*. 2017) pertencente a suíte Granítica Serra dos Carajás.

1.3.3 Terreno granítico-granulítico Canaã dos Carajás

O TGGCC (Fig 2c) é formado por unidades mesoarqueanas intrudidas por granitoides neoarqueanos (Oliveira *et al.* 2010, Moreto *et al.* 2011, Santos *et al.* 2013a, Feio *et al.* 2013, Rodrigues *et al*. 2014, Dall' Agnol *et al.* 2013, 2017, Marangoanha *et al*. 2019a).

Este domínio compreende granitoides arqueanos e, subordinadamente, rochas granulíticas, charnoquíticas e rochas máficas a ultramáficas (Vasquez & Rosa-Costa *et al.* 2008). A seguir serão apresentadas as principais unidades do Terreno Canaã dos Carajás, com exceção daquelas já mencionada anteriormente, que também ocorrem no Terreno Sapucaia.

Complexo Chicrim-Cateté, integra os núcleos granulíticos do Terreno Canaã dos Carajás (Oliveira *et al.* 2023), e é composto pelos corpos do **Granulito Chicrim-Cateté** (Araújo & Maia 1991, Vasquez & Rosa-Costa 2008, Silva *et al*. 2021), anteriormente considerados como fazendo parte do Complexo Pium (3,00 a 2,85 Ga, Pidgeon *et al.* 2000, Araújo & Maia 1991) e **Granulito Ouro Verde** (Marangoanha *et al.* 2019b, Oliveira *et al.* 2023), cujo protólito forneceu idade de 3,07–2,93 Ga (Pidgeon *et al.* 2000, Marangoanha *et al.* 2019b, Silva *et al.* 2021), enquanto o metamorfismo granulítico regional teve idade estimada entre 2,89–2,84 Ga (Pidgeon *et al.* 2000, Marangoanha *et al.* 2019b, Silva *et al.* 2021).

Complexo tonalítico Bacaba (Protólito de ~3,00 Ga; Moreto *et al.* 2011, Feio *et al.* 2013).

Greenstone belts: representados pelos grupos **Sequeirinho** (>2,97 Ga Tavares 2014, 2015) e **Rio Novo** (não datado; Hirata *et al.* 1982, Meireles *et al.* 1982, Araújo & Maia 1991, Oliveira *et al.* 1994, Costa *et al.* 2016), o qual também ocorre na Bacia Carajás.

Complexo Xingu Indiferenciado: representa o embasamento do Domínio Carajás e foi definido como ortognaisses e migmatitos mesoarqueanos, bimodais em decorrência da presença de anfibolitos (Vasquez & Rosa-Costa 2008). Nas últimas décadas, a área de ocorrência deste complexo tem sido radicalmente reduzida, devido à individualização de diferentes unidades a partir do mesmo. As idades do protólito variam de 3,07-2,93 Ga (Tavares 2015).

Suíte Rio Verde (Oliveira *et al.* 2023, Ribeiro-Silva *et al*. 2022), possui afinidade com as sequências TTG e é composta pelo **Trondhjemito Rio Verde** (2,92–2,84 Ga; Feio *et al.* 2013), **Trondhjemito Ourilândia** (~2,92 Ga; Ribeiro-Silva *et al*. 2022) e **Trondhjemito**

Água Fria (2,86–2,84 Ga; Macambira *et al.* 2000, Leite *et al.* 2004, Almeida *et al.* 2011), este situado no Terreno Sapucaia.

Suíte Ourilândia é composta pelo **Granodiorito Arraias** (~2,92; Ribeiro-Silva *et al*. 2023), **Granodiorito Ourilândia** (2,88-2,87 Ga Ga; Ribeiro-Silva *et al*. 2023) e **Complexo Campina Verde** (2,87–2,85 Ga; Feio *et al.* 2013, Moreto *et al.* 2015a, Oliveira *et al.* 2023)

Suíte Canaã dos Carajás (Ribeiro-Silva *et al*. 2022): engloba granitos com assinatura cálcico-alcalina e é formada por quatro unidades litoestratigráficas mesoarqueanas: (i) **Granito Canaã dos Carajás** (2,95-2,92 Ga; Feio *et al*. 2013); (ii) **Granito Cruzadão** (2,87–2,84 Ga, Feio *et al*. 2013); (iii) **Granito Boa Sorte** (2,89– 2,84 Ga; Rodrigues *et al.* 2014, Ribeiro-Silva *et al*. 2022); (iv) **Granito Serra Dourada** (2,86–2,83 Ga; Moreto *et al.* 2011, Feio *et al.* 2013); e uma neoarqueana, (v) **Granito Velha Canadá** (2,73–2,75 Ga Leite-Santos & Oliveira 2016, Leite-Santos *et al*. 2023).

Supersuíte Planalto (Félix *et al*. 2023): é formada por suítes que afloram no Terreno Canaã dos Carajás como a **Suíte Granítica Planalto** (2,75–2,74 Ga; Huhn *et al*. 1999, Sardinha *et al*. 2004, Feio *et al*. 2012) associada ao **Trondhjemito Pedra Branca** (~2,76 Ga; redefinido a partir da Suíte Pedra Branca; Feio *et al.* 2013, Santos-Silva et al., 2020, Oliveira *et al.* 2023), **Suíte Vila União** (2,75–2,73 Ga; Oliveira *et al*. 2018a, Marangoanha *et al*. 2019a, 2020) e por suítes e granitos que ocorrem na Bacia Carajás como a **Suíte Igarapé Gelado**, **Complexo Granítico Estrela** e **Granito Serra do Rabo**. Todos estes granitos serão abordados detalhadamente em tópico a seguir.

S**uíte Pium** (Oliveira *et al.* 2023): representa o magmatismo charnoquítico da Província Carajás e é composta pelos corpos do **Diopsídio-Norito Pium** (2,74– 2,73 Ga; Ricci 2006, Feio *et al.* 2012, Santos *et al.* 2013b), **Enderbito Café** (2,75–2,73 Ga; Marangoanha *et al.* 2019b, 2022), **Charnoquito Rio Seco** (de idade indefinida; Felix *et al.* 2020, Oliveira *et al.* 2023).

Magmatismo máfico-ultramáfico: é formado por plútons alongados da **Suíte Intrusiva Cateté** (~2,76 Ga, Lafon *et al.* 2000) e rochas metaultramáficas do **Complexo Vermelho**.

Suíte Plaquê (2,73–2,72 Ga): formada por corpos alongados segundo orientação E-W, (Araújo & Maia 1991, Avelar 1996, Macambira & Vale 1997, Avelar *et al.* 1999, Vasquez & Rosa-Costa, 2008) interpretados como produto de retrabalhamento crustal. Grande parte dos granitos originalmente incluídos nesta suíte, em função da redefinição de sua assinatura geoquímica fazem atualmente parte da Supersuíte Planalto.

Recentemente, porções do complexo Xingu no oeste do Domínio Canaã dos Carajás, foram redefinidos como **Gnaisse Nova Índia** e **Complexo Carapanã** (Costa *et al*. 2016), sendo este último formado por granodioritos e subordinados tonalitos, isotrópicos a levemente foliados.

1.3.4 Bacia Carajás

A Bacia Carajás (BC) situa-se na porção norte da Província Carajás (Fig. 2c) e é constituída principalmente por unidades supracrustais neoarqueanas, representadas por vulcanismo máfico a intermediário e formações ferríferas bandadas do Grupo Grão-Pará (Gibbs *et al.*1986, Teixeira & Egler 1994, Wirth *et al.* 1986, Machado *et al.* 1991, Vasquez & Rosa-Costa *et al.* 2008, Martins *et al.* 2017). Estas são cortadas por intrusões máfico-ultramáficas (Complexo Luanga e Gabro Santa Inês) e por granitos neoarqueanos, incluindo os da Suíte Igarapé Gelado alvo deste estudo e granitos do Complexo Estrela, granitos Serra do Rabo, Old Salobo, Itacaiúnas, Gt-46, Rio Sereno, Lavrado (Machado *et al.* 1991, Souza *et al.* 1996b, Sardinha *et al.* 2006, Barros *et al.* 2009, Melo *et al.* 2016, Silva *et al*. 2023) e paleoproterozoicos (Suíte Serra dos Carajás; Gonçalez *et al.* 1988, Javier Rios *et al.* 1994a, b, Dall'Agnol *et al.* 2005, Teruiya *et al.* 2008). A síntese dos dados geocronológicos das unidades metavulcanossedimentares neoarqueanas da Província Carajás pode ser consultada na tabela 1.

Supergrupo Itacaiúnas: é uma sequência de rochas metavulcanossedimentares que ocorre em grande parte da BC e cujas idades se encontram sumarizadas na tabela 1. Conforme o reagrupamaento realizado por Costa *et al*. (2016) compreende: (1) **Grupo Grão Pará (**2,76-2,74 Ga) que representa as sequências de base compostas por rochas (meta) vulcânicas máficas a ácidas (**Formação Parauapebas**) e ao menos um horizonte de formações ferríferas bandadas (**Formação Carajás**), além de anfibolitos e quartzitos da **Formação Tapirapé** (Gibbs *et al.* 1986, Docegeo 1988, Machado *et al.* 1991, Trendall *et al.* 1998, Krymsky *et al.* 2002, Martins *et al.* 2017). (2) o **Grupo Serra da Bocaína** (2,77-2,73 Ga) que representa sequências de topo, constituídas por formações dominantemente (meta) sedimentares clasto-químicas com contribuições vulcânicas interdigitadas (**Formações Igarapé Cigarra, Salobo-Pojuca, Igarapé Bahia**, Machado *et al.* 1991, Pimentel *et al.* 2003, Lobato *et al.* 2005, Tallarico *et al.* 2005, Galarza *et al.* 2008). (3) a **Formação Buritirama**, uma sequência marinha plataformal que aflora no extremo norte da PC (Salgado *et al*. 2019a, 2019b, 2021, 2023). Dois modelos tectônicos foram sugeridos para geração das sequências metavulcanossedimentares. O primeiro indica uma evolução relacionada a ambiente de rifte

continental (Gibbs *et al*. 1986, Docegeo 1988, Olszewski *et al*. 1989, Oliveira *et al*. 1993, Macambira J.B. 2003, Martins *et al.* 2017, Tavares *et al*. 2018), enquanto um segundo modelo admite ambiente de arcos magmáticos (Meirelles & Dardenne 1991, Teixeira 1994, Lindenmayer *et al*. 2005, Lobato *et al*. 2005, Zucchetti 2007).

Magmatismo máfico-ultramáfico: é composto por rochas ultrabásicas e básicas acamadadas do **Complexo intrusivo Luanga** (Medeiros Filho & Meireles 1985) cuja datação por U-Pb em zircão, forneceu idade de 2763±6 Ma (Tab. 1), interpretada como a idade de cristalização/intrusão destas rochas (Machado *et al*. 1991), e pelo **Gabro Santa Inês**, representado por gabros e anortositos (Vasquez & Rosa-Costa 2008).

As unidades arqueanas são parcialmente recobertas pela extensa sedimentação paleoproterozoica da Formação **Água Claras** (>2,06 Ga; Fabre *et al.* 2011, Tavares *et al.* 2018, Araújo & Sousa 2018, Araújo-Filho *et al.* 2020), **Formação Serra Sul** (2,58–2,06 Ga; Araújo & Nogueira 2019), **Formação Azul (**2,37–2,06 Ga Araújo-Filho *et al.* 2020), e **Formação Caninana** (2,01–1,88 Ga, Pereira *et al.* 2009, Tavares *et al.* 2018). Pontualmente, nos domínios da formação Águas Claras, aflora a **Formação Igarapé Boa Sorte** e a norte, no limite com Domínio Bacajá, ocorre o **Grupo Paredão** (Costa *et al*. 2016). Em geral estas unidades são formadas por sedimentos plataformais marinhos, submarinos glacial a subglacial costeiros e de ambientes continentais relacionados a leques aluviais e a ambiente fluvial entrelaçado e fluvial do tipo *braided.*

Granitos tipo-A anorogênicos paleoproterozoicos: Representado por plutons da Suíte Serra dos Carajás (1,87-1,88 Ga, **granitos Serra dos Carajás, Pojuca, Formiga e Cigano**, Machado *et al*. 1991, Teixeira *et al*. 2018, Dall'Agnol *et al*. 2005).

Recentemente, Costa *et al*. (2016) descreveram no extremo oeste da área (Fig. 2c), sequências metavulcanossedimentares dos grupos **Liberdade** e **Aquiri**. Estes estão espacialmente associados ao Metagranito Lavrado (2,65 Ga, Silva *et al*. 2023), bem como a rochas vulcânicas félsicas da **Formação Santa Rosa.**

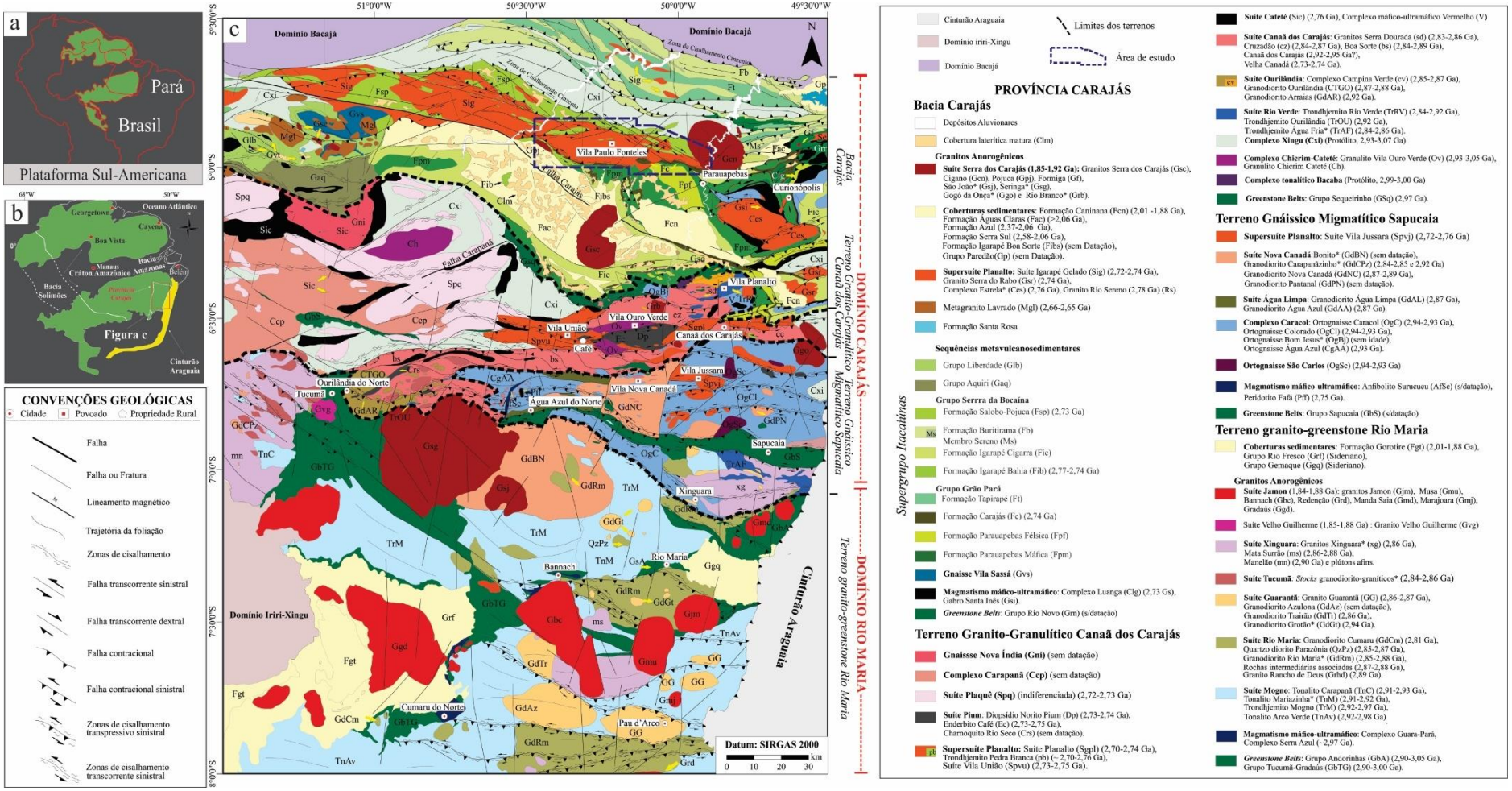

Figura 2- a) Mapa de localização do Cráton Amazônico. B) Mapa de localização da Província Carajás no Cráton Amazônico. c) Mapa geológico integrado da Província Carajás (modificado de Costa *et al*. 2016, Oliveira *et al*. 2023). Os terrenos Granito Greenstone Rio Maria, Sapucaia e Canaã dos Carajás são baseados em Oliveira *et al*. (2023). A Bacia Carajás e a porção oeste do Domínio Canaã dos Carajás estão de acordo com Costa *et al.* (2016). * Podem ocorrer em Terrenos/ Unidades diferentes da indicada na legenda. Ver Mapa.

1.3.5 Granitoides Neoarqueanos de Carajás

A granitogênse neoarqueana (~2,75 – 2,55 Ga) da Província Carajás é marcada por um expressivo volume de rochas que seccionaram unidades mesoarqueanas e neoarqueanas dos Terrenos Sapucaia, Canaã dos Carajás e Bacia Carajás (Fig. 2c). As rochas plutônicas formadas neste período são representadas por 6 tipos de granitoides: (i) granitos metaluminosos a levemente peraluminosos afins dos granitos tipo A; (ii) granitos peralcalinos a metaluminosos; (iii) granitos calcico-alcalinos; (iv) rochas charnoquíticas e enderbíticas; (v) granitoides sódicos de assinatura toleítica; e (vi) metagranitoides indiferenciados. A síntese dos dados geocronológicos do magmatismo neoarqueano de Carajás pode ser consultado na tabela 1.

1.3.5.1 Granitos metaluminosos a peraluminosos afins dos granitos tipo A

Recentemente, em função de suas notáveis afinidades, estes granitos foram agrupados na **Supersuíte Planalto** (Felix *et al*. 2023a, Oliveira *et al*. 2023). São constituídos por batólitos e *stocks* alongados, orientados nas direções WNW-ESE a E-W, estando suas rochas afetadas por zonas de cisalhamento, intensamente foliadas, e, por vezes, milonitizadas (Fig. 2c). São formados dominantemente por monzogranitos a sienogranitos, com tonalitos, granodioritos, álcali-feldspato granitos e quartzo dioritos subordinados. Anfibólio e biotita figuram como as principais fases máficas. Clinopiroxênio e ortopiroxênio são raros ou ausentes e, quando ocorrem, se apresentam em forma reliquiar parcialmente substituídos por anfibólio. Os minerais acessórios primários são zircão, apatita e ilmenita geralmente associadas a titanita, allanita e, por vezes, magnetita. A maioria dessas rochas possui afinidade com os granitos tipo A ferrosos reduzidos (Barros *et al.* 1997, 2001, 2009, Sardinha *et al.* 2006, Feio *et al.* 2012, 2013, Cunha *et al.* 2016), exceto aquelas das Suítes Vila Jussara e Igarapé Gelado e granitoides de Vila União que apresentam também granitos ferrosos oxidados e, no caso da primeira, magnesianos (Barros *et al.* 2009; Oliveira *et al.* 2018a, Dall'Agnol *et al.* 2017, Marangoanha *et al.* 2019). No geral, são metaluminosos a peraluminosos. A principal hipótese para explicar a origem dos magmas dos granitos neoarqueanos Estrela, Serra do Rabo, Planalto e Vila Jussara admite sua derivação por fusão parcial de crosta granulítica enriquecida (Barros *et al.* 2009; Feio *et al.* 2012, Dall'Agnol *et al.* 2017). Além disso, pesquisas recentes admitem que as rochas das suítes Vila Jussara e Vila União apresentam evidências do processo de mistura de magmas em sua origem (Marangoanha *et al.* 2018, Silva *et al.* 2025). As fontes granulíticas dos magmas dos granitos reduzidos teriam caráter toleítico e, portanto, reduzido, porém, no caso específico da Suíte

Vila Jussara, elas seriam, localmente, cálcico-alcalinas e oxidadas (Dall'Agnol *et al.* 2017). Esta crosta granulítica teria sido formada devido à colisão do Domínio Rio Maria com a porção norte da Província Carajás, no Mesoarqueano (~2,85 Ga.; Sardinha *et al.* 2006, Tavares 2015). Posteriormente, com o fechamento da Bacia Carajás, por processos colisionais, foram gerados em ambiente sintectônico granitos neoarqueanos, deformados durante a colocação e resfriamento do magma (Barros *et al.* 2009). Uma segunda hipótese admite que estes granitos sejam oriundos de intrusões em ambiente extensional e foram, posteriormente, deformados e metamorfisados com o fechamento da Bacia Carajás em torno de 2,68 Ga (Tavares 2015).

Suíte Planalto

Esta suíte ocorre no domínio Canaã dos Carajás e é formada por pequenos plutons lenticulares de até 10 km de extensão, intrusivos em granitoides mesoarqueanos e em unidades supracrustais neoarqueanas do Supergrupo Itacaiúnas (Fig. 2c). Apresentam foliação subvertical penetrativa e, por vezes, lineação mineral de alto ângulo, bem como bandas de cisalhamento tipo-C (Feio *et al.* 2012). Os milonitos evidenciam movimentação sinistral e, subordinadamente, dextral. As rochas dessa suíte estão espacialmente associadas com o **Diopsídio Norito Pium** e o ***Trondhjemito Pedra Branca,*** ambos com assinatura toleítica. São observadas evidências de *mingling* entre o Granito Planalto e charnoquitos máficos a intermediários do Pium (Feio *et al.* 2012, 2013). A Suíte Planalto é composta por sienogranitos e monzogranitos com álcali-feldspato granitos subordinados (Feio *et al.* 2012, Cunha *et al.* 2016). Os anfibólios são K-hastingsita a Cl-K-hastingsita e possuem razão Fe/(Fe+Mg) > 0,8. A biotita também exibe alta razão Fe/(Fe+Mg) e foi classificada como annita (Cunha *et al.* 2016). Cunha *et al.* (2016) definiram dois grupos de rochas baseados na suscetibilidade magnética (SM): (1) granitos com ilmenita com baixa suscetibilidade magnética (SM) e (2) granitos com magnetita e ilmenita com SM comparativamente alta, porém moderada. Os parâmetros de cristalização obtidos para o magma Planalto foram: pressão de geração de 900 a 700 MPa e de colocação entre 500 a 300 Mpa; temperaturas iniciais de cristalização entre 900°C e 830°C e o conteúdo estimado de água no magma de 4%. Apresenta idades de cristalização entre 2,74 e 2,71 Ga (Huhn *et al.* 1999, Gomes, 2003, Sardinha *et al.* 2004, Feio *et al.* 2012, Galarza *et al.* 2017, Tab. 1)**.**

Tabela 1- Síntese dos dados geocronológicos em zircão do magmatismo e das unidades metavulcanossedimentares neoarqueanas da Província Carajás.

(continua)

Terreno Sapucaia				
Suítes/Grupos	**Corpos/Unidades**	**Litologia**	**Método**	**Idade/Referências**
Suíte Granítica Canaã dos Carajás	Granito Velha Canadá	Granodiorito	Evaporação de Pb	2733±1 Ma (1)
		Granodiorito	Evaporação de Pb	2747±2 Ma (2)
Suíte Vila Jussara*	Magnesiano	Hb-Bt monzogranito	Evaporação de Pb	2748±2 Ma (3)
		Hb-Bt monzogranito	Evaporação de Pb	2749±3 Ma (3)
		Bt-Hbl tonalito	U-Pb SHRIMP	2766±9 Ma (4)
			U-Pb SHRIMP	2769±9 Ma (5)
	Fe-Oxidado	Bt-Hbl monzogranito	Evaporação de Pb	2754±2 Ma (6)
		Bt-Hbl-monzogranito	U-Pb SHRIMP	2743±11 Ma (4)
	Fe-Reduzido	Bt-Hbl monzogranito	U-Pb SHRIMP	2743±9 Ma (5)
		Bt-Hbl-monzogranito	U-Pb SHRIMP	2745±20 Ma (4)
Suíte Pium	Enderbito de Sapucaia		Sem datação	
Magmatismo máfico ultramáfico	Peridotito Fafá	Peridotito serpentinizado	U-Pb SHRIMP	2757 ± 14 Ma (7)
Terreno Canaã dos Carajás				
	Diorito Cristalino	Diorito	Evaporação de Pb	2738±6 Ma (8)
	Granito Curral	Granito	U-Pb SHRIMP	2739±4M Ma (9)
	Granito Sossego	Granito	U–Pb LA–ICP–MS	2740±26 Ma (9)
Suíte Plaquê		Granitoide	Evaporação de Pb	2727±29 Ma (10)
		Granitoide	Evaporação de Pb	2736±24 Ma (10)
Suíte Vila União*		Quartzo diorito	U-Pb LA-ICP-MS	2734±9 Ma (11)
		Leucomonzogranito	U-Pb SHRIMP	2744±5 Ma (11)
		Bt-Hbl monzogranito	Evaporação de Pb	2746±1.2 Ma (11)
		Bt-Hbl monzogranito	U-Pb SHRIMP	2745±7,1Ma (12)
		Bt-Hb tonalito	U-Pb SHRIMP	2745±9,9Ma (12)
Suíte Planalto*		Granite	Evaporação de Pb	2747±2 Ma (8)
		Bt-Hb sienogranito (AMR-187B)	Evaporação de Pb	2733±2 Ma (13)
			U-Pb LA-MC-ICP-MS	2729±17 Ma (13)
			U-Pb SHRIMP	2738±3 Ma (14)
		Hb-Bt sienogranito (ARC-109)	Evaporação de Pb	2731±1 Ma (13)
			U-Pb LA-MC-ICP-MS	2710±10 Ma (13)
			U-Pb SHRIMP	2730±5 Ma (14)
		Bt sienogranito (GRD-77)	Evaporação de Pb	2736±4 Ma (13)
			U-Pb LA-MC-ICP-MS	2706±5 Ma (13)
		Bt-Hbl tonalito (AMD-01A)	Evaporação de Pb	2741±0,1 Ma (15)
		Bt-Hbl sienogranito (AMD-01B)	Evaporação de Pb	2730±0 Ma (15)
		Bt-Hbl monzogranito (AMD-02)	Evaporação de Pb	2731±0,8 Ma (15)
	Trondhjemito Pedra Branca	Trondhjemito	Evaporação de Pb	2749±6 Ma (18)
		Trondhjemito	U-Pb TIMS	2765±39 Ma (18)
		Trondhjemito (AMR-191A)	U-Pb LA-MC-ICP-MS	2750±5 Ma (14)
Suíte Pium	Enderbito Café	Opx-tonalito	U–Pb LA–ICP–MS	2730±7 Ma (16)
		Opx- trondhjemito	U-Pb SHRIMP	2740±8 Ma (10)
		Opx trondhjemito	Evaporação de Pb	2754±1 Ma (16)
	Diopsídio Norito Pium	Quartzo gabro	Evaporação de Pb	2744,2±1 Ma (17)
		Quartzo gabro	U-Pb ICPMS	2735±5Ma (13)
		Gabronorito	Evaporação de Pb	2744±0,8 Ma (17)
		Norito	Evaporação de Pb	2745±1,2 Ma (17)
		Granitoides associados	Evaporação de Pb	2732±1 a 2742 ±1 Ma (15)
	Charnoquito Rio Seco		Sem datação	
Suíte Cateté		Gabro	U-Pb SHRIMP	2766±6 Ma (19)

(conclusão)

Bacia Carajás				
Suítes/Grupos	**Corpos/Unidades**	**Litologia**	**Método**	**Idade/Referências**
Granitos associados a mineralizações IOCG	Granito Velho Salobo	Granitoide	U-Pb ID-TIMS	2573±3 Ma (20)
		Granitoide	U-Pb SHRIMP	2547±5 Ma (21)
		Granitoide	U-Pb SHRIMP	2551±9 Ma (21)
		Bt monzogranito	U-Pb LA-ICP_MS	2497±41 Ma (22)
		granodiorito a tonalito	U-Pb LA-ICP_MS	2554 ± 3, 2549 ± 7, 2594 ± 6 Ma (23)
	Depósito GT-46 (Granito Igarapé Cinzento)	Granito isotrópico	U-Pb LA-ICP_MS	2557±26 Ma (24) 2564 ± 4 Ma (23)
		Tonalito foliado	U-Pb LA-ICP_MS	2532±26, 2639±16 Ma (24) 2560 ± 3, 2576 ± 4 Ma (23)
		Pegmatito		2562 ± 39 Ma (24)
	Granito Itacaiúnas	Granitoide	Evaporação de Pb	2560±37 Ma, 2525 ± 38 (25)
Suíte Igarapé Gelado*		Monzogranito	Evaporação de Pb	2731±2 Ma (26)
		Tonalito foliado	U-Pb LA-ICP-MS	2680 ± 18, 2640 ± 16, 2623 ± 5, 2579 ± 28 Ma (23)
		Monzogranito Ultramilonitizado	U-Pb LA-ICP-MS	2561 ± 5 Ma (23)
		Granitoide milonitizado	U-Pb LA-ICP-MS	2701±30 Ma (21)
		Granitoide	U-Pb SHRIMP	2763 ± 4 Ma (21)
		Granitoide	U-Pb LA-ICP-MS	2744 ± 4, 2731 ± 7 Ma (23)
		Hb-Bt monzogranito	U-Pb SHRIMP	2682±25 Ma (22)
		monzogranito	U-Pb SHRIMP	2611±28, 2665±29 Ma (27)
		Granodiorito	U-Pb SHRIMP	2659.7±6 Ma (27)
	Granito Serra do Rabo*	Hb-sienogranito	U-Pb-TIMS	2743±1 Ma (26)
	Complexo Estrela*	Granitoide	Evaporação de Pb	2763±7 Ma (26)
	Metagranito Rio Sereno	Granodiorito foliado	U-Pb LA-ICP-MS	2787±73 Ma (28)
Suíte Lavrado	Metagranitoides	Granodiorito isotrópico	U-Pb SHRIMP	2666±78 Ma (29)
		Granito foliado	U-Pb SHRIMP	2651±14 Ma (29)
	Granito Buritirama	Granito foliado	U-Pb LA-ICP-MS	2549±6 Ma (30)
Magmatismo máfico ultramáfico	Complexo Luanga	Gabro	U-Pb ID-TIMS	2763±6 Ma (20)
	Complexo Vermelho		Sem datação	
	Gabro Santa Inês		Sem datação	
Sequências Metavulcanossedimentares				
Grupo Serra da Bocaína	Grupo Igarapé Pojuca	Anfibolito	U-Pb ID-TIMS	2732±3 Ma (20)
		Metandesito	Isócrona Sm–Nd **	2719±80, 2757±81 Ma (31)
	Grupo Igarapé Salobo	Anfibolito	U–Pb LA–ICP–MS	2761±3 Ma (20)
	Grupo Igarapé Bahia	Rocha metavulcânica máfica	U–Pb SHRIMP	2748±34 Ma (32)
		Rocha metavulcânica máfica	Evaporação de Pb**	2745±1 Ma (33)
		Rocha Metapiroclástica	Evaporação de Pb	2758±36 Ma (33)
		Mt-brecha	U–Pb SHRIMP (Monazita)	2575±12 Ma (32)
Grupo Grão Pará	Formação Carajás	Formação ferrífera bandada	U–Pb SHRIMP	2743±11 Ma (34)
		Dolerito	U–Pb SHRIMP	2740±8 Ma (34)
		Traquito saprolitizado	U–Pb ID–TIMS	2751±4 Ma (35)
	Formação Parauapebas	Riolito	U–Pb ID–TIMS	2758±39 Ma (36)
		Riodacito saprolitizado	U–Pb ID–TIMS	2759±2 Ma (20)
		Basalto	U–Pb SHRIMP	2745±52, 2749±6,52Ma (37)
		Metariolito milonitizado	U–Pb SHRIMP	2757±71 Ma (34)
		Metariolito porfirítico	U–Pb SHRIMP	2760±11 Ma (34)

(*) Integram a Supersuíte Planalto (Félix *et al.* 2023). (**) Análise por rocha total.

Fontes: (1) Leite-Santos P.J.L. *et al.* (2010); (2) Sousa *et al.* (2010); (3) Oliveira *et al.* (2010); (4) Silva *et al.* 2025; (5) F.V. Guimarães, R. Dall'Agnol e J.O.S. Santos (não publicado); (6) Silva M.L.T. *et al.* (2010); (7) Santos-Silva *et al.* (2023) (8) Huhn *et al.* (1999); (9) Moreto *et al.* (2015b);(10) Avelar *et al.* (1999); (11) Marangoanha *et al.* 2019b; (12) Marangoanha *et al.* (2020); (13) Feio *et al.* 2012; (14) Feio *et al.* 2013; (15) Galarza *et al.* (2017); (16) Marangoanha *et al.* (2019a); (17) Santos *et al.* (2013b); (18) Sardinha *et al.* (2004); (19) Lafon *et al.* (2000); (20) Machado *et al.* (1991); (21) Melo *et al.* (2016); (22) Tavares *et al.* (2021); (23) Toledo *et al.* (2023); (24) Toledo *et al.* (2019); (25) S.R. Souza *et al.* (1996); (26) Barros *et al.* (2009); (27) Reis (2017); (28) Tavares e Silva, (2015); (29) Silva *et al.* (2023); (30) Salgado *et al.* (2019a); (31) Pimentel *et al.* (2003); (32)Tallarico *et al.* (2005); (33) Galarza 2002; (34) Trendall *et al.* (1998); (35) Krymsky *et al.* (2002); (36) Gibbs *et al.* (1986); (37) Martins *et al.* (2017).

Granitoides de Vila União

Os granitoides de Vila União foram descritos por Oliveira *et al.* (2018a) e Marangoanha *et al.* (2019a) e são representados por um batólito e um *stock* que afloram no centro do Domínio Canaã dos Carajás, em região cujo embasamento fora anteriormente enquadrado no Complexo Xingu (Fig. 2c). O grau de deformação destas rochas aumenta com a proximidade das zonas de cisalhamento, ao longo das quais se observa desenvolvimento de textura protomilonítica a milonítica ou, raramente, ultramilonítica. Apresentam geralmente foliação de alto ângulo e, por vezes, lineação mineral. Estão associados a rochas máficas e intermediárias que ocorrem em forma de enclaves arredondados e achatados. Em alguns pontos é possível observar contatos irregulares e/ou gradacionais entre magmas menos evoluídos e os magmas graníticos. Compreendem como rochas dominantes biotita-hornblenda monzogranitos e biotita granitos/leucogranitos, com biotita-hornblenda tonalitos e quartzo dioritos espacialmente associados. Os anfibólios são K-hastingsita e, localmente, Cl-K hastingsita, edenita e Mg hastingsita. Oliveira *et al.* (2018a) distinguiram dois grupos de rocha: (1) Granitos com valores de SM baixos, contendo apenas ilmenita; e (2) granitos com valores comparativamente elevados de SM, apresentando magnetita como principal óxido de Fe e Ti. As razões Fe/(Fe+Mg) em anfibólios da fácies biotita-hornblenda monzogranito são relativamente altas e indicam formação em condições de baixa a moderada fugacidade de oxigênio, ao passo que a mica da fácies biotita leucogranito exibiu menores valores desta razão, indicando condições mais oxidantes de cristalização. As temperaturas de cristalização calculadas variam entre 830°C e 930 °C nas diferentes fácies, enquanto as pressões definidas com base em geobarômetros de Al em anfibólio oscilam de 400 a 800 Mpa. Marangoanha *et al.* (2019a) dataram esses granitoides através dos métodos U-Pb por SHRIMP e LA-MC-ICP-MS e obtiveram idades de 2,75 a 2,73 Ga (Tab. 1). Marangoanha (2018) admite que o magma dos granitoides de Vila União é híbrido, gerado por processo de mistura entre líquidos leucograníticos de origem crustal e máficos de origem mantélica. Conforme o autor, estes últimos foram gerados a partir da fusão do manto superior e, em seguida, colocados na crosta mesoarqueana de composição granulítica félsica (*underplating* máfico) e induziram a fusão desta crosta, gerando líquido leucogranítico.

Suíte Vila Jussara

A Suíte Vila Jussara ocorre no norte e no centro do Domínio Sapucaia e compreende diversos *stocks* graníticos (Fig. 2c), os quais são intrusivos no Trondhjemito Colorado (2.93-2,87 Ga; Silva *et al.* 2014). Os *stocks* são formados por rochas anisotrópicas, com foliações penetrativas e textura milonítica com indicadores cinemáticos indicando movimentações

transcorrentes sinistrais (Dall'Agnol *et al.* 2017, Sousa *et al.* 2022, Silva *et al.* 2020, 2025). Em diversos plútons, particularmente nas suas bordas, controladas por zonas de cisalhamento, notam-se marcantes evidências de *mingling* entre monzogranito (*mush*) e granodiorito (líquido) gerando uma rocha híbrida monzogranítica porfirítica (Silva *et al.* 2020, 2025). Sousa *et al.* (2022) realizaram estudos detalhados de petrologia magnética nas rochas desta suíte, os quais, aliados com as características geoquímicas, permitiram distinguir quatro grandes variedades: (1) Biotita-hornblenda monzogranito, que engloba desde amostras com ilmenita e desprovidas de magnetita, para as quais estimou-se condições de fugacidade de oxigênio redutoras equivalentes às da Série Ilmenita e aos granitos tipo A ferrosos, até amostras em que a ilmenita ocorre associada com magnetita, em que as razões Fe/(Fe+Mg) em biotita e anfibólio sugerem condições moderadamente reduzidas, transicionais entre Série Ilmenita e Série Magnetita e aos granitos ferrosos oxidados; (2) Biotita-hornblenda tonalito, caracterizado pela dominância de sulfetos (pirita ± calcopirita), acompanhados por magnetita e, subordinadamente, ilmenita, o qual teria se formado em condições moderadamente oxidantes; (3) Biotita monzogranito com magnetita dominante, seguida de pirita (±calcopirita), intensamente transformada em goethita, e com rara ilmenita associada. Esta variedade possui características de granitos magnesianos formados em condições oxidantes; (4) Hornblenda-biotita granodiorito, com dominância ora de hornblenda, ora de biotita, porém sendo ambos sempre constituintes expressivos e cujas composições possibilitaram estimar condições de fugacidade de oxigênio que variam de intermediária a alta e composição da mica equivalente às da Série Magnetita. Estas rochas mostram as mesmas associações de opacos e se formaram em condições similares às do grupo anterior. Além disso, foram descritos biotita-hornblenda sienogranitos a monzogranitos com alta SM e caráter fortemente reduzido que exibem comportamento particular e contraditório, não se enquadrando nos grupos precedentes. Em geral, as principais fases máficas são anfibólio (K hastingsita com Mg hastingsita subordinada; $0,95 \geq Fe/(Fe + Mg) \geq 0,47$) e biotita ($0,88 \geq Fe/(Fe+Mg) \geq 0,52$), com rara ocorrência de cristais de clinopiroxênio reliquiares (Dall'Agnol *et al.* 2017). Os magmas desses granitos foram formados em temperaturas do liquidus ≥ 900°C e pressões de 800 a 1000 Mpa, tendo sido colocados a pressões entre 200 e 500 Mpa. O conteúdo de água dos magmas seria ≥ 4% em peso (Dall'Agnol *et al.* 2017) e as condições de oxidação mostraram forte variação desde redutoras (FMQ ± 0,5), até oxidantes (NNO ± 0,5). Datações geocronológicas forneceram idades entre 2725±5 a 2769 ±10 Ma (por evaporação do Pb em zircão e U-Pb SHRIMP em zircão; Oliveira *et al.* 2010, Dall'Agnol *et al.* 2017, F.V Guimarães, não publicado, Silva *et al.* 2025). O modelo petrogenético adotado por Silva *et al.*

(2025) para gerar os magmas primários desta suíte admite como rocha geradora granulitos similares aqueles mesoarqueanos da área Ouro Verde do subdomínio Canaã dos Carajás. Os granitoides que compõem a Suíte Vila Jussara são formados por múltiplas injeções de magmas gerando extensa hibridização. Seus magmas foram colocados ao longo de estruturas pré-existentes sob regime tectônico transtensional dominado por cisalhamento puro em um contexto sintectônico pós-colisional.

Complexo Granítico Estrela

O Complexo Granítico Estrela é formado por coalescência de três plútons (37 x 15 km), que ocorrem no sudeste da Bacia Carajás, intrusivos em rochas metavulcânicas e formações ferríferas do Supergrupo Itacaiúnas (Fig. 2c). No geral são alongados, formando trends estruturais E-W, com exceção de um plúton que exibe orientação N-S. Estes plútons apresentam auréolas de metamorfismo que alcançam a fácies hornblenda *hornfels* em anfibolitos e podem atingir 1 a 2 km de extensão (Barros *et al.* 2001). Estes granitos apresentam acamamentos ígneos primários (S_0) e foliação desenvolvida por deformação sinmagmática (S_1), cuja presença é mais acentuada nas bordas dos plútons. Estes são constituídos por hornblenda monzogranitos e biotita monzogranitos com pegmatitos relacionados, bem como tonalitos, granodioritos e sienogranitos subordinados. Os anfibólios são Fe-pargasitas e hastingsitas ($0{,}98 \geq Fe/(Fe + Mg) \geq 0{,}79$) e as biotitas são annitas ($0{,}97 \geq Fe/(Fe + Mg) \geq 0{,}86$) (Barros *et al.* 2001). Os óxidos de Fe e Ti são representados por ilmenita com magnetita subordinada. Comumente os cristais de ilmenita são bordejados por auréolas de titanita. Além disso, cristais secundários de magnetita são formados por desestabilização de minerais máficos. Foram estimadas temperaturas de colocação médias de 860° C e 870°C, utilizando, respectivamente, geotermômetros de zircão e apatita. A pressão de colocação foi estimada entre 110 e 380 Mpa (geobarômetros de Al em anfibólio de tonalito). A estabilidade de ilmenita na presença de hedenbergita indica condições de fugacidade de oxigênio menor do que FMQ + 1 (Wones 1989), portanto redutoras. Barros *et al.* (2001) dataram estas rochas e obtiveram idades de cristalização através do método Pb-Pb por evaporação de zircão de 2763 ± 7 Ma (Tab. 1).

Granito Serra do Rabo

O Granito Serra do Rabo (Sardinha *et al.* 2006, Barros *et al.* 2009) aflora na Bacia Carajás, próximo ao extremo leste da Falha Carajás, como dois *stocks* alongados, acompanhando a estruturação regional E-W (Fig. 2c). Suas feições estruturais são similares às

do Complexo Granítico Estrela. Estes plútons graníticos se diferenciam dos demais granitos neoarqueanos por serem constituídos principalmente por álcali-feldspato granitos com sienogranitos subordinados, apresentando as seguintes fácies: Leucomicroclina granito, hornblenda microclina granito, biotita–hornblenda microclina granito, hornblenda sienogranito e, subordinadamente, aplitos (Sardinha *et al.* 2006). Os anfibólios são ferro pargasitas e hastingsitas (0,99≥ Fe/(Fe + Mg) ≥ 0,86) e as biotitas são annitas (Fe/(Fe + Mg) ~0,82) (Barros *et al.* 2009). Os cristais de zircão deste granito são bastante preservados, diferentemente daqueles encontrados nos demais granitos neoarqueanos, os quais se encontram majoritariamente metamícticos. Sardinha *et al.* (2006) obtiveram para este granito idade de cristalização por U-Pb em zircão de 2,74 Ga (Tab. 1).

Granito Igarapé Gelado

As novas informações obtidas sobre o Granito Igarapé Gelado, atualmente redefinido como suíte (Tavares *et al.* 2021, Oliveira *et al.* 2023), são abordadas nos capítulos subsequentes da tese. Aqui serão sumarizados apenas os dados geoquímicos e geocronológicos e suas respectivas interpretações divulgados em trabalhos anteriores (Barbosa 2004; Barros *et al.* 2009; Melo *et al.* 2016). Tais autores classificaram as rochas da SIG como cálcico-alcalinas com alcalinas subordinadas. Ambas apresentam teores moderados a altos de Nb e Zr e revelam afinidades com granitos tipo-A. Os altos valores de Zr apontam para temperaturas elevadas e possível derivação por fusão parcial de crosta continental. Diferenças no comportamento dos elementos terras raras entre as rochas cálcico-alcalinas e alcalinas traduziriam diferenças nas rochas fonte ou diferenças nas profundidades de origem dos respectivos magmas. Os magmas cálcico-alcalinos são mais empobrecidos em ETRP e seriam gerados em níveis crustais mais profundos. As datações de cristais de zircão da SIG pelo método Pb-Pb por evaporação forneceram uma idade de 2731 ± 26 e cinco idades entre 2588 ±5 e 2508 ± 14Ma (Barbosa 2004), enquanto pelo método U-Pb por SHRIMP forneceu uma idade 2763 ± 4.4 e por LA-ICP-MS forneceu idade 2701 ± 30 (Melo *et al.* 2016). De acordo com Melo *et al.* (2016), a idade de 2508 ± 14 Ma pode estar relacionada ao evento tectono-termal de reativação do lineamento do Cinzento (2,5 Ga), o qual poderia ter reaberto o sistema U-Pb no zircão. Estas idades mais jovens são similares às atribuídas ao depósito IOCG do Salobo (2555 ± 4 e 2497 ± 5 Ma, U-Pb em zircão e titanita, respectivamente, Machado *et al.* 1991), bem como ao Granito Velho Salobo associado aquele depósito (2547 ± 5.3, U-Pb em zircão, Melo *et al.* 2016) e ao Granito Itacaiúnas (2560±3 Ma, Pb-Pb em zircão,

Souza *et al.* 1996b), todos provavelmente afetados pelo evento de reativação do lineamento do Cinzento.

1.3.5.2 Granitos peralcalinos a metaluminosos com idades de 2,63-2,53 Ga

No geral estes granitos afloram apenas localmente na porção oeste da área de estudo e não podem ser representados na escala do mapa geológico da Figura 2c). São afetados pela zona de cisalhamento Cinzento (Pinheiro *et al.* 2013), e estão associados a depósitos do tipo IOCG (Melo *et al.* 2016).

***Granito Velho* Salobo**

O Granito Velho Salobo é um diminuto corpo com apenas algumas dezenas de metros, intrusivo em rochas hidrotermalizadas e milonitizadas, que ocorre na porção nordeste da mina Salobo. São tonalitos a granodioritos médios, equigranulares foliados e localmente isotrópicos que apresentam augita como máfico principal. Conforme Melo (2018), este granito é tipo-A ferroso, peralcalino (Frost *et al.* 2001), do tipo A2 (Eby 1992) e intraplaca (Whalen 1987). Machado *et al.* (1991) dataram este granito utilizando o método U-Pb em zircão e obtiveram idade de 2573 ± 3 Ma. Mais recentemente, Melo *et al.* (2016) obtiveram idades de 2547 ± 5,3 Ma e 2535 ± 8,4 Ma para estas rochas (U-Pb em zircão - SHRIMP), as quais poderiam representar idades de cristalização ou reequilíbrio total do sistema U-Pb no zircão durante o importante evento tectonotermal relacionado com a zona de cisalhamento do Cinzento (Tab.1).

Granito Itacaiúnas

Este granito foi descrito por Souza *et al.* (1996b) como corpos aflorantes às margens do rio Itacaiúnas, próximo à ponte da rodovia PA-275, a 15 km a SE da ocorrência do Granito Velho Salobo. É composto por monzogranito com sienogranito subordinado. De acordo com Souza *et al.* (1996b), embora apresente bandamento gnáissico e esteja geralmente milonitizado, ao microscópio exibe aspectos texturais ígneos preservados como cristais de plagioclásio euédricos e zonados. Souza *et al.* (1996b) obtiveram para este granito idade U-Pb em zircão de 2,56 Ga, similar à obtida para o Granito Velho Salobo por Melo *et al.* (2016).

Granito GT-46 (Granito Rio Cinzento)

Mais recentemente, Toledo *et al.* (2019) descreveram granitoides que cortam as rochas hidrotermalizadas do depósito GT-46. Estes granitoides são tonalitos e granodioritos intensamente deformados, seccionados por granitos isotrópicos e pegmatitos. Os cristais de biotita dos tonalitos e granodioritos encontram-se em avançado estado de cloritização com cristais de epidoto associados. Dados U-Pb em zircões (por LA-ICP-MS) dos tonalitos, granitos e pegmatitos forneceram idades de entre 2,63 e 2,53 Ga (Tab. 1; Toledo *et al.* 2019), próximas às idades dos granitos Old Salobo e Itacaiúnas. Tais granitos teriam sido importantes no processo de formação dos depósitos IOCG da região, pois a exsolução de fluidos magmáticos durante a cristalização dos magmas destes granitos (~2,57 Ga), pode representar o mecanismo de geração de fluidos mineralizantes hipersalinos e quentes, que migraram por zonas de cisalhamento profundas e ascenderam até níveis crustais mais rasos. De acordo com Melo (2018), esta hipótese é fortalecida por dados de $\delta^{18}O$ e δD no depósito Salobo e de $\delta^{18}O$, δD e $\delta^{13}C$ nos estágios iniciais do depósito Igarapé Bahia que apontam para fontes magmáticas para os fluidos mineralizantes.

1.3.5.3 Granitos calcio-alcalinos

Leucogranito Velha Canadá

É um batólito que aflora à norte da Vila Nova Canadá no limite entre os terrenos Sapucaia e Canaã dos Carajás, se estendendo para norte do mesmo até o contato com o Diopsídio-norito Pium e para sul até o contato com o Leucogranodiorito Nova Canadá (Fig. 2c). É formado por leucogranitos cálcio-alcalinos, hololeucocráticos, de granulação fina a média, com pronunciada foliação, os quais se destacam pela relativa abundância de titanita. Distinguem-se geoquimicamente dos leucogranodioritos de alto Ba-Sr por seu caráter ligeiramente ferroso e pelo enriquecimento em K_2O, Fe_2O_3, TiO_2, Y, Zr, Rb e Nb, e são similares aos leucogranitos mesoarqueanos que compõem as suítes de alto-K (Leite-Santos & Oliveira 2016), em particular ao Granito Cruzadão que mostra enriquecimento em HFSE e tendência mais alcalina quando comparado com os demais granitos cálcio-alcalinos mesoarqueanos (Feio & Dall'Agnol 2012). As idades Pb-Pb em zircão obtidas para estas rochas variam entre 2,73 e 2,74 Ga (Leite-Santos *et al.* 2010, Sousa *et al.* 2010, Tab 1).

1.3.5.4 Rochas Charnoquíticas e enderbíticas

De acordo com Felix *et al.* (2023b) a **Suíte Charnoquítica Pium** (SCP) é composta pelos plútons do **Diopsídio Norito Pium, Enderbito Café, Charnoquito Rio Seco**, e **rochas máfico-enderbíticas de Sapucaia**, cristalizados em torno de 2,74 ±0,01 Ga. Variam de noritos a charnoquitos *lato sensu*. São intrusivos no embasamento mesoarqueano onde estão dispostos segundo *trend* E-W a NE-SW, e mostram uma relação espaço-temporal com o magmatismo subalcalino do tipo-Planalto. A ascensão e colocação dos magmas geradores da SCP se deu ao longo de zonas de cisalhamento que atuaram como condutos para o transporte de magmas derivados do manto para a crosta superior.

Charnoquito Rio Seco

O charnoquito Rio Seco (Félix *et al.* 2020) é formado pelas fácies ortopiroxênio granodiorito e clinopiroxênio monzogranito. É associado a anfibólio monzogranitos e gabronoritos. Forma corpos orientados na direção NE-SW a E-W. Suas rochas exibem textura magmática bem preservada, são leucocráticas e de granulação média a grossa. Os minerais acessórios primários são allanita, epidoto, zircão, apatita, magnetita e ilmenita. Textura em coroa formada por anfibólios bordejando piroxênios é comum em todas as variedades. São rochas metaluminosas de afinidade magnesiana, que possuem caráter cálcio alcalino e cálcio alcalino de alto K. As razões Fe/(Fe+Mg) tanto nas biotitas quanto nos anfibólios, indicam condições intermediarias de fO_2, acima do tampão FMQ. As temperaturas de cristalização para os piroxênios variam entre 855°C e 1061°C, 713°C e 800°C nos anfibólios, e a pressão de cristalização foi estimada entre 1,9 a 3,1 kbar. A concentração de água no magma varia de 4,1 a 6,5% em peso. Modelamento geoquímico indica que tais granitoides evoluíram por cristalização fracionada a partir de um magma parental máfico, em contraponto ao modelo de fusão parcial, admitido como principal processo responsável pela origem dos demais granitoides neoarqueanos de Carajás.

Enderbito Café

O Enderbito Café se apresenta na forma de plútons lenticulares (~5 km) formados por trondhjemitos, tonalitos e, subordinadamente, quartzo noritos. Esses plútons cortam unidades mesoarqueanas representadas pelo Granulito Ouro Verde e Granito Cruzadão e estão espacialmente associados ao Diopsídio-norito Pium e a granitóides híbridos da Suíte Vila União (Fig. 2c; Marangoanha *et al.* 2020). Pontualmente estas rochas mostram migmatização. A trajetória de foliação milonítica e as zonas de cisalhamento exibem padrão sigmoidal com

orientação principalmente segundo E-W. Essas zonas de cisalhamento também marcam os contatos entre as rochas enderbíticas e os granitóides híbridos de Vila União e Diopsidio-norito Pium. Os piroxênios são representados por diopsídio, ferrosilita e, subordinadamente, enstatita. Os anfibólios possuem maior variedade podendo ocorrer hastingsita, ferropargasita, Mg hornblenda e edenita. As biotitas são magnesianas e os plagioclásios variam de andesina a oligoclásio.

O Enderbito Café tem idades de cristalização entre 2,75 e 2,73 Ga. Os magmas menos evoluídos do Enderbito Café (quartzo diorito) teriam sido formados pela fusão parcial da crosta inferior máfica que, por cristalização fracionada, evoluíram para formar as variedades sódicas (tonalitos e trondhjemitos com ortopiroxênio).As condições de cristalização estimadas (Marangoanha *et al.* 2022) foram: Temperatura de 1.150–850°C, pressão de 750–600 MPa, alta fugacidade de oxigênio (FMQ até NNO + 1,7) e teor de H_2O elevado (4,8–5,6%). Além disso, essas rochas exibem Hf-T_{DM}^2 de 3,46-3,29 Ga e valores de $\varepsilon_{Hf}(t)$ (−4,8 a −1,9), que indicam maior tempo de residência crustal (~ 700-500 Ma) (Marangoanha *et al.* 2019b).

Diopsídio Norito Pium

De acordo com Santos *et al.* (2013b) o Diopsídio-Norito Pium ocorre a sul da Bacia Carajás e é constituído dominantemente por noritos (± gabronoritos com variações para quartzo-gabros e enderbitos e, subordinadamente, rochas cumuláticas. Relações de contemporaneidade (magma *mingling*) são observadas, uma vez que a variedade de composição norítica ocorre ora como enclaves angulosos e de contatos retilíneos no interior das rochas quartzo-gabroicas, evidenciando alto contraste de viscosidade, ora como um enxame de enclaves arredondados (blebs/autólitos) no interior da variedade hornblenda-gabro. Os dados geoquímicos demonstram que estas rochas possuem enriquecimento em FeOt em relação ao MgO, apontando a natureza subalcalina toleítica das mesmas, e uma origem a partir da fusão parcial do manto peridotítico. Estas rochas possuem afinidades geoquímicas com basaltos intraplacas e apontam para um processo de evolução magmática a partir dos noritos até os enderbitos. Idades Pb-Pb de cristalização estão entre 2745 ± 1 Ma e 2744 ± 1 Ma. As análises Sm-Nd forneceram idades-modelo Nd-T_{DM} entre 3,14 e 3,06 Ga, e valores de εNd (T = 2,74 Ga) entre -2,78 e -1,58, indicando um significativo envolvimento de fontes crustais em sua gênese. As idades-modelo confirmam um importante período de formação de crosta no Mesoarqueano na Província Carajás. Por outro lado, Feio *et al.* (2013) sugerem que estes charnoquitos neoarqueanos associados ao Complexo Pium têm composições químicas

compatíveis com a derivação a partir do Norito Pium (mesoarqueano) por fusão parcial (~ 17%).

1.3.5.5 Metagranitoides indiferenciados

Suíte Lavrado

É composta por biotita metatonalitos e metagranodioritos, com foliação incipiente a bem desenvolvida (Fig. 2c). Forma corpos elípticos e pode estar possivelmente relacionada à Suíte Igarapé Gelado, visto suas similaridades composicionais e mineralógicas, além de sua idade entre 2,66 e 2,65 Ga, (Costa *et al.* 2016, Fraga *et al.* 2020, Silva *et al.* 2023).

Granito Rio Sereno

É um corpo pequeno que ocorre no extremo leste da área (Fig. 2c), formado por metagranodioritos e metatonalitos subordinados. São foliados e formam localmente protomilonitos, metamorfisados em fácies xisto verde. São ligeiramente mais velhos que os demais granitos neoarqueanos de Carajás (2,78 Ga, Costa *et al.* 2016).

1.4 PROBLEMÁTICA E JUSTIFICATIVA

Existe uma gama de dados geológicos, petrográficos, geoquímicos e geocronológicos sobre os granitoides que compõem a Suíte Igarapé Gelado (Barbosa 2004, Barros *et al.* 2009, Melo *et al.* 2016, Tavares *et al.* 2021, Toledo *et al.* 2023), os quais fornecem uma visão geral das características deste magmatismo. No entanto, permanecem lacunas importantes no conhecimento do corpo. A aplicação recente de técnicas mais modernas e diversificadas quando de estudos de outros granitoides neoarqueanos de Carajás (Feio *et al.* 2012, 2013, Cunha *et al.* 2016, Dall'Agnol *et al.* 2017, Oliveira *et al.* 2018a, Felix *et al.* 2020, Marangoanha *et al.* 2018, 2019a, 2019b, 2020, 2022, Silva *et al.* 2020, 2025, Sousa *et al.* 2022, Silva *et al.* 2023, Toledo *et al.* 2023) revelou que, para que se possa avançar no conhecimento da SIG e as atuais incógnitas sejam superadas, é necessária uma reavaliação dos dados obtidos até o momento, bem como aprofundamento da pesquisa com a aplicação de novos métodos. Entre os principais questionamentos existentes podem ser destacados:

1. Conforme os últimos mapas disponibilizados pelo Serviço Geológico do Brasil (SGB) a SIG forma aparentemente um único corpo alongado e orientado concordantemente com o *trend* regional (Oliveira *et al.* 2018b, Tavares *et al.* 2021). Suas rochas se encontram intensamente foliadas e seccionadas por zonas de cisalhamento, ao longo das quais o granito

encontra-se milonitizado. Contudo, apresenta em imagens de satélite expressivos contrastes texturais, que colocam em questão se o corpo é efetivamente formado por apenas uma unidade ou se corresponde a uma justaposição de várias intrusões. Além disso, é formado predominantemente por monzogranitos e granodioritos, com tonalitos, charnoquitos, leucomonzogranitos e sienogranitos subordinados. Como estas variedades litológicas estão distribuídas no corpo? Quais processos foram responsáveis por essa diversificação faciológica? Seriam as diferentes variedades contemporâneas e derivadas de um mesmo magma? Ou seriam cogenéticas, mas não comagmáticas? Ou elas poderiam não ser nem cogenéticas, nem comagmáticas?

2. Não se dispõe de dados sobre a composição químico-mineralógica dos principais minerais ferromagnesianos e plagioclásio presentes nas fácies do corpo os quais podem fornecer importantes indicações sobre as características do seu magma formador. Quais as composições dos minerais mencionados nas diferentes variedades? Quais são as condições de cristalização (temperatura, pressão, fugacidade de oxigênio e conteúdo de água) do magma gerador? Tais condições indicam fontes e processos homogêneos ou heterogêneos? Os parâmetros de cristalização da Suíte Igarapé Gelado se assemelham ou divergem dos já descritos na literatura para outros granitos neoarqueanos de Carajás?

3. Embora os estudos geoquímicos em rocha total realizados por Barbosa (2004) tenham permitido uma caracterização geral das rochas do corpo granítico, eles precisam ser aprofundados para permitir comparações mais detalhadas entre a SIG e os demais granitos tipo A neoarqueanos de Carajás. Há diversas questões pendentes: a) Qual o significado da assinatura geoquímica variada da Suíte Igarapé Gelado evidenciada nos diagramas $100[(MgO + FeO_t + TiO_2)/SiO_2]$ x $(Al_2O_3 + CaO)/(FeOt + Na_2O + K_2O)$ de Sylvester (1989) e Al_2O_3 x $FeO_t/(FeO_t+MgO)$ de Dall'Agnol & Oliveira (2007) , nos quais se observam amostras nos campos de granitos calcico-alcalinos / alcalinos e oxidados / reduzidos, respectivamente? Tais variações geoquímicas são compatíveis com derivação a partir de um mesmo líquido magmático? b) Por que motivo a SIG apresenta em algumas amostras assinatura geoquímica de granitos do subtipo A1, enquanto os demais granitos neoarqueanos são do subtipo A2 (Eby 1992)? Teria o magma da SIG maior grau de influência mantélica? c) Por que a SIG apresenta razões (La/Yb) relativamente elevadas, destoantes do padrão dos outros granitos tipo A neoarqueanos (Dall'Agnol *et al.* 2017)? d) Como explicar o fato de seus padrões de ETR serem geralmente distintos dos encontrados nos demais granitos neoarqueanos de Carajás?

4. As idades obtidas para a SIG em estudos anteriores em zircão por diversos métodos (Tab. 1) se superpõem dentro do erro com as dos demais granitos tipo A neoarqueanos de Carajás (Barbosa 2004, Barros *et al.* 2009, Feio *et al.* 2013, Dall'Agnol *et al.* 2017, Toledo *et al.* 2019, Silva *et al.* 2020, 2025). Entretanto, a idade de 2,73 Ga obtida pelo método Pb-Pb em zircão não foi definida com grande precisão e novas idades discordantes mais jovens têm sido registradas (~2.5 a 2.68 Ga, Reis 2017, Silva *et al.* 2023, Toledo *et al.* 2023). Desta forma, considerando a dimensão batolítica do corpo da SIG e as grandes variações litológicas que apresenta, bem como o intenso grau de deformação/alteração hidrotermal em algumas porções, torna-se indispensável ampliar consideravelmente o número de amostras datadas, bem como submetê-las a análises isotópicas, até então não utilizadas. Em função da ausência de dados isotópicos, não se dispõe de informações sobre as possíveis fontes do(s) magma(s) do batólito. Portanto, pergunta-se: Se houve diferentes pulsos magmáticos no batólito separados no tempo? Qual a natureza das possíveis fontes do magma formador dos granitoides da SIG? Em que momento se deu a separação do manto destas fontes? Quais as relações entre os eventos superimpostos (hidrotermal/deformacional) à colocação magmática durante a evolução da SIG e como eles podem ter influenciado na assinatura geoquímica das rochas e na textura e química de cristais de zircão? São as idades dos granitoides do batólito coincidentes com as definidas para os depósitos IOCG da região (Salobo, GT-46 e Furnas; Moreto *et al.* 2015a, Melo *et al.* 2016, 2019, Toledo *et al.* 2019, 2023, Trunfull *et al.* 2020)?

5. As rochas aflorantes da SIG, assim como aquelas de outros granitoides neoarqueanos da Bacia Carajás e dos terrenos Canaã dos Carajás e Sapucaia encontram-se em geral moderadamente a intensamente recristalizadas. Tal aspecto é resultado da atuação de processos no estágio subsolidus ligados à colocação de seus magmas ou representam efeitos de metamorfismo regional superimposto? Quais suas implicações para a evolução da Bacia Carajás?

1.5 OBJETIVOS

Com base nos problemas expostos, o principal objetivo deste trabalho é aprimorar a caracterização da porção centro-leste da SIG, definir a idade de cristalização de suas diversas fácies, procurar estimar os seus parâmetros de cristalização, entender como se desenvolveu sua evolução magmática, quais os processos geradores do(s) seu(s) magma(s) e a natureza das suas fontes. Pretende-se ainda compreender até que ponto o hidrotermalismo afetou as rochas

da suíte e qual o real significado da deformação nestes granitoides. Espera-se dessa forma, contribuir para o avanço do conhecimento sobre a evolução tectônica e magmática da Província Carajás e definir a importância da Suíte Igarapé Gelado no contexto do magmatismo neoarqueano de Carajás. Para isso foram estabelecidos os seguintes objetivos específicos:

- Caracterizar as variedades faciológicas presentes na porção centro-leste no corpo e definir sua distribuição espacial, permitindo aprimorar o mapa geológico existente (Barbosa 2004, Oliveira *et al.* 2018b);

- Aprofundar a caracterização geoquímica e mineralógica, reavaliar a assinatura geoquímica e tipologia dos granitoides, avaliar possíveis processos de diferenciação magmática e estimar os parâmetros de cristalização (P, T, fO_2 e X_{H2O}) em que se formou ou se formaram o(s) magma(s) gerador(es) do corpo granítico;

- Confrontar os resultados fornecidos pelos diferentes geotermômetros e geobarômetros com os resultados estimados por meio de modelamento termodinâmico buscando definir com mais precisão as condições reinantes durante a cristalização da SIG.

- Definir as idades de cristalização das variedades petrográficas da SIG, verificar se há variações significativas entre elas e estabelecer comparações com os dados já disponíveis na literatura de possíveis eventos contemporâneos;

- Definir a natureza e idade de separação do manto de possíveis fontes do(s) magma(s) da SIG; avaliar a contribuição de fontes crustais e/ou mantélicas na sua origem e propor um modelo petrogenético para a formação da suíte;

- Definir as assinaturas hidrotermais das rochas e cristais de zircão da Suíte Igarapé Gelado e comparar com rochas associadas aos depósitos IOCGs da região;

- Discutir a história deformacional da Suíte Igarapé Gelado, enfatizando os processos deformacionais e ambiente de colocação;

- Situar a Suíte Igarapé Gelado no contexto dos granitos neoarqueanos de Carajás e de outros crátons.

1.6 MATERIAIS E MÉTODOS

1.6.1 Pesquisa bibliográfica

Durante o desenvolvimento do trabalho foi realizado um levantamento bibliográfico acerca da geologia arqueana da Província Carajás enfatizando o magmatismo granítico neoarqueano em seus diferentes aspectos. Também foram pesquisados os granitos neoarqueanos, a evolução de outros crátons arqueanos, bem como trabalhos relacionados a granitos sintectônicos, em geral. Em paralelo, foram realizadas leituras no âmbito das metodologias que foram aplicadas na presente pesquisa (geologia estrutural, microtexturas e microestruturas; geoquímica de rochas graníticas; química mineral; determinação de parâmetros de cristalização de rochas granitoides; modelamentos geoquímico e termodinâmico; estudos isotópicos Sm-Nd em rocha total e pelos métodos Lu-Hf, U-Pb e ETR *in situ* em zircão).

1.6.2 Mapeamento geológico e amostragem

Foram realizadas duas campanhas de campo, das quais a primeira ocorreu no período de 27 a 28 de maio de 2017, com apoio de geólogos do setor de exploração mineral da Vale SA e teve como objetivo realizar um breve reconhecimento geológico da área de estudo. A segunda campanha ocorreu no período de 15 a 26 de julho de 2019 com a participação do Dr. José de Arimatéia Costa de Almeida do PPGG-IG-UFPA e do geólogo Diwhemerson Barbosa. Nesta campanha foi efetuado mapeamento geológico na escala de 1:100.00 da SIG, com auxílio de imagens de radar SRTM (*Shuttle Radar Topography Mission*) com resolução de 30 m, imagens de satélite (*Landsat* TM, *Google Earth*) e imagens de levantamentos aerogeofísicos (magnetometria e aerogamaespectrometria) previamente processados em ambiente SIG (Oliveira *et al.* 2018b, Costa *et al.* 2020a, Tavares *et al.* 2021). As atividades realizadas foram amostragem em sua porção centro-leste, bem como a tomada de medidas estruturais em afloramentos já visitados por Barbosa (2004) e pela equipe do SGB dos projetos “Carta Geológica da Folha Caldeirão” e “Mapa Geológico-Geofísico do Lineamento Cinzento” (Oliveira *et al.* 2018b). É importante destacar que foram cedidas ao presente autor diversas amostras do acervo do SGB coletadas durante a realização dos projetos supracitados, contribuindo desta forma para adensar a amostragem disponível. Novos pontos foram amostrados ao longo de perfis perpendiculares à orientação principal do corpo,

preferencialmente em áreas dissecadas por drenagens, visto a espessa capa intempérica da região. No total foram amostrados 58 pontos que podem ser visualizados no mapa de amostragem, com o tipo de estudo efetuado nas amostras coletadas em cada ponto (Figura 3).

1.6.3 Estudos petrográficos

Inicialmente foi realizado um exame petrográfico de amostras de mão e, em seguida, foram confeccionadas lâminas polidas na Oficina de Laminação do Programa de Pós-Graduação em Geologia e Geoquímica (PPGG), que foram estudadas em microscópio ótico Leica DM 2700p do laboratório de petrografia do PPGG do Instituto de Geociências (IG) da UFPA. As observações envolveram microscopia ótica em luz transmitida e também em luz refletida, essa direcionada para os minerais opacos. Nesta etapa foi efetuada a identificação e descrição sistemática dos minerais e identificadas as texturas magmáticas, deformacionais e de alteração. Os principais aspectos texturais foram documentados por meio de fotomicrografias. As composições modais de 43 amostras das 4 variedades foram obtidas por meio de contador de pontos automático Stageledge, marca Endeeper (média de 2000 pontos por lâmina delgada analisada, em malha de 0,4 mm) e as rochas foram classificadas conforme recomendações da Subcomissão de Nomenclatura de Rochas Ígneas da IUGS (Le Maitre *et al.* 2020). As observações petrográficas permitiram uma melhor definição e caracterização das variedades litológicas, bem como avaliação dos processos magmáticos e deformacionais que afetaram as rochas da SIG. As descrições de microestruturas e microtexturas foram realizadas conforme recomendado por diversos autores (Blenkinsop 2000, Passchier & Trouw 2005, Vernon 2005, Trouw *et al.* 2009, Fossen 2018, Nedelec & Bouchez 2015).

As observações petrográficas também serviram de suporte para as análises de química mineral e para seleção das amostras para análises geoquímicas em rocha total, geocronológicas e isotópicas.

1.6.4 Geoquímica

Foram selecionadas 34 amostras representativas de 4 variedades litológicas da SIG. Cerca de 0.5 a 5 kg das amostras escolhidas passaram por trituração, pulverização e homogeneização usando britadores de mandíbulas, moinhos de anel e disco e, em seguida, pulverizadas em um moinho de balanço de ágata até um tamanho de partícula <10 μm. Estes procedimentos foram realizados na Oficina de Preparação de Amostras (OPA) e no Laboratório de Sedimentologia, do Instituto de Geociências da UFPA. Posteriormente, foram

realizadas análises químicas em rocha total em laboratórios da empresa ALS Geochemistry Ltda. Os métodos e limites de detecção utilizados estão disponíveis no site da empresa (www.alsglobal.com/br). O produto das análises compreende os conteúdos de elementos maiores e menores (SiO_2, TiO_2, Al_2O_3, Fe_2O_3t, MgO, CaO, MnO, Na_2O, K_2O, P_2O_5) determinados por Espectrometria de Emissão Atômica com Plasma Indutivamente Acoplado (ICP-AES) e elementos-traço (Rb, Sr, Ba, Ga, Y, Zr, Nb, U, Th, Hf, Cr, Ni, V), inclusive terras raras (La, Ce, Pr, Nd, Sm, Eu, Gd, Tb, Dy, Ho, Er, Tm, Yb e Lu), por Espectrometria de Massa com Plasma Indutivamente Acoplado (ICP-MS).

A caracterização geoquímica destas rochas foi realizada com base nos princípios gerais discutidos em Rollinson (1993), sendo os resultados tratados e avaliados em diagramas geoquímicos clássicos. Os diagramas de variação geoquímica foram gerados utilizando o software livre GCDkit 6.1 (Janoušek *et al.* 2006).

1.6.4.1 Modelamento Geoquímico

O modelamento geoquímico foi realizado a partir do balanço de massa dos elementos maiores para investigar fontes e processos que formaram os magmas que originaram as variedades da SIG. Para tal foi utilizado o *software* GENESIS 4.0 (Teixeira 2005). Neste método é feito o ajuste das proporções relativas de minerais residuais da fonte para atingir a composição do líquido inicial estimado. Os dados calculados são confiáveis se a soma dos resíduos quadrados ($\sum R^2$) for ≤1.2 (Wyers & Barton 1986). O resultado obtido foi testado por modelamento dos elementos traço a partir de planilhas de excel usando a equação de fusão parcial em equilíbrio, $C_L/C_0 = 1/F+D-FD$ (Willson, 1989), onde CL e C0 são as concentrações dos elementos traço no magma e na fonte, respectivamente, F é porcentagem de magma formado e D é o coeficiente de distribuição para o sólido residual no momento em que o magma é removido do sistema. Os coeficientes de partição mineral/líquido utilizados foram extraídos de Rollisson & Pease (2021) e https://kdd.earthref.org/KdD.

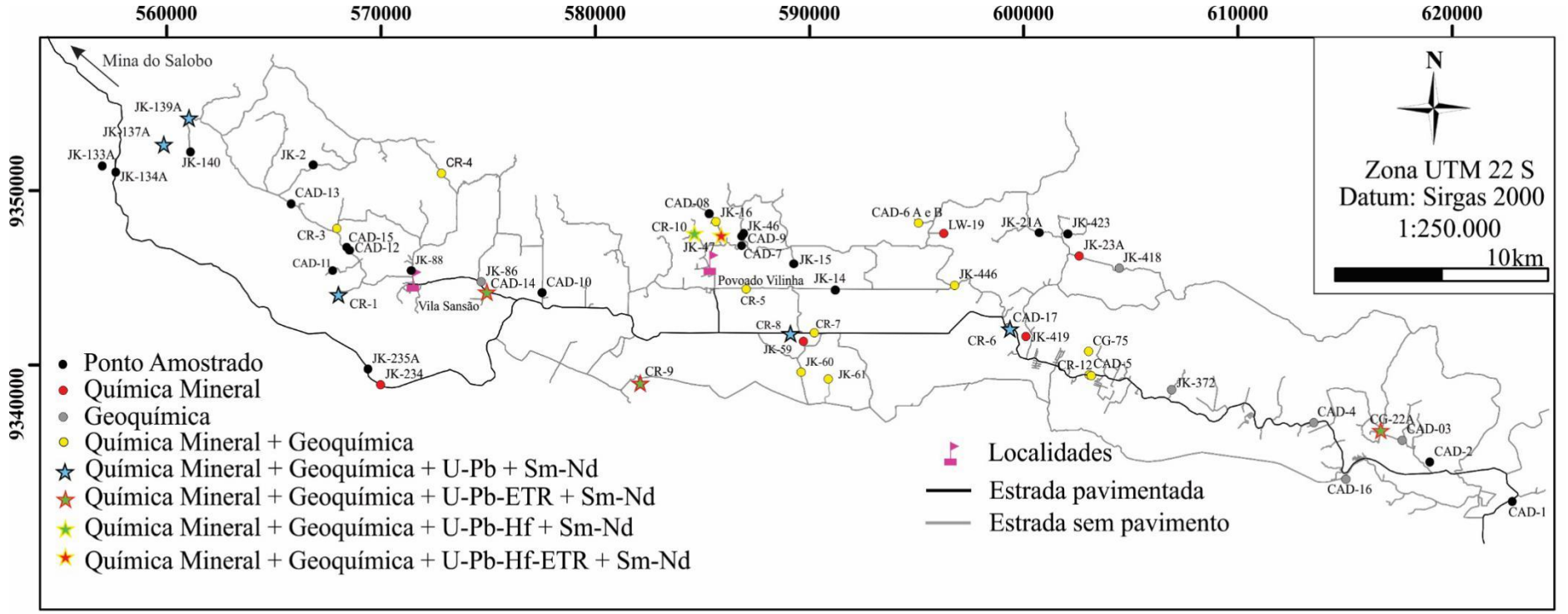

Métodos: Química mineral por WDS e/ou EDS; Geoquímica em rocha total por ICP-AES e ICP-MS; Sm-Nd em rocha total por TIMS; U-Pb e ETR em zircão por SHRIMP IIe; Lu-Hf em zircão por LA-MC-ICP-MS.

Figura 3- Mapa de amostragem do Granito Igarapé Gelado indicando os estudos efetuados nas amostras coletadas.

1.6.5 Química mineral

Esta etapa foi realizada no Laboratório de Microanálises no Instituto de Geociências da Universidade Federal do Pará. Inicialmente, foram realizadas observações texturais por imagens de elétrons retroespalhados em MEV da marca Zeiss modelo SIGMA-VP, na ocasião pertencente ao Instituto Tecnológico Vale (ITV), cedido em contrato de comodato para o IG-UFPA e análises semiquantitativas das composições de minerais selecionados via EDS (*Dispersive Energy Spectroscopy,* modelo Sedona-SD). Com base nas observações no MEV e na petrografia de amostras representativas das 4 variedades da SIG, foram definidas as seções para análises em microssonda eletrônica, tendo sido selecionadas para análises em microssonda 15 amostras das quatro variedades da SIG. Os minerais analisados foram: ortopiroxênio, clinopiroxênio, anfibólio, biotita e plagioclásio. Foi utilizada uma microssonda eletrônica JEOL JXA-8230, equipada com 5 espectrômetros WDS (*Wavelength Dispersive X-ray Spectroscopy*) e um espectrômetro EDS. As lâminas polidas foram previamente metalizadas com película de carbono e as condições de operação da microssonda foram: tempo de aceleração 15kv, corrente elétrica 20nA, diâmetro do feixe 10µm para silicatos. O tempo de análise foi de 20s para Si, Ca e Ti e 30s para Na, Al, F, Mg, Sr, K, Cr, Ni, Fe, Mn, Ba, Cl e V. O efeito de matriz foi corrigido pelo método ZAF com precisão analítica de ± 1% e ± 10% para elementos maiores e menores, respectivamente. Os cristais usados para análise foram: TAP para Si, Al, Mg, Na, F e Sr; PETJ para Cr, Ca e K; LIF para Ni, Fe, Mn e Ba; PETH para Cl e V. Os padrões utilizados foram: SiO_2 (Si), rutilo (Ti), córindon (Al), Fe_2O_3 (Fe), wollastonita (Ca), rodonita (Mn), periclásio (Mg), sodalita (Na e Cl), microclina (K) e fluorita (F).

Para estimar os principais parâmetros de cristalização foram utilizados os dados de química mineral (anfibólio, plagioclásio, piroxênios) e de análise química em rocha total (termômetro de zircão). Para tal, foram selecionados minerais e rochas sem evidências de transformações marcantes. Os cálculos de diferentes parâmetros (P, T, fO_2, XH_2O) foram realizados no programa WinAmptb (Yavuz & Doner 2017) para anfibólio, plagioclásio e líquido e no programa WinPyrox (Yavuz 2013) para piroxênios. Os parâmetros estimados a partir de análise química em rocha total foram calculados em tabela do microsoft excel 2023. Dentre mais de 130 equações fornecidas por Yavuz (2013) e Yavuz & Doner (2017), foram selecionadas aquelas que, em sua calibração, foram considerados aspectos químicos e mineralógicos que mais se aproximam dos observados nas rochas da SIG.

1.6.6 Modelamento termodinâmico

O modelamento foi realizado com o software GeoPS 3.5 (Xiang & Connolly 2022), utilizando a base de dados do sistema KNCFMASHTO (K_2O–Na_2O–CaO–FeO–MgO–Al_2O_3–SiO_2–H_2O–TiO_2–O_2) e modelos a-X, ambos conforme descrito em Holland *et al.* (2018). Quartzo, titanita e H_2O são considerados fases puras. Para o modelamento foram selecionadas amostras representativas das variedades Px-Bt-Hbl tonalito a granodiorito (PBHTnGd) e Bt-Hbl monzogranito reduzido (BHMzGR) desprovidas de alteração hidrotermal marcante. Admite-se que sejam representativas da composição do líquido parental da respectiva variedade. As composições químicas destas amostras foram recalculadas a 100% assumindo diferentes conteúdos iniciais de água. As condições de fO_2 dos magmas foram obtidas com o software fO_2Melt (Holland *et al.* 2018), tendo sido definidas como FMQ+0.5 (PBHTnGd) e FMQ-0.5 (BHMzGR). Foi considerado o intervalo de pressão entre 8 e 2 kbar e o de temperatura entre 1200°C e 600°C.

1.6.7 Geocronologia

Foram submetidas a datações 10 amostras representativas das 4 variedades petrográficas da SIG, utilizando o método U-Pb em zircão (*in situ*) por SHRIMP (*Sensitive High-Resolution Ion MicroProbe*).

Primeiramente foram realizados na Oficina de Preparação de Amostras (OPA) do Instituto de Geociências da UFPA, britagem e moagem das amostras selecionadas por meio de britadores primário e secundário. Em seguida, as amostras foram tratadas no Laboratório de Preparação Mineral (LPM) do Instituto de Geociências da Universidade Federal do Pará (UFPA), utilizando técnicas convencionais para separação de zircão. São elas: peneiramento úmido em frações de 250, 175, 125 e 75 μm, separação por densidade (bateamento com água e microbateameno com álcool), separação com caneta magnética (imã de neodímio) e com separador eletromagnético Frantz. Por fim, cerca de 100 cristais de zircão foram separados com auxílio de lupa binocular e agulha. Foram obtidas imagens de microscópio eletrônico de varredura (MEV) com catodoluminescência (CL) e elétrons retroespalhados (BSE) para examinar a textura dos cristais de zircão, estruturas internas, sobrecrecimentos, fraturas e inclusões. As análises de U-Pb foram realizadas com equipamento SHRIMP IIe no Laboratório de Geocronologia de Alta Resolução do Instituto de Geociências da Universidade de São Paulo Paulo, sob supervisão do pesquisador Key Sato. Posteriormente, as imagens foram interpoladas utilizando o Adobe Photoshop 20.0 para uma análise conjunta das informações fornecidas pelos dois métodos (Cl e BSE). Os procedimentos analíticos para o

sistema SHRIMP IIe seguem o definido por Stern (1998), Williams (1997) e Sato *et al.* (2008, 2014). Os padrões utilizados são o SL 13 para a composição referência do U (238 ppm, Sato *et al.* 2014) e o zircão TEMORA-2 (416,78±0,33 Ma, Black *et al.* 2004) para razões isotópicas padrão, o qual foi analisado em um intervalo de 5:1. Os pontos de análises nos cristais foram direcionados sobre áreas com ~30 μm de diâmetro, livres de fraturas, inclusões e evidências de metamictização, quando possível. Os dados foram reduzidos utilizando o software SQUID 1.03 (Ludwig, 2009). As idades foram calculadas usando o programa Isoplot 4.15 (Ludwig 2008), com erros da razão isotópica de 1σ, sendo que os das elipses de idade foram calculados com 2σ (absoluto). Os critérios de seleção dos cristais de zircão analisados para o cálculo das idades envolveram: (a) verificação do conteúdo de chumbo comum (^{204}Pb), com exclusão das análises que contém razões ^{204}Pb/^{206}Pb maiores que 0,0004; (b) precisão analítica, excluindo-se as razões isotópicas com erros maiores que 3,0%; e (c) grau de discordância, sendo considerados aptos os valores mais próximos de zero.

1.6.8 Análise isotópica Lu-Hf em zircão

Para as análises de isótopos Lu-Hf em zircão (*in situ*) foram utilizadas 2 amostras da variedade Bt-Hbl monzogranito reduzido que forneceram idades U-Pb SHRIMP concordantes. Os pontos de análise foram feitos nos mesmos domínios dos cristais analisados por SHRIMP. As análises Lu-Hf foram realizadas no Laboratório de Geologia Isotópica (Pará-Iso) do Instituto de Geociências da UFPA com um *Laser Ablation Multi-Collector Ion Coupled Plasma Mass Spectrometer* (LA-MC-ICP-MS) de alta resolução, modelo Neptune, marca Thermo Finnigan, equipado com uma sonda laser Nd:YAG 213nm, modelo LSX-213 G2 da marca CETAC. A operação do ICP-MS é realizada utilizando os seguintes parâmetros analíticos: 16,0 l/min de fluxo de gás argônio (Ar) resfriador; 0,7 a 0,8 l/min de gás argônio auxiliar; 1,2 a 1,3 l/min de gás argônio de arraste, 1200 W de potência, –2000 de extração, em modo de análise estático em baixa resolução, utilizando oito coletores de Faraday. O *spot* do laser atinge 50μm de diâmetro e o fluxo de gás hélio, pelo qual é transportado o material de ablação até o ICP-MS, variou de 450–500 ml/min, 10 Hz e tempo total de ablação de 60 segundos. Utilizou-se potência de 50%, que forneceu uma densidade de energia de 4–5 J/cm^2 e permitiu gerar sinal da ordem de 1 a 3 volts para ^{178}Hf. O fracionamento elementar induzido pelo laser e a discriminação instrumental de massa foram corrigidos utilizando as razões isotópicas do zircão de referência GJ-1 (608,5 ± 1,5 Ma; Jackson *et al.* 2004) e Mud Tank (732 ± 1 Ma, Black & Gulson 1978, Horstwood *et al.* 2016). Os isótopos de Lu, Hf e Yb foram mensurados simultaneamente e, para realizar as correções de interferências isobáricas

dos isótopos ^{176}Lu e ^{176}Yb, , foram consideradas as razões isotópicas ^{173}Yb/^{171}Yb, ^{179}Hf/^{177}Hf, ^{175}Lu/^{177}Hf e ^{176}Hf/^{177}Hf. Desta forma, as interferências isobáricas do ^{176}Lu e ^{176}Yb foram corrigidas utilizando uma equação que envolve um fator de fracionamento de massa (β) para Lu e Yb e a intensidade dos sinais observados nos isótopos livres de interferência ^{175}Lu e ^{173}Yb. Os sinais foram normalizados a partir de suas abundâncias isotópicas conhecidas: ^{176}Lu/^{175}Lu = 0,026549 (Chu *et al.* 2002) e ^{176}Yb/^{173}Yb = 0,786956 (Thirlwall & Anczkiewicz 2004). O fator β (Hf, Yb e Lu) foi calculado para cada medida realizada, pois seu valor depende diretamente da razão entre os isótopos de interesse. Contudo, para corrigir o fracionamento isotópico provocado pelo equipamento, conforme a lei exponencial (Russell *et al.* 1978), as razões isotópicas de Yb foram normalizadas assumindo valor de 1,12346 para ^{173}Yb/^{171}Yb (Thirlwall & Anczkiewicz 2004) e as de Hf foram normalizadas utilizando valor de 0,7325 para a razão ^{179}Hf/^{177}Hf (Patchett & Tatsumoto 1981). Para a realização destes cálculos de correção e obtenção dos valores corrigidos das razões ^{176}Hf/^{177}Hf e ^{176}Lu/^{177}Hf, os dados brutos foram processados em macro Microsoft Excel (Milhomem Neto & Lafon 2019).

As idades-modelo dois estágios ou crustais (Hf-T_{DM}^{C}) e os parâmetros épsilon háfnio no tempo t, $\varepsilon_{Hf}(t)$ foram calculados em planilhas do Excel nas quais também foram gerados os diagramas de evolução do Idade vs. Hf. Para os cálculos foi usada a constante de decaimento λ^{176}Lu de 1,867x10^{-11} anos^{-1} (Söderlund *et al.* 2004), razão ^{176}Lu/^{177}Hf de 0,015 para o valor médio da crosta continental (Griffin *et al.* 2002) e razões ^{176}Lu/^{177}Hf e ^{176}Hf/^{177}Hf atuais para o Reservatório Uniforme Condrítico (CHUR) de 0,0336 e 0,282785 (Bouvier *et al.* 2008) e para o manto empobrecido (DM) de 0,0388 e 0,28325 (Andersen *et al.* 2009).

1.6.9 Análise isotópica de elementos terras raras em zircão

Para as análises isotópicas de ETR em zircão, foram selecionadas quatro amostras das variedades Px-Bt-Hbl Tonalito a granodiorito (1), Bt-Hbl Tonalito a granodiorito (2) e Bt-Hbl monzogranito reduzido (1). Os procedimentos para separar e obter imagens dos cristais de zircão são descritos no tópico 1.6.7. A determinação da composição isotópica dos ETR do zircão foi obtida através de SHRIMP (*Sensitive High-Resolution Ion MicroProbe*), no Laboratório de Geocronologia de Alta Resolução do Instituto de Geociências da Universidade de São Paulo Paulo, sob supervisão dos pesquisadores Key Sato e Maurício Borba. Os *spots* foram posicionados próximos aos *spots* U-Pb e as análises intercaladas com o padrão NIST 610. Foram analisados os seguintes elementos: La, Ce, Pr, Nd, Sm, Eu, Gd, Tb, Dy, Ho, Er, Tm, Yb e Lu. O procedimento completo e a configuração do equipamento são descritos em Sato *et al.* (2016), e o limite de detecção para o SIMS é conforme Wiedenbeck *et al.* (2004).

1.6.10 Análise isotópica Sm-Nd (rocha total)

Para as análises isotópicas Sm-Nd foram selecionadas 12 amostras representativas das 4 variedades da SIG previamente preparadas para geoquímica em rocha total seguindo os mesmos procedimentos de trituração, pulverização e homogeneização realizados em oficinas e laboratórios da Universidade Federal do Pará. As análises foram realizadas no Laboratório de Estudos Geodinâmicos, Geocronológicos e Ambientais (LEGGA) da Universidade de Brasília (UNB) sob supervisão do professor Elton Dantas. Os procedimentos analíticos seguem o descrito por Gioia & Pimentel (2000). Para as análises foi utilizado um espectrômetro de massa MAT Finnigan MAT 262 (ID-TIMS). Aproximadamente 50 mg de pó de rocha foram misturados com um *spike* de ^{149}Sm-^{150}Nd e dissolvidos em cápsulas de Savillex. Sm e Nd foram extraídos por meio de troca catiônica em colunas de Teflon com resina L-N spec (HDEHP-*diethylhexyl phosphoric acid supported on PTFE powder*). Os elementos foram então colocados em um filamento de rênio e detectados em modo estático. A precisão para Sm/Nd e $^{143}Nd/^{144}Nd$ é maior do que ± 0,5% (2σ) e ± 0,005% (2σ), respectivamente, com base em análises repetidas dos padrões internacionais de rochas BHVO-1 e BCR-1. A razão $^{143}Nd/^{144}Nd$ foi normalizada para $^{146}Nd/^{144}Nd$ igual a 0,7219, e a constante de decaimento usada foi $6{,}54 \times 10^{-12}$ a^{-1}. As idades-modelo TDM foram calculadas conforme Depaolo (1981) por meio da macro Isoplot 4.15 (Ludwig 2008) via EXCEL (Microsoft).

CAPÍTULO 2: CRYSTALLIZATION PARAMETERS AND THERMODYNAMIC MODELING OF THE IGARAPÉ GELADO SUITE: IMPLICATIONS FOR THE NEOARCHEAN MAGMATISM OF THE CARAJÁS PROVINCE, BRAZIL.

Publicado em: Journal of South American Earth Sciences - Qualis CAPES A2
Doi: https://doi.org/10.1016/j.jsames.2025.105357

Devido aos direitos autorais do *Journal of South American Earth Sciences*, a formatação, citações e referências bibliográficas do capítulo 2 seguem o formato da publicação na revista.

Journal of South American Earth Sciences 153 (2025) 105357

Contents lists available at ScienceDirect

Journal of South American Earth Sciences

journal homepage: www.elsevier.com/locate/jsames

Crystallization parameters and thermodynamic modeling of the Igarapé Gelado suite: Implications for the Neoarchean magmatism of the Carajás province, Brazil

Caio José Soares Mesquita [a,b,*], Roberto Dall'Agnol [b,c], Arthur Santos da Silva Neri [a,b], Ingrid Roberta Viana da Cunha [b], José de Arimatéia Costa de Almeida [a,b], Junny Kyley Mastop de Oliveira [d]

[a] Post-Graduate Program in Geology and Geochemistry (PPGG), Institute of Geosciences (IG), Federal University of Pará (UFPA), Post office 8608, CEP-66075-110 Belém, Pará, Brazil
[b] Group of Research on Granitoid Petrology (GRGP), IG, UFPA, Brazil
[c] Vale Institute of Technology, Post office 955, CEP- 66055-090, Belém, Pará, Brazil
[d] CPRM – Geological Survey of Brazil, Post office, 346, CEP-66095-904, Belém, Pará, Brazil

ARTICLE INFO

Keywords:
Mineral chemistry
Crystallization parameters
Thermodynamic modeling
A-type granite
Carajás
Amazonian craton
Archean

ABSTRACT

The Igarapé Gelado suite (IGS) is located near the northern border of the Carajás Province, almost at the boundary with the Bacajá Domain, along the Cinzento lineament and is intrusive in metamafic rocks and banded iron formations. The central-eastern portion of the IGS comprises four rock varieties: tonalite to granodiorite with varying contents of biotite and amphibole, (1) with associated clinopyroxene and/or orthopyroxene (PBHTnGd) or (2) devoid of pyroxenes (BHTnGd); and biotite-amphibole monzogranites that exhibit variable biotite and amphibole content, and can be (3) moderately (BHMzG) or (4) strongly (RBHMzG) reduced. These varieties occur as elongated sigmoidal bodies and exhibit penetrative to locally incipient WNW-ESE to E-W foliation. The structural features suggest that deformation was controlled by shear zones, with the magmas being affected by progressive deformation until the end of the cooling stage.The PBHTnGd shows ferrosilite and/or augite with subordinate hedenbergite. The amphiboles are K-hastingsite and, subordinately, Fe-Tschermakite in monzogranites. Biotites are ferroan, and in reduced granites show #Fe > 0.90. These micas are alkaline to subalkaline and compositionally akin of primary magmatic biotites. Plagioclase is oligoclase. The IGS granites crystallized at pressures of 550 ± 100 MPa, higher than those attributed to other Neoarchean granites in Carajás. The estimated *liquidus* temperature for the IGS pyroxene variety is −1000 ± 50 °C. BHTnGd and BHMzG formed within a similar temperature range to PBHTnGd, while RBHMzG had lower *liquidus* temperatures (≤900 °C). *Solidus* temperatures of around −660 °C were estimated for the four IGS varieties. The BHMzG magma evolved under conditions of low fO_2, slightly above or below the FMQ buffer (FMQ±0.5), like those of the Planalto suite and the reduced granites of the Vila Jussara and Vila União suites of Carajás province. In the magmas of the PBHTnGd and BHTnGd varieties the oxygen fugacity attained FMQ+0.5. The RBHMzG crystallized under strongly reduced conditions equivalent to FMQ-0.5 to FMQ-1. The magmas of the monzogranitic varieties evolved with a high H_2O content (≥4 wt%) attaining 7% in the case of the reduced monzogranites. This is comparable to, or slightly exceeding, the levels typically attributed to the Neoarchean granites of Carajás (>4%). In contrast, the variety with pyroxene has a water content (−4%) like that of Café enderbite and Rio Seco charnockite from Carajás, and Matok Pluton from Limpopo belt. The integration of thermobarometry results (T, P, fO_2, H_2O) and thermodynamic modeling and their comparison with the paragenesis present in natural rocks allowed a better interpretation of magmatic evolution and improved the estimation of crystallization parameters. The results reveal that despite the similarities with other Neoarchean granites in Carajás, the Igarapé Gelado

* Corresponding author. Post-Graduate Program in Geology and Geochemistry (PPGG), Institute of Geosciences (IG), Federal University of Pará (UFPA), Post office 8608, CEP-66075-110 Belém, Pará, Brazil.
E-mail addresses: caiiogeologo@gmail.com (C.J. Soares Mesquita), robdal@ufpa.br (R. Dall'Agnol), arthur.santos.silva@ig.ufpa.br (A.S. da Silva Neri), ingridvcunha@gmail.com (I.R.V. Cunha), ari@ufpa.br (J.A.C. Almeida).

https://doi.org/10.1016/j.jsames.2025.105357
Received 4 November 2024; Received in revised form 9 January 2025; Accepted 9 January 2025
Available online 11 January 2025

Crystallization parameters and thermodynamic modeling of the Igarapé Gelado suite: Implications for the Neoarchean magmatism of the Carajás province, Brazil

Caio José Soares Mesquita[a,b],
Roberto Dall'Agnol[b,c],
Arthur Santos da Silva Neri[a,b],
Ingrid Roberta Viana da Cunha[b],
José de Arimatéia Costa de Almeida[a,b],
Junny Kyley Mastop de Oliveira[d]

a-Post-Graduate Program in Geology and Geochemistry (PPGG), Institute of Geosciences (IG), Federal University of Pará (UFPA), Post office 8608, CEP-66075-110 Bélém, Pará, Brazil. E-mails: caiojsm@gmail.com, arthur.santos.silva@ig.ufpa.br, ari@ufpa.br,
b-Group of Research on Granitoid Petrology (GRGP), IG, UFPA, Brazil. E-mail: ingridvcunha@gmail.com
c-Vale Institute of Technology, Post office 955, CEP- 66055-090, Belém, Pará, Brazil. Email: robdal@ufpa.br
d-CPRM – Geological Survey of Brazil, Post office, 346, CEP-66095-904, Belém, Pará, Brazil. E-mail: junny.oliveira@cprm.gov.br

ABSTRACT

The Igarapé Gelado suite (IGS) is located near the northern border of the Carajás Province, almost at the boundary with the Bacajá Domain, along the Cinzento lineament and is intrusive in metamafic rocks and banded iron formations. The central-eastern portion of the IGS comprises four rock varieties: tonalite to granodiorite with varying contents of biotite and amphibole, (1) with associated clinopyroxene and/or orthopyroxene (PBHTnGd) or (2) devoid of pyroxenes (BHTnGd); and biotite-amphibole monzogranites that exhibit variable biotite and amphibole content, and can be (3) moderately (BHMzG) or (4) strongly (RBHMzG) reduced. These varieties occur as elongated sigmoidal bodies and exhibit penetrative to locally incipient WNW-ESE to E-W foliation. The structural features suggest that deformation was controlled by shear zones, with the magmas being affected by progressive deformation until the end of the cooling stage.The PBHTnGd shows ferrosilite and/or augite with subordinate hedenbergite. The amphiboles are K-hastingsite and, subordinately, Fe-Tschermakite in monzogranites. Biotites are ferroan, and in reduced granites show #Fe > 0.90. These micas are alkaline to subalkaline and compositionally akin of primary magmatic biotites. Plagioclase is oligoclase. The IGS granites crystallized at pressures of 550 ± 100 MPa, higher than those attributed to other Neoarchean granites in Carajás. The estimated *liquidus* temperature for the IGS pyroxene variety is ~1000±50°C. BHTnGd and BHMzG formed within a similar temperature range to PBHTnGd, while RBHMzG had lower *liquidus* temperatures (≤900°C). *Solidus* temperatures of around ~660 °C were estimated for the four IGS varieties. The BHMzG magma evolved under conditions of low fO_2, slightly above or below the FMQ buffer (FMQ±0.5), like those of the Planalto suite and the reduced granites of the Vila Jussara and Vila União suites of Carajás province. In the magmas of the PBHTnGd and BHTnGd varieties the oxygen fugacity attained FMQ+0.5. The RBHMzG crystallized under strongly reduced conditions equivalent to FMQ-0.5 to FMQ-1. The magmas of the monzogranitic varieties evolved with a high H_2O content (≥4 wt%) attaining 7% in the case of the reduced monzogranites. This is comparable to, or slightly exceeding, the

levels typically attributed to the Neoarchean granites of Carajás (>4%). In contrast, the variety with pyroxene has a water content (~4%) like that of Café enderbite and Rio Seco charnockite from Carajás, and Matok Pluton from Limpopo belt. The integration of thermobarometry results (T, P, fO_2, H_2O) and thermodynamic modeling and their comparison with the paragenesis present in natural rocks allowed a better interpretation of magmatic evolution and improved the estimation of crystallization parameters. The results reveal that despite the similarities with other Neoarchean granites in Carajás, the Igarapé Gelado suite has singularities that allow advances in understanding the petrogenesis of A-type Archean granites, which still have many unresolved issues.

Keywords: Mineral Chemistry, Crystallization parameters, thermodynamic modeling, A-type Granite, Carajás, Amazonian craton, Archean.

1 INTRODUCTION

A-Type granites are generally formed in extensional, anorogenic, or post-collisional environments. (Eby, 1992; King et al., 1997; Nardi and Bitencourt, 2009; Sylvester, 1989; Whalen et al., 1987) and were initially described as isotropic, alkaline, formed under anhydrous conditions, and at low fO_2 (Loiselle and Wones, 1979). However, the existence of oxidized A-type granites that crystallized with moderate to high water contents has been demonstrated (Anderson and Smith, 1995; Anderson and Morrison, 2005; Dall'Agnol et al., 1999; Dall'Agnol and Oliveira, 2007). Neoarchean foliated syntectonic granites (~2.75 - 2.73 Ga) have also been commonly described in the Carajás province (CP). These granites are metalluminous to slightly peraluminous and have affinity with reduced ferroan A-type granites (Barros et al. 1997, 2001, 2009; Sardinha et al. 2006; Feio et al. 2012, 2013; Cunha et al. 2016), except those in the Igarapé Gelado (Barros et al., 2009), Vila Jussara (Dall'Agnol et al., 2017; Silva et al., 2020, submitted; Sousa et al., 2022) and Vila União suites (Marangoanha et al., 2019a), which also include oxidized ferroan and even slightly magnesian granitoids. High water contents (>4 % by weight) have been estimated for these granites, which are sometimes associated with charnockites (Feio et al., 2012; Felix et al., 2020; Marangoanha et al., 2022).

The Igarapé Gelado suite (IGS) forms a batholithic body located in the northern portion of the Carajás Basin (Fig. 1b), close to the CP boundary with the Bacajá Domain (Barbosa, 2004; Barros et al., 2001, 1997, 2009) and intrusive in metabasic rocks and banded iron formations of the Itacaiúnas Supergroup. Preliminary studies have characterized this magmatism and defined its Neoarchean age (Barbosa, 2004; Barros et al., 2009; Melo et al., 2016; Tavares et al., 2021; Toledo et al., 2023). Nevertheless, there are still significant gaps in

the knowledge of this plutonic suite. As a result, a research on the geology, petrography, microstructure, mineral chemistry, geochemistry, geochronology, and petrogenesis of the IGS has been carried out in the central-eastern portion of the batholith. This article will present the new geology, petrography, mineral chemistry, and thermodynamic modeling data obtained.

The chemical composition and associations of silicate minerals and Fe-Ti oxide minerals combined with geothermobarometry studies allow the estimation of crystallization parameters (T, P, fO_2, XH_2O) of granitic rocks (Bogaerts et al., 2003; Cunha et al., 2016; Felix et al., 2020; Marangoanha et al., 2022; Rapopo, 2011). Thermodynamic equilibrium modeling has also been increasingly used to improve understanding of the geological processes present in magmatism (Klimm et al., 2003; Semprich et al., 2015; Zhang et al., 2023; Zhao et al., 2023, 2018, 2017). Based on established pressure-temperature (P-T) conditions (Xiang and Connolly, 2022), this approach enables by the use of adequate softwares (e.g. THERMOCALC, Powell and Holland, 1988; TWQ, Berman, 1991; Perple_X, Connolly, 2005; Theriak Domino, de Capitani and Petrakakis, 2010; rhyolite-MELTS, Gualda et al., 2012, Gualda and Ghiorso, 2015; GeoPs, Xiang and Connolly, 2022) to simulate the behavior of magmatic systems and predict stable mineral assemblages. The combination of thermodynamic modeling with thermobarometry developed in this work is unprecedented in CP studies. It has provided a deeper discussion of the evolution of IGS rocks, furnishing petrological information that will contribute to the establishment of comparisons with other Neoarchean granites from Carajás and other cratons. The aim is to contribute to understanding the Neoarchean magmatism of Archean cratons, particularly the A-type granites and associated charnockites.

2 GEOLOGICAL FRAMEWORK

The Carajás province (CP) is the main Archean block of the Amazonian Craton (AC). It is located in the southeastern portion of the AC (Fig. 1a) and is bordered along the north by the Bacajá domain, on the south by the Santana do Araguaia domain, to the east by the Araguaia belt and on the west by the Central Amazon province (Santos et al., 2006). According to the tectonic models proposed for the AC, the CP is its oldest core, generated and tectonically stabilized during the Archean; subsequent episodes of crustal accretion occurred around it throughout the Paleoproterozoic and Mesoproterozoic periods (Santos et al., 2006; Tassinari and Macambira, 2004).

The CP is subdivided into two domains: Rio Maria (RMD) to the south and Carajás (CD) to the north (Santos, 2003; Vasquez and Rosa-Costa, 2008). i) The RMD has a Mesoarchean age and is a remarkably well-preserved granite-greenstone terrane (3.05-2.86 Ga; Almeida et al., 2011, 2013; Macambira and Lancelot, 1996; Oliveira et al., 2011; Souza et al., 2001). ii) The CD dates from the Mesoarchean to Neoarchean (3.07-2.70 Ga.); Avelar et al., 1999; Feio et al., 2013; Machado et al., 1991; Marangoanha et al., 2019a; Pidgeon et al., 2000; Silva et al., 2020; Tavares et al., 2018), and has a more complex geological evolution, being subdivided into the Sapucaia and Canaã dos Carajás terranes and the Carajás Basin (Dall'Agnol et al., 2013; Silva et al., 2022). The Mesoarchean and Neoarchean supracrustal units of the Carajás Domain are intruded by syntectonic Neoarchean (cf. Fig. 1b; Barros et al., 2009; Cunha et al., 2016; Dall'Agnol et al., 2017; Feio et al., 2012; Marangoanha et al., 2019a; Melo et al., 2016; Silva et al., 2020; Sousa et al., 2022;), and anorogenic Paleoproterozoic granites (Dall'Agnol et al., 2005; Gonçalez et al., 1988; Teixeira et al., 2019, 2018; Teruiya et al., 2008).

2.1 NEOARCHEAN GRANITIC MAGMATISM OF THE CARAJÁS PROVINCE

The Neoarchean granitogenesis (~2.75 - 2.57 Ga) of the CP is represented by: (i) granites geochemically akin of A-type granites (Planalto, Vila União, Vila Jussara, and Igarapé Gelado suites; Estrela complex; Serra do Rabo granite; Barros et al., 1997, 2001, 2009; Cunha et al., 2016; Dall'Agnol et al., 2017; Feio et al., 2012, 2013; Marangoanha et al., 2019a; Oliveira et al., 2018a; Sardinha et al., 2006; Silva et al., 2020; Sousa et al., 2022); (ii) peralkaline to metaluminous granites (Velho Salobo, Itacaiúnas e GT-46; Diniz et al., 2023; Machado et al., 1991; Melo et al., 2016; Souza et al., 1996; Toledo et al., 2019); (iii) calc-alkaline potassic granites (high potassium granites from Velha Canada; Leite-Santos et al., 2010; Leite-Santos and Oliveira, 2016); (iv) charnockitic rocks from Ourilândia do Norte (Rio Seco charnockite; Felix et al., 2020) and enderbites of Vila Ouro Verde (Café enderbite; Marangoanha et al., 2019b, 2022); (v) sodic granitoid with a tholeiitic signature from the Pedra Branca suite (Feio et al., 2013; Santos-Silva et al., 2020; Sardinha et al., 2004); and (vi) undifferentiated Neoarchean granites (Plaquê suite; Araújo et al., 1988; Avelar et al., 1999; Jorge João and Araújo, 1992). The geochronological data of Neoarchean magmatism in the Carajás Basin are summarized in Supplementary Table 1.

The Neoarchean rocks that have an affinity with type A granites from Carajás are metaluminous to slightly peraluminous and are reduced ferroan (Barros et al., 1997, 2001, 2009; Sardinha et al., 2006; Feio et al., 2012, 2013; Cunha et al., 2016), except for those of

the Igarapé Gelado granite (Barros et al., 2009, Mesquita et al., submitted), which also have oxidized ferroan granites, and the granitoids of the Vila Jussara (Dall'Agnol et al., 2017; Silva et al., 2020; Sousa et al., 2022; Silva et al., 2024) and Vila União suites (Marangoanha et al., 2019), which also include oxidized ferroan and even mildly magnesian granitoids.

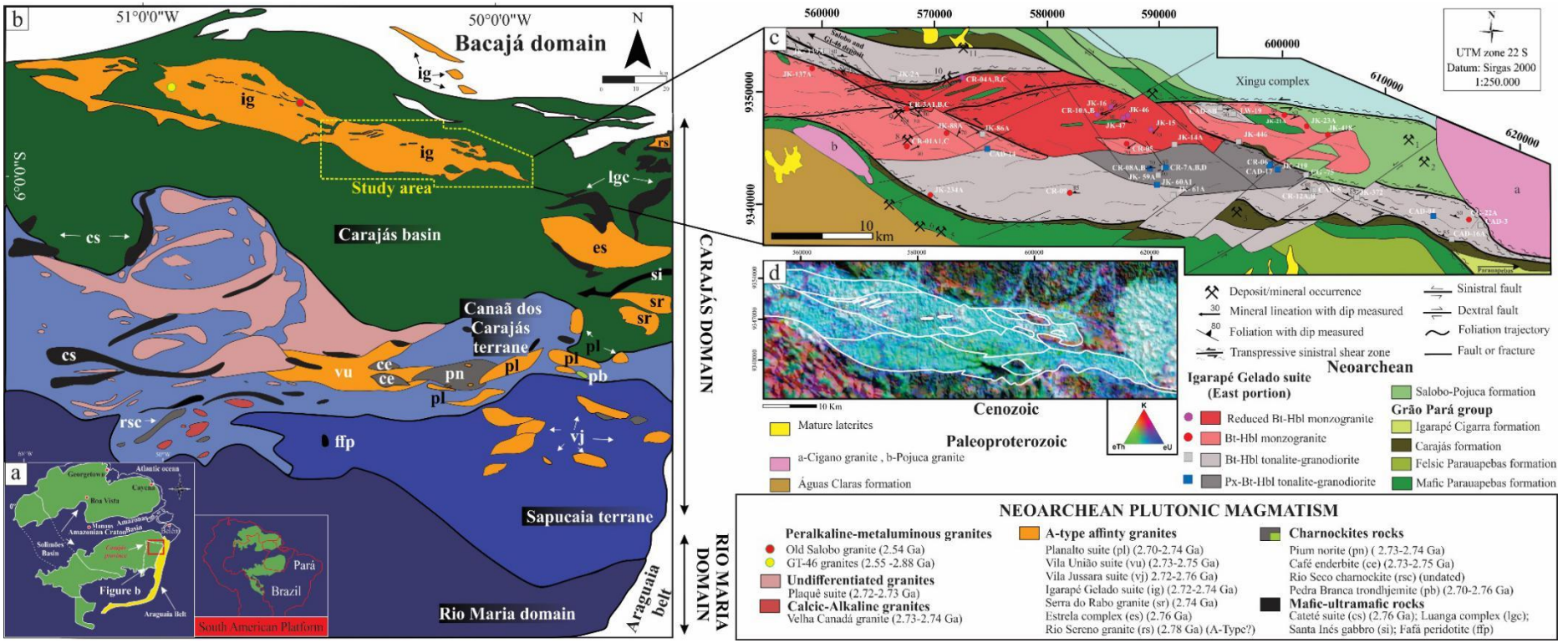

Figure 1. a) Location map of the Amazonian craton showing the Carajás province (CP); b) Simplified geological map of the CP highlighting the Neoarchean plutonic rocks; c) Geological map of the central-eastern portion of the Igarapé Gelado suite; d) RGB ternary distribution map (K, eTh, eU) merged with the Digital Terrain Model (DTM) with outlines of the geological units in figure 1C. Geological map of the underlying units and structural features based on Oliveira et al., (2018b, modified). Types of mineral deposits and occurrences (Tavares et al., 2021): IOCG (1-Furnas, 3-Circular, 5-Grota Funda, 10-Paulo Afonso and 11-Japim); VMS (7-Pojuca); Au placer (2-Mesquita, 4-Madeirinha and 8-Cazuza) and Granite-related (6-Gameleira and 9-Grota da Cruz).

3 GEOLOGY AND FIELD FEATURES

The geological map of the IGS area of occurrence (Fig. 1c) was produced according to the interpretation of radar images and supported by recent aerogeophysical and geological maps (Oliveira et al., 2018b; Tavares et al., 2021), along with fieldwork, petrography, mineral chemistry, and whole rock geochemical analyses that made possible the definition of the different facies present and their spatial distribution. Therefore, four varieties were recognized in the studied portion of the IGS: 1 and 2 - equigranular to heterogranular tonalite-granodiorite with varied biotite and amphibole content and presence of clinopyroxene and/or orthopyroxene (PBHTnGd facies, Figs. 2a and 4a, b) or devoid of pyroxenes (facies BHTnGd, Figs. 2b, c and 4c, d); 3 and 4 - heterogranular biotite-amphibole monzogranite (facies BHMzG Fig. 2d, e and 4e, f), occasionally with a strongly reduced character (facies RBHMzG, Fig. 2f and 4g, h).

Data of an aerogeophysical survey undertaken by the Geological Survey of Brazil (Tavares et al., 2021) were synthesized in an RGB ternary distribution image (K, eTh, eU), and merged with a Digital Terrain Model (Fig 1d). It is observed in it, that the tonalitic-granodioritic varieties are distinguished from the granitic ones by the more marked influence of Th (greenish tones), instead of U (bluish tones). The IGS consists of elongated sigmoidal bodies that extend over an area of approximately 80 km x 15 km. The granitoids in the central-eastern portion form plutons limited by shear zones (SZ) and are intrusive in metavolcanic-sedimentary sequences belonging to the Itacaiúnas Supergroup (Fig. 1c, Barbosa, 2004; Barros et al., 1997, 2001, 2009). The western portion of the IGS was not studied because access was limited due to the presence of dense tropical rainforest. The contact relationships between the IGS granites and their country rocks are not well exposed in the field.

In general, the IGS rocks exhibit a penetrative foliation (Fig. 2), with a WNW-ESE to E-W direction and local variations to WSW-ENE, reflecting the sigmoid shape of the plutons (Fig. 1c). These directions are consistent with the regional trend (Cinzento lineament, Pinheiro and Holdsworth, 2000), and, in general, with those observed in the other Neoarchean granites of the CP. The foliation dominantly shows intermediate to high-angle dips (50° to 85°, Fig. 2b), with variable inclination to south and north, although sub-horizontal dips occur occasionally. The foliation is regular and continuous at the mesoscopic level, being marked by intercalations of orientated mafic-enriched and quartz-feldspathic bands (Fig. 2b, d, and 4h)

and sometimes reinforced by concordant granitic/quartz veins. However, discordant pegmatitic veins and felsic or mafic veins are more common.

Rocks with an expressive mineral lineation, in a direction discordant to the regional trend,classified as L tectonites, are found mainly in the northern part of the body. The dominant stretching direction is NE-SW, with subordinate NW-SE, and it shows sub-horizontal dip (~30°). This differs from the foliation, in which NW-SE and WNW-ESE directions predominate. Deformation is often moderate to strong and controlled by the greater or lesser proximity of the SZ, being more marked at the borders of the body and in its interior near the contact zones between granite varieties. The shear bands are centimetric to metric and marked by the development of mylonitic to ultramylonitic rocks. Radar image interpretations suggest that the SZs are sinistral (Oliveira et al., 2018b). Broadly, compared to the other varieties of the IGS, the PBHTnGd variety exhibits a lower level of deformation.

Fractures in conjugate pairs and sinistral or distal faults are common (Oliveira et al., 2018b, Fig.1c). Normal faults occur occasionally, and stretches are observed on the fault planes. A brittle-ductile structure characterized by fractures that permitted small ductile movements within the foliation was observed locally (Fig. 2f). Additionally, there are occurrences of the BHMzG variety with varied grain sizes and mafic mineral content, intercalated laterally and parallel to the direction of the regional trend (Fig. 2e). There are also injection of Bt-Opx-Hbl MzG into Bt-Opx-Hbl Tnl, both of which belong to the PBHTnGd variety, showing an abrupt contact (Fig. 2a). Locally, mingling textures between the Bt-Hbl MzG and Bt-Hbl Tnl facies of the BHTnGd variety were noted (Fig. 2c).

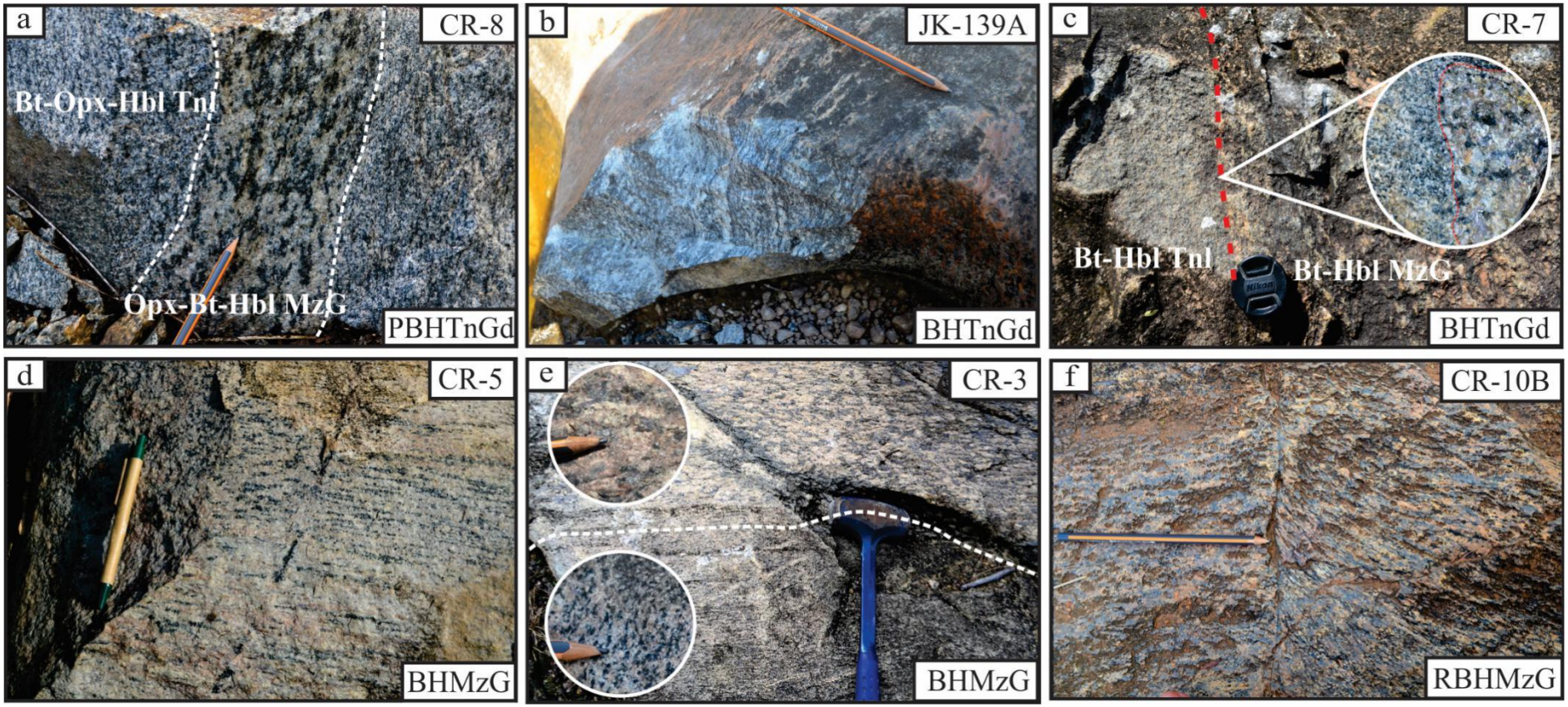

Figure 2. General field aspects of the Igarapé Gelado suite: a) A medium-grained Bt-Opx-Hbl tonalite abruptly intersected by a coarse-grained Opx-Bt-Hbl monzogranite; b) BHTnGd foliation with a high-angle dip; c) Contact between the Bt-Hbl Tnl and Bt-Hbl MzG facies with evidence of mingling; d) BHMzG displaying alternating layers enriched in felsic and mafic minerals, showing preferential orientation in the foliation plane; e) Contact between rocks of the BHMzG variety with textural variations and differing mafic content; f) RBHMzG presenting a brittle-ductile structure, with fractures leading to small ductile movements along the foliation.

4 PETROGRAPHY

4.1 MODAL COMPOSITION AND CLASSIFICATION

The petrographic study involved mesoscopic and microscopic analyses combined with the definition of modal composition in thin sections of 51 samples (Supplementary Table 2). Endeeper Hardledge software was employed for modal analyses with a grid of ~2000 points per sample at a spacing of 0.4mm. The four rock varieties of the IGS were classified following Le Maitre et al. (2020) (Fig. 3). In general, in addition to quartz, plagioclase, and potassium feldspar, biotite and amphibole occur as varietal minerals, accompanied in the PBHTnGd variety by clinopyroxene and orthopyroxene. In the latter, subhedral crystals of reddish-brown biotite and olive-green hornblende are distinctive (Fig. 4b). Biotite varieties in BHTnGd, BHMzG, and RBHMzG exhibit pleochroism from light to dark brown (see Fig. 4d, f, h) and are often associated with bluish-green amphibole crystals, which in monzogranites typically occupy the interstitial spaces between quartz and feldspars (Fig. 4f).

The mafic content ranges from 2.9 to 20.9% and is systematically higher in tonalitic and granodioritic rocks (Fig. 3). The primary accessories are titanite, allanite, ilmenite, magnetite, zircon, and apatite. The secondary minerals are ferromagnesian amphibole, epidote, chlorite, scapolite, muscovite, carbonates, and, in hydrothermalized granitoids, sulfides (chalcopyrite and pyrite). Titanite is anhedral to subhedral and usually occurs bordering ilmenite (Fig. S1a) or in isolated crystals. The crystals of allanite are anhedral and granular, often associated with epidote and opaque minerals. Zircon is subhedral, metamict or, more rarely, preserved. Apatite is subhedral and mainly included in plagioclase and quartz. Epidote and chlorite are the products of alteration of plagioclase and biotite, respectively.

IGS rocks commonly exhibit intense deformation, which increases sharply near and along shear zones. A detailed study was conducted to identify the microstructural features and their implications for the evolution of the body. In summary, it is assumed that the emplacement of the IGS granitoids were controlled by shear zones, and that the initial stages of deformation occurred in the final stages of their crystallization, and persisted in subsolidus conditions after the granitoids have, already entirely crystallized.

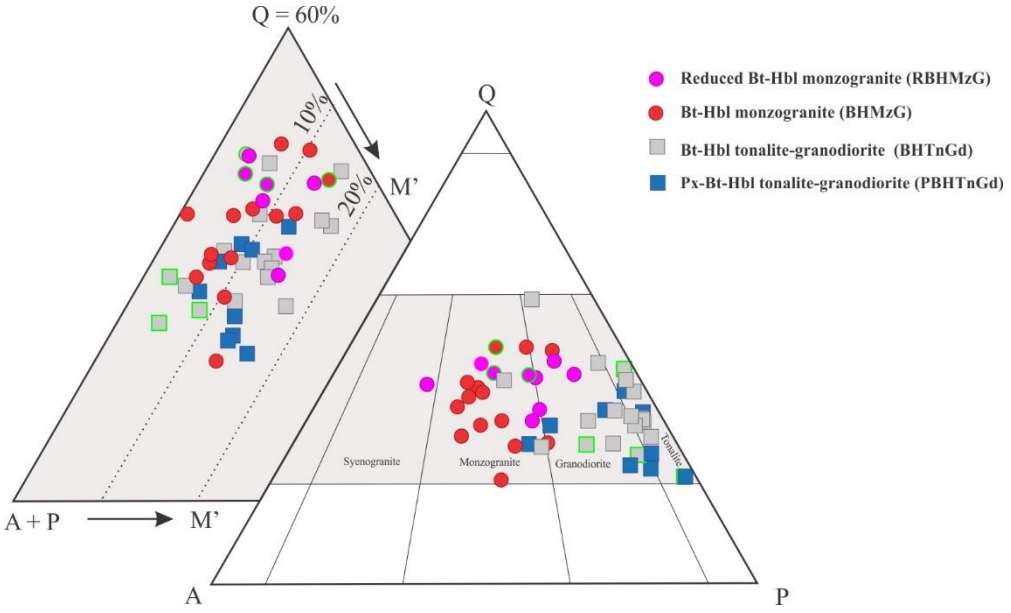

Figure 3. QAP and Q-A+P-M' diagrams (Le Maitre et al., 2020) for the varieties of the Igarapé Gelado suite. Abbreviations: A = alkali feldspar; P = Plagioclase; Q = Quartz; M'= M - (apatite + muscovite + carbonates). Symbols with a green border = hydrothermalized rocks.

5 MINERAL CHEMISTRY

5.1 ANALYTICAL PROCEDURES

Based on microscopic petrography, textural observations, and semi-quantitative analysis using a scanning electron microscope (SEM), 15 samples of the four IGS varieties: PBHTnGd (4), BHTnGd (4), BHMzG (5), and RBHMzG (2) were selected for microprobe analysis. The analyzed minerals included orthopyroxene, clinopyroxene, amphibole, biotite, and plagioclase. A JEOL JXA-8230 electron microprobe equipped with 5 WDS spectrometers and one EDS spectrometer was used at the Microanalysis Laboratory of the Geosciences Institute of the UFPA. Polished thin sections were previously coated with carbon film. The microprobe operated under conditions of 15 kV acceleration, 20 nA current, and a 10 µm beam diameter for analyzing silicates. The analysis time was 20 seconds for Si, Ca, and Ti and 30 seconds for Na, Al, F, Mg, Sr, K, Cr, Ni, Fe, Mn, Ba, Cl, and V. The matrix effect was corrected using the ZAF method, resulting in an analytical precision of ± 1% and ± 10% for major and minor elements, respectively. The crystals used for analysis included TAP for Si, Al, Mg, Na, F, and Sr; PETJ for Cr, Ca, and K; LIF for Ni, Fe, Mn, and Ba; PETH for Cl and V. The standards used were SiO_2 (Si), rutile (Ti), corundum (Al), Fe_2O_3 (Fe), wollastonite (Ca), rhodonite (Mn), periclase (Mg), sodalite (Na and Cl), microcline (K) and fluorite (F).

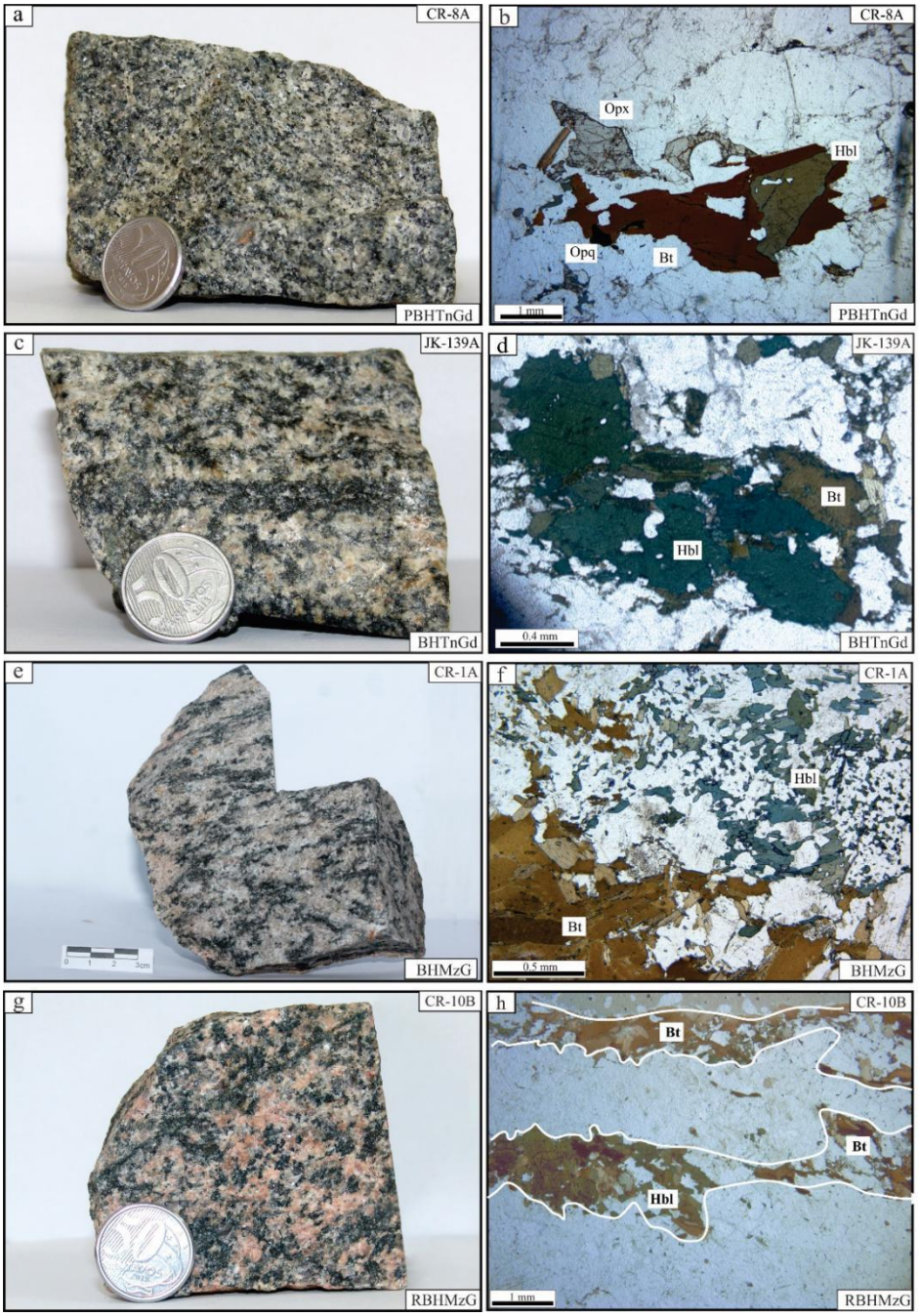

Figure 4. Mesoscopic and microscopic textural aspects of the varieties from the Igarapé Gelado suite: a) PBHTnGd - Medium heterogranular biotite-orthopyroxene-hornblende tonalite; b) Typical association of PBHTnGd mafic minerals, with reddish-brown biotite, orthopyroxene, olive-green hornblende, and opaques; c) BHTnGd - Coarse biotite-hornblende granodiorite; d) Brown biotite anhedral crystals, associated with bluish-green amphibole crystals; e) BHMzG - Coarse foliated biotite-hornblende monzogranite; f) Anhedral crystals of bluish-green hornblende filling interstices and associated with brown biotite lamellae; g) RBHMzG - Medium to coarse biotite-hornblende monzogranite of reduced character; h) Alternated mafic and felsic enriched levels in foliated rock. H = hornblende, a general term to represent calcium amphiboles (Leake, 1997). Abbreviations, according to Whitney and Evans, (2010).

5.2 PYROXENE

Orthopyroxene has a ferrosilite composition (Morimoto et al., 1988), and its compositional variation (Table S3) is $Wo_{1-2}En_{22-33}Fs_{65-77}$ (Fig. 5a). Meanwhile, clinopyroxene ploted close to the border between the augite and hedenbergite fields (Fig.5a) and has a

composition of $Wo_{42-46}En_{24-25}Fs_{30-33}$ (Table S3). , As illustrated in the X_{Al} vs X_{Mg} diagram (Fig. 5b), employed to to distinguish magmatic and metamorphic orthopyroxene in charnockitic assemblages (Rajesh et al., 2011), the orthopyroxene from the PBHTnGd facies has low Al content (0.03 to 0.04 apfu) that suggests it has a magmatic origin.

5.3 AMPHIBOLE

The structural formulas of amphibole were calculated using 23 oxygen atoms (Leake et al., 1997), and its classification was based on Hawthorne et al. (2012). The normalization pattern for calcium amphiboles was 13 cations minus Ca, Na, and K (13eCNK). The proportions of Fe^{+3} and Fe^{+2} were calculated by mass balance (Schumacher method, in Leake et al., 1997). The dominant amphibole of the four IGS varieties is K-hastingsite, with subordinate Fe-Tschermakite occurring in the BHMzG and RBHMzG (Fig. 5c, d). The K-hastingsite of PBHTnGd and BHTnGd have Mg/(Mg+Fe) ratio varying of 0.23 to 0.28 and 0.15 to 0.37, respectively, with one isolated sample showing a ratio ≤0.10 (CAD-14). The amphibole of BHMzG shows ratios of 0.12 to 0.32, which overlap with those of the BHTnGd, while that of the RBHMzG exhibits much lower ratios, between 0.06 and 0.11 (Fig. 5c; Table S4). The analyses of the crystals indicate that there is no significant contrast in composition between their cores and borders. The total Al content of the IGS varieties ranges from 1.54 to 2.11 apfu, with the lower values in the RBHMzG variety (Table S4). The Cl content in all varieties is higher than the F concentration, which is inexpressive, and is >0.5 apfu in the PBHTnGd and BHTnGd and <0.5 apfu in the BHMzG and <0.1 in the RBHMzG.

5.4 BIOTITE

The structural formulas of biotite were calculated using 22 oxygen atoms, and the total iron was assumed to be Fe^{2+} (Table S5). The Fe/(Fe+Mg) vs. Si diagram (Deer et al., 2013) reveals that the IGS biotites are ferroan (Fig. 6a), and those of the RBHMzG variety are positioned near the line linking the annite and siderophyllite poles (Fig. 6b, Deer et al., 1992). The Fe/Fe+Mg ratio (Fig. 6b; Table S5) increases gradually from the PBHTnGd (0.69-0.77) to the BHTnGd (0.74-0.77) and BHMzG (0.77-0.85), reaching maximum values in the RBHMzG (0.92 to 0.94). The Al_{total} of the biotite displays minimum values (2.44-2.5) in PBHTnGd and in the other IGS varieties, it ranges between 2.53 and 2.87 (Fig. 6c; Table S5).

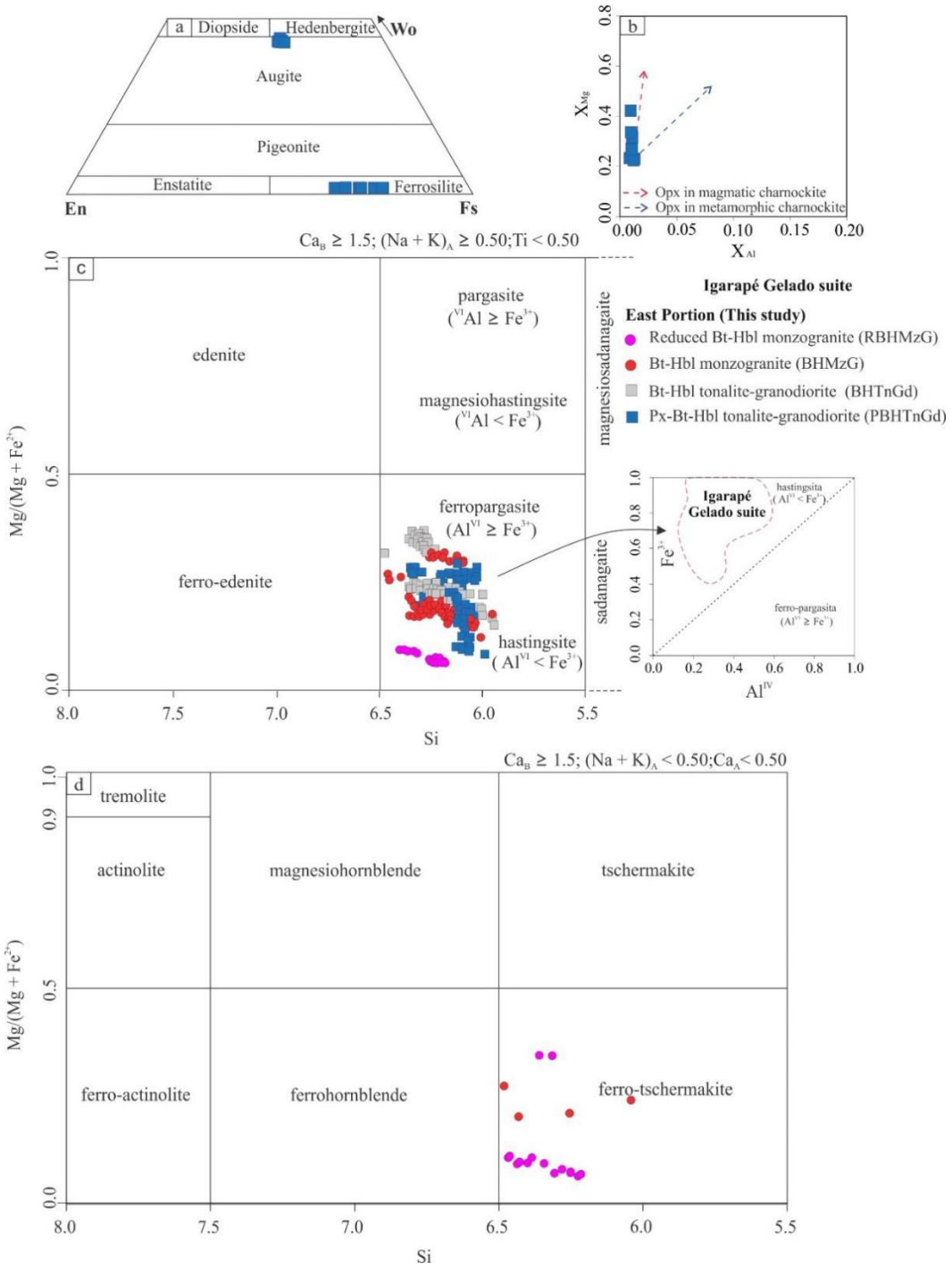

Figure 5. Classification diagrams for pyroxene and amphibole from IGS: a) Wollastonite-enstatite-ferrosilite diagram (Morimoto et al., 1988); b) Igneous vs. metamorphic orthopyroxene discrimination diagram (Rajesh et al., 2011); Calcium amphibole classification diagram (Leake, 1997) with c) $Ca_B \geq 1.50$; $(Na + K)_A \geq 0.50$; $Ti < 0.50$; and d) $Ca_B \geq 1.50$; $(Na + K)_A < 0.50$; $Ca_A < 0.50$.

Consequently, in the Mg x Al_t diagram (Fig. 6c; fields from Nachit et al., 1985), the biotite of the PBHTnGd variety plots in the alkaline biotite field and that of the BHTnGd in the subalkaline field. Meanwhile, the biotite of the RBHMzG variety is alkaline to slightly subalkaline, and that of the BHMzG variety is mostly subalkaline. In the ternary diagram

(FeOt+MnO)-(10*TiO_2)-MgO (Fig. 6d; Nachit et al., 2005 fields), the biotites of IGS plot in the field of primary magmatic crystals, except two BHMzG analyses that plot in the field of re-equilibrated biotites. In the biotites of all varieties, Cl > F and the F contents are below the detection limit, except for the PBHTnGd variety (0.04-0.2 apfu). Cl contents decrease from the PBHTnGd towards BHTnGd, BHMzG, and RBHMzG varieties (Table S5).

5.5 PLAGIOCLASE

The plagioclase of the IGS varieties is oligoclase (An_{16-24}) and has no significant compositional variations, as seen in the Ab-An-Or diagram (Fig. 6e, Deer et al., 2013). The An level in the PBHTnGd (An_{22-24}) and BHTnGd (An_{20-22}) varieties is higher than in the RBHMzG (An_{16-20}) variety (Table S6). The compositional contrast between the core and border of the analyzed crystals is minimal.

6 THERMODYNAMIC MODELING

6.1 EMPLOYED METHODS

The modeling was conducted with the GeoPS 3.5 software using the KNCFMASHTO (K_2O-Na_2O-CaO-FeO-MgO-Al_2O_3-SiO_2-H_2O-TiO_2-O_2) system database and a-X models, both as described by Holland et al. (2018). Quartz, titanite, and water (H_2O) are pure phases. Representative samples of the PBHTnGd and RBHMzG varieties, devoid of significant hydrothermal alteration, were selected for modeling. These compositions represent the parental liquid associated with each respective variety. The chemical compositions of these samples were recalculated at 100%, considering the different initial water content (Table S7). The fO_2 conditions of the magmas were obtained using the fO_2Melt software (Holland et al., 2018), and were defined as FMQ+0.5 (PBHTnGd) and FMQ-0.5 (RBHMzG). The pressure range adopted was between 2 and 8 kbar, and the temperature range was between 1200°C and 600°C.

The H_2O contents were selected to cover a large spectrum (Table S7). Experimental studies suggest < 2 wt% H_2O content for pyroxene-bearing rocks (Klimm et al., 2003; Naney, 1983; Zhao et al., 2018). However, the amphibole remains unstable under these conditions and becomes stable only at levels >4 wt% of H_2O (Bogaerts et al., 2006; Dall'Agnol et al., 1999; Klimm et al., 2003; Naney, 1983). Given the above, testing was conducted to evaluate the effects of water at weights of 1%, 4%, and 5% for the PBHTnGd (Fig. 7a, b, c) and at 1%, 4%, and 7% for the RBHMzG (Fig. 7d, e, f).

The position of the *liquidus* and *solidus* curves and the stability domains of the crystallized phases vary with the system's initial P, T, and XH_2O (Fig. 7a, b, c). In general, except for ilmenite (Ilm) and magnetite (Mag), the stability curves of the various phases exhibit a reduction in temperature as pressure decreases (pressures between 5 and 6 kbar will be considered as a reference to define temperatures). The temperature of the *liquidus* is not affected by pressure variations and stands around 1145°C, 1050°C, and 1030°C, with minor variations for contents of 1, 4, and 5 wt% of H_2O, respectively. The *solidus* temperature is ~660°C for all tested water contents in the system (see Fig. 7 a, b, c), with a slight decrease observed as pressure increases. At an initial H_2O concentration of 1 wt% in the magma (see Fig. 7a), plagioclase (Pl) is the *liquidus* phase, followed by Mag and Ilm, which crystallize above 1000°C. With decreasing temperature, orthopyroxene (Opx), quartz (Qz), clinopyroxene (Cpx), and biotite (Bt) successively crystallize, and the emergence of Bt coincides approximately with the destabilization of Opx (ca. 750°C). The stability temperatures of these phases increase slowly with pressure in the case of Opx and Bt and more intensely for Qz and Cpx. The destabilization of Ilm, the crystallization of titanite (Ttn) and K-feldspar (Kfs), and saturation in H_2O only occur at temperatures very close to the *solidus* (Fig. 7a).

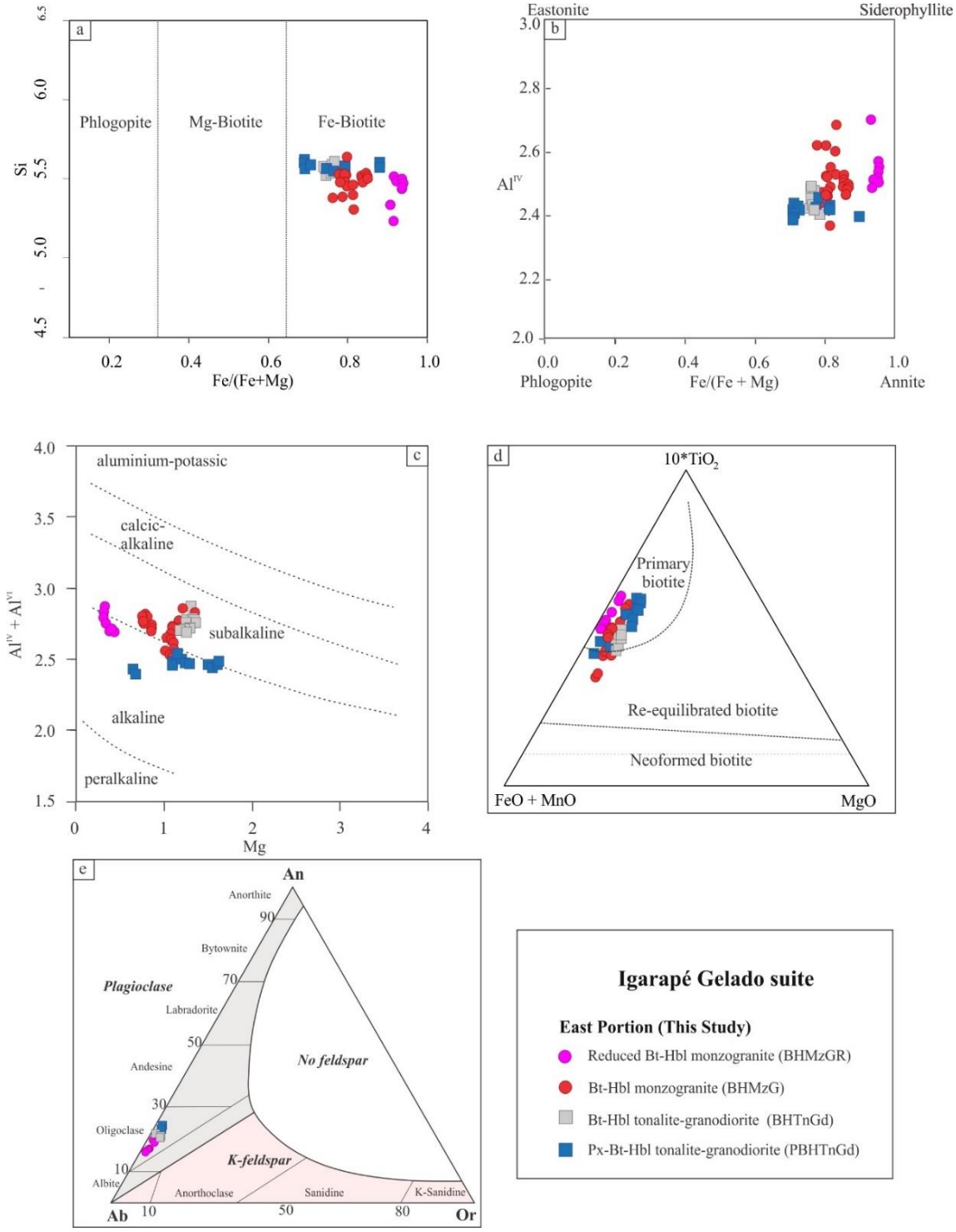

Figure 6. Classification of Biotite and Plagioclase Diagrams from the IGS: a) Si vs. Fe/(Fe+Mg) diagram (Deer et al., 2013); b) Fe/(Fe+Mg) x Al^{IV} diagram (Deer et al., 1992); c) Mg x Al_t diagram (Nachit, 1985); d) (FeO+MnO)-(10*TiO_2)-MgO diagram with fields from (Nachit et al. 2005); e) Ab-An-Or diagram for feldspars (Deer et al., 2013).

6.2 JK-60 - ORTHOPYROXENE-AMPHIBOLE-BIOTITE TONALITE (PBHTnGd)

In the composition with 4 wt% of H_2O, the high-temperature paragenesis is similar to that with 1 wt% of water, with successive appearance of Pl, Mag, Ilm, Opx, and Cpx,

although at comparably lower temperatures. In addition, unlike that observed with low H_2O content, Qz starts crystallizing at a lower temperature than Cpx, and amphibole (Amp) crystallizes from ~800°C at a temperature just below that of Cpx. On the other hand, the stability field of Opx decreases (860 to 760°C), and Bt crystallizes at ~740°C at a lower temperature than the destabilization temperature of Opx. At approximately 690±10°C, near the solidus temperature, the Amp becomes unstable, and H_2O saturation occurs in the system. Subsequently, Ilm destabilizes, and Ttn and Kfs crystallize. The composition calculated from the modeling of the Pl formed near the *liquidus* is notably more calcic (An_{82}) than those obtained from natural samples (An_{21-22}), which, according to the modeling, would be stable at temperatures around ~670°C and varying pressures (Fig. 7b).

With an initial 5 wt% of H_2O in the magma, the field of stability of Opx is even more restricted (~830-800°C), there is only a limited domain of stability for the two pyroxenes above ~7 kbar (Fig. 7c), and Amp starts crystallizing at temperatures slightly higher than the destabilization temperatures of Opx. In addition, under these conditions, there is no Bt crystallization, and Mag destabilizes at ~800°C (Fig. 7c). Qz starts to crystallize around 750°C and saturation in H_2O occurs at temperatures slightly higher than the *solidus.* There is no indication of Ilm destabilization or presence of Ttn.

6.3 JK-47 – BIOTITE-AMPHIBOLE REDUCED MONZOGRANITE (RBHMzG)

The temperatures predicted for the *liquidus* and *solidus* curves and those at the start of crystallization of the different phases vary in function of the initial P, T, and XH_2O (Fig. 7 d, e, f). Generally, except for Ilm, the stability curves of the phases decrease in temperature as pressure falls (Fig. 7d, e). The *liquidus* curve predicted for this sample is considerably lower than for PBHTn, ranging from ~1020°C to ~920°C for the contents of 1 and 4 wt% of H_2O, respectively. It is characterized by the saturation of Pl, which shows a subtle decrease in temperature at lower pressures (Fig. 7d, e). In contrast, with 7 wt% of H_2O, the *liquidus* temperature is mainly characterized by Mag saturation, which occurs at a lower temperature (~850°C) than in samples with lower H_2O content (Fig. 7f). The *solidus* temperatures for the three tested H_2O contents are relatively close, at around 655°C, and slightly lower at higher pressures, reaching ~640°C at 8 kbar.

In compositions with 1% and 4 wt% of H_2O, after Pl, at a pressure below 5.5 kbar, Ilm crystallize and is followed by Mag, however, that order is reversed when the pressure exceeds 5.5 kbar (Fig. 7d, e). Subsequently, with 1 w% of H_2O, between ~950°C and ~780°C, the crystallization of Qz, Kfs, fayalite (Fa), Bt, and Cpx begins successively. The curves indicating the beginning of stability domains of Bt and Cpx are closely aligned, as is the curve

marking the end of the stability field of Fa (Fig. 7d). At ~730°C, Ilm becomes unstable, and Ttn crystallizes. At pressures above 5 kbar and temperatures slightly above the *solidus*, the Amp stability curve appears, coinciding with the curve of Cpx-out. Saturation in H_2O occurs only near the *solidus*. At pressures >7 kbar and temperatures between 920 and 860°C, a restricted field of garnet stability (Grt) is established. Additionally, at pressures >5.6 kbar and temperatures close to the *solidus*, epidote (Ep) is stable (Fig. 7d).

In a composition with 4% H_2O, the Fe-Ti oxides first crystallize, and are followed by Qz, Amp, and Bt. This occurs within a brief temperature interval between 820°C and 780°C (Fig. 7e), with the biotite stability curve coinciding with the curve of amphibole-out. No pyroxenes are crystallized in this composition, and Fa is only stable below 5 kbar in a short temperature range (790 to 755°C). Following the decrease in temperature, at ~710°C, the Kfs initiates its crystallization process. At slightly lower temperatures, Ilm destabilizes, and Ttn begins to crystallize, as observed in the other pseudosections. Saturation in H_2O only occurs adjacent to the *solidus* curve (Fig. 7e). At pressures> 5.5 kbar, there are small Amp and Ep stability fields, and at pressures >6.8 kbar, there is a restricted Grt stability field. The composition of the plagioclase formed adjacent to the *liquidus* is significantly more calcic (An_{68}) than what is observed in natural samples (An_{16-21}). According to the modeling, a plagioclase with the natural composition would be stable between ~670-650°C, but only at pressures exceeding 5.6 kbar (see Fig. 7e).

In the case of the composition with 7 wt% of H_2O, after the crystallization of Mag, Ilm, and Pl begin to crystallize, in that order, when below 5.8 kbar and inversely when above 5.8 kbar (Fig. 7f). At pressures exceeding 5 kbar, the stability field for Amp begins to form, displaying an irregular curve below 750°C. Additionally, at approximately 5.5 kbar, Bt and Qz start to crystallize. Subsequently, at ~680°C, the Ilm-Tit relationship described above is again observed. Finally, saturation in H_2O occurs close to but well above the *solidus* curve. Nevertheless, the Amp destabilizes at pressures >6 kbar, and the Ep stability field begins. Under reduced conditions and with a high H_2O content, depending on the composition evaluated, Fa and pyroxenes do not crystallize.

Table 1: Estimate of crystallization parameters for the Igarapé Gelado suite

Variety	PBHTnGd	BHTnGd	BHMzG	RBHMzG
Temperature (°C)				
Watson & Harrison (1983) - Zircon	937-852	947-837	931-740	1012-896
Holland & Blundy (1994) - Amphibole and plagioclase	873-739	782-692	-	715-671
Ridolfi et al. (2010) - Amphibole	899-852	907-835	891-810	848-797
Putirka (2016) - Amphibole	777-720	785-740	762-680	705-660
Putirka (2016) - Amphibole and liquid	830-782	833-783	792-749	770-750
Molin and Zanazzi (1991) - Clinopyronexe	897-881			

Brey and Köhler (1990) - Orthopyroxene	1223-1136			
Pressure (MPa)				
Al-in-amphibole geobarometer				
Hammarstron & Zen (1986)	802-555	882-532	840-521	702-531
Hollister et al. (1987)	863-586	952-560	906-547	751-559
Johnson & Rutherford (1989)	658-450	725-431	690-421	574-430
Schmidt et al. (1992)	829-595	904-618	865-563	734-572
Ridolfi et al. (2010)	583-302	733-269	710-261	439-269
Mutch et al. (2016)	700-470	780-451	736-443	601-453
Clinopyroxene geobarometer (Purtika 2008)	848-582			
Oxygen fugacity				
Fegley (2013) - FMQ buffer (log fO^2)	-16.1 to -14.8	-16.2 to -14.9	-17.6 to -15.1	-18.3 to -16.7
Frost et al. (2001) - ΔFMQ (graphical estimation)	+0.5	+0.5	+0.5 to -0.5	-0.5 to -1
H_2O_{melt} (wt.%)				
Ridolfi et al. (2010)	5-6	5-6	5.5-8.5	7.6-9.4

100 MPa = 1 kbar

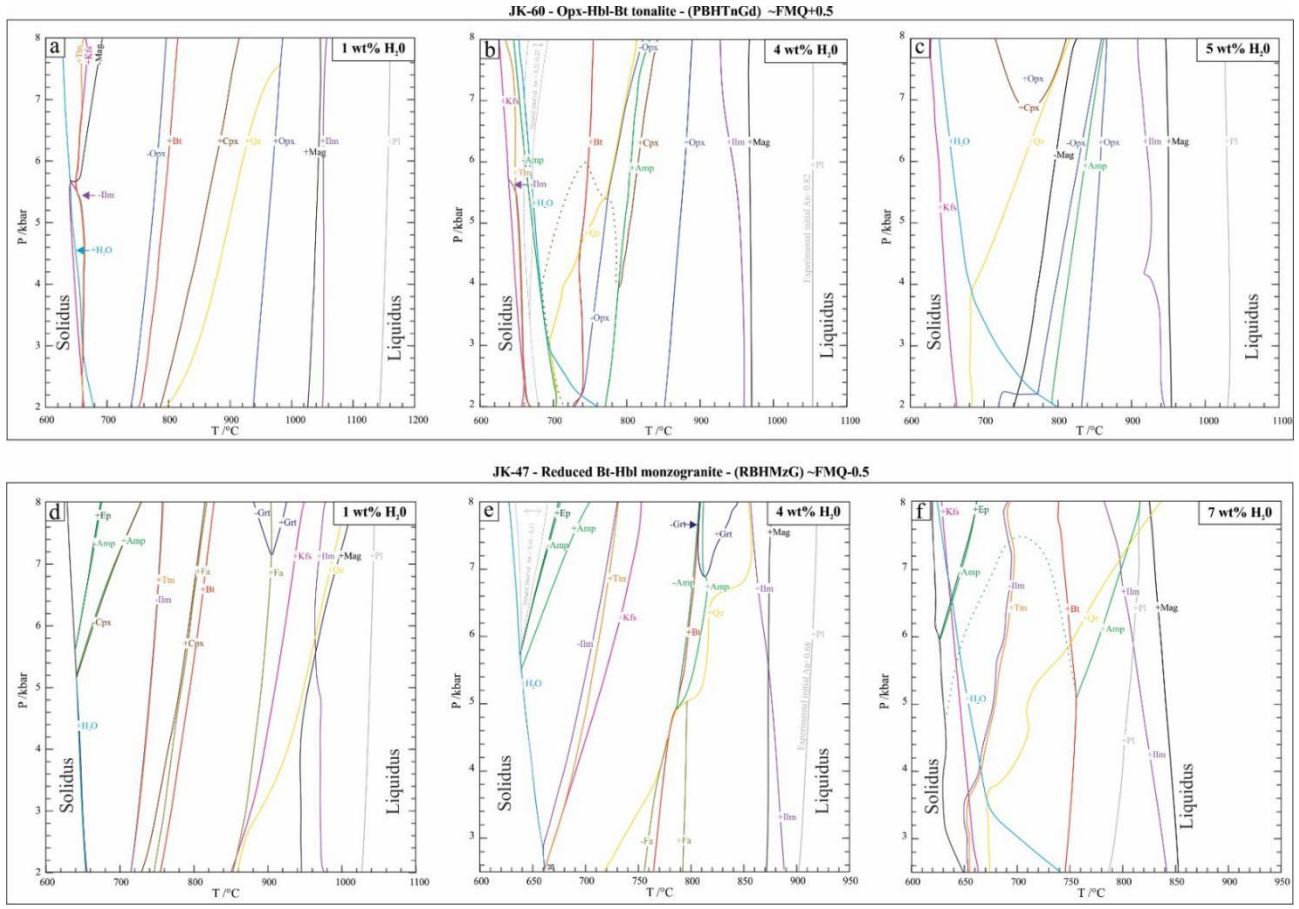

Figure 7. P-T pseudosections from the Igarapé Gelado suite. Sample JK-60-Opx-Hbl tonalite (PBHTnGd) at FMQ+0.5, (a) 1 wt% of H_2O; (b) 4 wt% of H_2O; (c) 5 wt% of H_2O. Sample JK-47-Bt-Hb-monzogranite (RBHMzG) at FMQ-0.5; (d) 1 wt% of H_2O; (e) 4 wt% of H_2O; (f) 7 wt% of H_2O. 1 kbar = 100 MP. Abbreviations according to Whitney and Evans, (2010). Dashed line - inconclusive limit generated by the software.

7 DISCUSSIONS

7.1 ESTIMATE OF CRYSTALLIZATION PARAMETERS

Mineral chemistry data (amphibole, plagioclase, pyroxenes) and whole-rock chemical analysis of zirconium (zircon thermometer, Table S8) were used to estimate the main crystallization parameters. For this purpose, minerals and rocks without evidence of significant transformations were selected. Calculations of different parameters (P, T, fO_2, XH_2O) were carried out using the WinAmptb program (Yavuz and Doner, 2017) for amphibole, plagioclase, and liquid and in the WinPyrox program (Yavuz, 2013) for pyroxenes. Table 1 summarizes values estimated by different methods for the physicochemical parameters. The results provided by the different geothermometers and geobarometers will be compared below with those obtained by thermodynamic modeling to define more precisely the conditions prevailing during the crystallization of IGS.

7.1.1 Temperature

Generally, the thermometer that relies on saturation in zircon (Watson and Harrison, 1983), an early mineral found as inclusions in mafic minerals and feldspars, indicates high temperatures ranging from 837 to 947 °C, except in the RBHMzG, where it reaches maximum values (1012 to 896°C, Table S8). In the PBHTnGd, the orthopyroxene geothermometer (Brey and Köhler, 1990) suggests a high temperature for the onset of crystallization (1223 to 1136°C). On the other hand, the augite geothermometer (Molin and Zanazzi , 1991) provided lower temperatures (897-881°C). As indicated by petrographic evidence, the high temperatures obtained by these three geothermometers indicate near *liquidus* temperatures. However, the temperatures suggested by zircon and augite geothermometers are closer to those expected in granites (~950-850°C) with associated charnockite rocks (~1150°C; Bucher and Frost, 2006; Frost and Frost, 2008; Frost et al., 1999; Weiss and Troll, 1989). For the variety with pyroxenes, significantly lower temperature values (873-739°C) were obtained using the amphibole and plagioclase thermometer (Holland and Blundy, 1994), and even lower temperatures (777° to 720°C) with the calcium amphibole thermometer (Putirka, 2016). This last geothermometer also recorded the lowest temperatures for the other varieties (BHTnGd-785-740°C; BHMzG-762-680°C; RBHMzG -705-660°C; Table 1). The amphibole and liquid thermometer (Putirka, 2016) indicated higher temperature values than those of amphibole (Putirka,2016) and gave contrasting temperature intervals for the TnGd (833-782°C) and BHMZG (792-749°C) of the IGS (Tab. 1). The thermometer for amphibole of Ridolfi et al. (2010) provided higher values than those for amphibole and liquid from Putirka

(2016). Finally, the thermometer of Holland and Blundy (1994) provided a temperature range that for PBHTnGd overlapped with that of amphibole and liquid of Putirka (2016) and was lower for the BHTnGd and RBHMzG varieties.

7.1.2 Pressure

For pressure estimates, the Al-in-amphibole and clinopyroxene geobarometers were employed. Only border analyses of amphibole crystals were selected to obtain pressures closer to *solidus* conditions. As established by Hammarstron & Zen (1986) and Hollister et al. (1987), the Al-in-amphibole geobarometer was originally defined for intermediate to felsic rocks with an equilibrium association of eight crystalline phases—amphibole, biotite, plagioclase, alkali-feldspar, quartz, titanite, ilmenite, and magnetite—along with residual liquid and volatiles. IGS contains this assembly deemed ideal or close to it, and the two mentioned methods provided setting pressures ranging from 952 to 521 MPa (Table 1). However, these values must be interpreted with caution. Anderson and Smith (1995) pointed out that temperature affects pressure calculations and that the Al-in-amphibole geobarometers available in the literature may not be ideal for rocks formed under low oxygen fugacity conditions, particularly those with high FeO/(FeO+MgO) ratios and amphibole with #Fe > 0.65. Therefore, as the FeO/(FeO+MgO) ratios in the IGS are high, other geobarometers were also tested. Schmidt et al. (1992) calibrated an experimental geobarometer for tonalites and granodiorites, which provided for PBHTnGd and BHTnGd values between 904 and 595 MPa (Table 1).

On these three geobarometers, in the PBHTnGd, BHTnGd, and BHMzG varieties, the pressures range from 952 to 521 MPa and overlap within the error (on average ±150 MPa) but are slightly lower in the RBHMzG (751-531 MPa). On the other hand, the geobarometers of Johnson and Rutherford (1989) and Mutch et al. (2016) yielded, respectively, pressures of 725 to 421 MPa and 780 to 443 MPa for the PBHTnGd, BHTnGd, and BHMzG (Table 1), and comparatively lower pressures for the RBHMzG (574-430 MPa and 601-453 MPa. respectively). The geobarometer by Ridolfi et al. (2010) differs from the others by indicating relatively low pressures for PBHTnGd.

Among the Al-in-amphibole geobarometers analyzed in this work, that of Mutch et al. (2016) offer the advantage of having been calibrated for temperatures close to the *solidus* and over a wide pressure range, extending from the minimum pressure for amphibole formation (~80 MPa) to pressures of around 1000 MPa. Moreover, this geobarometer could be applied to a wide range of granitoid rocks. The pressure ranges obtained by this method for the

PBHTnGd, BHTnGd, and BHMzG are similar, ranging from 780 to 443 MPa, while lower pressures are indicated for the RBHMzG (601-453 Mpa). Based on these geobarometers, it was assumed a pressure of 5.5 ± 1.0 kbar for the different granites of IGS .

7.1.3 Oxygen fugacity

Temperature variations primarily affect oxygen fugacity (fO_2), which is also influenced by pressure, water volume, and volatiles in the magma. This makes fO_2 an essential petrological indicator, because its variations can affect the equilibrium conditions and the formation of Fe-Ti oxide minerals and Fe-bearing silicate phases in the Fe-Si-O system (Anderson and Smith, 1995; Carmichael, 1991; Frost, 2018; Gaillard et al., 2001; Moore et al., 1995). To estimate the fO_2 conditions during the magmatic evolution of the IGS, the Fe/Fe+Mg ratios of amphibole and biotite were employed, as these ratios strongly depend on fO_2 (Anderson et al., 2008; Anderson and Smith, 1995; Clark, 1999; Dall'Agnol et al., 2005, 1999, 1997, 2017; Dall'Agnol and Oliveira, 2007; Fegley, 2013; Frost, 2018; Ishihara, 2004; Putirka, 2016; Wones, 1989).

In the Al^{IV} vs. Fe/(Fe+Mg) diagram, the amphiboles of the RBHMzG plot exclusively in the low fO_2 field due to their higher Fe/Fe+Mg ratios (0.89-0.94). In contrast, the other varieties show overlap in composition and appear in the intermediate and low fields with ratios ranging from 0.63 to 0.92 (Fig. 8a, Table S4). The Fe/Fe+Mg ratio in biotite (Table S5) allows a better distinction of the varieties, with RBHMzG standing out with the highest ratios (0.92-0.94), being usually followed by BHMzG (0.77 to 0.85) and reaching the lowest values in PBHtnGd and BHTnGd (0.69 to 0.77). In the $Al^{IV} + Al^{VI}$ vs. Fe/(Fe+Mg) diagram (Fig. 8b), the biotites of RBHMzG and BHMzG belong to the ilmenite series, and those of PBHTnGd and BHTnGd plot in the transition between the ilmenite and magnetite series or in the magnetite series. The $Al^{IV} + Al^{VI}$ vs. Fe/(Fe+Mg) diagram also suggests fO_2 conditions for IGS between FMQ-1 and FMQ+0.5.

To improve the definition of the prevalent fO_2 conditions during IGS crystallization, log fO_2 calculations were carried out based on the amphibole composition using the Fegley (2013) method and pressure values based on Purtika (2016) (Table 1). In the PBHTnGd and BHTnGd varieties, the log fO_2 values are very close and oscillate between -16.2 and -14.9, plotting them above the FMQ buffer in the log fO_2 vs T diagram of Frost et al. (2001) (Fig. 8c). Most BHMzG samples show log $fO_2 > -17$ and plot above FMQ but at a lower temperature than the TnGd facies. In contrast, all the samples of RBHMzG and some of the BHMzG have log fO_2

between -17 and -18.3 and plot below FMQ, indicating their reduced character compared to the other varieties (Fig. 8c).

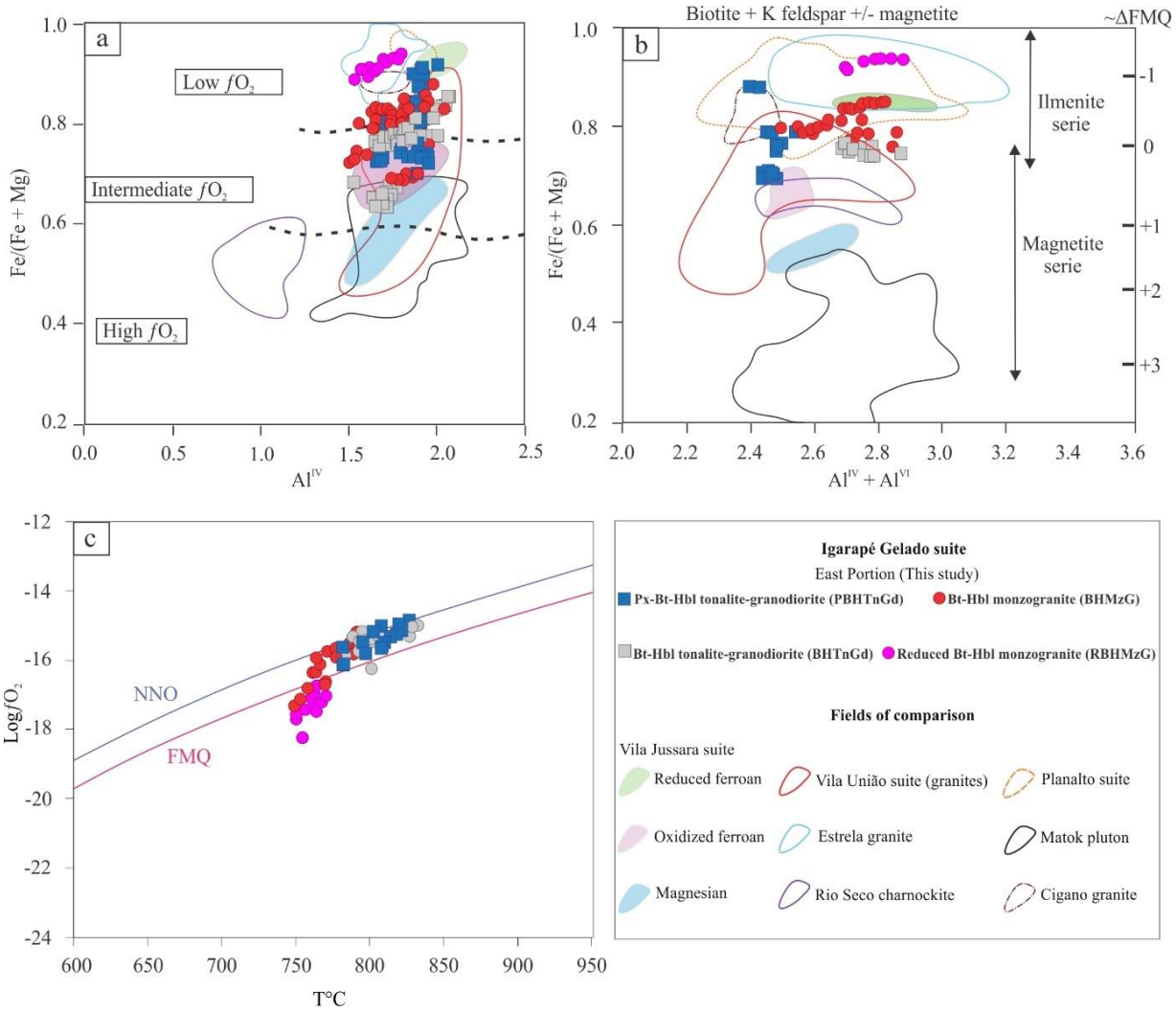

Figure 8. Diagrams for crystallization parameter estimates for IGS based on amphibole and biotite mineral chemistry: a) Fe/(Fe+Mg) x Al^{IV} diagram showing the compositional variation of amphiboles (low, intermediate and high fO_2 fields according to Anderson and Smith, 1995); b) Fe/(Fe + Mg) vs. Al^{IV} + Al^{VI} diagram displaying the compositional variation of biotites (ilmenite and magnetite series according to Anderson et al., 2008); c) Log fO_2 x T°C binary diagram based on amphibole composition (calculations according to Fegley, 2013). Fields of selected granites are given for comparison: Vila Jussara suite (Dall'Agnol et al., 2017; Sousa et al., 2022); Vila União suite (Oliveira et al., 2018a); Estrela granite (Barros et al., 2009); Planalto suite (Cunha et al., 2016); Rio Seco charnockite (Felix et al., 2020); Matok pluton (Bohlender, 1992); Cigano granite (Dall'Agnol et al., 2005).

7.1.4 H_2O Content

Experimental data for granitic systems reveal that the stability of calcium amphiboles depends on the concentration of H_2O and CaO in the magma. At magma temperatures and pressures between 200 and 400 MPa, amphibole is only stable with a minimum content of 4% H_2O (Bogaerts et al., 2006; Dall'Agnol et al., 1999; Klimm et al., 2003; Naney, 1983). Furthermore, estimates based on the content of Al^{iv}-in-amphiboles (Ridolfi et al., 2010) indicate high H_2O content in the magmas of IGS rocks. These estimated contents decrease

from the RBHMzG variety (7.6 to 9.4 wt%) to BHMzG (5.5 to 8.5 wt%), reaching a minimum value in PBHTnGd (5 to 6 wt%). The obtained data indicate relatively high H_2O content in the IGS magmas, and this hypothesis will be tested using thermodynamic modeling.

7.2 INTEGRATION OF THE THERMODYNAMIC MODELING AND THERMOBAROMETRY

This section compares the data provided by thermobarometry (Table 1) and thermodynamic modeling (Fig. 7). Thermodynamic modeling is a petrological tool that simulates crystallization conditions based on a consolidated database (Holland et al., 2018; Holland and Powell, 2011; Jennings and Holland, 2015). Thermobarometry, meanwhile, assumes importance for the accuracy of the estimations based on rigorous experiments that allowed the calibration of different geobarometers and geothermometers (Anderson and Smith, 1995; Brey and Köhler, 1990; Holland and Blundy, 1994; Mutch et al., 2016; Putirka, 2016; Ridolfi et al., 2010; Watson and Harrison, 1983). The combined evaluation of these tools makes possible a more reliable discussion of magmatic rock evolution.

The water content in the magma is a critical variable, affecting the equilibrium conditions of different phases during the granitic magma evolution. Therefore, compositions with variable concentrations of H_2O were tested in the modeling. The fO_2 also exerts a strong influence on the evolution of magmas, however, the different obtained data converge in the direction of crystallization under moderately oxidizing conditions (FMQ+0.5) for the IGS varieties and for reduced conditions for the RBHMzG (FMQ-0.5), and these values were assumed in the modeling. The other critical variables to be considered are pressure and temperature, which are represented in the P-T sections of the modeling (Fig. 7).

For concentrations of 1 wt% of H_2O, the PBHTnGd modeling (Fig. 7a) indicates a paragenesis that differs from the natural one since amphibole, a mafic mineral with significant modal content, is absent and the crystallization of minerals not present in the natural rock, such as clinopyroxene and, at low temperatures, titanite should occur. In contrast, in the modeling with 4 wt% of initial H_2O in the magma (Fig. 7b), the minimum content for amphibole stability (Bogaerts et al., 2006; Dall'Agnol et al., 1999; Klimm et al., 2003; Naney, 1983), the main natural phases are present. Essential aspects observed for this composition are the formation of Amp and Bt, and the fact that the mica start crystallizing at a temperature close to that of Opx destabilization. This suggests the possibility of a peritectic reaction involving Opx, Bt, and the liquid. Another relevant point is the crystallization of Kfs close to

the *solidus*. The modeling suggests the crystallization of clinopyroxene, but there are indications that it destabilized during magmatic cooling, which could explain its absence in the modal composition of the natural rock. Crystallization of titanite at low temperatures is also indicated, but it is absent in the natural sample. Finally, with 5% by weight of initial H_2O in the magma (Fig. 7c), the crystallized phases are also close to the natural mineral assemblage because Opx is present in all the considered pressure interval and Cpx should be only stable at pressures > 7kbar and over a restricted temperature range. Despite being abundant in the rock, biotite should not crystallize according to the modeling. In conclusion, an initial content of 4% by weight of H_2O in the magma would be the most appropriate to explain the mineral associations and the magmatic evolution of PBHTnGd.

Using 4% H_2O, the stability curves of the minerals typically exhibit minimal changes with pressure variation, except for clinopyroxene that does not crystallize at pressures <4 kbar (Fig. 7b). Therefore, considered isolatedly, modeling is unable to establish the pressure during crystallization. Nonetheless, as previously discussed, the pressure suggested by the geobarometers stands at 5.5 ± 1.0 kbar (Table 1), possibly being slightly higher in the PBHTnGd than in the RBHMzG, and that pressure may be assumed for the emplacement of PBHTnGd. The *liquidus* temperature is defined by the crystallization of plagioclase (An_{82}) at ~1060°C (Fig. 7b), well below that obtained by the orthopyroxene geothermometer (1223-1136°C; Brey and Köhler, 1990) and considerably higher than that indicated by the zircon geothermometer (937-852°C). The Putirka (2016) thermometer for amphiboles and liquid provided temperatures in the 830-782°C range, consistent with the onset of amphibole crystallization (~810°C, Fig. 7b). The data set suggests that the crystallization of PBHTnGd began at a temperature of 1000±50°C and concluded near 660°C. BHTnGd and BHMzG formed within a similar temperature range as PBHTnGd, while RBHMzG likely experienced slightly lower *liquidus* temperatures.

In the case of the RBHMzG (fO_2 = FMQ-0.5), with 1 wt% of initial H_2O in the magma (Fig. 7d), amphibole, an abundant mineral in the natural sample, is stable only over a short temperature range, close to *solidus* and above 5.5 kbar. In contrast, minerals not found in natural rock, such as fayalite, clinopyroxene, and magnetite, crystallized over the entire pressure range. The modeling with 4 wt% of H_2O indicates that fayalite would crystallize at pressures <5 kbar, while amphibole only forms at pressures >5 kbar, although it remains stable only in a small temperature range. Kfs began to crystallize immediately after Amp and Bt.

Modeling of the RBHMzG composition with 7% initial H_2O in the magma indicates that Amp crystallized at pressures >5 kbar, followed by the formation of Bt and Qz. Kfs formed at temperatures near to *solidus*, and minerals such as clinopyroxene, fayalite, and garnet were absent. Furthermore, the proximity of the Ilm disappearance curves and the onset of Tit crystallization, around ~700 °C (Fig. 7f), is consistent with the occurrence of ilmenite crystals bordered by titanite in the natural rock and other Neoarchean granites of Carajás with a reduced character (Planalto, Cunha et al., 2016; Vila Jussara suite, Souza et al., 2022). However, the three compositions considered reveal an inconsistency in the formation of magnetite, a phase that should not be in equilibrium at fO_2 lower than FMQ. For the remaining 7 wt% of H_2O composition, the phase correlations observed in the modeling agree well with those present in the natural rock; in comparison, they are less pronounced for the 4 wt% of H_2O composition and disagree for the 1 wt% of H_2O composition. Assuming that the RBHMzG crystallized with an initial content of 7% H_2O, as amphibole and biotite coexist in equilibrium in the rock, there is a pressure window of 5 to 6 kbar for the final evolution of the magma, and a pressure of 5.5 ± 0.5 kbar, similar to that predicted for the PBHTnGd, can also be considered for the emplacement of RBHMzG. Note that the amphibole-liquid geothermometer (Putirka, 2016) provided amphibole crystallization temperatures (770-750°C) close to those indicated in the modeling (Fig. 7f).

The GeoPs developers (Xiang and Connolly, 2022) proposed a robust optimization of the Gibbs energy minimization process, which allows complex algorithms and a consistent database to predict mineral assemblages during magma crystallization. Modeling compositionally complex rocks, such as the IGS granites, can reveal certain inconsistencies, such as the presence of phases that do not form part of the natural assemblage, and stability curves with patterns incompatible with magmatic evolution can be generated. This is evident in the curves for clinopyroxene in the modeling at 4 wt% of H_2O of the PBHTnGd variety and amphibole at 7 wt% of H_2O of the RBHMzG (Fig. 7b, f, dashed lines). Moreover, the software presents limitations for computing reactions between minerals that result in partial or total substitutions between phases, such as those between mafic phases in IGS. The challenge of establishing a correspondence between natural systems and modeling phases is also evident in experimental petrology. This demonstrates that the evolution of granitic magmatic systems may not always be faithfully replicated in laboratory settings (Bogaerts et al., 2006; Cunha, 2023), although this can occur (cf. Dall'Agnol et al., 1999). Despite these caveats, the phase relationships in the IGS rocks and the thermodynamic modeling results show reasonable

accordance. The thermodynamic modeling contributed significantly to a better understanding of the crystallization processes and the relationships between mineral phases.

7.3 COMPARISON OF THE IGARAPÉ GELADO SUITE WITH SIMILAR GRANITES AND CHARNOCKITES

The granites selected for comparison with the IGS ones are mostly Neoarchean, A-type granites that exhibit weak to intense deformation. They correspond to the granites of the Vila Jussara (Dall'Agnol et al., 2017; Silva et al., 2020; Sousa et al., 2022), Planalto (Feio et al., 2012), and Vila União (Oliveira et al., 2018a; Marangoanha et al., 2019a) suites, and Estrela granite complex (Barros et al., 2009). The Palaeoproterozoic anorogenic Cigano granite was also included (Gonçalez et al., 1988; Teruya et al., 2008; Dall'Agnol et al., 2005). The rocks containing ortho- and clinopyroxenes of the PBHTnGd are compared with charnockitic rocks from the CP (Café enderbite, Marangoanha, et al., 2022; Rio Seco charnockite, Félix et al., 2020), as well as with those from the Matok pluton of the Limpopo Belt (Bohlender, 1992, Rapopo, 2011).

7.3.1 Mineral chemistry

In the Planalto, Vila Jussara, and Vila União suites, pyroxenes are rare (reliquary) or absent (Dall'Agnol et al., 2017; Cunha et al., 2016; Oliveira et al., 2018a). However, pyroxenes occur in the Café enderbite, in the granodioritic facies of the Rio Seco charnockite, and the in PBHTnGd from IGS. The orthopyroxene identified in the PBHTnGd of the IGS is preferentially ferrosilite, similarly to that observed in the mentioned rocks, while clinopyroxene is mostly augite, as occurs in the charnockites of the Matok pluton and Rio Seco, and subordinately hederbegite, a mineral described in the Estrela complex (Barros et al., 2009).

In the IGS, as well as in the reduced varieties of the Planalto and Vila Jussara suites and the Estrela complex), (K)hastingsite is the dominant amphibole. Cl-hastingsite and Fe-pargasite were identified in the Planalto suite and Estrela complex, respectively. In the reduced rocks of these units, as well as in the Palaeoproterozoic Cigano granite (hastingsite), the dominant amphiboles feature extremely high Fe/(Fe+Mg) ratios (>0.9), similar to those of the RBHMzG variety (Fig. 8a; Table S4). Lower #Fe values (generally between 0.83 and 0.88; Fig. 8a; Table S4), but still in the low fO_2 range, are recorded mainly in amphiboles of the BHMzG variety from IGS and in parts of the Vila União suite (hastingsite and edenite). The other IGS amphiboles, in particular those dominant in PBHTnGd and BHTnGd, are located in the intermediate fO_2 field (#Fe<0.8), as are the amphiboles of oxidized ferroan

granites from the Vila Jussara and Vila União suites, and from the Matok pluton. Amphiboles with #Fe <0.6, which plot in the high fO_2 field (Fig. 8a), occur only in magnesian granites from the Vila Jussara suite (Mg-hastingsite), Matok Pluton (edenite), Rio Seco charnockite (Mg-Fe hornblende), Café enderbite (hastingsite, Mg-hornblende and pargasite) and Vila União suite (edenite, Mg-hastingsite).

Table 2. Comparison between crystallization parameters of IGS and similar granitoids

Units	Temperature (C°)				Pressure (MPa)				Oxygen Fugacity	H_2O_{melt} (wt.%)	References
Igarapé Gelado Suite											This Study
PBHTnGd	937-852[1]	899-852[2]	777-720[4]	897-881[5]	658-450[a]	583-302[b]	700-470[c]		Reduced FMQ+0.5	5-6[**]	
BHTnGd	947-837[1]	907-835[2]	785-740[4]		725-431[a]	733-269[b]	780-451[c]		Reduced FMQ+0.5	5-6[**]	
BHMzG	931-740[1]	891-810[2]	762-680[4]		690-421[a]	710-261[b]	736-443[c]		Reduced FMQ±0.5	5.5-8.5[**]	
RHBMzG	1012-896[1]	848-797[2]	705-660[4]		574-430[a]	439-269[b]	601-453[c]		Reduced FMQ-0.5 to -1	7.6-9.4[**]	
Planalto Suite	897-854[1]		910-850[2]		750-500[a]	808-341[b]	890-620 [d]	500-300[e]	Reduced FMQ±0.5	>4	Cunha et al. (2016)
Estrela Complex	893–782[1]				380-180[d]				Reduced <FMQ		Barros et al. (2001)
Vila União Suite	1091-976[1]	926-831[2]			682-423[a]	814-532[d]			FMQ±0.5 to NNO±0.5	>4	Oliveira et al. (2018)
Vila Jussara*	915-885[1]		907-860[2]		740-630[a]	770-530[b]	880-760[d]		Reduced FMQ ± 0.5	>4	Dall'Agnol et al. (2017)
Café Enderbite	912-833[2]	919-693[3]	817-782[4]	906-862[5]	578-312[a]	444-280[b]	597-342[c]		Oxidized FMQ to NNO + 1.7	4.8-5.6[**]	Marangoanha et al. (2022)
Rio Seco Charnockite	800-713[2]	816-676[3]	777-666[4]	906-833[5]	270-100[a]	310-110[d]	310-190[c]		Oxidized >NNO	>4	Félix et al. (2020)
Cigano Granite	<850[6]				270-100[e]				Reduced FMQ +0.5		Dall'Agnol et al. (2005)
Matok Pluton	900-800[1]				860-330[d]				Oxidized >NNO	>5	Rapopo (2011)

PBHTnGd = Px-Bt-Hb Tonalite-Granodiorite; BHTnGd = Bt-Hbl Tonalite-granodiorite; BHMzG = Bt-Hbl Monzogranite; RBHMzG = Reduced Bt-Hbl Monzogranite. *Only reduced granites; ** Ridolfi et al. (2010)

Geothermometers: [1]Watson & Harrison (1983) - Zircon; [2]Ridolfi et al. (2010) - Amphibole; [3]Holland & Blundy (1994) - Amphibole and plagioclase; [4]Putirka (2016) - Amphibole;

[5]Molin and Zanazzi (1991) - Clinopyronexe; [6]Estimated. 100 MPa = 1 kbar

Al-in-amphibole geobarometer: [a]Johnson & Rutherford (1989); [b]Ridolfi et al. (2010); [c]Mutch et al. (2016); [d]Anderson and Smith (1995) ; [e]Estimated

*Only reduced granites; ** Ridolfi et al. (2010)

.

The biotites display similar behavior to the amphiboles, with #Fe reaching values above 0.9 in the RBHMzG (Fig. 8b, Table S5) and varying between 0.77 and 0.85 in the BHMzG, showing overlap with the composition of biotites from reduced granites of the Vila Jussara and Planalto suites and Estrela complex. The biotites from PBHTnGd and BHTnGd usually exhibit #Fe between 0.77 and 0.69. Furthermore, biotites from PBHTnGd occasionally have a higher #Fe and slightly lower Alt content, similar to the Cigano Palaeoproterozoic granite (Fig. 8b). The diagram $Al^{IV}+Al^{VI}$ vs Fe/(Fe+Mg) (Fig. 8b) indicates that the granites with biotites having #Fe>0.8 are from the ilmenite series. The remaining granites show biotites with #Fe <0.80 that are found in part of the BHMzG and TnGd, and are concentrated in the transitional field between the ilmenite and magnetite series, overlapping mainly with the biotites from the Vila União suite and oxidized granites of the Planalto suite.

The biotites with the lowest #Fe of the PBTnGd variety are close to those of the oxidized ferroan granites of the Vila Jussara suite and Rio Seco charnockite, and all plot in the field of the magnetite series (Fig. 8b). No compositional correspondence is found between the IGS biotites and those of the Matok pluton and magnesian granites of the Vila Jussara and Vila União suites, which have #Fe<0.6 (Fig. 8b). The biotites of the IGS are ferroan and similar to those described in the Planalto suite, Estrela complex, and reduced rocks of the Vila Jussara suite. Nevertheless, they differ from those of the ferroan oxidized and magnesian varieties from the Vila Jussara and Vila União suites and from the Rio Seco charnockite, which micas are transitional between magnesian and ferroan biotites and plot in the magnetite series field (Fig. 8b).

Generally, biotites and amphiboles of the Neoarchean A-type granites of Carajás, including IGS, are enriched in Cl relative to F, contrarily to that observed in the Palaeoproterozoic granites of Carajás (Dall'Agnol et al., 2017). This relative enrichment in Cl could be linked to the occurrence of the Neoarchean granites along the northern and southern Carajás copper belts, which are related to IOCG deposits that are also Cl-enriched (Dreher et al., 2005; Melo et al., 2016; Monteiro et al., 2008; Moreto et al., 2015).

The plagioclase of the IGS is predominantly oligoclase (An_{16-24}), as in most of the Neoarchean granites of Carajás (An_{10-30}). Compositional zoning from the core to the border of crystals is restricted, as equally observed in the Vila Jussara suite (Dall'Agnol et al., 2017). Albite crystals also occur, as in the Vila União (An_6) and Planalto (An_{2-9}) suites, and in the latter, they correspond to new recrystallized grains (Cunha et al., 2016). In contrast, the charnockite rocks tend to develop more calcic crystals, ranging from oligoclase to andesine in

the Café enderbite (An_{20-40}), as well as in the Matok pluton (An_{15-34}), and from andesine to labradorite in the Rio Seco charnockite (An_{28-60}).

7.3.2 Thermobarometry

The temperatures obtained using the zircon saturation thermometer (Watson and Harrison, 1983), representing temperatures close to liquidus, were >900°C, reaching values above 1000°C in the Vila União suite (Oliveira et al., 2018a) and RBHMzG of IGS (Table 2). The temperatures suggested by the Ridolfi et al. (2010) geothermometer for amphibole are slightly lower than indicated by the zircon geothermometer. However, the temperature ranges provided by these two methods overlap widely and are certainly appropriate for the IGS rocks. Moreover, the temperatures indicated by the method of Ridolfi et al. (2010) for granitic rocks without pyroxene in the CP are close to those attributed to the *solidus* temperature of granitic rocks associated with charnockites (950°C to 850°C; Bucher and Frost 2006; Frost et al. 1999; Frost and Frost 2008; Weiss and Troll 1989). This aspect and the occurrence in thee IGS granitic complex of pyroxene-bearing and pyroxene-free rocks reinforce the hypothesis that the Neoarchean granites with A-type affinity of Carajás could be related to charnockites (Feio et al., 2012).

The PBHTnGd, like the recorded in Café enderbite (Marangoanha et al., 2022) and Rio Seco charnockite (Félix et al., 2020), showed temperature values around 900°C when measured using thermometers based on clinopyroxene composition (see Table 2). When using thermometers based on orthopyroxene, the temperatures exceeded 1100°C (Purtika, 2008; Brey and Köhler,1990; Marangoanha et al., 2022). Such temperatures lie close to the estimated *liquidus* for charnockitic magmas (~1150°C, Bucher and Frost, 2006; Frost and Frost, 2008; Frost et al., 1999; Weiss and Troll, 1989), however, thermodynamic modeling indicates that the liquidus phase for the PBHTnGd variety with 4 wt% of H_2O is plagioclase (An_{82}) (T ~1050°C; Fig. 7b). Meanwhile, the geothermometer by Purtika (2016), based on the amphibole composition, revealed temperatures considerably lower than those suggested by the thermometers already discussed. The measured temperatures ranged from approximately 800°C to 660°C, aligning more closely with the expected solidus temperature for IGS rocks (~660°C).

Due to the overestimation of pressure of emplacement resulting from applying Al-in-amphibole geobarometers for rocks generated under reduced fO_2 (Anderson and Smith, 1995), based on field observations, Cunha et al. (2016) estimated a pressure between 300 and 500MPa for emplacement of the Planalto suite in the mesozone. This pressure range was also

accepted for the Vila Jussara suite (Dall'Agnol et al., 2017). A single sample (CG-75) of the BHTnGd variety has amphibole with #Fe<0.65 and provided a pressure range between 479 and 523MPa with lower values than the other varieties. These values overlap with those estimated for the oxidized ferroan to magnesian granitoids of the Vila Jussara suite (670-230 MPa) and rocks with pyroxenes such as Café enderbite (578-280 MPa) and Rio Seco charnockite (310-110 MPa), which are also oxidized (#Fe<65). In contrast, an isolated sample of tonalite from the Estrela Complex (Barros et al., 2001) with #Fe close to the limit established by Anderson and Smith (1995) provided a relatively low-pressure range (110-380 MPa). Considering the differences presented and the ranges obtained by most geobarometers (Table 1), combined with the pressure stability fields of the phases generated in the thermodynamic modeling (Fig. 7), it is suggested that IGS crystallized at 550 ± 100 MPa, within the pressure range accepted for rocks with and without pyroxene in the Matok pluton (860 to 330 Mpa; Rapopo, 2011).

The magma of the BHMzG variety from IGS evolved in conditions of low oxygen fugacity (Table 2), slightly above or below the FMQ buffer (FMQ±0.5), in similar situations to those of the Planalto suite and the reduced granites of the Vila Jussara and Vila União suites. At the same time, the magmas of the PBHTnGd and BHTnGd reached oxygen fugacity equivalent to FMQ+0.5, of the same order as the Palaeoproterozoic Cigano granite. Unlike the other IGS granitoids, the RBHMzG variety crystallized under strongly reduced conditions equivalent to FMQ-0.5 to FMQ-1, as indicated by the compositional diagrams of amphibole (Fig. 8a; Anderson and Smith, 1995) and biotite (Fig. 8b; Anderson et al., 2008), as well as the fO_2 vs. T diagram (Fig. 8c; Frost et al., 2001). Furthermore, contrary to the pyroxene-bearing varieties of the IGS, the Rio Seco charnockite, the Café enderbite, the charnockites in the Matok pluton, and some rocks of the Vila União suite are strongly oxidized and evolved mainly above NNO.

Numerous discussions have focused on the H_2O content of Neoarchean A-type granites of Carajás, considering that they are interpreted as hydrated biotite-amphibole granites occasionally associated with charnockites (Cunha et al., 2016; Dall'Agnol et al., 2017; Feio et al., 2012). Cunha et al. (2016) conducted experimental studies to determine the minimum water content needed for amphibole stability. They estimated that the magma forming the reduced rocks of the Planalto Suite contains more than 4 wt% of H_2O. Similar values have been accepted for other Neoarchean granites with A-type affinity in the Carajás region (Dall'Agnol et al., 2017; Oliveira et al., 2018a) (Table 2). This high H_2O content makes

pyroxene crystallization unfeasible in the rocks of the Vila Jussara, Vila União, and Planalto suites, where pyroxenes are rare (reliquary) or absent.

Feio et al. (2012) suggested that the biotite-hornblende granites of the Planalto suite could be related to charnockites, as described by Elliott (2003) and Frost & Frost (2008), who considered that granites similar to those of the Planalto suite might be hydrated residual magmas derived from evolved charnockite magmas. This hypothesis initially seems to be reinforced by the occurrence of granites and charnockites in the IGS. However, no geochemical evidence suggests a cogenetic relationship between PBHTnGd and BHMzG (Mesquita et al., submitted). Furthermore, the high water content suggested for the magma of the PBHTnGd variety (4 wt% H_2O, according to thermodynamic modeling, Fig. 7 b) is atypical. However, similar contents have been accepted for Neoarchean rocks with pyroxene from the CP, such as Café enderbite (4.8-5.6 %), Rio Seco charnockite (4.1-6.5 %), and also in the Matok Pluton (H_2O > 5 %). Marangoanha et al. (2022) proposed for the Café enderbite that, with ~4 and 6 % H_2O, that pyroxene stability is possible at temperatures between ~1000-800°C and a pressure of 5 kbar, as observed in the studies by Percival and Mortensen (2002). These values are within the range of pyroxene stability recommended by the thermodynamic modeling applied to PBHTnGd (Fig. 7b, c). Rocks enriched in Zr (400 to 600 ppm) and P_2O_5 (0.4 to 0.8 wt%) facilitate the extraction of hydrated fusion from an orthopyroxene-rich *mush*, favoring progressive crystallization of orthopyroxene without the influence of volatiles (Zhao et al., 2023). Thus, at the end of crystallization, orthopyroxene would be in equilibrium with hydrated minerals, as observed in the PBHTnGd, which contains Zr and P_2O_5 (Table S8) close to those considered critical by Zhao et al. (2023). However, with a degree of crystallization of the magma between 40 and 50%, the pyroxene could react with the hydrated fusion before segregation. This situation likely occurred during the crystallization of certain rocks from the PBHTnGd and BHTnGd varieties and even in a sample of BHMzG (Table S2). This is indicated by the replacement of clinopyroxene by Fe-Mg-amphibole (Fig. S1b), which is analogous to what has been described in the monzogranites associated with the Rio Seco charnockite, where relics of clinopyroxene are surrounded by amphiboles (Félix et al., 2020). Such observations indicate a peritectic reaction and increased H_2O content in the residual liquid during magmatic evolution.

8 CONCLUSIONS

The central-eastern portion of the IGS comprises four facies that form elongated sigmoidal bodies with incipient to strongly penetrative foliation in preferential directions from

WNW-ESE to E-W. The different facies consist of tonalites and granodiorites with varying amounts of biotite and amphibole having or not associated clinopyroxene and/or orthopyroxene. Additionally, monzogranites contain biotite and amphibole, and are classified as moderately or strongly reduced rocks. The deformation of the IGS rocks was conditioned by shear zones, through which the magmas probably migrated, and they suffered progressive deformation until total cooling occurred.

The variety with pyroxenes includes orthopyroxene (ferrosilite) and clinopyroxenes, augite with subordinate hedenbergite. The amphiboles of the four varieties are classified as K-hastingsite and, subordinately, Fe-Tschermakite. The biotites are ferroan, and those of the strongly reduced monzogranites have #Fe > 0.9. The tonalites and granodiorites with pyroxenes have alkaline biotites, and those without pyroxenes have subalkaline biotites. The biotites of the strongly reduced monzogranites are mainly alkaline, while those of the other monzogranites are subalkaline. The biotites of all the varieties are predominantly primary magmatic. The plagioclase of the different varieties is oligoclase (An_{16-24}) and has no significant compositional variations.

PBHTnGd from IGS crystallized in the range between 1000±50°C and ~660°C, in a similar interval to that recorded in the Vila União suite. The BHTnGd and BHMzG formed in a similar temperature range to the PBHTnGd, while the RBHMzG had lower *liquidus* temperatures (≤900°C). The estimated emplacement pressure for PBHTnGd is 5.5 ± 1.0 kbar. A similar pressure was deduced for RBHMzG (5.5 ± 0.5 kbar) and is also valid for the other varieties. Such pressures are slightly higher than those attributed to other Neoarchean granites of Carajás (Barros et al., 2009; Cunha et al., 2016; Dall'Agnol et al., 2017). The magma of the BHMzG evolved under low oxygen fugacity, slightly above or below FMQ. This is similar to the conditions registered in the Planalto suite and the reduced granites of the Vila Jussara and Vila União suites. In contrast, the magma of the tonalitic and granodioritic varieties exhibited a fugacity corresponding to FMQ+0.5. Finally, the RBHMzG crystallized under strongly reduced conditions, equivalent to the FMQ-0.5 to FMQ-1 buffer.

The IGS monzogranitic variety magmas presented high H_2O contents (>4%, reaching 7% in the RBHMzG), similar to or potentially higher than those attributed to the Neoarchean granites of Carajás (>4%). Furthermore, the variety with pyroxene has an estimated water content of ~4%, close to Café enderbite (4.8-5.6%; Marangoanha et al., 2022), Rio Seco charnockite (4.1-6.5%; Félix et al., 2020) and Matok pluton (H_2O > 5%; Rapopo, 2011).

The integration of thermobarometry and thermodynamic modeling results, in conjunction with a comparison to the modal paragenesis present in natural rocks, enabled the definition of constraints for the evolution of the magma and refined the estimates of crystallization parameters.

9 ACKNOWLEDGMENTS

The authors acknowledge the Group of Research on Granitoid Petrology (GRGP), the Post-Graduate Program in Geology and Geochemistry (PPGG) and the Microanalyses Laboratory of the University Federal of Pará (UFPA) for their technical support. We thank Geological Survey of Brazil for concessions of the samples. This research was financed in part by the Conselho Nacional de Desenvolvimento Científico e Tecnológico (CNPq) (R. Dall'Agnol; Proc.3006767/2019-8) and by the Coordenação de Aperfeiçoamento de Pessoal de Nível Superior (CAPES) for granting a scholarship to the first author (C. J. S. Mesquita; 88882.347890/2019-01)

10 REFERENCES

Almeida, J.A.C., Dall'Agnol, R., Oliveira, M.A., Macambira, M.J.B., Pimentel, M.M., Rämö, O.T., Guimarães, F.V., Leite, A.A.S., 2011. Zircon geochronology, geochemistry and origin of the TTG suites of the Rio Maria granite-greenstone terrane: Implications for the growth of the Archean crust of the Carajás province, Brazil. *Precambrian Res* 187, 201–221.

Almeida, J.A.C., Dall'Agnol, R., Leite, A., 2013. Geochemistry and zircon geochronology of the Archean granite suites of the Rio Maria granite-greenstone terrane, Carajás Province, Brazil. *J. South Am. Earth* Sci. 42, 103–126. https://doi.org/10.1016/j.jsames.2012.10.008

Anderson, J., Barth, A., Wooden, J., Mazdab, F., 2008. Thermometers and Thermobarometers in Granitic Systems. Reviews in Mineralogy & Geochemistry – Ver. *Mineral. Geochem*. 69, 121–142. https://doi.org/10.2138/rmg.2008.69.4

Anderson, J.L., Smith, D., 1995. The effects of temperature and fO_2 on the Al-in-hornblende barometer. *American Mineralogist* 80, 549–559. https://doi.org/10.2138/am-1995-5-614

Anderson, J.L., Morrison, J., 2005. Ilmenite, magnetite, and peraluminous Mesoproterozoic anorogenic granites of Laurentia and Baltica. *Litho*s 80, 45–60. https://doi.org/https://doi.org/10.1016/j.lithos.2004.05.008

Araújo, O.J.B. de, Maia, R.G.N., João, X.S.J., Costa, J.B.S., 1988. A megaestruturação arqueana da folha Serra dos Carajás, in: Congresso Latino-Americano de Geologia. SBG-NO Belém, pp. 324–338.

Araújo Filho, R.C., Nogueira, A.C.R., Araújo, R.N., 2020. New stratigraphic proposal of a Paleoproterozoic siliciclastic succession: Implications for the evolution of the Carajás Basin, Amazonian craton, Brazil. *J. South Am. Earth Sci*.102, 102-665.

Avelar, V.G., Lafon, J.-M., Correia Jr, F.C., Macambira, E.M.B., 1999. O magmatismo arqueano da região de Tucumã-Província Mineral de Carajás: novos resultados geocronológicos. *Brazilian Journal of Geology* 29, 453–460.

Barbosa, J.P.O., 2004. Geologia estrutural, geoquímica, petrografia e geocronologia de granitoides da região do Igarapé gelado, norte da Província Mineral de Carajás. Master's degree dissertation. Universidade Federal do Pará, Belém.

Barros, C.E., Barbey, P., Boullier, A.-M., 2001. Role of magma pressure, tectonic stress and crystallization progress in the emplacement of syntectonic granites. The A-type Estrela Granite complex (Carajás Mineral Province, Brazil*). Tectonophysics* 343, 93–109. https://doi.org/10.1016/S0040-1951(01)00260-8

Barros, C.E., Dall'Agnol, R., Barbey, P., Boullier, A.-M., 1997. Geochemistry of the Estrela granite complex, Carajás region, Brazil: An example of an Archaean A-type granitoid*. J. South Am. Earth Sci*.10, 321–330. https://doi.org/10.1016/S0895-9811(97)00017-5

Barros, C.E., Sardinha, A., Barbosa, J.P.O., Macambira, M., Barbey, P., Boullier, A.-M., 2009. Structure, petrology, geochemistry and zircon U/Pb and Pb/Pb geochronology of the synkinematic archean (2.7 ga) a-type granites from the carajás metallogenic province, northern Brazil. *Canadian Mineralogist – Can. Mineralogy*. 47, 1423–1440. https://doi.org/10.3749/canmin.47.6.1423

Berman, R.G., 1991. Thermobarometry using multi-equilibrium calculations: a new technique, with petrological applications. *Can. Mineral*. 29, 833–855.

Bogaerts, M., Scaillet, B., Auwera, J. V., 2006. Phase Equilibria of the Lyngdal Granodiorite (Norway): Implications for the Origin of Metaluminous Ferroan Granitoids. *Journal of Petrology* 47, 2405–2431.

Bogaerts, M., Scaillet, B., Liégeois, J. P., Auwera, J. V., 2003. Petrology and geochemistry of the Lyngdal granodiorite (Southern Norway) and the role of fractional crystallisation in the genesis of Proterozoic ferro-potassic A-type granites. *Precambrian Research*, 124 2-4, 149-184.

Bohlender, F.B.D., 1992. Igneous and metamorphic charnockitic rocks in the southern marginal zone of the Limpopo belt with special emphasis on the matok enderbitic-granitic suite. Doctoral thesis.

Brey, G.P., Köhler, T., 1990. Geothermobarometry in four-phase lherzolites II. New thermobarometers, and practical assessment of existing thermobarometers. *Journal of Petrology* 31, 1353–1378. https://doi.org/10.1093/petrology/31.6.1353

Bucher, K., Frost, B.R., 2006. Fluid transfer in high-grade metamorphic terrains intruded by anorogenic granites: the thor range, Antarctica. *Journal of Petrology* 47, 567–593. https://doi.org/10.1093/petrology/egi086

Capitani, C., Petrakakis, K., 2010. The computation of equilibrium assemblage diagrams with Theriak/Domino software. *American Mineralogist* 95, 1006–1016. https://doi.org/doi:10.2138/am.2010.3354

Carmichael, I.S.E, 1991. The redox states of basic and silicic magmas: a reflexion of their source regions. *Contributions to Mineralogy and Petrology* 106, 129–141. https://doi.org/10.1007/BF00306429

Clark, D., 1999. Magnetic petrology of igneous intrusions: Implications for exploration and magnetic interpretation. *Exploration Geophysics – Explor. Geophys*. 30. https://doi.org/10.1071/EG999005

Connolly, J.A.D., 2005. Computation of phase equilibria by linear programming: a tool for geodynamic modeling and its application to subduction zone decarbonation. *Earth Planet Sci*. Lett. 236, 524–541.

Cunha, I.R.V., Dall'Agnol, R., Feio, G.R.L., 2016. Mineral chemistry and magnetic petrology of the Archean Planalto Suite, Carajas province–Amazonian Craton: Implications for the evolution of ferroan Archean granites. *J. South Am. Earth Sci*.67, 100–121.

Cunha, I.R.V., 2023. Petrologia experimental e química mineral das suítes neoarqueanas Vila Jussara e Planalto, Província Carajás, Amazônia, Brasil. Doctoral thesis. Universidade Federal do Pará, Belém. 167p.

Dall'Agnol, R., Cunha, I.R.V., Guimarães, F., Oliveira, D.C., Teixeira, M.F.B, Feio, G.R.L., Lamarão, C.N., 2017. Mineralogy, geochemistry, and petrology of Neoarchean ferroan to magnesian granites of Carajás province, Amazonian Craton: The origin of hydrated granites associated with charnockites. *Lithos* 277, 3-32. https://doi.org/10.1016/j.lithos.2016.09.032

Dall'Agnol, R., Oliveira, D.C., 2007. Oxidized, magnetite-series, rapakivi-type granites of Carajás, Brazil: Implications for classification and petrogenesis of A-type granites. *Lithos* 93, 215–233.

Dall'Agnol, R., Oliveira, D.C. de, Guimarães, F. V, Gabriel, E.O., Feio, G.R.L., Lamarão, C.N., Althoff, F.J., Santos, P.A., Teixeira, M.F.B., Silva, A.C., 2013. Geologia do Subdomínio

de Transição do Domínio Carajás–implicações para a evolução arqueana da Província Carajás-Pará. Simpósio de Geologia da Amazônia 13, 1082–1085.

Dall'Agnol, R., Pichavant, M., Champenois, M., 1997. Iron-titanium Oxide Minerals of the Jamon granite, Eastern Amazonian Region, Brazil: Implications for the Oxygen Fugacity in Proterozoic, A-type granites. *An Acad Bras Cienc* 69, 324–347.

Dall'agnol, R., Scaillet, B., Pichavant, M., 1999. An Experimental Study of a Lower Proterozoic A-type Granite from the Eastern Amazonian Craton, Brazil. *Journal of Petrology* 40, 1673–1698. https://doi.org/10.1093/petroj/40.11.1673

Dall'Agnol, R., Teixeira, N.P., Rämö, O.T., Moura, C.A. V, Macambira, M.J.B., de Oliveira, D.C., 2005. Petrogenesis of the Paleoproterozoic rapakivi A-type granites of the Archean Carajás metallogenic province, Brazil. *Lithos* 80, 101–129.

Deer, W.A., Howie, R.A., Zussman, J., 2013. An introduction to the rock-forming minerals. Mineralogical Society of Great Britain and Ireland.

Deer, W.A., Howie, R.A., Zussman, J., 1992. An Introduction to the Rock-Forming Minerals. Second (ed) Longman Scientific and Technical.

Diniz, A.C., Melo, G.H.C., Lana, C.C., Queiroga, G.N., Castro, M.P., Reis, H.L.S., 2023. Unravelling magmatic-hydrothermal processes at Salobo and GT-46 IOCG deposits, Carajás mineral province, Brazil: Constraints from whole-rock geochemistry and trace elements in apatite. *J. South Am. Earth Sci*.125, 104290. https://doi.org/https://doi.org/10.1016/j.jsames.2023.104290

Dreher, A., Xavier, R., Sérgio, Martini, L., 2005. Fragmental rocks of the Igarapé Bahia CU-AU deposit, Carajas Mineral province, Brazil. *Revista Brasileira de Geociências* 35. https://doi.org/10.25249/0375-7536.2005353359368

Eby, G.N., 1992. Chemical subdivision of the A-type granitoids: petrogenetic and tectonic implications. *Geology* 20, 641–644.

Elliott, B., 2003. Petrogenesis of the post-kinematic magmatism of the Central Finland Granitoid complex II; Sources and magmatic evolution. *Journal of Petrology* 44, 1681–1701. https://doi.org/10.1093/petrology/egg053

Fegley, B., 2013. Practical chemical thermodynamics for geoscientists, https://doi.org/10.1016/C2009-0-22615-8

Feio, G.RL., Dall'Agnol, R., Dantas, E., Macambira, M., Santos, J., Althoff, F., Soares, J., 2013. Archean granitoid magmatism in the Canaã dos Carajás area: Implications for crustal evolution of the Carajás province, Amazonian craton, Brazil. Precambrian Res. 227, 157–185. https://doi.org/10.1016/j.precamres.2012.04.007

Feio, G.R.L., Dall'Agnol, R., Dantas, E.L., Macambira, M.J.B., Gomes, A.C.B., Sardinha, A.S., Oliveira, D.C., Santos, R.D., Santos, P.A., 2012. Geochemistry, geochronology, and origin of the Neoarchean Planalto Granite suite, Carajás, Amazonian craton: A-type or hydrated charnockitic granites? *Lithos* 151, 57–73. https://doi.org/https://doi.org/10.1016/j.lithos.2012.02.020

Felix, W., Oliveira, D.C., Silva, L.R., Silva, F.F., 2020. Charnockites from Carajás province, SE Amazonian Craton (Brazil): Petrogenetic constraints and intensive crystallization parameters. J. *South Am. Earth Sci.*102598. https://doi.org/10.1016/j.jsames.2020.102598

Frost, B.R., 2018. Introduction to oxygen fugacity and its petrologic importance, in: Oxide Minerals. De *Gruyter*, pp. 1–10.

Frost, B.R., Barnes, C.G., Collins, W.J., Arculus, R.J., Ellis, D.J., Frost, C.D., 2001. A geochemical classification for granitic rocks. *Journal of Petrology* 42, 2033–2048.

Frost, B.R., Frost, C.D., 2008. On charnockites. *Gondwana Research* 13, 30–44. https://doi.org/https://doi.org/10.1016/j.gr.2007.07.006

Frost, C.D., Frost, B.R., Chamberlain, K.R., Edwards, B.R., 1999. Petrogenesis of the 1.43 Ga Sherman Batholith, SE Wyoming, USA: a Reduced, Rapakivi-type Anorogenic Granite. *Journal of Petrology* 40, 1771–1802. https://doi.org/10.1093/petroj/40.12.1771

Gaillard, F., Scaillet, B., Pichavant, M., Bény, J.-M., 2001. The effect of water and fO_2 on the ferric–ferrous ratio of silicic melts. *Chem. Geol.* 174, 255–273.

Gonçalez, M.G.B., Dall'Agnol, R., Vieira, E.A.P., Macambira, M.J.B., Sena, N.D., 1988. Geologia do Maciço Anorogênico Cigano. Vale do Rio Parauapebas-PA. SBG, *Congr. Bras. Geol* 35, 1132–1146.

Gualda, G.A.R., Ghiorso, M.S., 2015. MELTS _ E xcel: AM icrosoft E xcel-based MELTS interface for research and teaching of magma properties and evolution. *Geochemistry, Geophysics, Geosystems* 16, 315–324.

Gualda, G.A.R., Ghiorso, M.S., Lemons, R. V, Carley, T.L., 2012. Rhyolite-MELTS: a Modified Calibration of MELTS Optimized for Silica-rich, Fluid-bearing Magmatic Systems. *Journal of Petrology* 53, 875–890. https://doi.org/10.1093/petrology/egr080

Hammastrom, J., Zen, E., 1986. Aluminum in hornblende: an empirical igneous geobarometer. Am Mineral. *American Mineralogist* 71, 1297–1313.

Hawthorne, F., Oberti, R., Harlow, G., Maresch, W., Martin, R.F., Schumacher, J., Welch, M., 2012. IMA report: Nomenclature of the amphibole supergroup. *American Mineralogist* 97, 2031–2048. https://doi.org/10.2138/am.2012.4276

Holland, T., Blundy, J., 1994. Non-ideal interactions in calcic amphiboles and their bearing on amphibole-plagioclase thermometry. *Contributions to Mineralogy and Petrology* 116, 433–447. https://doi.org/10.1007/BF00310910

Holland, T.J.B., Green, E.C.R., Powell, R., 2018. Melting of peridotites through to granites: a simple thermodynamic model in the system KNCFMASHTOCr. *Journal of Petrology* 59, 881–900.

Holland, T.J.B., Powell, R., 2011. An improved and extended internally consistent thermodynamic dataset for phases of petrological interest, involving a new equation of state for solids. *Journal of metamorphic Geology* 29, 333–383.

Hollister, L., Grissom, G., Peters, E., Stowell, H., Sisson, V., 1987. Confirmation of the empirical correlation of Al in hornblende with pressure of solidification of calc-alkaline plutons. *American Mineralogist* 72, 231–239.

Ishihara, S., 2004. The redox state of granitoids relative to tectonic setting and earth history: The magnetite–ilmenite series 30 years later. *Earth Environ. Sci. Trans. R. Soc. Edinb*. 95, 23–33. https://doi.org/DOI: 10.1017/S0263593300000894

Jennings, E.S., Holland, T.J.B., 2015. A simple thermodynamic model for melting of peridotite in the system NCFMASOCr. *Journal of Petrology* 56, 869–892.

Johnson, M., Rutherford, M., 1989. Experimental calibration of the aluminum-in-hornblende geobarometer with applicable to Long Valley Caldera (California) volcanic rocks. *Geology* 17, 837–841. https://doi.org/10.1130/0091-7613(1989)017<0837:ECOTAI>2.3.CO;2

Jorge João, X.S., Araújo, J.B., 1992. Magmatismo granítico sin-cisalhamento Itacaiúnas no SW do Estado do Pará, in: SBG, *Congresso Brasileiro de Geologia*. pp. 36–38.

King, P.L., White, A.J.R., Chappell, B.W., Allen, C.M., 1997. Characterization and Origin of Aluminous A-type Granites from the Lachlan Fold Belt, Southeastern Australia. *Journal of Petrology* 38, 371–391. https://doi.org/10.1093/petroj/38.3.371

Klimm, K., Holtz, F., Johannes, W., King, P.L., 2003. Fractionation of metaluminous A-type granites: an experimental study of the Wangrah Suite, Lachlan Fold Belt, Australia. *Precambrian Res* 124, 327–341. https://doi.org/https://doi.org/10.1016/S0301-9268(03)00092-5

Leake, B. E., Wooley, A. R., Arps, C. E. S., Birch, W. D.,Gilbert, M. C., Grice, J. D., Hawthorne, F. C., Kato, A., Kisch,H. J., Krivovichev, V. G., Linthout, K., Laird, J., Mandarino,J. A., Maresch, W. V., Nickel, E. H., Schumacher, J., Smith,J. C., Stephenson, N. C. N., Ungaretti, L., Whittaker, E. J.W., Youzhi, G. 1997. Nomenclature of amphiboles: report of the subcommittee on amphiboles of the international mineralogical association commission on new minerals and mineral names. *Mineral. Mag*. 61, 295–321. https://doi.org/10.1180/minmag.1997.061.405.13

Leite-Santos, P.J., de Oliveira, D.C., 2016. Geologia, petrografia e geoquímica das associações leucograníticas arqueanas da área de Nova Canadá: Província Carajás. *Geologia USP. Série Científica* 16, 37–66.

Leite-Santos, P.J., Oliveira, D.C., Galarza, M.A., Macambira, M.J.B., 2010. Geologia, petrografia e geocronologia das rochas granitóides do complexo Xingu da região de Nova Canadá, município de Água Azul do Norte-Província Mineral de Carajás, in: SBG, *Congresso Brasileiro de Geologia.*

Loiselle, M.C., Wones, D.R., 1979. Characteristics and origin of anorogenic granites. *Geol. Soc. Am. Abstr. Prog.* 11, 468.

Macambira, J.M.B., Lancelot, J.R., 1996. Time constraints for the formation of the Archean Rio Maria crust, southeastern Amazonian Craton, Brazil. *Int Geol* Rev 38, 1134–1142.

Machado, N., Lindenmayer, Z., Krogh, T.E., Lindenmayer, D., 1991. U-Pb geochronology of Archean magmatism and basement reactivation in the Carajás area, Amazon shield, Brazil. *Precambrian Res* 49, 329–354.

Maitre, R., Streckeisen, A., Zanettin, B., Le Bas, M., Bonin, B., 2020. Igneous rocks: a classification and glossary of terms.

Marangoanha, B., Oliveira, D.C, Oliveira, V.E.S., Galarza, M.T., Lamarão, C.N., 2019a. Neoarchean A-type granitoids from Carajás province (Brazil): New insights from geochemistry, geochronology and microstructural analysis. *Precambrian Res* 324, 86–108. https://doi.org/10.1016/j.precamres.2019.01.010

Marangoanha, B., Oliveira, D.C., Lamarão, C.N., Marques, G., Silva, L.R., 2022. Geothermobarometry and geochemical modeling of Archean charnockites from Carajás province, Amazonian craton, Brazil. *Brazilian Journal of Geology* 52. https://doi.org/10.1590/2317-4889202220210092

Marangoanha, B., Oliveira, D.C., Dall'Agnol, R., 2019b. The Archean granulite-enderbite complex of the northern Carajás province, Amazonian craton (Brazil): Origin and implications for crustal growth and cratonization. *Lithos* 350–351, 105275. https://doi.org/https://doi.org/10.1016/j.lithos.2019.105275

Melo, G.H.C., Monteiro, L., Xavier, R., Moreto, C., Santiago, E., Dufrane, S.A., Aires, B., Santos, A., 2016. Temporal evolution of the giant Salobo IOCG deposit, Carajás province (Brazil): constraints from paragenesis of hydrothermal alteration and U-Pb geochronology. *Miner Depos* 52. https://doi.org/10.1007/s00126-016-0693-5

Mesquita, C.J.S., Dall'Agnol, R., Borba, M.L., Tassinari, C.C.G., Galarza, M.A., Dantas, E.L. Submitted. Petrogenesis, U-Pb SHRIMP geochronology, and zircon composition of neoarchean granitoids of the Igarapé Gelado suite, Carajás province, Amazonian craton.

Molin, G., Zanazzi, P.F., 1991. Intracrystalline Fe-$^{2+}$-Mg ordering in augite-experimental-study and geothermometric applications. *European Journal of Mineralogy* 3, 863–875.

Monteiro, L.V.S., Xavier, R.P., Carvalho, E.R., Hitzman, M.W., Johnson, C.A., de Souza Filho, C.R., Torresi, I., 2008. Spatial and temporal zoning of hydrothermal alteration and mineralization in the Sossego iron oxide–copper–gold deposit, Carajás Mineral province, Brazil: paragenesis and stable isotope constraints. *Miner. Depos*. 43, 129–159. https://doi.org/10.1007/s00126-006-0121-3

Moore, G., Righter, K., Carmichael, I.S.E., 1995. The effect of dissolved water on the oxidation state of iron in natural silicate liquids. *Contributions to Mineralogy and Petrology* 120, 170–179.

Moreto, C.P.N., Monteiro, L.V.S., Xavier, R.P., Creaser, R.A., DuFrane, S.A., Melo, G.H.C., Silva, M.A., Tassinari, C.C.G., Sato, K., 2015. Timing of multiple hydrothermal events in the iron oxide–copper–gold deposits of the Southern Copper Belt, Carajás Province, Brazil. *Miner. Depos.* 50, 517–546. https://doi.org/10.1007/s00126-014-0549-9

Morimoto, N., Fabries, J., Ferguson, A.K., Ginzburg, I. V, Ross, M., Seifert, F.A., Zussman, J., Aoki, K., Gottardi, G., 1988. Nomenclature of Pyroxenes. *Mineral Mag* 52, 535–550. https://doi.org/DOI: 10.1180/minmag.1988.052.367.15

Mutch, E., Blundy, J., Tattitch, B., Cooper, F., Brooker, R., 2016. An experimental study of amphibole stability in low-pressure granitic magmas and a revised Al-in-hornblende geobarometer. *Contributions to Mineralogy and Petrology* 171. https://doi.org/10.1007/s00410-016-1298-9

Nachit, H., Ibhi, A., Abia, E., Ohoud, M., 2005. Discrimination between primary magmatic biotites, reequilibrated biotites and neoformed biotites. *Comptes Rendus Geosciences* 337, 1415–1420. https://doi.org/10.1016/j.crte.2005.09.002

Naney, M.T., 1983. Phase equilibria of rock-forming ferromagnesian silicates in granitic systems. *Am J Sci* 283, 993–1033.

Nardi, L.V.S., Bitencourt, M.F., 2009. A-type granitic rocks in post-collisional settings in southernmost Brazil: their classification and relationship with tectonics and magmatic series. *The Canadian Mineralogist* 47, 1493–1503.

Oliveira, J.K.M., Tavares, F.M., Costa, I.S.L., 2018b. Mapa geológico-geofísico do lineamento cinzento:[Estado do Pará]. CPRM.

Oliveira, M.A, Dall'Agnol, R., Almeida, J.A.C., 2011. Petrology of the Mesoarchean Rio Maria suite and the discrimination of sanukitoid series. *Lithos* 127, 192–209. https://doi.org/10.1016/j.lithos.2011.08.017

Oliveira, V.E.S., Oliveira, D.C., Marangoanha, B., Lamarão, C.N., 2018a. Geology, mineralogy and petrological affinities of the Neoarchean granitoids from the central portion of the Canaã dos Carajás domain, Amazonian craton, Brazil. J. *South Am. Earth Sci*.85, 135–159. https://doi.org/https://doi.org/10.1016/j.jsames.2018.04.022

Percival, J.A., Mortensen, J.K., 2002. Water-deficient calc-alkaline plutonic rocks of northeastern Superior province, Canada: significance of charnockitic magmatism. *Journal of Petrology* 43, 1617–1650. https://doi.org/10.1093/petrology/43.9.1617

Pidgeon, R.T., Macambira, M.J.B., Lafon, J.-M., 2000. Th–U–Pb isotopic systems and internal structures of complex zircons from an enderbite from the Pium complex, Carajás province, Brazil: evidence for the ages of granulite facies metamorphism and the protolith of the enderbite. *Chem. Geol.* 166, 159–171.

Pinheiro, R.V.L., Holdsworth, R.E., 2000. Evolução tectonoestratigráfica dos sistemas transcorrentes Carajás e Cinzento, Cinturão Itacaiúnas, na borda leste do Craton Amazônico, Pará. *Brazilian journal of geology*. 30.

Powell, R., Holland, T.J.B., 1988. An internally consistent dataset with uncertainties and correlations: 3. Applications to geobarometry, worked examples and a computer program. *Journal of Metamorphic Geology* 6, 173–204.

Putirka, K., 2016. Amphibole thermometers and barometers for igneous systems and some implications for eruption mechanisms of felsic magmas at arc volcanoes. *American Mineralogist* 101, 841–858. https://doi.org/10.2138/am-2016-5506

Rajesh, H.M., Santosh, M., Yoshikura, S., 2011. The Nagercoil charnockite: a magnesian, calcic to calc-alkalic granitoid dehydrated during a granulite-facies metamorphic event. *Journal of Petrology* 52, 375–400.

Rapopo, M., 2011. Petrogenesis of the syntectonic Matok pluton in the Limpopo Belt (South Africa) and its implications on the geodynamic environment. Master's degree dissertation.

Ridolfi, F., Renzulli, A., Puerini, M., 2010. Stability and chemical equilibrium of amphibole in calc-alkaline magmas: an overview, new thermobarometric formulations and application to subduction-related volcanoes. *Contributions to Mineralogy and Petrology* 160, 45–66. https://doi.org/10.1007/s00410-009-0465-7

Santos, J.O.S. dos, Hartmann, L.A., Faria, M.S.G. de, Riker, S.R., Souza, M.M. de, Almeida, M.E., McNaughton, N.J., 2006. A compartimentação do Cráton Amazonas em províncias: avanços ocorridos no período 2000-2006. *Simpósio de geologia da Amazônia* 9, 156–159.

Santos J.O.S. 2003. Geotectônica do Escudo das Guianas e Brasil-Central. In: Bizzi L.A. (Ed.). Geologia, tectônica e recursos minerais do Brasil: texto, mapas e SIG. Brasília: CPRM-*Serviço Geológico do Brasil.* p. 169-226, il.

Santos-Silva, A.N., Feio, G.R.L., Silva, J.P.A., Dall'Agnol, R., Almeida, J.A.C., Gomes, A., 2020. Mineralogy, petrology, and origin of the Pedra Branca Suite: a tonalitic-trondhjemitic association with high Zr, Ti and Y, Carajás province, Amazonian Craton. *Brazilian Journal of Geology*, 50. https://doi.org/10.1590/2317-4889202020190093

Sardinha, A.S., Dall'Agnol, R., Gomes, A.C.B., Macambira, M.J.B., Galarza, M.A., 2004. Geocronologia Pb-Pb e U-Pb em zircão de granitóides arqueanos da região de Canaã dos Carajás, Província Mineral de Carajás, in: *Congresso Brasileiro de Geologia*. p. 2004.

Sardinha, A.S., Barros, C.E., Krymsky, R., 2006. Geology, geochemistry, and U–Pb geochronology of the Archean (2.74 Ga) Serra do Rabo granite stocks, Carajás Metallogenetic province, northern Brazil. *J. South Am. Earth Sci.*20, 327–339.

Schmidt, M., 1992. Amphibole composition in tonalite as a function of pressure: an experimental calibration of the Al-in-hornblende barometer. *Contributions to Mineralogy and Petrology* 110, 304–310. https://doi.org/10.1007/BF00310745

Semprich, J., Moreno, J.A., Oliveira, E.P., 2015. Phase equilibria and trace element modeling of Archean sanukitoid melts. *Precambrian Res* 269, 122–138.

Silva, F.F., Oliveira, D.C., Dall'Agnol, R., Santos, J.O.S., Galarza, M.A.T., Guimarães, F.V., Souza, L.A.M. 2024. Geochemistry, SHRIMP U-Pb Zircon geochronology, and Hf-Nd isotope composition on the Neoarchean Vila Jussara granitoid complex from Carajás province, Amazonian Craton: petrogenesis and tectonic implications.

Silva, F.F., Oliveira, D.C., Dall'Agnol, R., Silva, L.R., Cunha, I.R.V., 2020. Lithological and structural controls on the emplacement of a Neoarchean plutonic complex in the Carajás province, southeastern Amazonian craton (Brazil). *J. South Am. Earth Sci*.102, 102696. https://doi.org/10.1016/j.jsames.2020.102696

Silva, L.R., Oliveira, D.C., Nascimento, A., Lamarão, C.N., Almeida, J.A.C, 2022. The Mesoarchean plutonic complex from the Carajás province, Amazonian craton: Petrogenesis, zircon U-Pb SHRIMP geochronology and tectonic implications. *Lithos* 432–433, 106901. https://doi.org/10.1016/j.lithos.2022.106901

Sousa, L.A.M. de, Dall'Agnol, R., Cunha, I.R.V., Silva, F.F., Oliveira, D.C., 2022. Magnetic petrology of the Neoarchean granitoids in the Vila Jussara Suite, Carajás province, Amazonian Craton. *Brazilian Journal of Geology* 52, e20201071. https://doi.org/10.1590/2317-4889202220210071

Souza, S.R.B., Macambira, M.J.B., Sheller, T., 1996. Novos dados geocronológicos para os granitos deformados do Rio Itacaiúnas (Serra dos Carajás, PA); implicações estratigráficas. Proceedings of the *Simpósio de Geologia da Amazônia,* Belém, Brazil 380–383.

Souza, Z.S., Potrel, A., Lafon, J.M., Althoff, F.J., Pimentel, M.M., Dall'Agnol, R., Oliveira, C.G., 2001. Nd, Pb and Sr isotopes in the Identidade Belt, an Archean greenstone belt of Rio Maria region (Carajás province, Brazil): implications for the geodynamic evolution of the Amazonian Craton. *Precambrian Res* 109, 293–315.

Sylvester, P., 1989. Post-Collisional Alkaline Granites Author(s): Post-collisional alkaline granites'. *J. Geol.* 97, 261–280.

Tassinari, C.C.G., Macambira, M.J.B., 2004. A evolução tectônica do Cráton Amazônico. In: V. Mantesso Neto., A. Bartorelli., C. D. R. Carneiro., B. B. Brito-Neves (Orgs.): Geologia do continente Sul-americano: evolução da obra de Fernando Flávio Marques de Almeida. *BECA,* São Paulo (pp. 471-486) (in Portuguese).

Tavares, F.M., Oliveira, J.K.M., Lima, R.B., 2021. Áreas de relevante interesse mineral-Província mineral de Carajás, PA: controles críticos das mineralizações de cobre e ouro do lineamento Cinzento. *Mineral Resources Reports.* CPRM.

Tavares, F.M., Trouw, R.A.J., da Silva, C.M.G., Justo, A.P., Oliveira, J.K.M., 2018. The multistage tectonic evolution of the northeastern Carajás province, Amazonian Craton, Brazil: Revealing complex structural patterns. J. *South Am. Earth Sci.* 88, 238–252. https://doi.org/https://doi.org/10.1016/j.jsames.2018.08.024

Teixeira, M.F.B., Dall'Agnol, R., Santos, J.O.S., Kemp, A., Evans, N., 2019. Petrogenesis of the Paleoproterozoic (Orosirian) A-type granites of Carajás Province, Amazon Craton, Brazil: Combined in situ Hf-O isotopes of zircon. *Lithos* 332, 1–22.

Teruiya, R.K., Paradella, W.R., Santos, A.R., Dall'Agnol, R., Veneziani, P., 2008. Integrating airborne SAR, Landsat TM and airborne geophysics data for improving geological mapping in the Amazon region: the Cigano granite, Carajás province, Brazil. *Int. J. Remote Sens*. 29, 3957–3974.

Toledo, P.I.S., Penteado Natividade Moreto, C., Xavier, R.P., Gao, J., da Silva Nogueira de Matos, J.H., de Melo, G.H.C., 2019. Multistage evolution of the Neoarchean (ca. 2.7 Ga) Igarapé cinzento (GT-46) iron oxide copper-gold deposit, Cinzento shear zone, Carajás province, Brazil. *Economic Geology* 114, 1–34.

Toledo, P.I.S., Moreto, C., Monteiro, L., Melo, G., Matos, F., Xavier, R., Carvalho, J., Medeiros Filho, C.A., Navarro, M., Lana, C., 2023. Breaking up the temporal link between granitic magmatism and iron oxide-copper–gold (IOCG) deposits in the Carajás Mineral province, NW Brazil. *Miner. Depos.* 59. https://doi.org/10.1007/s00126-023-01224-5

Vasquez, M.L., Rosa-Costa, L.T., 2008. Geologia e recursos minerais do estado do Pará. CPRM.

Watson, E., Harrison, T.M., 1983. Zircon saturation revisited: temperature and composition effects in a variety of crustal magma types. Earth Planet. Sci. Lett. 64, 295-304. *Earth Planet Sci* Lett 64, 295–304. https://doi.org/10.1016/0012-821X(83)90211-X

Weiss, S., Troll, G., 1989. The Ballachulish igneous complex, Scotland: petrography, mineral chemistry, and order of crystallization in the monzodiorite-quartz diorite suite and in the granite. *Journal of Petrology* 30, 1069–1115.

Whitney, D., Evans, D., 2010. Abbreviations for names of rock-forming minerals

Whalen, J.B., Currie, K.L., Chappell, B.W., 1987. A-type granites: geochemical characteristics, discrimination, and petrogenesis. *Contributions to mineralogy and petrology*. 95, 407–419.

Wones, D.R., 1989. Significance of the assemblage titanite+ magnetite + quartz in granitic rocks. *American Mineralogist* 74, 744–749.

Xiang, H., Connolly, J.A.D., 2022. GeoPS: An interactive visual computing tool for thermodynamic modeling of phase equilibria. *Journal of Metamorphic Geology* 40, 243–255.

Yavuz, F., 2013. WinPyrox: A Windows program for pyroxene calculation classification and thermobarometry. *American Mineralogist* 98, 1338–1359. https://doi.org/10.2138/am.2013.4292

Yavuz, F., Doner, Z., 2017. WinAmptb: A Windows program for calcic amphibole thermobarometry. *Periodico di Mineralogia.* 86, 135–167. https://doi.org/10.2451/2017PM710

Zhang, Q.-Q., Gao, X.-Y., Zheng, Y.-F., 2023. The different responses of trace elements to equilibrium and disequilibrium melting: Implications for crustal differentiation and granite compositions. *Chem. Geol.* 625, 121426. https://doi.org/https://doi.org/10.1016/j.chemgeo.2023.121426

Zhao, K., Xu, X., Erdmann, S., 2018. Thermodynamic modeling for an incrementally fractionated granite magma system: Implications for the origin of igneous charnockite. *Earth Planet Sci*. Lett 499, 230–242. https://doi.org/https://doi.org/10.1016/j.epsl.2018.07.039

Zhao, K., Xu, X., Erdmann, S., 2017. Crystallization conditions of peraluminous charnockites: constraints from mineral thermometry and thermodynamic modeling. Contributions to Mineralogy and Petrology, 172. https://doi.org/10.1007/s00410-017-1344-2

Zhao, K., Xu, X., Klemd, R., He, Z., Zhang, X., 2023. A review of the genetic mechanisms generating igneous charnockite: CO_2 flushing and crystal-melt segregation in mushy reservoirs. Earth Sci. Ver. 237, 104295. https://doi.org/https://doi.org/10.1016/j.earscirev.2022.104295

DADOS SUPLEMENTARES DO CAPÍTULO 2

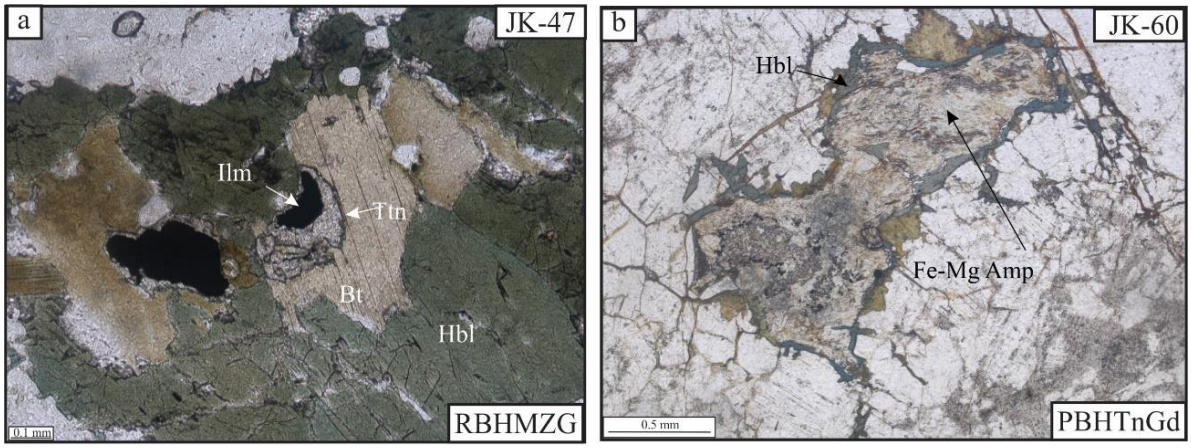

Supplementary Figure 1. a)Titanite bordering ilmenite; b) Replacement of pyroxene by Fe-Mg-amphibole in PBHTnGd.

Supplementary Table 1. Synthesis of the geochronological data for the Neoarchean units from the Carajás basin

Carajás Basin	Rock type	Geochronologic method	Age (Ma)
Old Salobo Granite	Granitoid	U-Pb´TIMS	2573±3 Ma (1)
	Granitoid	U-Pb SHRIMP	2547±5 Ma (2)
	Granitoid	U-Pb SHRIMP	2551±9 Ma (2)
GT-46 deposit (Igarapé Cinzento Granite)	Bt monzogranite	U-Pb LA-ICP_MS	2497±41Ma (3)
	granodiorite to tonalite	U-Pb LA-ICP_MS	2554 ± 3, 2549 ± 7 , 2594 ± 6 Ma (4)
	Isotropic granite	U-Pb LA-ICP_MS	2557±26 Ma (5) 2564 ± 4 Ma (4)
	Foliated tonalite	U-Pb LA-ICP_MS	2532±26, 2639±16 Ma (5) 2560 ± 3, 2576 ± 4 Ma(4)
	Pegmatite		2562 ± 39 Ma (5)
Itacaiúnas Granite	Granitoid	Evaporation-Pb	2560±37 Ma, 2525 ± 38 (6)
Igarapé Gelado Suite	Monzogranite	Evaporation-Pb	2731±2 Ma (7)
	Foliated tonalite	U-Pb LA-ICP-MS	2680 ± 18, 2640 ± 16, 2623 ± 5 ,2579 ± 28 Ma (4)
	Ultramylonitic Monzogranite	U-Pb LA-ICP-MS	2561 ± 5 Ma (4)
	Mylonitized granitoid	U-Pb LA-ICP-MS	2701±30Ma (2)
	Granitoid	U-Pb SHRIMP	2763 ± 4Ma (2)
	Granitoid	U-Pb LA-ICP_MS	2744 ± 4, 2731 ± 7 Ma (4)
	Hb-Bt monzogranite	U-Pb SHRIMP	2682±25Ma (3)
	Monzogranite	U-Pb SHRIMP	2611±28, 2665±29 Ma (8)
	Granodiorite	U-Pb SHRIMP	2659.7±6 Ma (8)
Serra do Rabo Granite	Hb-syenogranite	U-Pb-TIMS	2743±1 Ma (7)
Estrela Complex	Granitoid	Evaporation-Pb	2763±7 Ma (7)
Rio Sereno Granite	Foliated granodiorite	U-Pb LA-ICP-MS	2787±73Ma (9)
Lavrado Suite - Aquiri	Isotropic granodiorite	U-Pb SHRIMP	2666±78Ma (10)
	Foliated granite	U-Pb SHRIMP	2651±14Ma (10)
Buritirama Granite	Foliated granite	U-Pb LA-ICP-MS	2549±6Ma (11)
Luanga Complex	Gabbro	U-Pb-TIMS	2763±6 Ma (1)

Fontes: (1) Machado et al., (1991); (2) Melo et al., (2016); (3) Tavares et al., (2021); (4) Toledo et al., (2023); (5) Toledo et al.,(2019); (6) Souza et al., (1996); (7) Barros et al., (2009); (8) Reis, (2017); (9) Tavares e Silva, (2015); (10) Castro et al., (2023); (11) Silas et al., (2019).

Supplementary Table 2. Modal compositions of the representative samples from the Igarapé Gelado suite varieties.

Variety	PBHTnGd								BHTnGd															
Sample	CR-8A	CAD-17	CAD-4	JK-60	CAD-14	CR-6A	CR-7D	CR-8B	CR-7B	CG-R-75	JK-86	JK-372	CAD-5	JK-59A	CAD-16A	CAD-3	CR-12B	JK-139A	CAD-6B	CR-12A	JK-446	JK-14A	JK-2A	CR-7A	JK-61A
Facies	Bt-Opx-Hbl Tnl	Hbl-Cpx Tnl	Hbl-Cpx-Bt Tnl	Opx-Hbl-Bt Tnl	Cpx-Opx-Hbl GrD	Cpx-Hbl GrD	Bt-Hbl GrD	Bt-Opx-Hbl MzG	Bt-Hbl Tnl		H Tnl		Hbl-Bt Tnl				Bt-Hbl GrD			Bt GrD		H GrD		Hbl-Bt MzG	Bt-Hbl MzG
Minerals (%)																									
Quartz	34.2	31.6	18.1	23.1	30.3	20.5	32.4	26.5	28.5	28.8	17.5	44.1	27.9	30.0	30.9	35.9	25.1	30.5	42.9	30.2	48.5	22.9	27.6	27.0	33.3
Plagioclase	47.2	53.9	61.1	57.3	41.7	56.8	48.8	40.2	52.3	52.4	68.0	51.7	50.8	51.5	56.4	51.1	51.6	47.2	44.0	46.2	23.1	64.3	50.8	43.0	25.6
Alcali feldspar	4.0	3.1	1.3	5.3	20.2	9.6	9.1	25.6	3.6	3.4	1.6	0.7	5.3	5.2	4.3	3.2	10.2	7.6	6.2	13.0	9.5	7.0	16.3	24.0	20.3
Biotite	2.0	-	6.7	5.1	x	x	2.8	1.3	2.4	0.8	1.3	0.2	9.3	7.8	4.9	7.3	6.1	6.4	0.3	10.0	18.4	0.9	0.2	3.3	3.2
Hornblende	9.3	2.2	4.7	3.5	4.6	9.9	6.3	4.1	12.4	13.8	3.20	2.6	6.2	5.1	2.2	2.1	6.5	8.0	4.1	0.5	0.4	-	0.5	0.6	16.2
Ferromagnesian amphibole	-	0.9	1.7	0.2	0.3	-	x	-	-		-	-	-	-	-	-	-	-	2.3	-	-	-	-	0.7	-
Orthopyroxene	2.6	-	0.5	3.9	1.7	-	-	1.8	-	-		-	0.1	-	0.1	-	-	-	-	-	-	-	-		-
Clinopyroxene	-	7.7	5.3	-	0.4	0.8	x	-	-	-		-	-	-	-	-	-	-	-	-	-	-	-		0.1
Opaque	0.6	0.6	0.4	1.1	0.7	1.1	0.2	0.3	0.4	0.4	0.2	0.5	-	0.1	0.2	0.3	0.3	0.1	0.2	x	-	0.1	0.6	0.3	0.4
Titanite	-	-	-	-	-	0.2	-	-	-	-	0.2	0.1	-	0.1	-	-	-	0.1	-	-	-	-	-	-	0.4
Epidote	x	-	0.1	0.2	-	x	x	x	x	x	0.5	0.1	x	x	0.2	0.1	-	x	x	x	x	x	x	0.1	x
Alanite	0.1	-	-	0.1	-	0.7	0.2	-	0.2	0.1		0.1	x	-	-	-	-	-	-	0.1	-	-	-	x	0.1
Chlorite	-	-	0.1	x	-	-	-	-	0.1	0.4	7.5	-	0.2	0.1	0.7	0.1	-	0.1	x	-	-	4.7	3.7	1.0	0.3
Carbonate	-	-	-	-	-	-	-	-	-	-		-	-	-	-	-	-	-	-	-	-	-	0.2	-	-
Scapolite	-	-	-	-	-	-	0.2	-	-	-		-	-	-	-	-	-	-	-	-	-	-	-	-	-
Muscovite	-	-	-	-	-	-	-	-	-	-		-	x	-	-	-	-	-	-	-	-	-	-	-	0.1
Accessories (Ap+Zr)	0.1	0.1	0.1	0.2	0.1	x	0.2	0.1	0.1	0.1	0.1	0.1	0.1	0.2	0.1	0.1	0.1	0.2	0.1	0.1	x	0.1	0.2	0.1	0.2
Felsic minerals	85.3	88.6	80.4	85.7	92.2	86.9	90.4	92.4	84.4	84.6		96.5	84.1	86.6	91.6	90.2	86.9	85.2	93.1	89.4	81.2	94.2	94.7	94.0	79.2
Mafic minerals	14.7	11.4	19.5	14.3	7.8	13.1	9.6	7.6	15.6	15.4		3.5	15.7	13.4	7.7	9.8	13.1	14.8	6.9	10.6	18.8	5.8	5.3	5.0	20.8
To 100%																									
Quartz	40.1	35.6	22.4	27.0	32.9	24.3	35.9	28.7	33.8	34.3		45.7	33.2	34.8	33.7	39.8	28.9	35.9	46.1	33.7	59.9	26.5	29.5	28.7	42.4
Alcali feldspar	4.7	3.5	1.6	6.2	21.9	11.4	10.1	27.8	4.3	4.0		0.7	6.3	6.1	4.7	3.6	11.7	8.9	6.6	14.5	11.8	8.1	17.5	25.5	25.8
Plagioclase	55.2	60.9	76.0	66.9	45.3	64.3	54.1	43.5	62.0	61.7		53.6	60.4	59.1	61.6	56.6	59.4	55.2	47.3	51.7	28.4	65.5	53.0	45.7	31.9

Abbreviations: Opx = orthopyroxene; Cpx = clinopyroxene; Hbl = hornblende; Bt = biotite; Ap = apatite; Zr = zircon; Tnl = tonalite; GrD = granodiorite e MzG = monzogranite and H = hydrothermalized
Acronym of the varieties according to figure 2
x - present on the thin sections, but not detected in the count

(-) absent in thin sections

Note: Epidote present is secondary, accounted for as plagioclase

Supplementary Table 2 (Cont.): Modal compositions of the representative samples from the Igarapé Gelado suite varieties.

Variety	BHMzG												RBHMzG					
Sample	JK-137A	CG-22A	CR-3C	CR-3B	JK-23A	CR-9	JK-418	CR-1A1	CR-1A	CR-3A	JK-234A	CR-5	JK-47	CR-10B	CR-10A	JK-16	CR-4C	CR-4A
Fácies	Bt Grd	Bt-Hbl Grd	Bt-Hbl MzG				Hbl-Bt MzG				H MzG	LMzG	Bt-Hbl GrD	Bt-Hbl MzG		Hbl-Bt Sg	H MzG	
Minerals (%)																		
Quartz	44.0	44.9	17.5	25.5	28.6	30.7	35.8	30.9	35.7	36.2	40.5	43.8	39.8	28.0	30.6	37.8	39.8	41.5
Plagioclase	29.1	36.7	38.0	36.5	29.1	32.9	21.8	30.3	24.8	25.7	22.6	25.2	33.3	34.8	35.0	16.7	26.8	38.3
Alcali feldspar	15.9	12.4	31.3	27.0	37.1	27.4	27.9	32.5	27.5	31.8	19.3	27.1	12.4	20.4	18.4	36.6	24.1	19.5
Biotite	9.7	1.6	2.5	0.7	0.9	3.6	7.5	3.3	5.5	2.1	2.1	2.7	4.9	2.4	1.3	4.9	8.9*	0.1
Hornblende	1.0	2.9	7.6	7.5	3.3	4.8	6.2	2.0	6.1	3.8	13.8	0.6	9.1	13.3	13.3	3.6	0.2	-
Ferromagnesian amphibole	-	-	1.5	0.3	-	-	-	-	-	-	-	-	-	-	-	-	-	-
Opaque	-	0.6	1.0	0.9	0.8	0.4	0.1	0.3	0.2	0.2	0.8	0.3	0.1	0.5	0.8	0.2	0.2	0.3
Titanite	-	0.4	0.1	-	0.0	-	x	0.2	-	-	0.4	-	0.1	-	0.2	-	-	-
Epidote	x	x	x	-	x	-	0.6	x	-	-	x	x	x	-	x	-	-	x
Alanite	0.1	-	0.2	1.3	0.2	0.1	0.1	0.3	0.2	-	0.1	0.2	-	-	0.1	0.1	x	0.4
Chlorite	-	0.5	-	-	0.1	-	-	-	-	-	0.3	-	-	0.4	-	-	0.1	-
Carbonate	-	-	-	-	-	-	-	-	-	-	-	-	-	-	-	-	-	-
Scapolite	-	-	-	0.3	-	-	-	0.1	-	x	-	-	-	-	-	-	-	-
Muscovite	-	-	-	-	-	-	-	-	-	-	-	-	-	0.1	-	-	-	-
Accessories (Ap+Zr)	0.2	0.1	0.3	0.2	0.1	0.1	x	0.3	0.1	0.2	0.1	0.1	0.3	0.2	0.4	0.1	x	x
Felsic minerals	89.0	94.0	86.9	89.0	94.7	91.0	85.6	93.7	88.0	93.7	82.4	96.1	85.5	83.2	84.0	91.1	90.6	99.2
Mafic minerals	11.0	6.0	13.1	11.0	5.3	9.0	14.4	6.3	12.0	6.3	17.6	3.9	14.5	16.8	16.0	8.9	9.4	0.8
To 100%																		
Quartz	49.7	48.6	20.7	28.8	30.4	33.8	41.9	33.0	40.6	38.6	49.4	45.6	46.6	33.9	36.6	41.5	43.9	43.6
k-feldspar	18.0	13.5	37.0	30.5	39.5	30.1	32.6	34.8	31.3	34.0	23.6	28.2	14.5	24.5	22.0	40.2	26.6	20.4
Plagioclase	32.3	37.9	42.3	40.7	30.1	36.1	25.5	32.2	28.1	27.4	27.1	26.2	39.0	41.7	41.4	18.3	29.5	35.9

Abbreviations: Hbl = hornblende; Bt = biotite; Ap = apatite; Zr = zircon; GrD = granodiorite; MzG = monzogranite; Sg= syenegranite; LMzG = leucomonzogranite and H = hydrothermalized

Acronym of the groups according to figure 2

x -present on the thin sections, but not detected in the count

(-) absent in thin sections

Note: Epidote present is secondary, accounted for as plagioclase

* Chloritized biotite

Supplementary Table 3. Electron microprobe analyses of pyroxene from the Igarapé Gelado suite.

Variety	PBHTnGd												
Sample		CAD-14			JK-60			CR-8A				CR-6A	
Analyses	C2_1-2	C2_1-5	C2_2-3	C2_1-1	C3_1-2	C3_1-4	C1_1-1	C1_2-1	C1_3-1	C4_1-1	C4_2-1	C4_2-2	C4_2-4
Type	Ferrosilite	Ferrosilite	Ferrosilite	Ferrosilite	Ferrosilite	Ferrosilite	Ferrosilite	Ferrosilite	Ferrosilite	Augite	Augite	Augite	Hedengerbite
SiO_2 (wt%)	48.01	47.46	47.67	49.17	48.72	48.69	48.30	48.13	48.20	51.44	51.65	51.70	51.59
TiO_2	0.06	0.09	0.11	0.07	0.09	0.07	0.09	0.10	0.09	0.11	0.09	0.04	0.04
Al_2O_3	0.20	0.43	0.50	0.42	0.47	0.47	0.48	0.46	0.45	0.79	0.82	0.76	0.61
FeO	42.70	43.39	42.65	38.11	39.49	38.99	40.80	41.14	40.91	18.59	17.59	17.19	17.21
MnO	0.46	0.45	0.47	0.40	0.44	0.40	0.35	0.37	0.38	0.24	0.22	0.24	0.30
MgO	7.44	6.88	7.46	10.97	9.89	10.12	8.69	8.63	8.72	8.02	7.90	8.19	7.83
CaO	0.40	0.62	0.69	0.58	0.68	0.45	0.63	0.64	0.61	18.97	19.9	19.96	21.01
Na_2O	0.00	0.01	0.02	0.02	0.02	0.02	0.02	0.01	0.02	0.35	0.38	0.33	0.36
K_2O	0.01	0.01	0.01	0.01	0.04	0.03	0.02	0.01	0.01	0.04	0.03	0.02	0.01
Number of cations on the basis of 6 oxygens													
Si	2.00	1.99	1.98	1.99	1.98	1.99	1.99	1.98	1.99	2.02	2.02	2.02	2.02
Al^{IV}	0.00	0.01	0.02	0.01	0.02	0.01	0.01	0.02	0.01	0.00	0.00	0.00	0.00
Sum T	2.00	2.00	2.00	2.00	2.00	2.00	2.00	2.00	2.00	2.02	2.02	2.02	2.02
Al^{VI}	0.01	0.01	0.01	0.01	0.01	0.01	0.01	0.01	0.01	0.04	0.04	0.03	0.03
Ti^{+3}	0.00	0.00	0.00	0.00	0.00	0.00	0.00	0.00	0.00	0.00	0.00	0.00	0.00
Mg	0.23	0.22	0.24	0.34	0.31	0.31	0.27	0.27	0.27	0.40	0.40	0.42	0.42
Fe^{+2}	0.75	0.77	0.76	0.65	0.69	0.67	0.71	0.72	0.72	0.52	0.50	0.49	0.52
M1 Sun	0.99	1.00	1.00	1.00	1.00	1.00	1.00	1.00	1.00	0.95	0.95	0.97	0.97
Mg	0.23	0.21	0.23	0.33	0.29	0.31	0.26	0.26	0.26	0.07	0.06	0.06	0.04
Fe^{+2}	0.74	0.75	0.72	0.63	0.66	0.66	0.69	0.70	0.69	0.09	0.07	0.07	0.05
Mn	0.02	0.02	0.02	0.01	0.02	0.01	0.01	0.01	0.01	0.01	0.01	0.01	0.01
Ca	0.02	0.03	0.03	0.03	0.03	0.02	0.03	0.03	0.03	0.80	0.84	0.84	0.88
Na	0.00	0.00	0.00	0.00	0.00	0.00	0.00	0.00	0.00	0.03	0.03	0.02	0.03
M2 Sun	1.00	1.00	1.00	1.00	1.00	1.00	1.00	1.00	1.00	1.00	1.00	1.00	1.00
Wo	1	1	2	1	1	1	1	1	1	42	45	45	46
En	23	22	23	33	30	31	27	27	27	25	25	25	24
Fs	76	77	75	65	68	68	71	72	71	33	31	30	30
X_{Mg}	0.24	0.22	0.24	0.34	0.31	0.32	0.28	0.27	0.28	0.43	0.44	0.46	0.45
X_{Al}	0.00	0.01	0.01	0.01	0.01	0.01	0.01	0.01	0.01	0.02	0.02	0.02	0.01
Fe/(Fe+Mg)	0.76	0.78	0.76	0.66	0.69	0.68	0.72	0.73	0.72	0.57	0.555	0.54	0.55

PBHTnGd = Px-Bt-Hbl Tonalite-Granodiorite.

Supplementary Table 4. Electron microprobe analyses of amphibole from the Igarapé Gelado suite.

Variety	PBHTnGd						BHTnGd						BHMzG						RBHMzG			
Sample	CR-8A		CR-6A		CAD-14		CAD-5		CG-75		CR-12A		CR-3A		CG-22A		CR-1A		JK-47		CR-10B	
Analyses	C1_3.3	C1_3-4	C2_1-2	C2_1-3	C7_1-6	C7_1-4	C2_4-1	C2_4-2	C2_3-2	C2_3-1	C3_1-2	C3_1-1	C2_1-6	C2_1-4	C2_1-3	C2_1-4	C2_1-2	C2_1-1	C1_1-6	C1_1-7	C1_2-2	C1_2-1
Type	KHs core	KHs rin	KHs core	KHs rin	KHs core	KHs core	KHs core	KHs rin	KHs core	KHs rin	KHs core	KHs rin	KHs core	KHs rin	KHs core	KHs rin	KHs core	KHs rin	KHs core	KHs rin	FeTsc core	KHs rin
SiO_2 (wt%)	38.61	38.24	39.62	39.90	36.90	36.04	36.67	37.86	39.82	40.41	38.45	38.11	39.27	35.88	38.67	39.86	37.61	36.86	38.75	38.65	40.13	39.14
TiO_2	1.88	1.70	1.90	2.00	1.39	0.84	0.01	1.27	1.65	1.49	1.47	1.25	1.34	0.41	0.73	0.65	0.35	0.04	0.17	0.18	0.04	0.42
Al_2O_3	10.61	11.33	10.03	10.27	11.07	11.95	13.30	11.60	10.59	10.72	10.94	11.29	10.60	11.04	12.07	11.26	11.73	13.19	11.27	11.30	9.69	11.37
Fe_2O_3	6.88	4.78	4.41	4.41	6.86	7.16	9.63	6.75	5.23	5.10	6.83	6.63	4.81	7.61	7.48	7.22	8.56	8.91	8.80	8.21	8.84	5.94
FeO	20.60	22.21	21.83	21.49	24.52	24.17	20.91	22.81	19.32	18.67	20.90	21.50	24.15	23.74	19.40	19.41	21.97	20.96	24.18	24.39	23.51	24.56
MnO	0.14	0.12	0.21	0.25	0.10	0.06	0.11	0.17	0.18	0.18	0.16	0.11	0.23	0.10	0.22	0.28	0.30	0.24	0.50	0.48	0.47	0.41
MgO	4.28	3.67	4.55	4.71	1.46	1.21	2.03	2.43	5.67	6.07	3.77	3.43	2.78	1.84	4.56	5.02	2.58	2.45	0.93	0.97	1.63	1.39
CaO	10.24	10.41	10.51	10.53	10.03	10.04	10.24	10.24	10.60	10.71	10.17	10.54	10.48	10.34	10.85	10.98	10.60	10.54	10.36	10.33	10.09	10.44
Na_2O	1.61	1.48	1.58	1.50	1.51	1.33	1.10	1.37	1.46	1.23	1.43	1.17	1.60	1.20	1.52	1.45	1.39	1.26	1.31	1.39	1.35	1.26
K_2O	1.93	2.23	1.91	1.94	2.27	2.67	2.38	2.16	1.90	1.98	2.04	2.06	1.79	2.99	1.65	1.53	2.03	2.21	1.53	1.57	1.21	1.50
F	0.19	0.00	0.00	0.00	0.00	0.00	0.00	0.00	0.11	0.09	0.00	0.00	0.00	0.00	0.07	0.07	0.00	0.00	0.00	0.00	0.00	0.00
Cl	2.15	2.37	1.81	1.81	3.06	3.85	2.12	2.36	1.82	1.74	2.27	2.07	1.08	4.55	0.52	0.40	1.67	1.62	0.31	0.28	0.25	0.31
H2O*	1.24	1.26	1.42	1.43	1.04	0.83	1.31	1.26	1.38	1.42	1.29	1.33	1.59	0.63	1.73	1.78	1.43	1.45	1.79	1.79	1.80	1.77
Subtotal:																						
O-F-Cl	0.57	0.53	0.41	0.41	0.69	0.87	0.48	0.53	0.45	0.43	0.51	0.47	0.24	1.03	0.15	0.12	0.38	0.36	0.07	0.06	0.06	0.07
Total	99.79	99.26	99.36	99.83	99.53	99.29	99.34	99.75	99.27	99.38	99.21	99.02	99.46	99.31	99.31	99.80	99.85	99.34	99.84	99.47	98.95	98.45
Number of cations on the basis of 23 oxygens																						
Si	6.16	6.17	6.33	6.32	6.08	5.99	5.94	6.12	6.30	6.34	6.19	6.15	6.31	6.01	6.11	6.24	6.06	5.95	6.23	6.24	6.46	6.34
Al^{IV}	1.84	1.83	1.67	1.68	1.92	2.01	2.06	1.88	1.70	1.66	1.81	1.85	1.69	1.99	1.89	1.76	1.94	2.05	1.77	1.76	1.54	1.66
Sum T	8.00	8.00	8.00	8.00	8.00	8.00	8.00	8.00	8.00	8.00	8.00	8.00	8.00	8.00	8.00	8.00	8.00	8.00	8.00	8.00	8.00	8.00
Al^{VI}	0.16	0.32	0.22	0.24	0.23	0.33	0.48	0.33	0.27	0.33	0.26	0.30	0.32	0.19	0.36	0.32	0.29	0.46	0.37	0.39	0.30	0.51
Ti^{+3}	0.23	0.21	0.23	0.24	0.17	0.10	0.00	0.15	0.20	0.18	0.18	0.15	0.16	0.05	0.09	0.08	0.04	0.00	0.02	0.02	0.00	0.05
Fe^{+3}	0.83	0.58	0.53	0.53	0.85	0.90	1.17	0.82	0.62	0.60	0.83	0.81	0.58	0.96	0.89	0.85	1.04	1.08	1.07	1.00	1.07	0.72
Fe^{+2}	2.75	3.00	2.91	2.85	3.38	3.36	2.83	3.08	2.55	2.45	2.81	2.90	3.24	3.33	2.56	2.54	2.96	2.83	3.25	3.29	3.17	3.33
Mn	0.02	0.02	0.03	0.03	0.01	0.01	0.02	0.02	0.02	0.02	0.02	0.01	0.03	0.01	0.03	0.04	0.04	0.03	0.07	0.07	0.06	0.06
Mg	1.02	0.88	1.08	1.11	0.36	0.30	0.49	0.59	1.34	1.42	0.90	0.82	0.67	0.46	1.07	1.17	0.62	0.59	0.22	0.23	0.39	0.34
Sum C	5.00	5.00	5.00	5.00	5.00	5.00	5.00	5.00	5.00	5.00	5.00	5.00	5.00	5.00	5.00	5.00	5.00	5.00	5.00	5.00	5.00	5.00
Ca	1.75	1.80	1.80	1.79	1.77	1.79	1.78	1.77	1.80	1.80	1.75	1.82	1.80	1.85	1.84	1.84	1.83	1.82	1.79	1.79	1.74	1.81
Na	0.25	0.20	0.20	0.21	0.23	0.21	0.22	0.23	0.20	0.20	0.25	0.18	0.20	0.15	0.16	0.16	0.17	0.18	0.21	0.21	0.26	0.19
Sum B	2.00	2.00	2.00	2.00	2.00	2.00	2.00	2.00	2.00	2.00	2.00	2.00	2.00	2.00	2.00	2.00	2.00	2.00	2.00	2.00	2.00	2.00
Na	0.25	0.26	0.28	0.25	0.25	0.22	0.13	0.20	0.24	0.18	0.20	0.19	0.30	0.24	0.30	0.28	0.27	0.22	0.19	0.22	0.16	0.21
K	0.39	0.46	0.39	0.39	0.48	0.57	0.49	0.44	0.38	0.40	0.42	0.42	0.37	0.64	0.33	0.31	0.42	0.46	0.31	0.32	0.25	0.31
Sum A	0.64	0.72	0.67	0.64	0.73	0.78	0.62	0.65	0.63	0.57	0.62	0.61	0.67	0.88	0.63	0.59	0.68	0.67	0.51	0.54	0.41	0.52
F	0.10	0.00	0.00	0.00	0.00	0.00	0.00	0.00	0.05	0.05	0.00	0.00	0.00	0.00	0.03	0.03	0.00	0.00	0.00	0.00	0.00	0.00
Cl	0.58	0.65	0.49	0.49	0.85	1.08	0.58	0.65	0.49	0.46	0.62	0.57	0.29	1.29	0.14	0.11	0.46	0.44	0.08	0.08	0.07	0.09
OH*	1.32	1.35	1.51	1.51	1.15	0.92	1.42	1.35	1.46	1.49	1.38	1.43	1.71	0.71	1.83	1.86	1.54	1.56	1.92	1.92	1.93	1.91
Al_{total}	2.06	2.04	1.90	1.91	2.10	2.11	2.06	2.04	1.90	1.83	1.99	2.00	1.85	2.04	1.98	1.83	1.98	2.05	1.79	1.78	1.54	1.71
Fe/(Fe+Mg)	0.73	0.77	0.73	0.72	0.90	0.92	0.85	0.84	0.66	0.63	0.76	0.78	0.83	0.88	0.70	0.68	0.83	0.83	0.94	0.93	0.89	0.91
Mg/(Mg+Fe)	0.27	0.23	0.27	0.28	0.10	0.08	0.15	0.16	0.34	0.37	0.24	0.22	0.17	0.12	0.30	0.32	0.17	0.17	0.06	0.07	0.11	0.09

PBHTnGd = Px-Bt-Hbl Tonalite-Granodiorite; BHTnGd = Bt-Hbl Tonalite-granodiorite; BHMzG = Bt-Hbl Monzogranite; RBHMzG = Reduced Bt-Hbl Monzogranite. Potassic prefix: $^{A}K > {}^{A}Na$, ^{A}ca; Ferro prefix: $^{C}Fe^{2+} > {}^{C}Mg$, $^{C}Mn^{2+}$ (Hawthorne et al., 2012)

Abbreviations: Fe= iron; K = potassian; Hs = hastingsite; Tsc = tschermakite

Supplementary Table 5. Electron microprobe analyses of biotite from the Igarapé Gelado suite.

Variety	PBHTnGd						BHTnGd						BHMzG						RBHMzG			
Sample	CAD-14	JK-60			CR-8A		CAD-5				CR-12A		JK-137A	CR-9	CR-3A			CR-1A	JK-47		CR-10B	
Analyses	C7_1-4	C2_1.1	C4_1-3	C4_2-1	C1_1-1	C1_6-1	C1_1-4	C1_1-5	C1_1-2	C3_1-4	C1_1-2	C1_1-3	C1_1-1	C1_1-4	C2_1-4	C2_1-5	C1_1-10	C2_1-1	C2_3-3	C2_2-1	C1_1-5	C1_1-6
SiO_2 (wt%)	33.69	34.21	35.04	34.86	35.32	35.29	34.47	34.47	34.85	34.88	34.46	34.20	33.68	34.43	34.44	33.22	34.54	33.91	33.07	33.57	33.74	33.18
TiO_2	3.07	4.13	4.15	4.27	4.47	4.61	3.06	2.72	3.17	3.01	2.65	2.63	3.45	3.07	2.80	3.08	4.44	1.92	3.45	3.88	4.78	4.26
Al_2O_3	12.39	13.07	13.15	13.03	13.01	13.00	14.30	14.13	14.23	14.36	14.56	15.08	14.36	14.78	14.28	13.63	13.38	14.39	14.85	14.43	14.04	13.82
FeO	34.54	29.59	26.83	27.60	26.54	26.17	28.65	29.16	28.74	28.64	28.33	28.20	31.16	31.51	29.25	32.24	29.97	30.62	34.19	33.52	32.09	33.06
MnO	0.00	0.06	0.03	0.06	0.04	0.05	0.08	0.12	0.12	0.10	0.06	0.10	0.19	0.22	0.15	0.07	0.06	0.18	0.22	0.24	0.19	0.10
MgO	2.63	4.99	6.74	6.33	6.68	6.56	5.24	5.06	4.88	5.38	5.60	5.41	3.06	3.28	4.97	4.42	4.46	4.76	1.30	1.24	1.64	1.58
CaO	0.02	0.00	0.01	0.00	0.00	0.00	0.01	0.00	0.02	0.00	0.00	0.00	0.00	0.00	0.03	0.02	0.15	0.02	0.02	0.05	0.03	0.06
Na_2O	0.04	0.07	0.10	0.10	0.07	0.13	0.10	0.08	0.05	0.12	0.13	0.08	0.15	0.03	0.13	0.03	0.12	0.08	0.05	0.16	0.04	0.12
K_2O	8.63	8.91	9.08	9.02	9.11	9.01	9.05	9.07	9.02	9.11	8.96	8.96	9.11	9.05	8.92	8.13	8.98	9.12	8.75	8.67	8.80	8.77
F	0.00	0.00	0.08	0.09	0.12	0.46	0.00	0.00	0.00	0.00	0.00	0.00	0.00	0.00	0.00	0.00	0.00	0.00	0.00	0.00	0.00	0.00
Cl	2.91	3.09	1.82	1.84	1.41	1.59	1.18	1.56	1.57	1.21	1.15	1.04	0.66	0.63	1.47	1.18	0.86	0.76	0.21	0.21	0.37	0.38
H_2O	2.86	2.91	3.26	3.24	3.36	3.14	3.42	3.31	3.33	3.44	3.43	3.46	3.50	3.57	3.34	3.35	3.52	3.48	3.60	3.61	3.58	3.53
Subtotal:	100.8	101.0	100.3	100.4	100.1	100.0	99.6	99.7	100.0	100.3	99.3	99.2	99.3	100.6	99.8	99.4	100.5	99.3	99.7	99.6	99.3	98.9
O-F-Cl	0.66	0.70	0.44	0.45	0.37	0.55	0.27	0.35	0.35	0.27	0.26	0.23	0.15	0.14	0.33	0.27	0.19	0.17	0.05	0.05	0.08	0.09
Total	100.1	100.3	99.8	100.0	99.8	99.5	99.3	99.3	99.6	100.0	99.1	98.9	99.2	100.4	99.4	99.1	100.3	99.1	99.6	99.5	99.2	98.8
Number of cations on the basis of 22 oxygens																						
Si	5.60	5.55	5.59	5.57	5.61	5.62	5.55	5.58	5.60	5.57	5.55	5.51	5.50	5.54	5.56	5.45	5.54	5.53	5.43	5.50	5.51	5.49
Al^{IV}	2.40	2.45	2.41	2.43	2.39	2.38	2.45	2.42	2.40	2.43	2.45	2.49	2.50	2.46	2.44	2.55	2.46	2.47	2.57	2.50	2.49	2.51
Al^{VI}	0.03	0.04	0.06	0.03	0.05	0.06	0.27	0.28	0.30	0.28	0.32	0.37	0.27	0.34	0.28	0.09	0.07	0.29	0.31	0.28	0.22	0.18
Ti	0.38	0.50	0.50	0.51	0.53	0.55	0.37	0.33	0.38	0.36	0.32	0.32	0.42	0.37	0.34	0.38	0.54	0.24	0.43	0.48	0.59	0.53
Fe	4.81	4.01	3.58	3.69	3.53	3.49	3.86	3.95	3.86	3.83	3.82	3.80	4.26	4.24	3.95	4.43	4.02	4.17	4.70	4.59	4.39	4.57
Mn	0.00	0.01	0.00	0.01	0.00	0.01	0.01	0.02	0.02	0.01	0.01	0.01	0.03	0.03	0.02	0.01	0.01	0.03	0.03	0.03	0.03	0.01
Mg	0.65	1.21	1.60	1.51	1.58	1.56	1.26	1.22	1.17	1.28	1.34	1.30	0.75	0.79	1.20	1.08	1.07	1.16	0.32	0.30	0.40	0.39
Ca	0.00	0.00	0.00	0.00	0.00	0.00	0.00	0.00	0.00	0.00	0.00	0.00	0.00	0.00	0.01	0.00	0.03	0.00	0.00	0.01	0.00	0.01
Na	0.01	0.02	0.03	0.03	0.02	0.04	0.03	0.03	0.02	0.04	0.04	0.02	0.05	0.01	0.04	0.01	0.04	0.03	0.02	0.05	0.01	0.04
K	1.83	1.84	1.85	1.84	1.85	1.83	1.86	1.87	1.85	1.86	1.84	1.84	1.90	1.86	1.84	1.70	1.84	1.90	1.83	1.81	1.83	1.85
OH*	3.18	3.15	3.47	3.46	3.56	3.34	3.68	3.57	3.57	3.67	3.69	3.72	3.82	3.83	3.60	3.67	3.77	3.79	3.94	3.94	3.90	3.89
F	0.00	0.00	0.04	0.04	0.06	0.23	0.00	0.00	0.00	0.00	0.00	0.00	0.00	0.00	0.00	0.00	0.00	0.00	0.00	0.00	0.00	0.00
Cl	0.82	0.85	0.49	0.50	0.38	0.43	0.32	0.43	0.43	0.33	0.31	0.28	0.18	0.17	0.40	0.33	0.23	0.21	0.06	0.06	0.10	0.11
Al_{Total}	2.43	2.50	2.47	2.46	2.44	2.44	2.72	2.70	2.70	2.71	2.76	2.86	2.76	2.80	2.72	2.64	2.53	2.77	2.87	2.79	2.70	2.69
Fe/Fe+Mg	0.88	0.77	0.69	0.71	0.69	0.69	0.75	0.76	0.77	0.75	0.74	0.75	0.85	0.84	0.77	0.80	0.79	0.78	0.94	0.94	0.92	0.92

PBHTnGd = Px-Bt-Hbl Tonalite-Granodiorite; BHTnGd = Bt-Hbl Tonalite-granodiorite; BHMzG = Bt-Hbl Monzogranite; RBHMzG = Reduced Bt-Hbl Monzogranite.

Supplementary Table 6. Electron microprobe analyses of plagioclase from the Igarapé Gelado suite.

Variety	PBHTnGd						BHTnGd			RBHMzG		
Sample	JK-60			CAD-14			CAD-6B			JK-47		
Analyses	C1_1-1	C1_1-2	C1_1-3	C6_1-2	C6_1-3	C6_1-6	C1_1-1	C1_1-3	C1_1-7	C3_1-1	C3_2-1	C3_6-1
SiO_2 (wt%)	62.58	62.80	62.50	62.51	61.77	62.03	62.32	62.91	62.34	63.08	63.91	62.22
TiO_2	0.00	0.01	0.00	0.02	0.03	0.02	0.00	0.01	0.01	0.03	0.01	0.00
Al_2O_3	23.67	23.63	23.63	23.85	24.13	24.00	23.65	23.48	23.50	22.95	22.69	23.39
FeO	0.12	0.08	0.03	0.04	0.05	0.03	0.06	0.01	0.05	0.05	0.03	0.01
MnO	0.00	0.00	0.00	0.01	0.00	0.00	0.02	0.00	0.00	0.00	0.00	0.00
MgO	0.01	0.01	0.00	0.00	0.00	0.00	0.00	0.00	0.01	0.00	0.00	0.00
CaO	4.60	4.42	4.58	4.72	5.00	4.83	4.73	4.45	4.66	3.79	3.46	4.27
Na_2O	8.90	8.93	8.93	8.81	8.58	8.61	8.72	8.96	8.75	9.29	9.63	8.97
K_2O	0.20	0.24	0.21	0.30	0.24	0.30	0.25	0.24	0.22	0.16	0.15	0.18
Total	100.06	100.12	99.87	100.26	99.80	99.82	99.76	100.05	99.55	99.35	99.87	99.05
Number of cations on the basis of 8 oxygens												
Si	2.77	2.78	2.77	2.76	2.74	2.75	2.77	2.78	2.77	2.80	2.82	2.78
Al	1.23	1.23	1.23	1.24	1.26	1.26	1.24	1.22	1.23	1.20	1.18	1.23
Fe	0.00	0.00	0.00	0.00	0.00	0.00	0.00	0.00	0.00	0.00	0.00	0.00
Ca	0.22	0.21	0.22	0.22	0.24	0.23	0.23	0.21	0.22	0.18	0.16	0.20
Na	0.76	0.77	0.77	0.76	0.74	0.74	0.75	0.77	0.75	0.80	0.82	0.78
K	0.01	0.01	0.01	0.02	0.01	0.02	0.01	0.01	0.01	0.01	0.01	0.01
Ab	76.94	77.43	77.00	75.85	74.58	75.00	75.82	77.41	76.26	80.86	82.73	78.38
An	21.95	21.18	21.83	22.44	24.03	23.27	22.75	21.24	22.46	18.21	16.45	20.62
Or	1.11	1.39	1.18	1.72	1.40	1.73	1.42	1.35	1.28	0.93	0.82	1.01

PBHTnGd = Px-Bt-Hbl Tonalite-Granodiorite; BHTnGd = Bt-Hbl Tonalite-granodiorite; RBHMzG = Reduced Bt-Hbl Monzogranite.

Supplementary Table 7. Chemical compositions of samples from the Igarapé Gelado suite utilized in the thermodynamic modeling.

JK-60 – Opx-Hbl-Bt Tonalito (PBHTnGd)			
	1%H_2O	4%H_2O	5%H_2O
SiO_2(wt. %)	66.4	64.5	63.8
TiO_2	0.6	0.6	0.6
Al_2O_3	15.6	15.2	15.0
FeO	5.2	5.0	5.0
MnO	0.0	0.0	0.0
MgO	0.9	0.9	0.9
CaO	3.6	3.5	3.5
Na_2O	4.8	4.7	4.6
K_2O	1.8	1.8	1.8
H_2O	1.0	4.0	5.0

JK-47 – Bt-Hbl monzogranite (RBHMzG)			
	1%H_2O	4%H_2O	7%H_2O
SiO_2(wt. %)	72.1	70.0	68.0
TiO_2	0.4	0.3	0.3
Al_2O_3	12.9	12.5	12.1
FeO	4.3	4.2	4.1
MnO	0.0	0.0	0.0
MgO	0.1	0.1	0.1
CaO	2.1	2.0	2.0
Na_2O	3.3	3.2	3.1
K_2O	3.8	3.7	3.6
H_2O	1	4	7

Values recalculated to 100% based on initial water content

All iron reported as FeO

Supplementary Table 8. P_2O_5 and Zr compositions of varieties from the Igarapé Gelado suite. PBHTnGd = Px-Bt-Hbl Tonalite-Granodiorite; BHTnGd = Bt-Hbl Tonalite-granodiorite; BHMzG = Bt-Hbl Monzogranite; RBHMzG = Reduced Bt-Hbl Monzogranite. * Hydrotermalized rocks

Variety	Sample	P_2O_5	Zr
PBHTnGd	CAD-4	0.18	389
	JK-60	0.17	431
	CR-6A	0.24	290
	CAD-14	0.11	309
	CR-7D	0.13	330
	CAD-17	0.51	204
	CR-8A	0.13	357
BHTnGd	JK-61	0.15	474
	CR-7B	0.14	425
	JK-86*	0.11	285
	JK-59	0.17	437
	CG-75	0.18	382
	CAD-16A	0.11	339
	CR-7A	0.07	292
	CR-12A	0.1	285
	CAD-5	0.11	323
	JK-139A	0.09	513
	CAD-3	0.1	365
	JK-446	0.09	241
	CAD-6B	0.1	160
	JK-372*	0.01	800
BHMzG	CR-3B	0.08	422
	CR-01A	0.06	205
	JK-137A	0.07	331
	CR-3A	0.06	317
	JK-418	0.09	348
	CG-22A	0.06	164
	CR-9	0.06	195
	CR-05	0.01	51
	CR-1A1	0.05	186
RBHMzG	CR-10B	0.12	846
	JK-47	0.07	760
	JK-16	0.03	285
	CR-4C*	0.02	23

CAPÍTULO 3: PETROGENESIS, U-Pb SHRIMP GEOCHRONOLOGY, AND ZIRCON COMPOSITION OF NEOARCHEAN GRANITOIDS OF THE IGARAPÉ GELADO SUITE, CARAJÁS PROVINCE, AMAZONIAN CRATON.

Autores:

Caio José Soares Mesquita
Roberto Dall'Agnol
Maurício Liska Borba
Colombo Celso Gaeta Tassinari
Marco Antonio Galarza
Elton Luiz Dantas
Arthur Santos da Silva Neri
José de Arimatéia Costa de Almeida
Junny Kyley Mastop de Oliveira

Submetido a: *Geoscience Frontiers* – Qualis CAPES-A1

Dear Ms Caio José Soares Mesquita,

We have received your article "PETROGENESIS, U-Pb SHRIMP GEOCHRONOLOGY, AND ZIRCON COMPOSITION OF NEOARCHEAN GRANITOIDS OF THE IGARAPÉ GELADO SUITE, CARAJÁS PROVINCE, AMAZONIAN CRATON" for consideration for publication in Geoscience Frontiers.

Your manuscript will be given a reference number once an editor has been assigned.

To track the status of your paper, please do the following:

1. Go to this URL: https://www.editorialmanager.com/gsf/

2. Enter these login details:
Your username is: Caio José Soares Mesquita

If you need to retrieve password details please go to: http://ees.elsevier.com/gsf/automail_query.asp

3. Click [Author Login]
This takes you to the Author Main Menu.

4. Click [Submissions Being Processed]

Thank you for submitting your work to this journal.

Kind regards,

Editorial Manager
Geoscience Frontiers

Devido aos direitos autorais de *Geoscience Frontiers,* a formatação, citações e referências bibliográficas do capítulo 3 seguem o padrão requerido pela revista.

Petrogenesis, U-Pb SHRIMP geochronology, and zircon composition of neoarchean granitoids of the Igarapé Gelado suite, Carajás province, Amazonian craton

Caio José Soares Mesquita[a,b],
Roberto Dall'Agnol[b,c],
Maurício Liska Borba[d,g]
Colombo Celso Gaeta Tassinari[d]
Marco Antonio Galarza [a,e]
Elton Luiz Dantas[f]
Arthur Santos da Silva Neri[a,b],
José de Arimatéia Costa de Almeida[a,b],
Junny Kyley Mastop de Oliveira[h]

a-Post-Graduate Program in Geology and Geochemistry (PPGG), Institute of Geosciences (IG), Federal University of Pará (UFPA), Post office 8608, CEP-66075-110 Bélém, PA, Brazil. E-mails: caiojsm@gmail.com, arthur.santos.silva@ig.ufpa.br, ari@ufpa.br,
b-Group of Research on Granitoid Petrology (GRGP), IG, UFPA, Brazil.
c-Vale Institute of Technology, Post office 955, CEP- 66055-090, Belém, PA, Brazil. Email: robdal@ufpa.br
d-Institute of Geosciences, University of São Paulo (USP), CEP- 05508-080, São Paulo, Brazil. E-mails: mauriciolborba@usp.br, ccgtassi@usp.br
e-Isotopic Geology Laboratory, IG, UFPA, Belém, PA, Brazil. E-mail: antogt@ufpa.br
f-Geoscience Institute, University of Brasília, Post office 04465, CEP 70919-970 – Brasília, DF, Brazil. E-mail: elton@unb.br
g-Geological Survey of Brazil, Post office 55, CEP-01304-010, São Paulo, SP, Brazil.
h-Geological Survey of Brazil, Post office, 346, CEP-66095-904, Belém, PA, Brazil. E-mail: junny.oliveira@cprm.gov.br

ABSTRACT

The Igarapé Gelado suite (IGS) comprises four petrographic varieties: biotite-amphibole tonalites to granodiorites with pyroxenes (PBHTnGd) or devoid of pyroxenes (BHTnGd); and biotite-amphibole monzogranites (BHMzG), which have associated a markedly reduced variety (RBHMzG). The rocks from IGS are ferroan, reduced to oxidized A-type-like granites, akin of other Neoarchean granite suites from the Carajás Province. A crystallization concordia age of ~2.68 Ga was obtained by U-Pb SHRIMP in zircon for the RBHMzG variety, and similar upper intercept ages were furnished by the other IGS varieties, except for ages of ~2.5 Ga that resemble the ages of the IOCG Salobo deposits associated with reactivation of the Cinzento Lineament. The IGS ages are younger than the 2.75-2.73 Ga ages attributed to Neoarchean granites from Carajás The IGS displays negative to slightly positive values of $\varepsilon_{Nd}(t)_{(-2.86\ to\ 0.18)}$ and $\varepsilon_{Hf}(t)_{(-3.3\ to\ 0.1)}$, and Paleoarchean to Mesoarchean T_{DM} ages [Nd-$T_{DM(2.98-2.84)}$ and Hf-$T_{DM}^{C}{}_{(3.27-3.12)}$]. The positive values of $\varepsilon_{Nd}(t)$ and $\varepsilon_{Hf}(t)$ for the RBHMzG variety, suggest possible juvenile contribution or contamination in the source of its magma. The IGS rocks come from the melting of contaminated mafic granulite at:19%-PBHTnGd; 14%-BHTnGd; and from the tholeiitic mafic granulite at 9%-BHMzG and 7%-RBHMzG. The area of occurrence of the IGS is marked by hydrothermalism and mineralizations that locally modified the composition of rocks and minerals, allowing the leaching of REE and Y that

induced the classification of some BHMzG as (false) A1-subtype granites. In addition, these processes were responsible for zircon metamictization, which resulted in grains showing massive textures, enrichment of U, Th, and LREE and allowed the generation of upper intercept U-Pb ages, except for the crystals of the RBHMzG variety that preserved primary characteristics and presented concordia Ages. This study reinforces the presence of associated granites and pyroxene-bearing (charnockitic) rocks in the Neoarchean suites of Carajás, demonstrates that the ages of the mentioned suites are not entirely coincident, and help to clarify the petrogenetic processes of origin of A-type-like Neoarchean granitoids.

Keywords: Geochronology, Geochemistry, Isotopes, Zircon, Carajás province, Amazonian craton, Archean

1 INTRODUCTION

The petrology and geochemistry of granitoid associations study provides insights into the crustal evolution. Their geochemical signatures can indicate different formation processes magma sources (Chappell and White, 1992; King et al., 1997; Frost et al., 2001; Dall'Agnol et al., 2005; Laurent et al., 2014; Moyen and Laurent, 2018) and tectonic setting (Pearce et al., 1984; Pearce, 1996; Moyen et al., 2016; Whalen and Hildebrand, 2019). At the end of Archean (3.0-2.5 billion years ago), notable shifts occurred in the continental crust differentiation processes in the Earth's geodynamics, potentially linked to changes in tectonic style (Laurent et al., 2014; Moyen and Laurent, 2018). These changes persisted into the early Paleoproterozoic, contributing to the diversification of granitoid magmatism. This resulted in the widespread occurrence of progressively richer K-bearing rocks that, in the transition of Mesoarchean to Neoarchean, led to the origin of the distinctive Mg-rich sanukitoid suites (Halla et al., 2009; Heilimo et al., 2010; Oliveira et al., 2011; Ribeiro-Silva et al., 2023), as well as leucogranodioritic to leucogranitic suites of a calc-alkaline character (Almeida et al., 2013; Dey et al., 2012; Feio et al., 2013; Feio and Dall'Agnol, 2012; Jayananda et al., 2020, 2006; Joshi et al., 2022; Kaur et al., 2019; Leite-Santos and Oliveira, 2016) or even suites with ferroan (A-type) affinities (Barros et al., 2009; Cunha et al., 2016; Dall'Agnol et al., 2017; Feio and Dall'Agnol, 2012; Marangoanha et al., 2020; Silva et al., 2020; Topno et al., 2018).

During the late Mesoarchean and Neoarchean in the Carajás province, there was a transition from vertical tectonics, with a concentration on the development of domes and keels (Leite et al., 2004: Clos et al., 2019; Costa et al., 2020; Nebel et al., 2018; Zibra et al., 2020) to dominant horizontal tectonics, involving collision between lithospheric plates and subduction (Brown et al., 2020; Dhuime et al., 2015, 2012; Laurent et al., 2014; Moyen et al., 2016; Ribeiro-Silva et al., 2023; Tang et al., 2016). In the Amazonian craton, these processes

are well documented in the Carajás province (CP), the craton's oldest portion (Almeida et al., 2013; Oliveira et al., 2011; Ribeiro-Silva et al., 2023).

The central and northern parts of the CP show intense Neoarchean magmatism formed by syntectonic granites that intrude the Mesoarchean units. The Neoarchean magmatism is represented mainly by granites from the Planalto supersuite and charnockites from the Pium suite (Barros et al., 2009; Cunha et al., 2016; Dall'Agnol et al., 2017; Feio et al., 2013, 2012; Felix et al., 2020; Huhn et al., 1999; Marangoanha et al., 2019a; Oliveira et al., 2018a; Sardinha et al., 2006; Silva et al., 2020, 2025; Sousa et al., 2022).

The Igarapé Gelado suite (IGS) is a body with batholitic dimensions and is intrusive in banded iron formations and metabasic rocks from the Itacaiúnas supergroup (Fig. 1c). It is located near the northern border from the Carajás Basin, almost on the CP border with the Bacajá domain, (Barros et al., 2009) along the Cinzento shear zone. Prior geology, petrography, geochemistry, mineral chemistry, and geochronology studies conducted on this granite permitted the preliminary characterization of the magmatism and the definition of its Neoarchean age (Barros et al., 2009; Melo et al., 2016; Mesquita et al., 2025; Tavares et al., 2021; Toledo et al., 2023). Our study focused on the central-eastern sector of the IGS and its geology and geochemistry are discussed, integrated with analyses of zircon, including U-Pb geochronology, REE data and Lu-Hf isotopes, and whole-rock Sm-Nd isotopes. The obtained results allowed the determination of new crystallization ages for the IGS, the comprehension of the processes involved in its magmatic evolution, the identification of the source(s) of its magma(s), and the assessment of its tectonic setting. Furthermore, the study evaluates the impact of recurrent hydrothermal events in the region on the zircon stability. The acquired data allowed comparisons with other Neoarchean granites from Carajás and Kaapvaal Craton, thereby contributing to the comprehension of Neoarchean magmatism, particularly of the granites akin to A-type granites.

2 GEOLOGICAL SETTING

The CP is situated in the southeastern region of the Central Amazonian geochronological province and represents the oldest Archean nuclei within the Amazonian craton (AC) (Tassinari and Macambira, 2004) Fig. 1a). Following the AC tectonic compartmentalization models, the CP was formed and tectonically stabilized during the Archean (Santos et al., 2006; Tassinari and Macambira, 2004). The CP is subdivided into two domains (Fig. 1b), Rio Maria (RMD) to the south and Carajás (CD) to the north (Santos, 2003; Vasquez and Rosa-Costa, 2008). (i) The Mesoarchean RMD is a preserved granite-

greenstone terrane (3.05–2.86 Ga; Almeida et al., 2011, 2013; Macambira and Lancelot, 1996; Souza et al., 2001). (ii) The CD has Mesoarchean to Neoarchean age (3.07–2.70 Ga; Avelar et al., 1999; Feio et al., 2013; Machado et al., 1991; Marangoanha et al., 2019a; Pidgeon et al., 2000; Silva et al., 2020; Tavares et al., 2018) and a complex geological evolution, being divided into the Sapucaia and Canaã dos Carajás terranes, as well as the Carajás basin (Dall'Agnol et al., 2013; Oliveira et al., 2023). The Mesoarchean and Neoarchean supracrustal units from the Carajás domain are intruded by Neoarchean syntectonic granitoids (Fig. 1b; Barros et al., 2009; Cunha et al., 2016; Dall'Agnol et al., 2017; Feio et al., 2012; Marangoanha et al., 2019a; Melo et al., 2016; Silva et al., 2020; Sousa et al., 2022;) and anorogenic Paleoproterozoic (Dall'Agnol et al., 2005; Teixeira et al., 2019; Teruiya et al., 2008).

2.1 NEOARCHEAN MAGMATISM FROM CARAJÁS PROVINCE

Neoarchean magmatism from the CP (~2.75 – 2.55 Ga) is represented by: (i) Granites with affinities to A-type granites and variable degrees of oxidation from Planalto supersuite (Planalto, Vila União, Vila Jussara, and Igarapé Gelado suites; Estrela complex; Serra do Rabo granite, Barros et al., 2009; Cunha et al., 2016; Dall'Agnol et al., 2017; Feio et al., 2012, 2013; Marangoanha et al., 2019a, 2020; Oliveira et al., 2018a; Sardinha et al., 2006; Silva et al., 2020; Sousa et al., 2022; Tavares et al., 2021; Toledo et al., 2023; Oliveira et al., 2023) associated to sodic rocks with tholeiitic signature from Pedra Branca trondhjemite (Feio et al., 2013; Santos-Silva et al., 2020; Sardinha et al., 2004); (ii) Peralkaline to metaluminous granites (Velho Salobo, Itacaiúnas e GT-46 (Diniz et al., 2023; Machado et al., 1991; Melo et al., 2016; Souza et al., 1996; Toledo et al., 2019); (iii) Calc-alkaline potassium magmatism from Canaã dos Carajás suite (Velha Canada granite; Leite-Santos et al., 2010; Leite-Santos and Oliveira, 2016); (iv) Pium suite from charnockitic magmatism (Rio Seco charnockite; Felix et al., 2020; Café enderbite; Marangoanha et al., 2019b; Pium Diopside-Norite; Santos et al. 2013, Feio et al. 2012; (v); and (vi) undifferentiated Neoarchean granites (Plaquê suite; Araújo et al., 1988; Avelar et al., 1999; Jorge João and Araújo, 1992). The geochronological data for the Neoarchean magmatism from CP are summarized on supplementary table 1.

In the area of occurrence of the IGS, Neoarchean granites geochemically related to A-type granites, are emplaced along an anastomosing network of high-strain shear zones (SZ), concordant with the dominant WNW-ESE to E–W regional trend (Cinzento lineament, Pinheiro and Holdsworth, 2000) (Fig. 1c). The prevailing hypothesis suggests that Neoarchean granite magmas originated from partial melting of enriched granulitic crust with

varying oxidation levels (Barros et al., 2009; Dall'Agnol et al., 2017; Feio and Dall'Agnol, 2012). This granulitic crust may have formed due to the collision between the RMD and the northern part of the CP during the Mesoarchean (~2.85 Ga.; Sardinha et al., 2006; Tavares et al., 2018). Subsequently, Neoarchean granites were formed in a syntectonic environment and were deformed during magma emplacement and cooling that were coeval with the closure of the Carajás Basin (Barros et al., 2009; Silva et al., 2020). A second hypothesis admits that these granites originated from intrusions in an extensional environment and were later deformed and metamorphosed during the closure of the Carajás basin around 2.65 Ga (Tavares, 2015). Overimposed tectono-thermal events may have affected the rocks north of the Carajás Basin. In this context, the ~2.5 Ga ages obtained in the IGS, corresponding to the IOCG Salobo deposit, may be related to the reactivation of the Cinzento lineament (2.5 Ga), which may have induced the opening of the U-Pb system in zircon crystals (Melo et al., 2016; Toledo et al., 2023, 2019).

2.2 GEOLOGICAL ASPECTS OF IGARAPÉ GELADO SUITE

The granitoids of the central-eastern portion of the IGS form coalescent plutons that are limited by shear zones (SZ) and are intrusive in metavolcanic-sedimentary sequences from the Itacaiúnas Supergroup (Fig. 1c, Barros et al., 2009). The IGS rocks exhibit incipient to strong penetrative foliation (Fig. 2a), commonly with high-angle dips (50° to 85°, locally subhorizontal; Fig. 2b) dipping towards the south and north. The foliation is marked by alternated mafic-enriched and quartz-feldspar bands (Fig. 2b and 3h). It is sometimes highlighted by concordant granitic/quartz veins, but there is a predominance of discordant pegmatitic and felsic or mafic veins (Fig. 2c). The deformation is moderate to strong and controlled by the greater or lesser proximity of SZ, being more marked at the borders of the body or, in its interior, close to the contact zones between different rock varieties. Generally, the pyroxene-bearing rocks variety shows less deformational features compared to the other ones. The shear bands are centimetric to metric, formed by mylonites to ultramylonites (Fig. 2d). Radar images suggest that SZ are sinistral (Oliveira et al., 2018b).

Local field features include: millimetric brittle-ductile shear band crosscutting the foliation (Fig. 2e); rocks of the BHMzG variety with distinct granulation and content of mafic minerals interspersed laterally and parallel to the direction of the regional trend (Fig. 2f); injections of Bt-Opx-Hbl MzG in Bt-Opx-Hbl Tnl, with abrupt contact between them, both belonging to the PBHTnGd variety (Fig. 2g); mingling relationships between the Bt-Hbl Mzg and Bt-Hbl Tnl facies of the BHTnGd variety (Fig. 2h).

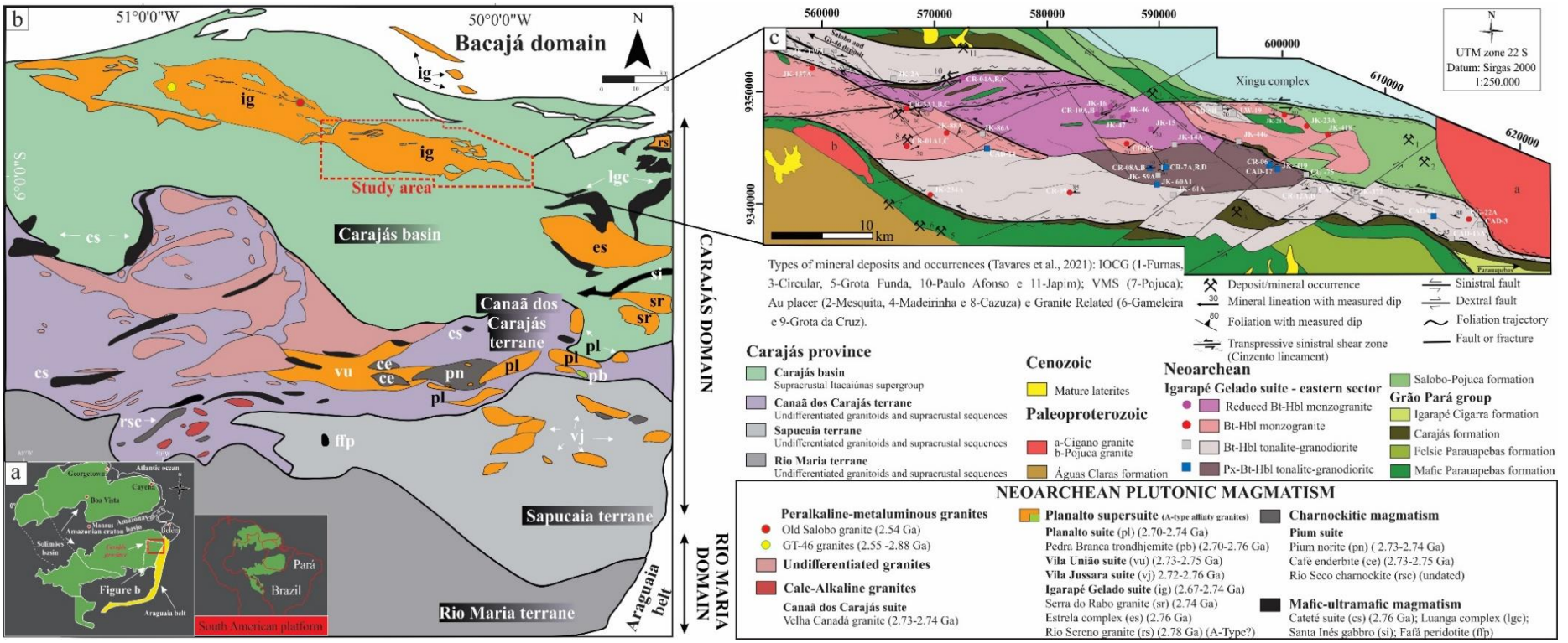

Figure 1 – a) Location map of the Amazonian Craton with emphasis on Carajás Province (PC); b) Simplified geological map of the CP with emphasis on Neoarchean plutonic rocks; c) Geological map of the central-eastern portion of the Igarapé Gelado batholith. Geologic map of adjacent units and structural features based on Oliveira et al. (2018b, modified) and Mesquita et al. (2025, Modified)

3 METHODS

3.1 PETROGRAPHY

The petrographic study involved mesoscopic and microscopic analyses combined with the definition of modal composition in thin sections of 51 samples (Table S2). Endeeper Hardledge software was employed for modal analyses with a grid of ~2000 points per sample at a spacing of 0.4mm. The four rock varieties of the IGS were classified following Le Maitre et al. (2020). A detailed reconnaissance of the deformational microstructures was performed by Passchier and Trouw (2005) and Vernon (2005).

3.2 WHOLE-ROCK GEOCHEMISTRY

Seven samples of the PBHTnGd variety, fourteen of BHTnGd, nine of BHMzG, and four of RBHMzG were selected for whole rock analyses (Table S3), summarizing thirty-four samples of the IGS. Initially, 0.5 to 5 kg were crushed and quartered using jaw crushers, ring and disc mills, and, finally, pulverized in an agate swing mill to a particle size <10 μm. All these procedures were carried out at the Institute of Geosciences of Federal University of Pará (Brazil).

The analyses were conducted in the ALS company laboratories. ICP-AES was used to detect major and minor elements, and ICP-MS was used to detect trace elements (including REE). More information about analytical methods can be found at www.alsglobal.com. The geochemical variation diagrams were generated using the free software GCDkit 6.1 (Janoušek et al., 2006). The obtained datasets are available in supplementary table 3.

3.3 GEOCHEMICAL MODELING

Geochemical modeling was initially carried out based on the mass balance of major elements to investigate the source and processes that formed the magmas that originated the IGS varieties (GENESIS 4.0 , Teixeira, 2005). This method adjusts the relative proportions of residual minerals from the source to achieve the desired liquid composition. The calculated data is reliable if the sum of the squared residuals ($\sum R^2$) is ≤1.2 (Wyers and Barton, 1986). In a second step, the obtained results were tested by trace element modeling using the partial melt equation in equilibrium, $C_L/C_0 = 1/F+D-FD$ (Willson, 1989), where C_L and C_0 represent, respectively, the concentrations of the trace elements in the magma and source, F is the percentage of formed magma, and D corresponds to the coefficient of distribution for the residual solid at the time when the magma is removed from the system. The mineral/liquid partition coefficients used here were extracted from Rolisson and Pease (2021) and https://kdd.earthref.org/KdD.

3.4 ZIRCON U–Pb–DATING

Zircon grains of ten representative samples of the IGS varieties were selected for geochronological analyses (3 samples of PBHTnGd, 1 of BHTnGd, 4 of BHMzG, and 2 of RBHMzG). These grains were separated at the Isotopic Geology Laboratory, Institute of Geosciences (IG) of the Federal University of Pará (UFPA). About 10 kg of rock were crushed, ground, and sieved into 250, 175, 125, and 75 μm fractions. These were processed using an isodynamic magnetic separator, and zircon grains were handpicked under a magnifying glass. Scanning Electron Microscope (SEM) with cathodoluminescence (CL) and backscattered electron (BSE) images were obtained to examine the zircon crystals' texture internal structures, overgrowths, fractures, and inclusions. U-Pb analyses were performed with a SHRIMP IIe at the High-Resolution Geochronology Laboratory, Institute of Geosciences, University of São Paulo. Subsequently, the images were interpolated using Adobe Photoshop 20.0 for a joint analysis of the information the two methods (Cl and BSE) provide. The SHRIMP analytical procedures follow the guidelines laid out by Stern (1998), Williams (1997), and Sato et al. (2014). The U standard reference composition used was SL 13 (238 ppm; Sato et al., 2014), and the zircon standard was TEMORA-2 (416.78±0.33 Ma; Black et al., 2004), analyzed at a 5:1 interval with a spot size of 30 μm. Data were processed using SQUID 2 software (Ludwig, 2009), and ages were calculated with the Isoplot 4.15 program (Ludwig, 2008). Isotopic ratio errors are reported at 1σ (%), while Age (1σ, absolute) and age ellipse errors are calculated at 2σ (diagrams Concordia). Zircon grains for age calculations were selected based on three criteria: (a) common lead contents (^{204}Pb), excluding ^{204}Pb/^{206}Pb ratios > 0.0004; (b) precision, excluding isotopic ratios with errors > 3.0%; and (c) minimal discordance, aiming for values ~0.

3.5 ZIRCON Lu-Hf ISOTOPE DATA

For the LA-MC-ICP-MS in situ zircon Lu-Hf analyses, twenty zircon grains from the JK-47 and CR 10B samples of RBHMzG, which had previously shown concordant U-Pb SHRIMP ages, were selected (Table S4). Analyses were conducted using a high-resolution multi-collector Neptune Thermo Finnigan mass spectrometer and a Nd:YAG LSX-213 G2 CETAC laser microprobe at the Isotope Geology Laboratory, IG – UFPA, Brazil. Milhomem Neto and Lafon (2019) provide detailed collector configuration and operational parameters. The Mud Tank zircon (732 ± 1 Ma; Black and Gulson, 1978) and GJ-1 zircon (608.5 ± 1.5 Ma; Jackson et al., 2004) were used as reference materials for the ^{176}Hf/^{177}Hf ratio that was analyzed at 3:1 interval, alternating patterns. To correct for the isobaric interferences of the

^{176}Lu and ^{176}Yb isotopes, the isotopes of Lu, Hf, and Yb were measured simultaneously for 60 seconds, based on the isotopic ratios ^{173}Yb/^{171}Yb, ^{179}Hf/^{177}Hf, ^{175}Lu/^{177}Hf, and ^{176}Hf/^{177}Hf (50 μm spot size). Isobaric interferences of ^{176}Lu and ^{176}Yb were corrected using a mass fractionation factor (β) for Lu and Yb, along with the signals from the interference-free isotopes ^{175}Lu and ^{173}Yb. These signals were normalized based on their isotopic abundances, specifically ^{176}Lu/^{175}Lu = 0.026549 (Chu et al., 2002) and ^{176}Yb/^{173}Yb = 0.786956 (Thirlwall and Anczkiewicz, 2004). Furthermore, to correct for the isotopic fractionation effects of the analytical instrument, the Yb isotopic ratios were normalized according to the exponential law (Russell et al., 1978) to ^{173}Yb/^{171}Yb, using a value of 1.12466 (Thirlwall and Anczkiewicz, 2004). Hf isotopic ratios were normalized using a value of 0.7325 for the ^{179}Hf/^{177}Hf ratio (Patchett and Tatsumoto, 1981). Lu exhibited mass distortion behavior similar to Yb. Correction calculations for the ^{176}Hf/^{177}Hf and ^{176}Lu/^{177}Hf ratios were performed using a Microsoft Excel macro (Milhomem Neto and Lafon, 2019)

3.6 ZIRCON REE GEOCHEMISTRY

For REE isotopic analyses, zircon crystals of four samples, one PBHTnGd, two BHMzG, and one RBHMzG were selected. The procedures for separating and imaging the zircons are described in topic 3.4. To ascertain the REE isotopic composition of the zircon, the spots were positioned close to the U-Pb spot and analyzed interspersed with NIST 610 standard. The following elements were analyzed: La, Ce, Pr, Nd, Sm, Eu, Gd, Tb, Dy, Ho, Er, Tm, Yb, and Lu. The complete procedure and equipment setting are described in Sato et al. (2016), and the detection limits for SIMS are following Wiedenbeck et al. (2004).

3.7 WHOLE ROCK Sm-Nd

The Sm-Nd isotopic analyses were performed on 12 representative samples previously prepared for whole-rock analyses. Analytical methods for whole-rock Nd isotopes analysis at LEGGA-UnB follow Gioia and Pimentel (2000). Analyses were carried out using a MAT Finnigan MAT 262 mass spectrometer (ID-TIMS). Approximately 50 mg of whole rock powders were mixed with a ^{149}Sm-^{150}Nd spike and dissolved in Savillex capsules. Sm and Nd were extracted through cationic exchange on Teflon columns using L-N spec resin (HDEHP on PTFE powder). The elements were placed in a rhenium filament and detected in static mode. Precision for Sm/Nd and ^{143}Nd/^{144}Nd is better than ± 0.5% (2σ) and ± 0.005% (2σ), respectively, based on repeated analyses of international rock standards BHVO-1 and BCR-1.

4 RESULTS

4.1 MODAL COMPOSITION AND CLASSIFICATION

The modal compositions of its rock varieties are given in supplementary table 2 and the QAP-QAPM' modal classification diagrams in Fig. S1 (Mesquita et al., 2025). In summary, the central-eastern portion of the IGS is formed by four faciological varieties: biotite-amphibole tonalite to granodiorite with clinopyroxene and/or orthopyroxene (PBHTnGd) or devoid of pyroxenes (BHTnGd); biotite-amphibole monzogranites (BHMzG), which have associated a markedly reduced variety (RBHMzG).

4.2 MICROSTRUCTURAL ASPECTS

The deformation degree of the IGS rocks reflects its distance from the SZ, regardless of the observed variety. However, no rocks of the monzogranitic varieties far away from SZ were recorded. Therefore, the PBHTnGd variety was selected to represent rocks distant from the SZ, and the BHTnGd, BHMzG, and RBHMzG varieties to represent rocks close to the SZ. Away from the shear zones, the rocks preserve primary fine- to medium-grained heterogranular hypidiomorphic texture (Fig. 3a). Quartz crystals are subhedral to anhedral (Fig. 3b, c) and sometimes globular and included in plagioclase. Its crystals show undulatory extinction with local formation of subgrains and bulges at their borders (Fig. 3b, d). The deformational features of plagioclase include diffuse contours of macle plains and rarely subgrains (Passchier and Trouw, 2005) (Fig. 3e). It also shows weak to moderate undulatory extinction. Biotite, hornblende, orthopyroxene, clinopyroxene, and opaques are subhedral to anhedral, generally have no preferential orientation, and form aggregates (Fig. 3f, g). Alkali feldspar displays an albite-pericline grid or perthitic intergrowths with weak undulatory extinction. Intergranular fractures are common in plagioclase, they are filled with epidote (Fig. 3e).

Near the SZ, the rocks have continuous tectonic foliation and exhibit comparatively finer grain (Fig. 3l). Generally, mafic-enriched and felsic bands alternate in the foliation plane (Fig. 3 h, o). Quartz occurs as: (1) fine to medium subhedral phenocrysts or phenoblasts, sometimes elongated, with strong undulatory extinction and expressive formation of (2) subgrains and (3) new recrystallized grains at their borders, characterizing a core-mantle texture (Fig. 3i). It is common the migration along grain borders with the formation of amoeboid quartz (Fig. 3k). Recovery processes generate the subgrains (Trouw et al., 2009), resulting in new recrystallized grains when the rotation angle of the subgrains exceeds 10° (Vernon, 2005). The new grains are part of the quartz-feldspar matrix (Fig. 3i, l).

Nevertheless, sometimes, they occur as aggregates with polygonalized contacts (Fig. 3j). In shear bands, ultramylonites are generated, and the new grains can form ribbons (Fig. 3l). Alkali feldspar is predominantly potassic, in the form of anhedral to subhedral medium-grained phenocrysts, with flame perthites. There is local formation of core-mantle textures (Fig. 3m). Plagioclase exhibits medium-grained, subhedral phenocrysts with lenticular macles of deformation and, sometimes, their original albite-carlsbad macles are erased by deformation or masked by sericitization and/or saussuritization. It can exhibit core-mantle texture (Fig. 3n) and fractures filled with fine quartz-feldspar like that of the matrix (Fig. 3n).

4.3 GEOCHEMISTRY

4.3.1 Major and minor elements

The PBHTnGd variety has the lowest average SiO_2 content (67.30 wt%), followed by BHTnGd (68.29 wt%). The monzogranitic varieties, BHMzG and RBHMzG, have the highest average silica contents at 71.67 wt% and 72.13 wt%, respectively. The Harker diagrams (Fig. 4a to e) show a negative correlation between SiO_2 and TiO_2, Al_2O_3, FeO_t, MgO, and CaO, and in the MALI diagram (Fig. 4f; fields of Frost et al. 2001), there is a positive correlation between SiO_2 and (Na_2O+K_2O-CaO). Generally, Al_2O_3, MgO, and CaO contents are higher in the tonalitic to granodioritic varieties and decrease towards the monzgranitic varieties (Fig. 4 b, d, e). The FeO_t typically ranges from 3 wt% to 5 wt% within the 66 wt% to 72 wt% range of SiO_2, regardless of the variety. (Fig. 4c).

4.3.2 Trace elements

Regarding the LILEs, Sr and Rb display a negative correlation (Fig. 5a), with higher Sr concentrations in the PBHTnGd (125-296 ppm) and BHTnGd (91.1-321 ppm, concentrated between 200 and 300 ppm), with a decrease in the direction of the BHMzG (68.1-197 ppm) and RBHMzG (22.3-152 ppm) varieties and an inverse behavior of Rb that increases from the PBHTnGd/ BHTnGd to BHMzG and RBHMzG (6.4-73.20 ppm, 6.3-140 ppm, 52.3-172.5 ppm and 68-237ppm, respectively; Fig. 5a). In the Rb/Sr vs Sr/Ba diagram (Fig. 5b), the PBHTnGd and BHTnGd varieties define a near vertical trend due to their low (<1) and little varied Rb/Sr ratios and more varied Sr/Ba ratios (0.09-0.85 with an outlier value of 1.35).

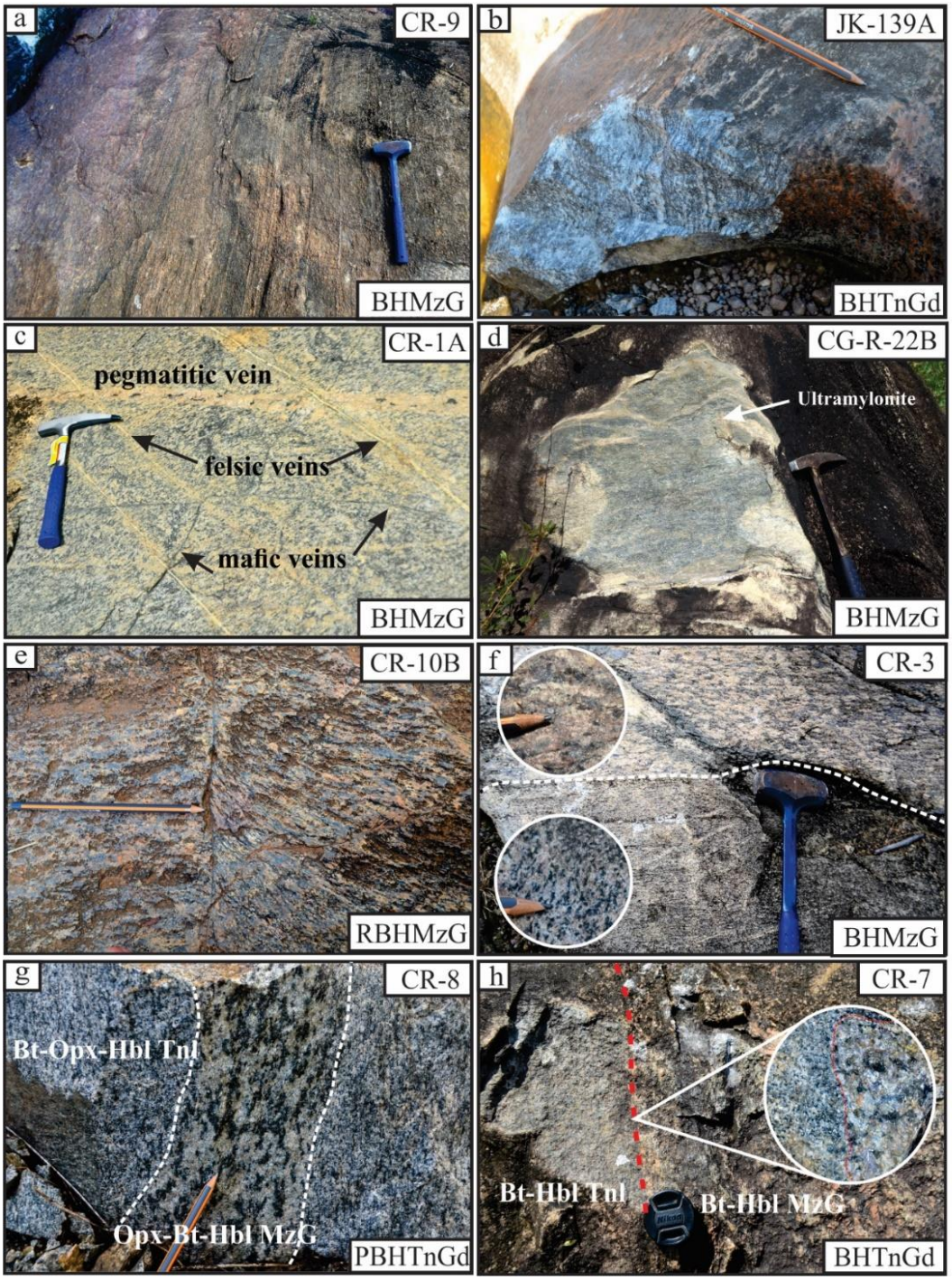

Figure 2. Field aspects of the varieties of the Igarapé Gelado suite. a) Penetrative foliation; b) BHTnGd showing foliation with high-angle dip and alternation between bands enriched in felsic and mafic minerals; c) Felsic, mafic and pegmatite veins discordant to foliation; d) Ultramylonitic rock; e) RBHMzG with brittle-ductile shear band crosscutting the foliation; f) Contact between facies of the BHMzG variety with contrast in texture and mafic content; g) Medium-grained Bt-Opx-Hbl tonalite abruptly sectioned by coarse-grained Opx-Bt-Hbl monzogranite; h) Contact between Bt-Hbl Tnl and Bt-Hbl MzG with evidence of mingling. Figures b, e, f, g, and h from Mesquita et al. (2025).

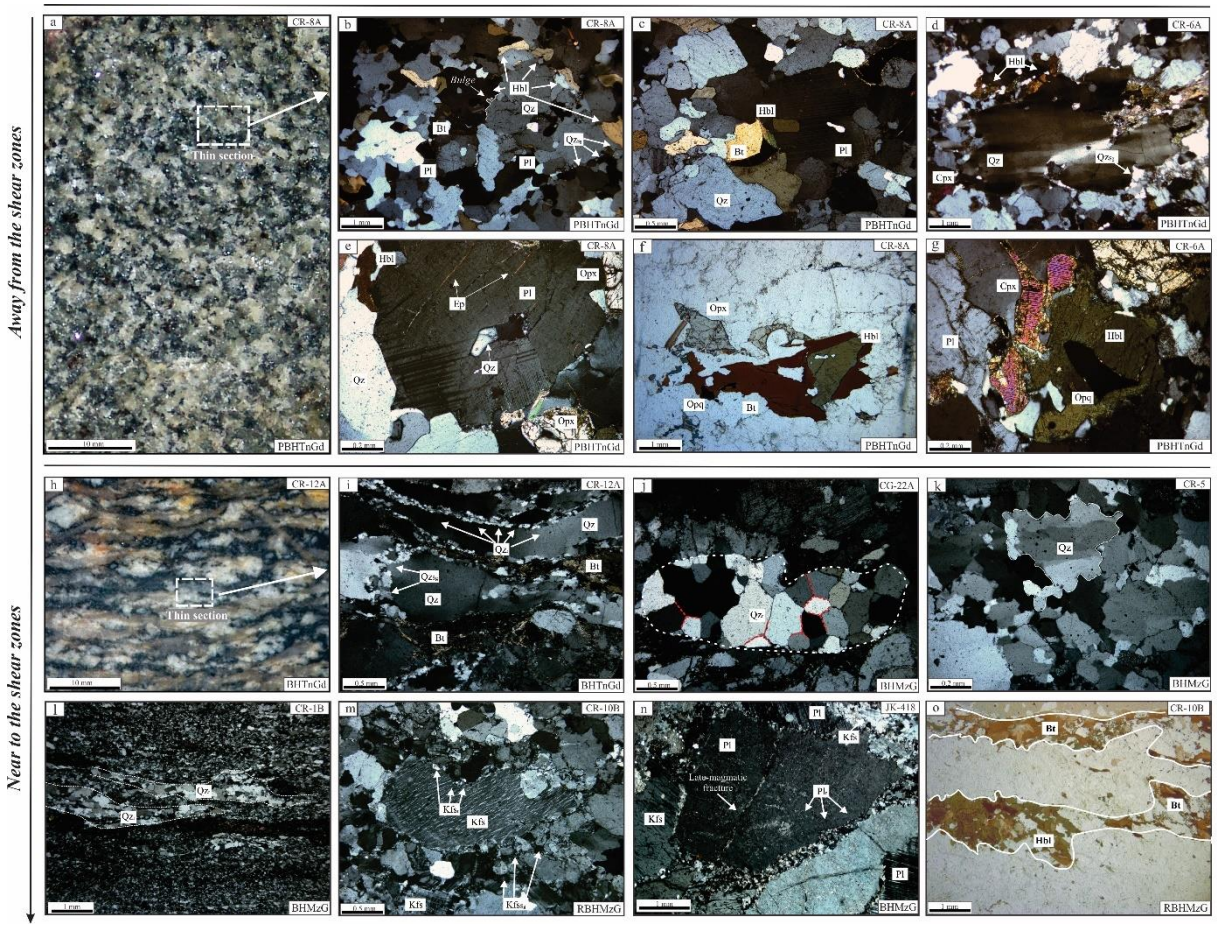

Figure 3. Textural and microstructural aspects of IGS granitoids. Rocks far away from the SZ - a) weak deformed medium-grained orthopyroxene-biotite-hornblende tonalite; b, c) PBHTn showing hypidiomorphic texture, with weak deformation, incipient formation of subgrains of quartz (Qz_{Sg}), bulges and globular quartz crystals included in plagioclase; d) Quartz phenocryst with undulatory extinction and incipient formation of subgrains at its border; e) Plagioclase crystal, with lenticular deformation macles and fractures filled with epidote; f) Little deformed PBHTnGd containing reddish-brown biotite, orthopyroxene, olive green hornblende, and opaques; g) Aggregate of mafic minerals in PBHTnGd formed by olive-green hornblende, opaques, and clinopyroxene. Rocks occurring near to the SZ h) Foliated biotite-hornblende granodiorite. i) Elongated quartz (Qz) crystals, with core-mantle texture and strong undulatory extinction in BHTnGd; j) Recrystallized quartz (Qz_r), with polygonal contacts subgrains in BHMzG; k) - amoeboid quartz crystals in BHMzG l) Quartz ribbons (Qz_r) oriented in the mylonitic foliation plan; m) Alkali feldspar phenocrysts with flame perthites and core-mantle texture, immersed in recrystallized quartz-feldspar matrix in a RBHMzG; n) Plagioclase crystals with core-mantle texture faded twinning and late-magmatic fractures filled with quartz-feldspar, associated with alkali feldspar crystal surrounded by recrystallized quartz-feldspasthic matrix. o) Mafic-enriched and felsic bands in foliated rocks. Abbreviations following Whitney and Evans (2010). Hornblende = a general term to represent calcium amphiboles (Leake et al., 1997).Figures f and o from Mesquita et al. (2025).

In that plot, the BHMzG and RBHMzG varieties display Sr/Ba ratio below 0.2 and Rb/Sr that varies in a wider spectrum from 0.27 to 2.42 (Fig. 5b). The Yb contents are concentrated between 1 and 4 ppm in all varieties (Fig. 5c). The BHMzG have a wide range of Sr/Y ratios (0.76-33.97) and Yb contents ranging from 0.29 to 5.79 ppm, with five samples having Yb contents <1 ppm. The PBHTnGd and BHTnGd samples have similar Yb contents (concentrated between 1.08-3.51 ppm), and Sr/Y ratios generally between 7.2 and 20.46. The reduced monzogranites also shows a restricted variation of the Sr/Y ratio (1.36-5.89) and similar Yb contents (1.1-3.73 ppm) compared to BHMzG (Fig. 5c). In terms of HFSE, the

analyzed samples generally show high Zr, Y, and Hf and moderate Nb contents. Zr is high in all varieties, with RBHMzG showing the highest values (285-846 ppm, Table S3). The Y contents have a wide variation in the PBHTnGd (17.8-41.7 ppm), BHTnGd (9.6-68.1 ppm), BHMzG (4.3-94 ppm), and RBHMzG (11.5-47 ppm) varieties. The BHMzG has five samples with low Y (4.3-5.8 ppm) and four with high Y (16.4-94 ppm, Table S3). Samples with low Y have low Yb contents and high Sr/Y ratios (Fig. 5c).

4.3.3 Patterns of rare earth elements and multi-element diagrams

The REE patterns of IGS rocks exhibit an enrichment of LREE relative to HREE (Fig. 6). The pyroxene-bearing rocks (Fig. 6a) has the lowest La_N/Yb_N ratios (9.65-35.96) and well-marked negative Eu anomalies (0.42-0.61). The BHTnGd variety shows similar La_N/Yb_N ratios (generally 6.22-47.81) to those of the pyroxene-bearing rocks but exhibits higher maximum values (62 and 74.84) and presents dominant moderate to discrete negative Eu anomalies (0.37-0.99) with two samples showing positive anomalies (1.18 and 2.25, Fig. 6a). The BHMzG is not geochemically homogeneous, exhibiting significant differences, particularly in the Y and Yb contents (Table S3; Fig. 5c). Rocks with higher contents of these elements have REE fractionation (Fig. 6b) close to BHTnGd (La_N/Yb_N 13.3-57.6), accentuated negative Eu anomalies (0.2-0.7) and high ΣREE (320-933 ppm). Rocks with low Y and Yb show low ΣREE (110-148 ppm), more pronounced HREE fractionation (Fig. 6b), as evidenced by higher La_N/Yb_N ratios (48-77.3, with an outlier value of 122.3.), and positive Eu anomalies (Eu/Eu*: 1.1-2.6). These rocks also present concavity in the HREE patterns, a feature not observed in the samples with Y and Yb enrichment of the BHMzG. Finally, except for the $(La/Yb)_N$ ratios, which are always low (7.1-36.5), the reduced monzogranites does not show homogeneous REE geochemical behavior, with quite varied ΣREE (149-679 ppm) and positive (Eu/Eu*: 1.1-2.7; Table S3) or negative (Eu/Eu*: 0.56-0.59) Eu anomalies (Fig. 6b). In multi-element diagrams normalized to the primitive mantle (Fig. 6e, f, g, h), all IGS samples exhibit similar patterns with overlapping element concentrations with subtle variations. The accentuated negative anomalies of P and Ti and the moderate anomalies of Nb and Ta stand out (Fig e, f).

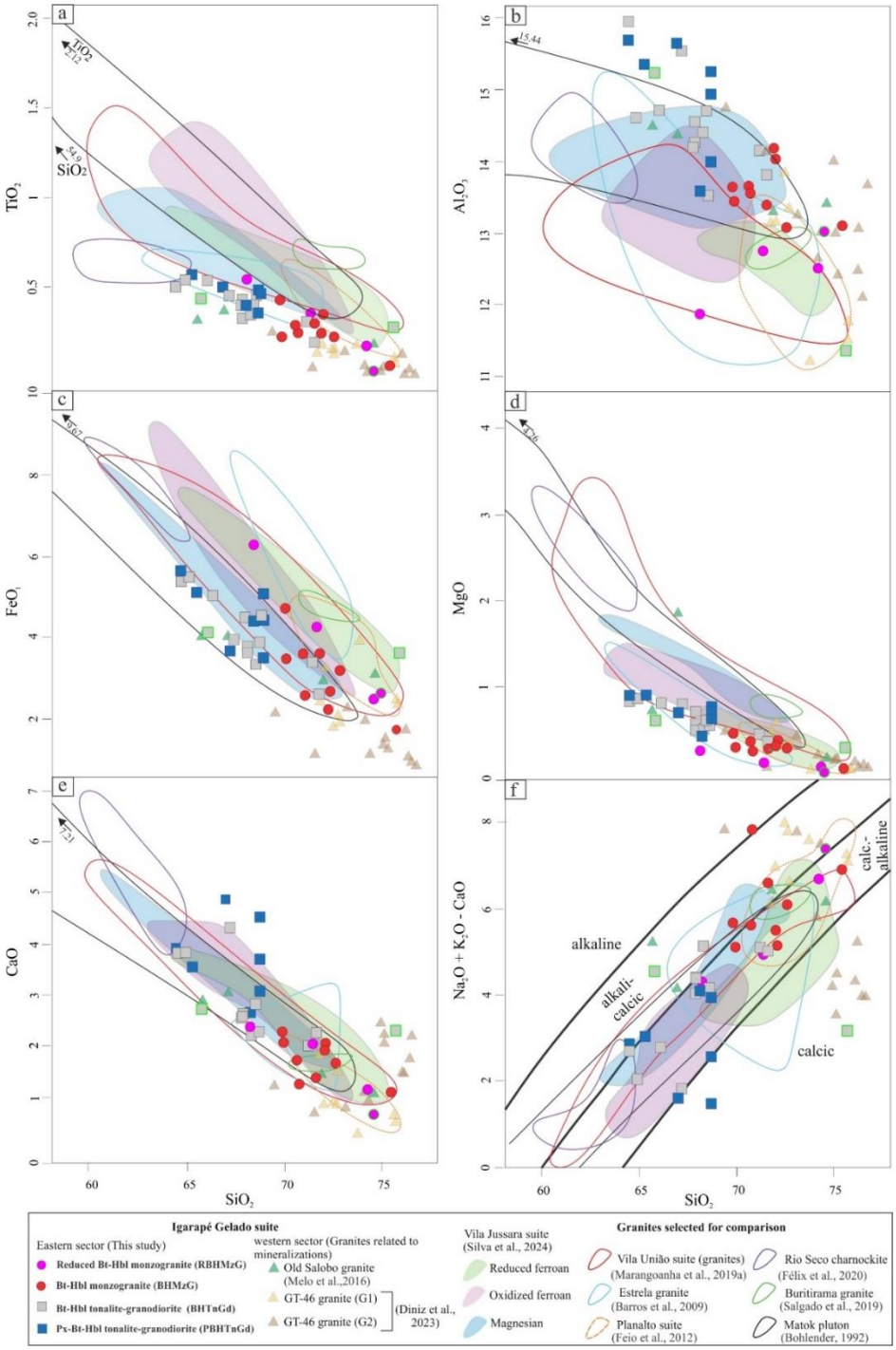

Figure 4. Compositional variations of IGS varieties. Other Neoarchean granites from the Carajás province and Matok Pluton are shown for comparison. Harker variation diagrams for major and minor element oxides versus silica (wt%). a- TiO_2, b- Al_2O_3, c-.FeOt, d- MgO, e- CaO; f- (Na_2O+K_2O-CaO) vs. SiO_2 diagram (fields of Frost et al., 2001).

4.4 CLASSIFICATION AND TYPOLOGY.

In the Q-P diagram (Debon & Le Fort, 1983), the IGS rocks plot (Fig. 7a) in the tonalite and granodiorite fields (PBHTnGd and BHTnGd) or in the monzogranite and syenogranite fields (BHMzG and RBHMzG). The compositional contrast between these two large groups of rocks in the IGS is well-marked. In the normative An-Ab-Or diagram (O'Connor, 1965,

with fields of Barker, 1979), the PBHTnGd and BHTnGd plot in the tonalite and granodiorite fields, and the BHMzG and RHBMzG in the granite field (Fig. 7b). The IGS granitoids are metaluminous to slightly peraluminous, as indicated by the A/NK vs. A/CNK diagram (Shand, 1950; Fig. 7c). They are calc-alkaline, as seen in the diagram $Na_2O + K_2O$-CaO vs. SiO_2 (Frost et al., 2001), with rare samples plotting in the calcic, alkali-calcic and alkaline fields (Fig. 4f). The IGS granitoids follow a calc-alkaline trend (Fig. 7e) in the Na-K-Ca diagram (Barker and Arth, 1976), with some samples of the PBHTnGd and BHTnGd plotting in the Archean TTG field (Martin, 1994). In the #mg vs. K_2O plot (Fig. 7d), the PBHTnGd and BHTnGd varieties can be distinguished from the BHMzG and RBHMzG by their higher #mg. However, in the FeOt/(FeOt+MgO) diagram (Frost et al., 2001), all analyzed samples plot in the field of ferroan granites (Fig. 7g). In both diagrams (Figs. 7d and 7g), three parallel trends can be observed. The first is defined by the PBHTnGd and BHTnGd varieties with higher #mg and lower values of the FeO* index (mostly 0.83-0.89, Table S3), which increase in the sense of the BHMzG (0.87-0.92) and attain maximum values in the reduced monzogranites (0.96-0.99). In the $CaO/FeO_t+MgO+TiO_2$ vs. Al_2O_3 diagram (Dall'Agnol and Oliveira, 2007), most IGS samples fall within the A-type field, with a few in the calc-alkaline field or outside of both these categories (Fig. 7h, i). In the (FeOt/(FeOt+MgO) vs. Al_2O_3 diagram, PBHTnGd and BHTnGd are mostly found in the oxidized A-type granite fields, while BHMzG and RBHMzG plot in the reduced A-type granite field (Fig. 7i). The IGS rocks present, for the most part, a geochemical signature akin to the A2 subtype (Eby, 1992), however, the five BHMzG samples that have low Y show characteristics of A1 subtype (Fig. 7j). HFSE-based diagrams, such as the Zr+Ce+Y+Nb diagram (Whalen,1987), also indicate A-type affinity (Fig. 7k), although four BHMzG samples are in the field of fractionated I-type granites. In addition, in Nb vs. Y tectonic setting discrimination diagram (Pearce et al., 1984), the IGS samples straddle the boundary between the intra-plate granite and syn-collisional/volcanic arc granite fields (Fig. 7l), as is often the case with post-collisional granites (Pearce, 1996). In this diagram and in the FeOt/MgO vs Zr+Nb+Ce+Y diagram, the Y-depleted- samples of BHMzG occur separated from the other varieties.

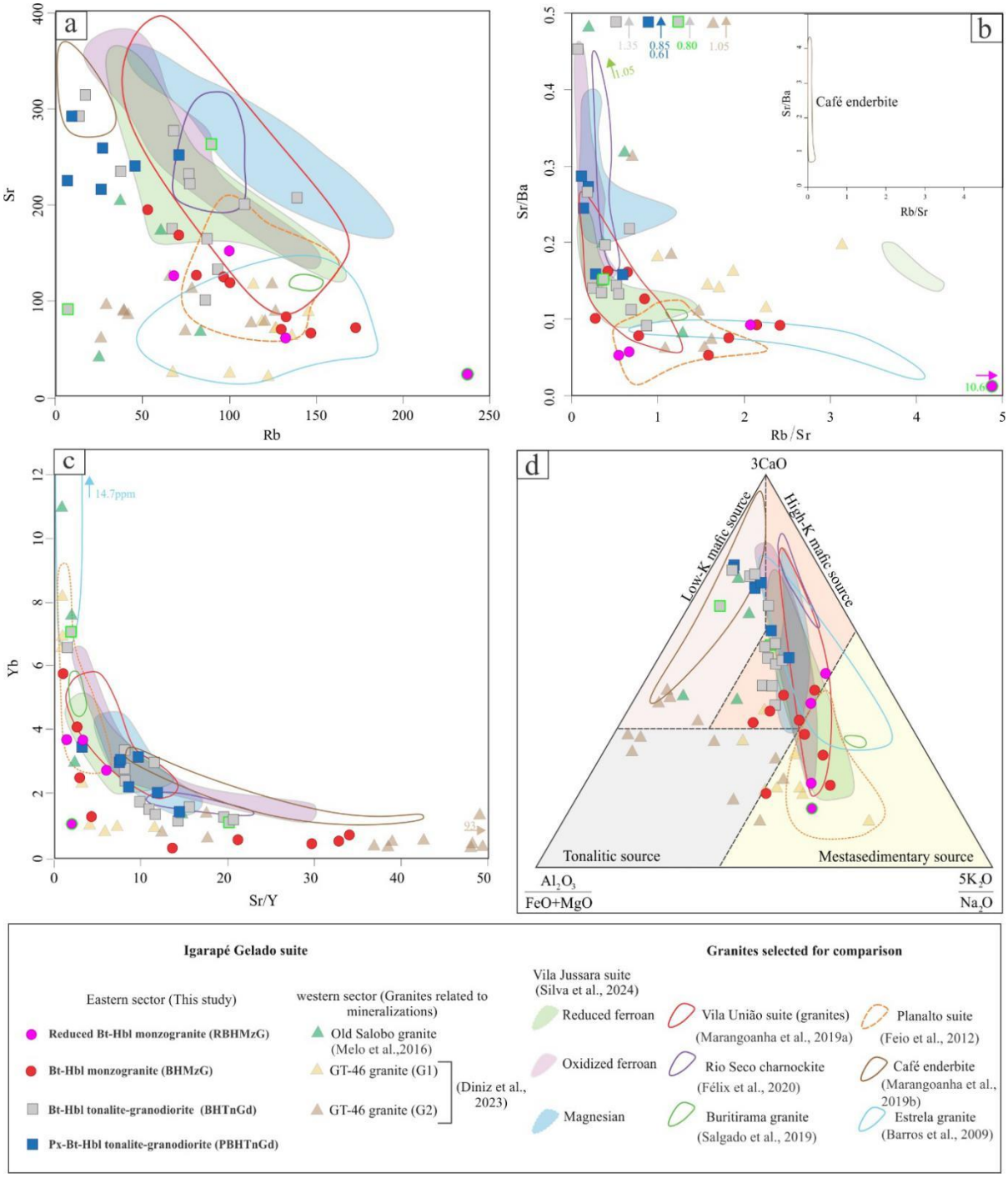

Figure 5. Geochemical diagrams for the varieties of IGS and Neoarchean granites of the Carajás province selected for comparison. a) Sr vs. Rb; b) Sr/Ba vs. Rb/Sr; c) Yb vs. Sr/Y; d) Source discrimination diagram for Archean granitoids (Fields of Laurent et al., 2014).

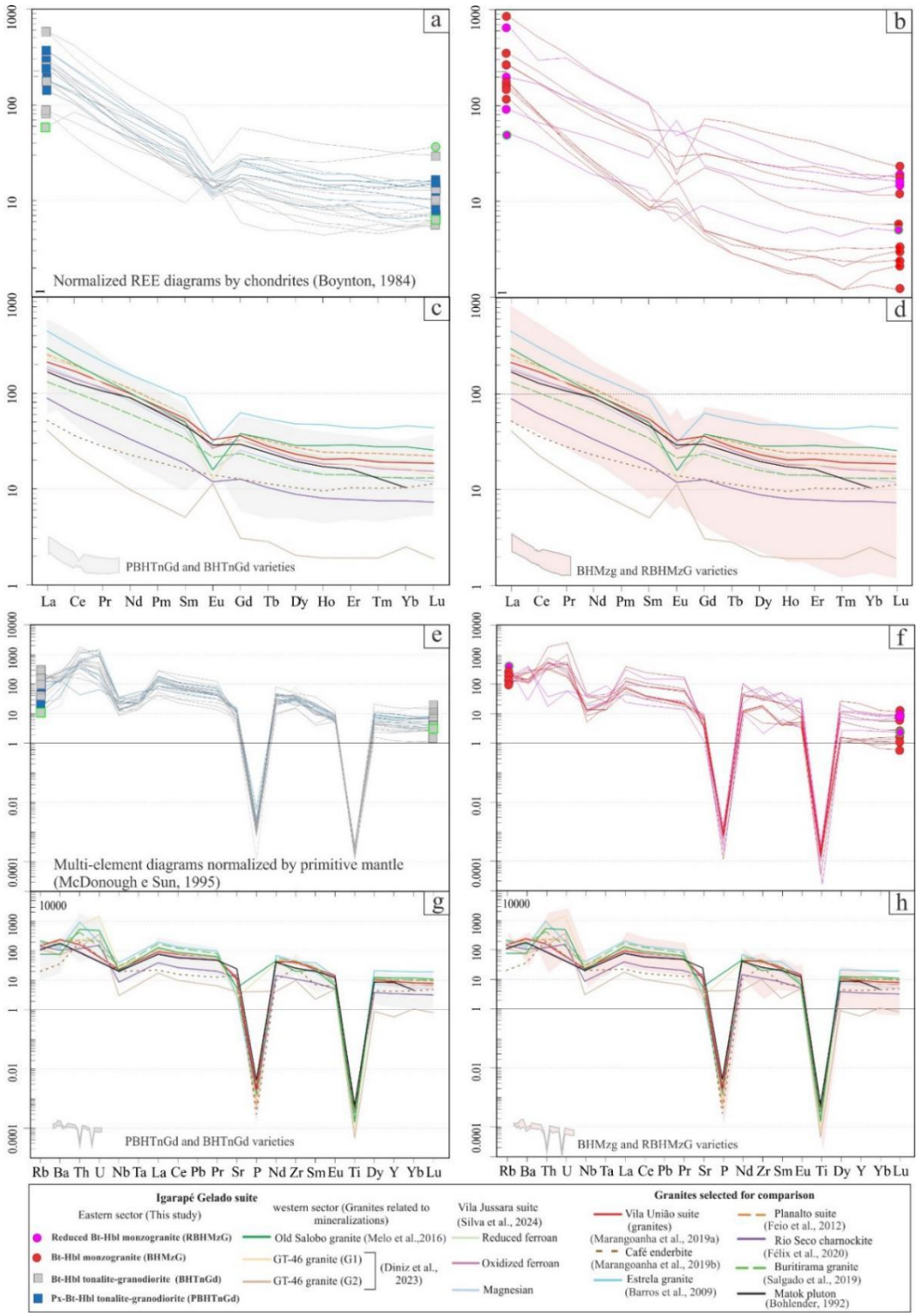

Figure 6. REE diagrams of the IGS rocks. a) PBHTnGd and BHTnGd; b) BHMzG and RBHMzG. REE diagrams from related rocks of the Carajás Province and Matok pluton compared with REE diagrams from the IGS varieties. Multi-element diagram from the e) PBHTnGd and BHTnGd; f) BHMzG and RBHMzG. Multielement diagrams from related rocks of the Carajás Province and Matok pluton compared with Multielement diagrams from the IGS varieties.

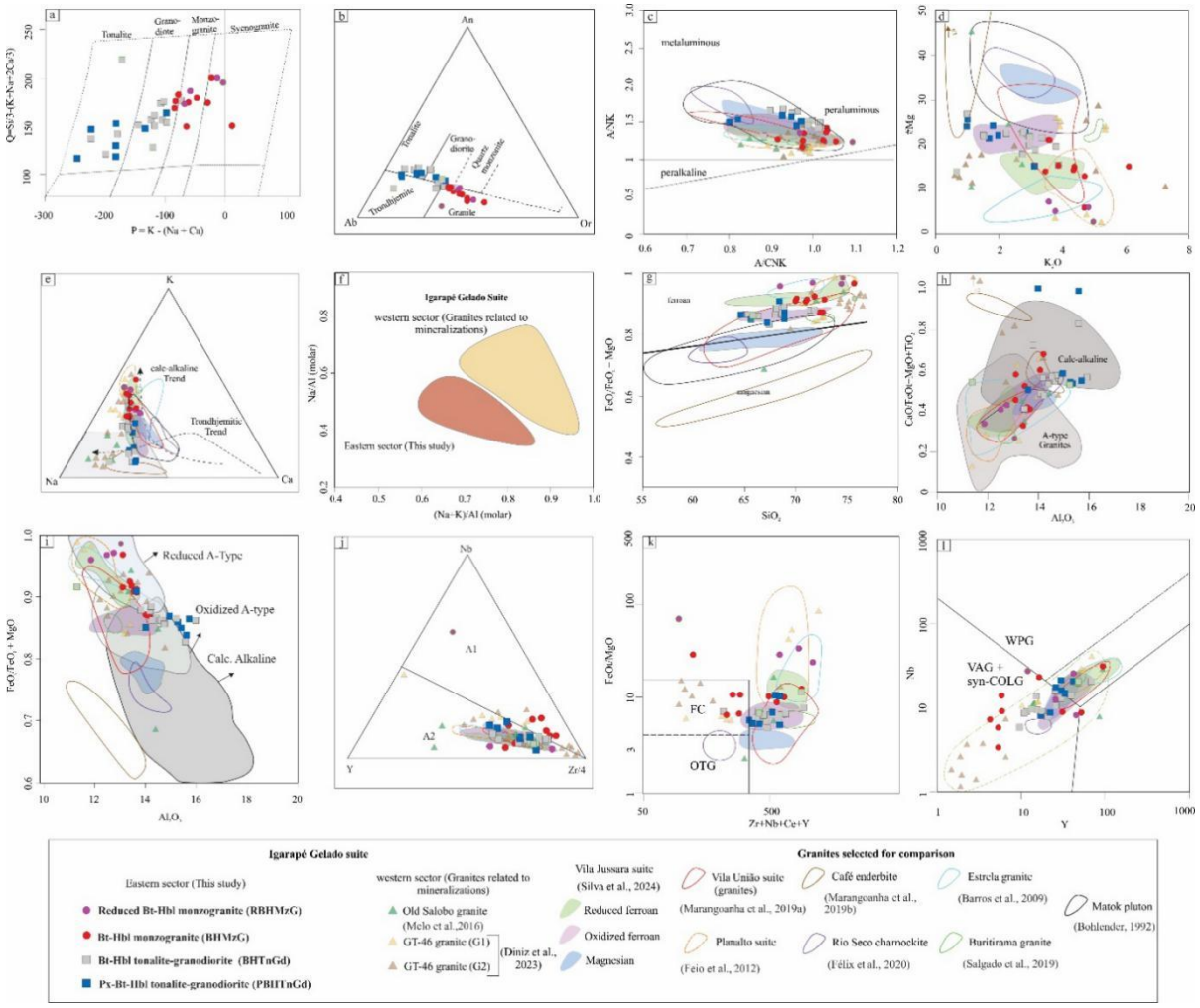

Figure 7. Geochemical discriminant diagrams for IGS granitoids. Neoarchean granites from the Carajás province and Matok pluton are shown for comparison. a) P-Q (Debon and LeFort, 1983); b) Normative An-Ab-Or diagram (O'connor, 1965); c) A/NK vs. A/CNK diagram (Shand, 1950); d) #mg vs. K_2O diagram; e) Na-K-Ca ternary diagram. The trondhjemitic and calc-alkaline trends are according to Barker and Arth, (1976). The gray field corresponds to Archean TTG (Martin, 1994); f) $(K + Na)/Al_{(molar)}$ vs. $Na/Al_{(molar)}$ diagram for IGS granites; g) $FeOt/(FeO_t+MgO)$ vs. SiO_2 diagram (Frost et al., 2001); h) $CaO/FeO_t+MgO+TiO_2$ vs. Al_2O_3 diagram and i) $FeO_t/(FeO_t+MgO)$ vs. Al_2O_3 diagram (Dall'Agnol and Oliveira, 2007); j) Y-Nb-Zr/4 diagram for A-Type granites (Eby, 1992); k) Zr+Ce+Y+Nb vs. FeOt/MgO (Whalen et al. 1987); l) Nb vs. Y tectonic setting discrimination diagram (Pearce et al., 1984).

4.5 ZIRCON U–Pb–DATING

The results of U-Pb SHRIMP analyses can be found in supplementary table 4. The zircons from the RBHMzG variety under the optical microscope are dark brown, pink, or occasionally colorless. These zircon grains are prismatic, ranging from subhedral to euhedral, are elongated, with some rounded grains, and their length typically varies from 60 to 340 µm. Their aspect ratios (length/width) ranging from 1 to 5. In CL-BSE interpolated images, most grains are light gray, exhibit concentric oscillatory zoning, are mostly fracture-free, and contain few inclusions (Fig. 8b, e). In the CR-10B sample (Fig. 8a) the population A, defined by seven spots, yielded a concordia age of 2670.7±6.4 Ma (MSWD = 0.0015, n = 7), while

the population B, consisting of five spots, gave a concordia age of 2602.8±9 Ma (MSWD = 0.019, n = 5). One grain is dated at 2515± 9 Ma ($^{207}Pb/^{206}Pb$ apparent age) Ma. The population A from the JK-47 sample (Fig. 8d, e) included three grains with a concordia age of 2683±8.6 Ma (MSWD = 1.6, n = 3), overlapping with the population A of the CR-10B sample. The population B, defined by six grains, shows a concordia age of 2646±6.2 Ma (MSWD = 5.4, n = 6). The population C that resulted from four spot analyses, has a concordia age of 2610±11 Ma (MSWD = 2.6, n = 5).

The analyzed zircon grains of the PBHTnGd (Fig. 9a), BHTnGd, and BHMzG (Fig. 9b, c) varieties share similar textural characteristics. They are generally colorless and matte with few transparent, mostly prismatic, euhedral to subhedral, with some elongated grains and others slightly rounded (PBHTnGd, 60-330 μm); BHTnGd, 70-260 μm; and BHMzG, 78-320 μm). The aspect ratios of the grains range from 1 to 4. In BSE-CL interpolated images, zircon grains usually show low to intermediate luminescence due to intense metamictization and contain few inclusions. Larger grains often feature concentric oscillatory zoning and fractures, while smaller grains typically have diffuse zoning or a massive texture (Fig. 9 a, b, c).

The concordia ages of the reduced monzogranites grain populations align closely with the ages of other varieties. Its age of population A ranges from 2680 to 2670 Ma, consistent with the upper intercept ages of the CR-1A1 sample (2695.7±5.1 Ma, MSWD = 1.5, n = 5) and CG-22 sample (2672±28 Ma, MSWD = 5.1, n = 11) from the BHMzG variety, as well as with that of the CR-8A sample (2684±15 Ma, MSWD = 4.6, n = 8) from the pyroxene-bearing rocks (Fig. 10a, b, d, respectively). Conversely, the population B of JK-47 sample is similar in age (2646±6.2 Ma) to the upper intercept ages of the CR-9 sample (2642±14 Ma, MSWD = 3, n = 11; Fig. 10c) and CR-6A sample (2656±30 Ma, MSWD = 21, n = 6;Fig. 10e) from the BHMzG and PBHTnGd varieties, respectively. In this case, the high MSWD values are closely related to the compositional heterogeneity of the zircon crystals that were strongly affected by the alteration (see topic 5.4). The CAD-14 sample (PBHTnGd) gave an upper intercept age of 2603±13 Ma (MSWD = 4.8, n = 11, Fig. 10f) which is similar to the ages of the population C of the JK-47 sample (2610±11 Ma) and the population B of the CR-10B sample (2602.8±9.9 Ma). The JK-139A (BHTnGd) and JK-137A (BHMzG) samples furnished upper intercept ages around 2550 Ma, similar to the isolated age given for a single spot in the RBHMzG variety (Fig. 10g, h).

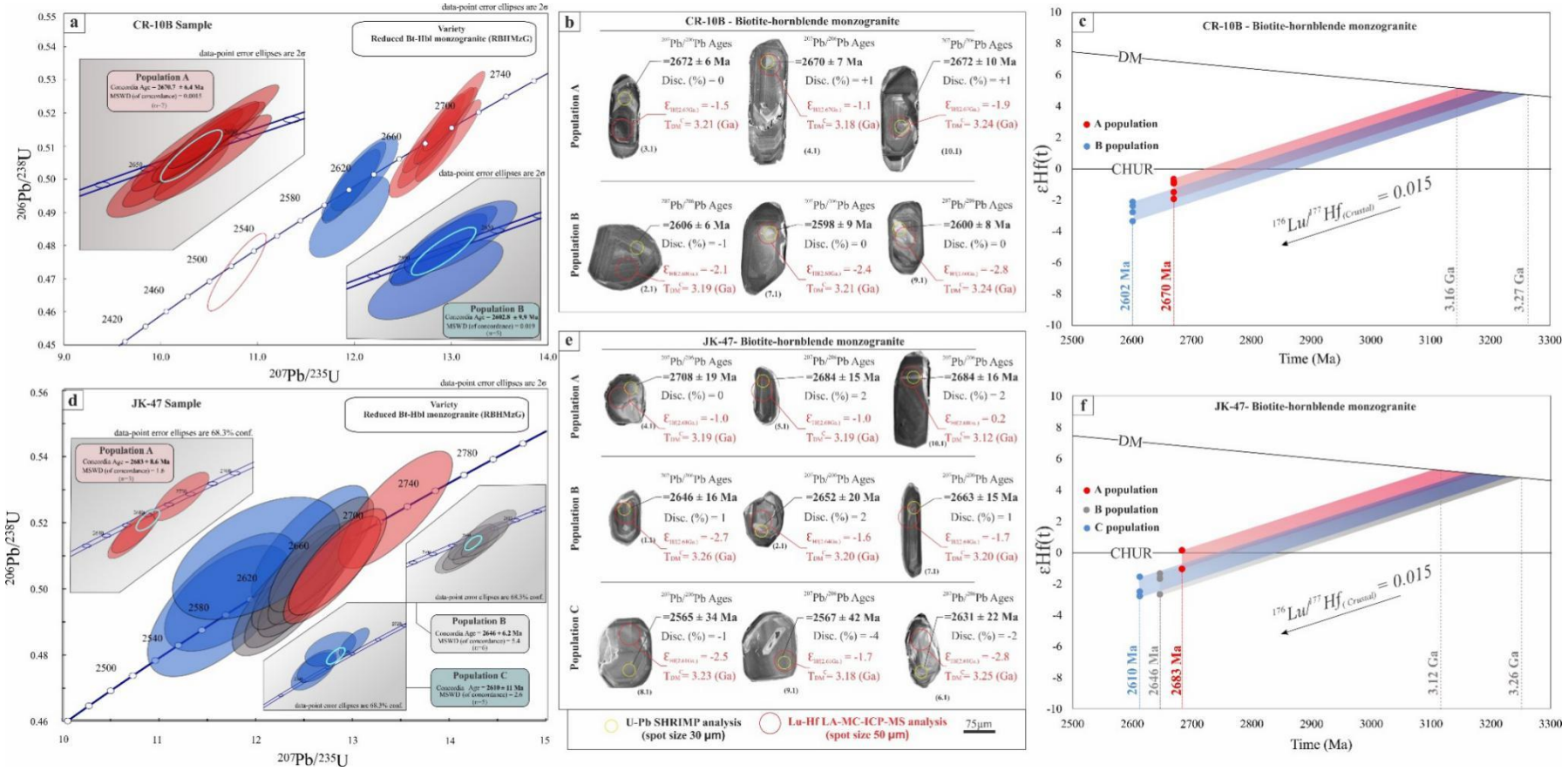

Figure 8: Zircon integrated study of the RBHMzG variety: $^{206}Pb/^{238}U$ vs. $^{207}Pb/^{235}U$ Concordia diagrams (SHRIMP analyses) a) of the sample CR-10B and d) of sample JK-47; CL-BSE interpolated. images with their respective in situ U-Pb ($^{207}Pb/^{206}Pb$ ages; in black) and Lu-Hf (ε_{Hf} and Hf-T_{DM}^{C}; in red) data b) of the CR-10B sample; and e) for the JK-47 sample. The numbers in parentheses correspond to the analyzed spots. The circles (see the legend) mark the position of the beam spot (scaled to size).; Time (Ma) vs. $\varepsilon_{Hf}(t)$ diagrams c) of the CR-10B; and f) JK-47 samples.

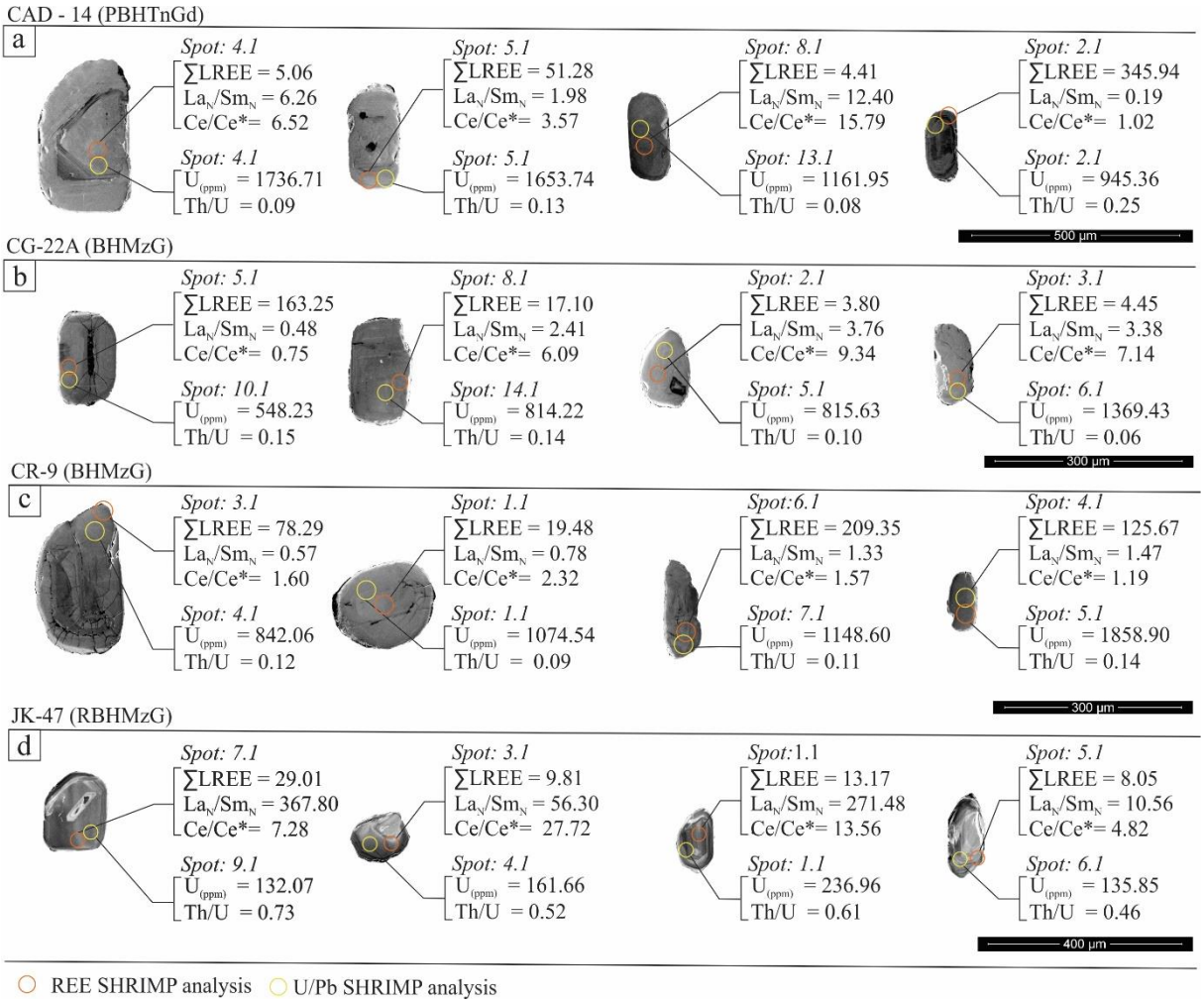

Figure 9. Interpolated images of CL and BSE with textural aspects, REE and U-Th/U data of the zircon crystals analyzed from IGS: a) PBHTnGd (CAD-14 Sample); b) BHMzG (CG-22 sample); c) BHMzG (CR-9 sample); d) RBHMzG (JK-47 sample).

4.6 ZIRCON Lu-Hf ISOTOPE DATA

The zircon Hf-isotope data from the RBHMzG are presented in Table 1. The population A of the CR-10B sample showed subchondritic $\varepsilon_{Hf}(t)$ values (-1.9 to 0.6) and Hf-T_{DM}^{C} ages ranging from 3.24 to 3.16 Ga (Fig.8c). In contrast, the population A of the JK-47 sample exhibited negative $\varepsilon_{Hf}(t)$ values (-1.03 to -1.0), along with one positive value (0.2), with Hf-T_{DM}^{C} ages ranging from 3.19 to 3.12 Ga (Fig. 8f). The population B of the CR-10B sample and the population C of the JK-47 sample, for which the U-Pb age is ~2600 Ma, exhibited subchondritic $\varepsilon_{Hf}(t)$ values (CR-10B, -3.3 to -2.1, and JK-47, -2.8 to -1.7) and Hf-T_{DM}^{C} ages ranging from 3.27 to 3.19 on CR-10B and 3.25 to 3.18 on JK-47. Ultimately, Population B of the JK-47 sample exhibited $\varepsilon_{Hf}(t)(t)$ varying from -2.7 to -1.3 and Hf-T_{DM}^{C} ages of 3.26 to 3.18 Ga that are within the range of the other presented populations.

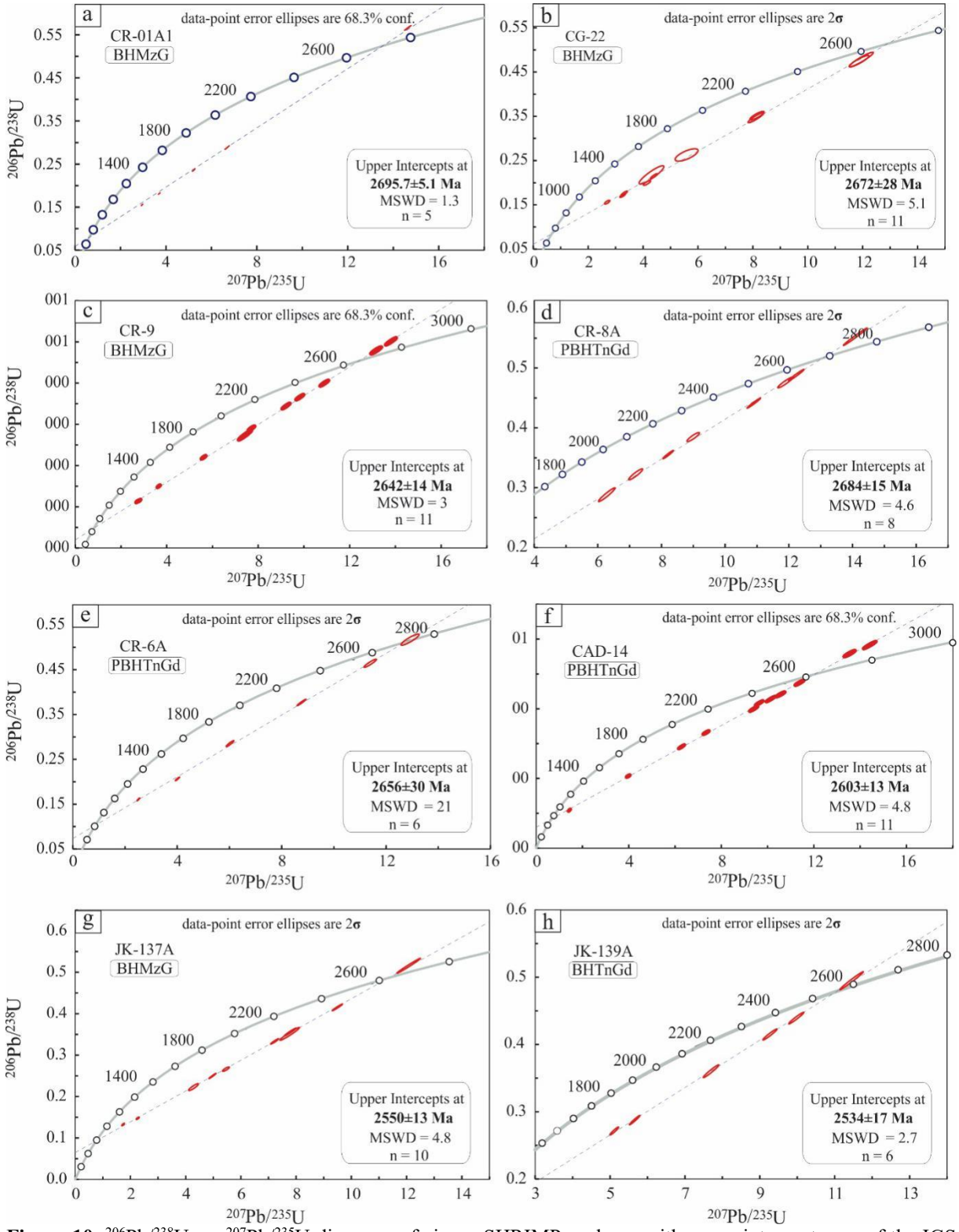

Figure 10. $^{206}Pb/^{238}U$ vs. $^{207}Pb/^{235}U$ diagrams of zircon-SHRIMP analyses with upper intercept ages of the IGS granitoids. a) BHMzG (CR-01A1); b) BHMzG (CG-22); c) BHMzG (CR-9); d) PBHTnGd (CR-8A); e) PBHTnGd (CR-6A); f) PBHTnGd (CAD-14); g) BHMzG (JK-137A); h) BHTnGd (JK-139A).

Table 1. Zircon Hf isotope data obtained by LA–MC–ICP-MS for the RBHMzG variety from the IGS.

ID Spot	$^{176}Hf/^{177}Hf$	2SE	$^{176}Lu/^{177}Hf$	2SE	$^{176}Yb/^{177}Hf$	2SE	$^{178}Hf/^{177}Hf$	2SE	$\varepsilon_{Hf}(0)$	t U-Pb (Ma)	$^{176}Hf/^{177}Hf_{(t)}$	$\varepsilon_{Hf}(t)$	$\varepsilon_{Hf}(t)$ 2SE	Hf-T_{DM}^{C} (Ga)
Bt-Hbl monzogranite (JK-47) - population A														
4.1	0.281054	0.000013	0.000459	0.000018	0.023225	0.000750	1.467187	0.000035	-61.2	2683	0.281030	-1.0	0.04	3.191
5.1	0.281070	0.000032	0.000762	0.000033	0.035973	0.001562	1.467180	0.000045	-60.7	2683	0.281031	-1.0	0.05	3.19
10.1	0.281090	0.000026	0.000508	0.000024	0.026894	0.001425	1.467261	0.000048	-60.0	2683	0.281064	0.2	0.01	3.12
population B														
1.1	0.281040	0.000022	0.000622	0.000025	0.032004	0.001083	1.467180	0.000036	-61.7	2646	0.281009	-2.7	0.11	3.26
2.1	0.281066	0.000019	0.000558	0.000038	0.029452	0.001866	1.467191	0.000060	-60.8	2646	0.281038	-1.6	0.11	3.20
3.1	0.281064	0.000018	0.000357	0.000015	0.016695	0.000541	1.467248	0.000048	-60.9	2646	0.281046	-1.3	0.06	3.18
7.1	0.281059	0.000020	0.000429	0.000032	0.020293	0.000799	1.467223	0.000034	-61.1	2646	0.281037	-1.7	0.13	3.20
population C														
6.1	0.281051	0.000013	0.000450	0.000036	0.022477	0.001448	1.467237	0.000038	-61.3	2610	0.281029	-2.8	0.16	3.25
8.1	0.281063	0.000015	0.000523	0.000060	0.025932	0.002100	1.467208	0.000031	-60.9	2610	0.281037	-2.5	0.08	3.23
9.1	0.281093	0.000026	0.000692	0.000056	0.033709	0.001802	1.467247	0.000053	-59.8	2610	0.281058	-1.7	0.01	3.18
Bt monzogranite (CR-10B) population A														
1.1	0.281076	0.000024	0.000659	0.000029	0.032546	0.001335	1.467216	0.000045	-60.4	2670	0.281042	-0.9	0.04	3.17
3.1	0.281063	0.000020	0.000712	0.000047	0.035478	0.001902	1.467236	0.000046	-60.9	2670	0.281026	-1.5	0.10	3.21
4.1	0.281062	0.000016	0.000461	0.000083	0.022915	0.003486	1.467218	0.000038	-60.9	2670	0.281038	-1.1	0.19	3.18
5.1	0.281064	0.000028	0.000376	0.000055	0.017373	0.001885	1.467231	0.000051	-60.9	2670	0.281045	-0.8	0.12	3.17
8.1	0.281079	0.000022	0.000585	0.000044	0.028921	0.002031	1.467240	0.000027	-60.3	2670	0.281050	-0.6	0.05	3.16
10.1	0.281051	0.000017	0.000736	0.000023	0.037450	0.000862	1.467187	0.000037	-61.3	2670	0.281014	-1.9	0.06	3.24
population B														
2.1	0.281085	0.000015	0.000626	0.000015	0.029056	0.000448	1.467252	0.000039	-60.1	2602	0.281054	-2.1	0.06	3.19
6.1	0.281054	0.000023	0.000716	0.000019	0.033136	0.003684	1.467211	0.000039	-61.2	2602	0.281019	-3.3	0.52	3.27
7.1	0.281077	0.000016	0.000632	0.000015	0.029116	0.000508	1.467254	0.000043	-60.4	2602	0.281046	-2.4	0.07	3.21
9.1	0.281064	0.000027	0.000590	0.000034	0.029473	0.001578	1.467222	0.000037	-60.8	2602	0.281035	-2.8	0.17	3.24

Concordia SHRIMP U-Pb ages from this study were used to calculate initial $^{176}Hf/^{177}Hf$ and $\varepsilon_{Hf}(t)$. For CHUR parameters, were applied $^{176}Lu/^{177}Hf = 0.0336$ and $^{176}Hf/^{177}Hf = 0.282785$ (Bouvier et al., 2008). For the depleted mantle (DM), were used $^{176}Lu/^{177}Hf = 0.0388$ and $^{176}Hf/^{177}Hf = 0.283250$ (Andersen et al., 2009). To derive the two-stage model age (Hf-T_{DM}^{C}), for the first stage, the measured $^{176}Lu/^{177}Hf$ values were calculated from the evolution curve (from today to t). For the second stage (from t to the intersection with the DM model), was adopted a representative value for continental crust of $^{176}Lu/^{177}Hf = 0.015$ (Griffin et al., 2002).

4.7 ZIRCON REE GEOCHEMISTRY

The data set for REE isotopic analyses is in Table 2. Zircon typically shows depletion in LREE and enrichment in HREE, exhibiting REE patterns normalized to chondrite (McDonough and Sun 1995) (Fig. 11) that are similar to typical zircon's patterns (Borba et al., 2021; Brotodewo et al., 2021; Fowler et al., 2002; Hoskin and Schaltegger, 2003; Hoskin, 2005). The reduced monzogranite (JK-47) shows ∑REE from 280 to 1096 and low ∑LREE values between 8.05 and 29.01 (Table 2), with La, Ce, and Pr <10 and distinct positive Ce anomalies (Fig. 11d). The Sm/La ratios are high, ranging from 10.56 to 367.80, often exceeding 200, while the Ce/Ce* ratios fall between 2.81 and 27.72 (Table 2). Eu/Eu* vary from 0.16 to 0.79 resulting negative Eu anomalies in all analyzed crystals. Compared to the other IGS rocks, the obtained REE patterns (Fig. 11d) are quite uniform and like those observed in magmatic zircon (Borba et al., 2021: Hoskin and Schaltegger, 2003; Fowler et al., 2002).

The zircon crystals of PBHTnGd and BHMzG varieties display more complex and diversified REE patterns (Fig. 11a, b, c), with ∑REE contents of 276 to 716 ppm (with an outlier value of 1310 ppm) and 246 to 812 ppm, respectively. Compared to the RBHMzG, zircon of both varieties show stronger variation in ∑LREE, ranging from 5.06 to 345 ppm in PBHTnGd (Fig. 9a) and 3.80 to 363 ppm in BHMzG, and lower $(Sm/La)_N$. Ce exhibits positive anomalies are almost always present (Fig. 11a, b, c), but they are less accentuated in the CR-9 (BHMzG) sample that shows also less pronouced or even positive Eu anomalies (Fig. 11c). The $(Sm/La)_N$ ratios are low in PBHTnGd (0.19 to 12.40; Table 2) and BHMzG (0.48 to 3.76, with an outlier value of 31.35; Table 2), averaging less than 4. The Ce/Ce* ratio is also low, with a mean under 4 and a maximum of 35.02. In the pyroxene-bearing rocks, Eu/Eu* ratios range from 0.15 to 0.40, displaying negative Eu anomalies (Table 2). Conversely, the BHMzG variety has more irregular ratios from 0.15 to 2.7, with a maximum of 5.88, showing both negative and positive Eu anomalies (Fig. 11b).

The U content and the Th/U ratio in the analyzed zircon crystals also put in evidence significant differences between the RBHMzG variety and the others (Table 2). The reduced monzogranites has low uranium content (132-236 ppm) and high Th/U ratios (0.44-0.76). In contrast, the pyroxene-bearing rocks has higher uranium values (908-1736 ppm) and generally low Th/U ratios, averaging less than 14. The BHMzG variety also has elevated uranium content (548-1858 ppm) and an average Th/U ratio of less than 15.

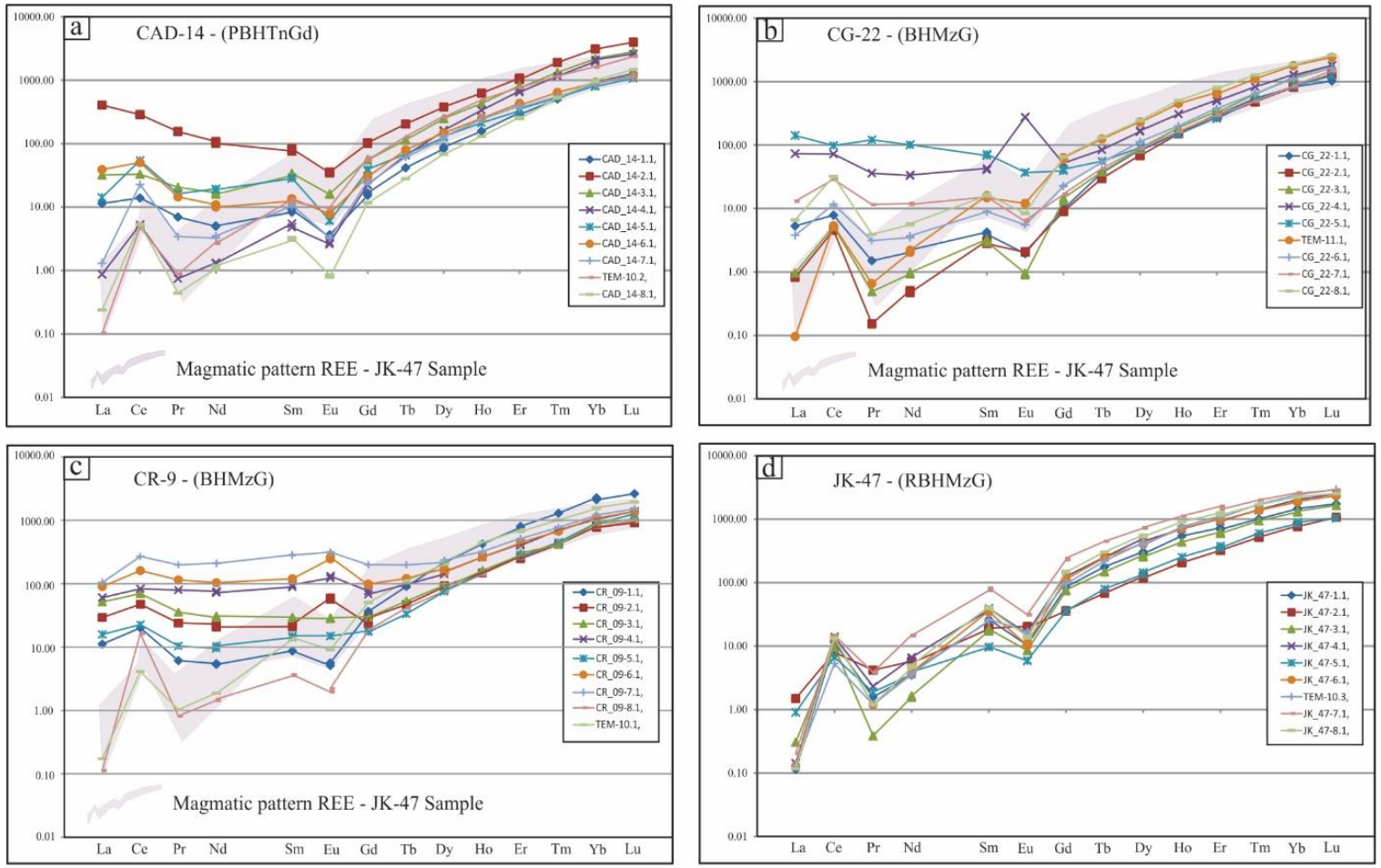

Figure 11. Zircon REE patterns from the IGS varieties: a) PBHTnGd (CAD 14); b) BHMzG (CG-22); c) BHMzG (CR-9); d) RBHMzG (JK-47).

Table 2. REE analyzes by SHRIMP of zircon from the IGS

Sample	CAD-14 (PBHTnGd)								JK-47 (RBHMzG)							
REE spot	1.1	2.1	3.1	4.1	5.1	6.1	7.1	8.1	1.1	2.1	3.1	4.1	5.1	6.1	7.1	8.1
^{139}La	2.70	96.20	7.56	0.21	3.37	9.25	0.31	0.06	0.03	0.35	0.07	0.03	0.22	0.03	0.05	0.03
^{140}Ce	8.53	175.89	20.25	3.24	33.29	30.87	14.02	3.28	7.00	4.89	5.91	8.57	4.12	8.23	9.07	8.30
^{141}Pr	0.65	14.41	1.91	0.07	1.50	1.34	0.32	0.04	0.15	0.39	0.04	0.22	0.17	0.11	0.36	0.11
^{146}Nd	2.32	46.11	7.28	0.59	8.60	4.57	1.61	0.54	1.75	2.47	0.75	3.05	1.79	1.77	6.68	2.29
^{147}Sm	1.23	11.38	4.64	0.81	4.17	1.83	1.53	0.44	3.67	2.74	2.57	5.45	1.42	5.30	11.10	6.14
^{151}Eu	0.19	1.94	0.89	0.15	0.35	0.44	0.18	0.05	0.58	1.15	0.48	0.87	0.33	0.58	1.75	0.80
^{155}Gd	3.04	20.05	11.22	4.42	7.44	6.05	5.06	2.33	16.60	7.09	14.90	26.78	7.00	23.34	45.64	30.19
^{159}Tb	1.50	7.39	4.13	2.37	2.48	2.88	2.21	1.01	6.43	2.46	5.33	9.10	2.88	8.92	16.14	10.95
^{161}Dy	20.35	92.49	60.76	38.74	30.57	36.68	29.50	16.86	75.54	30.79	66.77	121.25	33.29	101.98	177.28	139.10
^{165}Ho	8.60	34.20	23.54	18.39	11.62	13.69	13.20	7.14	29.69	11.27	23.90	38.32	13.86	39.08	61.15	49.46
^{167}Er	46.03	164.04	120.99	103.84	56.13	64.42	58.97	39.32	110.20	51.67	94.85	148.54	56.40	154.15	228.38	185.97
^{169}Tm	12.54	47.05	32.91	28.78	13.18	15.86	13.74	13.12	24.91	12.80	23.26	34.77	14.91	34.16	49.35	41.64
^{171}Yb	147.74	501.18	350.15	316.89	131.32	147.79	140.28	155.43	233.44	126.40	208.45	326.79	136.81	299.11	418.50	362.71
^{175}Lu	31.52	98.04	69.43	64.10	26.48	28.85	28.39	36.40	42.86	26.30	40.59	61.75	25.74	57.39	71.14	62.30
∑LREE	15.61	345.94	42.53	5.06	51.28	48.30	17.96	4.41	13.17	11.98	9.81	18.20	8.05	16.01	29.01	17.67
∑REE	286.93	1310.36	715.66	582.60	330.52	364.52	309.31	276.01	552.84	280.76	487.87	785.50	298.93	734.14	1096.59	900.00
Sm/La$_N$	0.73	0.19	0.98	6.26	1.98	0.32	7.93	12.40	217.48	12.41	56.30	258.35	10.56	274.91	367.80	356.16
Ce/Ce*	1.52	1.02	1.26	6.52	3.57	1.88	9.69	15.79	13.56	2.81	27.72	11.32	4.82	20.32	7.28	20.59
Eu/Eu*	0.30	0.39	0.38	0.24	0.19	0.40	0.20	0.15	0.23	0.79	0.24	0.22	0.32	0.16	0.24	0.18
U/Pb spot	1.1	2.1	3.1	4.1	5.1	8.1	10.1	13.1	1.1	2.10	4.1	5.1	6.1	7.1	9.1	10.1
U ppm	1367.52	945.36	1292.91	1736.71	1653.74	1611.22	908.24	1161.95	236.96	162.62	161.66	204.11	135.85	227.83	132.07	233.96
Th/U	0.12	0.25	0.10	0.09	0.13	0.14	0.08	0.08	0.61	0.44	0.52	0.63	0.46	0.48	0.73	0.47

Sample	CR-9 (BHMzG)								CG-22A (BHMzG)							
Spot	1.1	2.1	3.1	4.1	5.1	6.1	7.1	8.1	1.1	2.1	3.1	4.1	5.1	6.1	7.1	8.1
^{139}La	2.64	6.92	12.21	14.30	3.75	21.33	24.76	0.03	1.26	0.20	0.23	17.34	33.46	0.89	3.08	1.57
^{140}Ce	12.27	29.10	42.68	50.85	13.90	98.42	164.87	9.98	4.82	2.80	3.19	44.32	60.13	7.13	17.70	19.70
^{141}Pr	0.57	2.23	3.31	7.38	0.96	10.65	18.36	0.08	0.14	0.01	0.05	3.35	11.18	0.29	1.07	0.36
^{146}Nd	2.43	9.45	14.12	33.08	4.78	47.34	95.68	0.69	1.02	0.22	0.45	15.40	46.31	1.70	5.32	2.63
^{147}Sm	1.29	3.10	4.38	13.16	2.10	17.74	42.10	0.52	0.63	0.46	0.48	6.33	10.08	1.32	2.24	2.36
^{151}Eu	0.29	3.35	1.58	6.91	0.85	13.87	17.69	0.11	0.11	0.12	0.05	15.41	2.09	0.31	0.35	0.47
^{155}Gd	6.81	4.62	6.00	15.22	3.58	18.88	39.47	3.64	2.05	1.78	2.66	10.08	7.81	4.44	3.31	12.86
^{159}Tb	3.26	1.69	1.91	3.51	1.20	4.37	7.11	1.50	1.32	1.07	1.37	3.03	2.01	1.93	1.54	4.72
^{161}Dy	53.09	21.91	23.30	34.80	18.54	42.48	53.25	18.86	20.60	17.12	21.16	40.06	22.38	27.63	21.94	59.89
^{165}Ho	23.22	8.04	8.81	14.38	8.04	14.38	17.63	7.72	8.41	8.22	10.17	16.80	8.07	10.91	8.88	27.52
^{167}Er	128.23	39.92	48.64	63.99	43.03	71.78	82.15	40.81	47.65	44.80	51.79	79.09	41.55	60.07	47.48	125.35
^{169}Tm	31.85	10.30	10.19	17.35	11.18	16.61	19.03	11.33	13.39	11.84	15.64	20.33	12.75	15.89	12.11	31.17
^{171}Yb	366.55	129.18	144.48	168.63	146.33	180.41	193.06	126.65	131.57	131.53	187.56	207.90	135.13	179.62	136.05	299.36
^{175}Lu	64.81	22.60	25.71	34.16	31.10	33.84	37.19	24.18	25.18	31.76	44.12	44.22	30.28	40.23	36.33	64.49
∑LREE	19.48	54.15	78.29	125.67	26.34	209.35	363.46	11.41	7.98	3.80	4.45	102.14	163.25	11.64	29.77	27.10
∑REE	697.31	292.42	347.34	477.72	289.34	592.08	812.35	246.09	258.17	251.92	338.92	523.65	423.24	352.35	297.41	652.45
Sm/La$_N$	0.78	0.72	0.57	1.47	0.90	1.33	2.72	31.35	0.80	3.76	3.38	0.58	0.48	2.36	1.17	2.41
Ce/Ce*	2.32	1.78	1.60	1.19	1.73	1.57	1.78	35.02	2.31	9.34	7.14	1.32	0.75	3.37	2.36	6.09
Eu/Eu*	0.30	2.70	0.94	1.49	0.94	2.31	1.32	0.24	0.29	0.39	0.15	5.88	0.72	0.39	0.39	0.26
U/Pb spot	1.1	3.1	4.1	5.1	6.1	7.1	8.1	12.1	1.1	5.1	6.1	7.1	10.1	12.1	13.1	14.1
U ppm	1074.54	1067.93	842.06	1858.90	774.01	1148.60	1020.30	1098.54	795.10	815.63	1369.44	1390.61	548.23	1204.96	1303.61	814.22
Th/U	0.09	0.12	0.12	0.14	0.10	0.11	0.10	0.11	0.12	0.10	0.06	0.38	0.15	0.14	0.09	0.14

BHMzG = Bt-Hbl monzogranite; PBHTnGd = Px-Bt-Hbl tonalite-granodiorite; RBHMzG = Reduced Bt-Hbl monzogranite; Ce/Ce* = $Ce_N/(La_N+Pr_N)/2$; Chondrite-normalized from McDonough and Sun (1995).
Eu/Eu*= $Eu_N/(Sm_N*Gd_N)^{1/2}$; Chondrite-normalized from McDonough and Sun (1995).

4.8 WHOLE ROCK Sm-Nd

The obtained data are listed in Table 3 and plotted in Figure 12. $^{147}Sm/^{144}Nd$ ratios vary from 0.0708 to 0.1267, initial $\varepsilon_{Nd}(t)$ values range between -2.86 and 0.18, and T_{DM} ages from 2.98 to 2.84 Ga. Despite the general similarities in $\varepsilon_{Nd}(t)$ values, those of RBHMzG are slightly higher (-0.19 to 0.18) and those of BHTnGd are slightly lower (-2.86 to -2.66) compared to the other varieties. Most obtained ages are upper intercept ages, hence the best estimated ages for the different dated samples of IGS (2.55 Ga and 2.67 Ga) were also employed for definition of $\varepsilon_{Nd}(t)$, resulting in minimal variations in the initial $\varepsilon_{Nd}(t)$ values (Fig. 12 box).

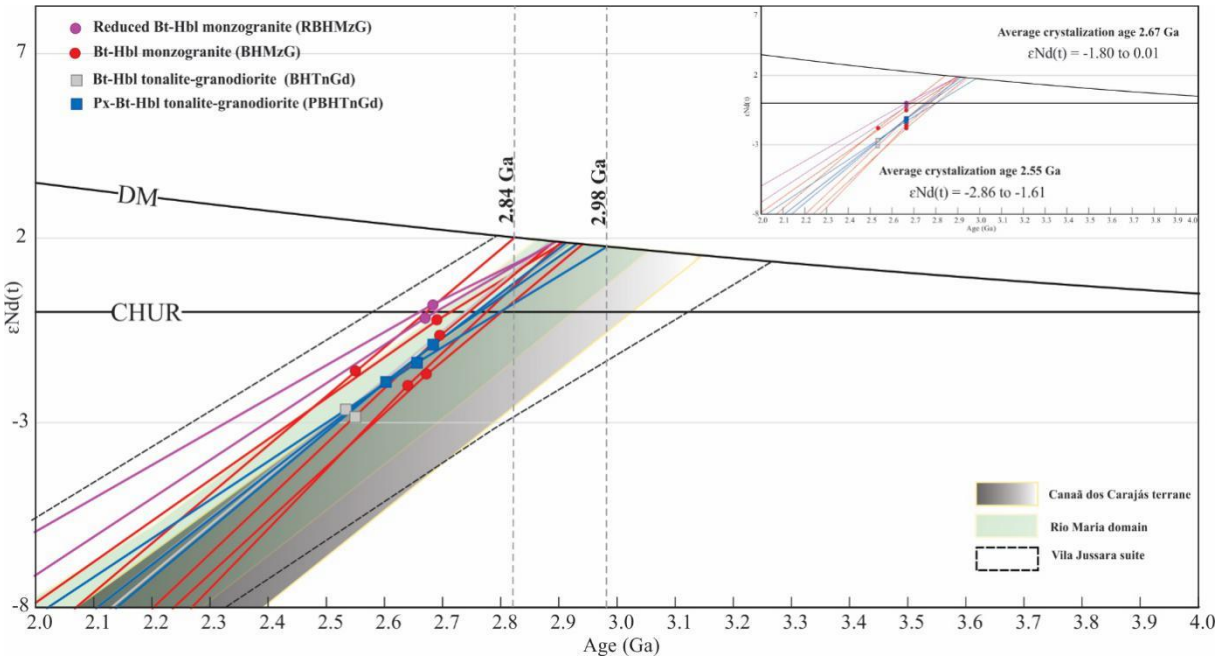

Figure 12: Age vs. $\varepsilon_{Nd}(t)$ plot for IGS varieties. In detail, diagram with the best estimated ages.

Table 3. Whole-rock Sm-Nd isotopic data for the IGS.

Sample/Variety	Sm (ppm)	Nd (ppm)	$^{147}Sm/^{144}Nd$	$^{143}Nd/^{144}Nd$	± 2SE	$f_{(Sm-Nd)}$	$\varepsilon_{Nd}(0)$	$\varepsilon_{Nd}(t)$	Nd-T_{DM} (Ga)	t_{U-Pb} (Ma)
BHMzG										
CR 1A1	2.31	17.27	0.0807	0.510542	11	-0.5897	-40.89	-0.65	2.89	2695
CR-3A	9.82	53.67	0.1106	0.511098	6	-0.4377	-30.04	-0.23	2.91	2690
CG-22	1.69	12.15	0.0839	0.510563	15	-0.5735	-40.48	-1.70	2.94	2672
CR-09	1.59	13.55	0.0708	0.510343	10	-0.6401	-44.77	-2.01	2.91	2640
JK-137A	8.08	52.37	0.0933	0.510817	5	-0.5257	-35.52	-1.61	2.84	2550
RBHMzG										
CR-10B	12.17	63.47	0.1159	0.511205	5	-0.4108	-27.95	-0.19	2.90	2670
JK 47	6.42	30.65	0.1267	0.511408	7	-0.3559	-23.99	0.18	2.90	2683
BHTnGd										
CR-12A	4.50	26.84	0.1013	0.510888	8	-0.4850	-34.14	-2.86	2.95	2550
JK 139 A	17.28	104.94	0.0996	0.51088	5	-0.4936	-34.29	-2.66	2.92	2534
PBHTnGd										
CR-6A	5.66	29.60	0.1155	0.511144	9	-0.4128	-29.14	-1.40	2.98	2656
CR-8A	5.99	35.87	0.1010	0.510897	6	-0.4865	-33.96	-0.91	2.93	2684
CAD-14	8.28	53.18	0.0941	0.510779	3	-0.5216	-36.26	-1.91	2.91	2603

Nd-T_{DM} and $\varepsilon_{Nd}(t)$ were calculated relative to CHUR and Depleted Mantle (DM) with present-day values of $^{143}Nd/^{144}Nd$ = 0.512638 and $^{147}Sm/^{144}Nd$ = 0.1967, following De Paolo and Wasserburg (1976) and De Paolo (1981) models, respectively, for Nd isotopic evolution of depleted mantle.

5 DISCUSSION

5.1 GEOCHEMICAL AFFINITIES

In terms of whole rock geochemistry, the monzogranites from the IGS are similar to the reduced Neoarchean granites of the Vila Jussara, Planalto, and Vila União suites and the Estrela complex (Fig. 4, 5, 7). In contrast, the PBHTnGd and BHTnGTd varieties are closer to the oxidized ferroan and magnesian varieties of the Vila Jussara suite and pyroxene-bearing rocks such as Café enderbite, Rio Seco charnockite, and Matok pluton (Bohlender, 1992). The IGS rocks are depleted in TiO_2 and MgO and more aluminous than the other units selected for comparison (Fig. 4a, b, d). In terms of the trace elements, the rocks from the eastern portion of the IGS batholith (this study) show similar Sr and Rb contents to those from western portion which are associated with IOCG deposits (Diniz et al., 2023; Melo et al., 2016; Toledo et al., 2019), as well as to those of Planalto suite and Estrela complex (Fig. 5a). Carneiro et al. (2023) demonstrated that potassium alteration is dominant in the Northern Copper Belt, although, early Na-Ca alteration is recorded, which imprints a higher molar concentration of K and Na in the rocks of the western sector of the IGS rocks associated with the IOCGs deposits (Fig. 7f). In general, the REE patterns of the PBHTnGd and BHTnGd varieties exhibit negative anomaly of Eu, moderate La/Yb ratio, and overlap with most of those of the granitoids selected for comparison (Fig. 6c). On the other hand, the BHMzG and RBHMzG varieties display less homogeneous REE patterns, with some samples exhibiting positive Eu anomalies and middle-REE depletion that indicates amphibole fractionation (Fig. 6d).

The Neoarchean granites of Carajás are metaluminous to slightly peraluminous, except for the Buritirama granite, Rio Seco charnockite, and Café enderbite, which are essentially metaluminous. The latter two, along with the Matok pluton, are markedly magnesian, whereas the magnesian granitoids from the Vila Jussara suite, and some samples from the Vila União suite are mildly magnesian. Overall, the Neoarchean granites of Carajás align with the calc-alkaline granite trend (Fig. 7e) and plot preferentially in the calc-alkaline field (Fig. 4f). Most of the analyzed samples plot in the A-type granite field (Fig. 7 h, i, k). Some samples from the PBhTnGd and BHTnGd varieties are situated in the calc-alkaline field (Fig. 7h, Dall'Agnol and Oliveira, 2007). According to figure 7i, the IGS granites, alike most of Neoarchean granites of Carajás province, fit into the fields of oxidized and reduced ferroan granites, except for the magnesian granites from the Vila Jussara suite, the Café enderbite, and the Rio Seco charnockite, which plot in the field of Cordilheiran granites or near it (field of calc-alkaline granites in that diagram).

5.2 ORIGIN OF THE IGARAPÉ GELADO SUITE MAGMAS

5.2.1 Neoarchean A-type granites sources

Many authors admit that A-type magmas form in rift environments or stable tectonic areas and result from significant fractionation of mantle-derived mafic magmas. (Bonin, 2007; Eby, 1992; Turner et al., 1992; Nardi et al., 2009; Whalen et al., 1987). However, there is also strong evidence of crustal sources for A-type magmas (Anderson and Bender 1989; Anderson and Morrison, 2005; Dall'Agnol et al., 2005; Rämö and Haapala, 2005; Teixeira et al., 2019). Thus, particularly in compressive or post-collisional environments, it is admitted that A-type granitic magmas could originate from the anatexis of continental crust (Sylvester, 1989; Eby, 1992; Dall'Agnol et al., 2012). The origin of the syntectonic A-type granites of Carajás is an important object of study (Barros et al., 2009; Dall'Agnol et al., 2017; Marangoanha et al., 2019; Silva et al., 2020, 2025). Feio and Dall'Agnol (2012) considered it unlikely that the magmas of the Planalto suite, geochemically analogous to IGS (Fig. 7), could have evolved by fractional crystallization and AFC from mafic magmas due to the high fractionation rate (>80%) required. On the other hand, these authors discussed several hypotheses of magma generation by crustal melt and concluded, based on geochemical evidence and modeling, that the Planalto suite evolved from different partial melting degrees of pyroxene-bearing mafic to intermediate tholeiitic source similar to the rocks of the Pium complex (Pidgeon et al., 2000; Santos et al., 2013). Additionally, Silva et al. (2025) concluded that a deep crustal source similar to the granulites from the Ouro Verde area of the Canaã dos Carajás terrane (Marangoanha et al., 2019b) was able to generate magmas similar to those of the Vila Jussara suite. Nevertheless, such magmas have relatively high water contents (>4%, Dall'Agnol et al., 2017), and their sources would need to be hydrated before melting. In addition, for this suite, heterogeneous sources were assumed, and a model of magma mixing was proposed to generate hybrid rocks showing different degrees of oxidation and varying from reduced and oxidized ferroan to magnesiam granitoids (Dall'Agnol et al., 2017; Silva et al., 2025; Sousa et al. 2022).

Another aspect to be considered is that, in addition to granites, the IGS comprises also pyroxene-bearing tonalites and granodiorites. Hence, it is relevant to compare the genesis of these rocks with proposed generation models for similar rocks of the Carajás province, like the Café enderbite (Marangoanha et al., 2019b) and the orthopyroxene-bearing quartz-gabbro associated with Pium diopside norite (Feio et al., 2012).

5.2.2 Sm-Nd and Lu-Hf isotopes: implications for the petrogenesis of Neoarchean magmatism of Carajás province

The Sm-Nd isotopes suggest that the source rocks of the IGS are dominantly crustal with $\varepsilon_{Nd}(t)$ values ranging from -2.89 to -0.19 and Nd-T_{DM} age between 2.84 Ga and 2.98 Ga, except for the samples of the RBHMzG, which presented slightly positive (JK-47 = 0.18) or mildly negative (CR-10B = -0.19) $\varepsilon_{Nd}(t)$, suggesting possible participation of a juvenile component. The $\varepsilon_{Nd}(t)$ values of the IGS overlap with those of the granitoids from the Vila Jussara, Vila União, and Planalto suites (-3.58 to 1.56; Silva et al., 2025; Marangoanha et al., 2019a; Feio et al., 2012; respectively), but their Nd-T_{DM} ages are slightly younger than the average of other Neoarchean granites (~3.0 Ga).

The $\varepsilon_{Hf}(t)$ values for the RBHMzG variety are generally subchondritic (-2.8 to -0.6) suggesting the involvement of an old crustal source, while the Hf-T_{DM}^{C} ages are Mesoarchean to Paleoarchean (3.17-3.27 Ga), and a little younger than those obtained in the reduced and oxidized amphibole monzogranites from the Vila Jussara suite (3.38-3.24 Ga; Silva et al., 2025) and Café enderbite (3.46-3.29 Ga; Marangoanha et al., 2019b). The negative values of $\varepsilon_{Hf}(t)$ are slightly higher than those obtained for the reduced monzogranites of the Vila Jussara suite (-3.8 to -1.2; Silva et al., 2025) and Vila União (-4.6 to –1.8; Marangoanha et al., 2019b). However, negative and positive values recorded in hybrid granitoids in the Vila Jussara suite are attributed to the occurrence of magma mixing processes with the participation of mantle components. In contrast, the RBHMzG from the IGS, there is no field or geochemical evidence of magma mixing between different varieties neither of significant interaction with country rocks. Hence, it is possible that the highest values of $\varepsilon_{Hf}(t)$ (Population A -1.19 to 0.1) and $\varepsilon_{Nd}(t)$ (-0.19 to 0.18) found in reduced monzogranites can be influenced by its source (see topic 5.2.3). Additionally, the potential influence of hydrothermal alteration on the Lu-Hf system in this variety was ruled out because the analyzed zircon crystals display preserved igneous texture and a magmatic signature of REE (Fig. 9d, 11d). Furthermore, studies indicate that this system is resistant to metamorphism and hydrothermal alteration (Gerdes and Zeh, 2009; Lenting et al., 2010).

Although the Hf-T_{DM}^{C} values in zircon indicate a Paleoarchean to Mesoarchean crust as the source of rocks of the RBHMzG variety, an exposed Paleoarchean record has not been found so far in the Carajás province. Paleoarchean zircon ages were registered only in detrital zircon from quartzites of the Rio Maria domain (Macambira et al., 1998) and rare xenocrystals from the São Felix do Xingu region (Teixeira et al., 2001). In conclusion, the

Mesoarchean Nd-T_{DM} ages of the IGS (2.84 to 2.98 Ga) and other Neoarchean granites from Carajás, with similar geochemical aspects, allow us to infer the genesis of these rocks associated with the anatexis of a lower crust composed of mafic to intermediate granulites, similar to that occurring in the Canaã terrane south of the Carajás basin, represented by the Ouro Verde granulite (Marangoanha et al., 2019b) and the Xicrim Cateté mafic granulites (Silva et al., 2021) crystallized between 3.05–2.93 Ga and metamorphosed at 2.89–2.84 Ga.

5.2.3 Partial melting modeling

Due to the proximity of IGS to IOCG deposits in the Northern Copper Belt (Moreto et al., 2015), it is essential to assess elemental mobility before discussing petrogenesis. This evaluation can be consulted in supplementary data 1.

In the first essay, the hypothesis of the evolution of the IGS granitoids by fractional crystallization from mafic magma was evaluated. It was discarded because mass balance tests confirmed the need for a high degree of mafic liquid fractionation to generate granitic magmas. This would imply a large volume of mafic magma and the absence of exposed mafic rocks in the batholith and the lack of significant intermediate terms in the association suggest it is unlikely (cf. Feio and Dall'Agnol, 2012). Additionally, A/NK vs A/CNK, #mg vs K_2O, and $FeO_t/(FeO_t+MgO)$ vs SiO_2 diagrams (Figs. 7c, d, g) clearly show discordant trends between the tonalite-granodiorite and monzogranitic varieties, a feature that do not favor their derivation from a same initial liquid.

In the source discrimination diagram of Laurent et al. (2014), samples of the tonalitic to granodioritic varieties occur exclusively in the fields of mafic sources with low and high potassium (Fig. 5d), although the pyroxene-bearing rocks are preferentially located in the low-potassium field and the BHTnGd in the high-K field (Fig. 5d). At low partial melt degrees, such sources tend to generate granitic magmas (Sisson et al., 2005). Among the Neoarchean granitoids in the CP, only the Café enderbite (Marangoanha et al., 2019b) is entirely in the field of low-K mafic sources. The other granitoids are generally distributed in the fields of high-K mafic sources extending to the field of metasedimentary source. In this last field, the reduced varieties of the different suites, as well as the Buritirama and G1 granites, are plotted (Fig. 5d).

Given the mentioned geochemical evidences and Sm-Nd isotopic data, samples from the Ouro Verde mafic granulite (Marangoanha et al., 2019b) and Chicrin-Cateté mafic granulites (Silva, 2018) were tested as a source for the (P)BHTnGd and the results in the mass

balance of major oxides were consistent. However, they did not exhibit a good fit in the modeling of trace elements. For this reason, a selected sample (XA12B; Silva et al., 2021) of contaminated Chicrin-Cateté mafic granulite was tested, and it provided excellent results (Table 4a, b). The enrichment of this mafic granulite in Th, Zr, U, and LREE indicates crustal contamination that can occur during the peak of metamorphism when the partial melting of gneisses occurs and the generated liquid (leucosome) interacts with the remaining mafic granulite, resulting in the contamination of the mafic granulite (Silva, 2018; Pearce and Peate, 1995).

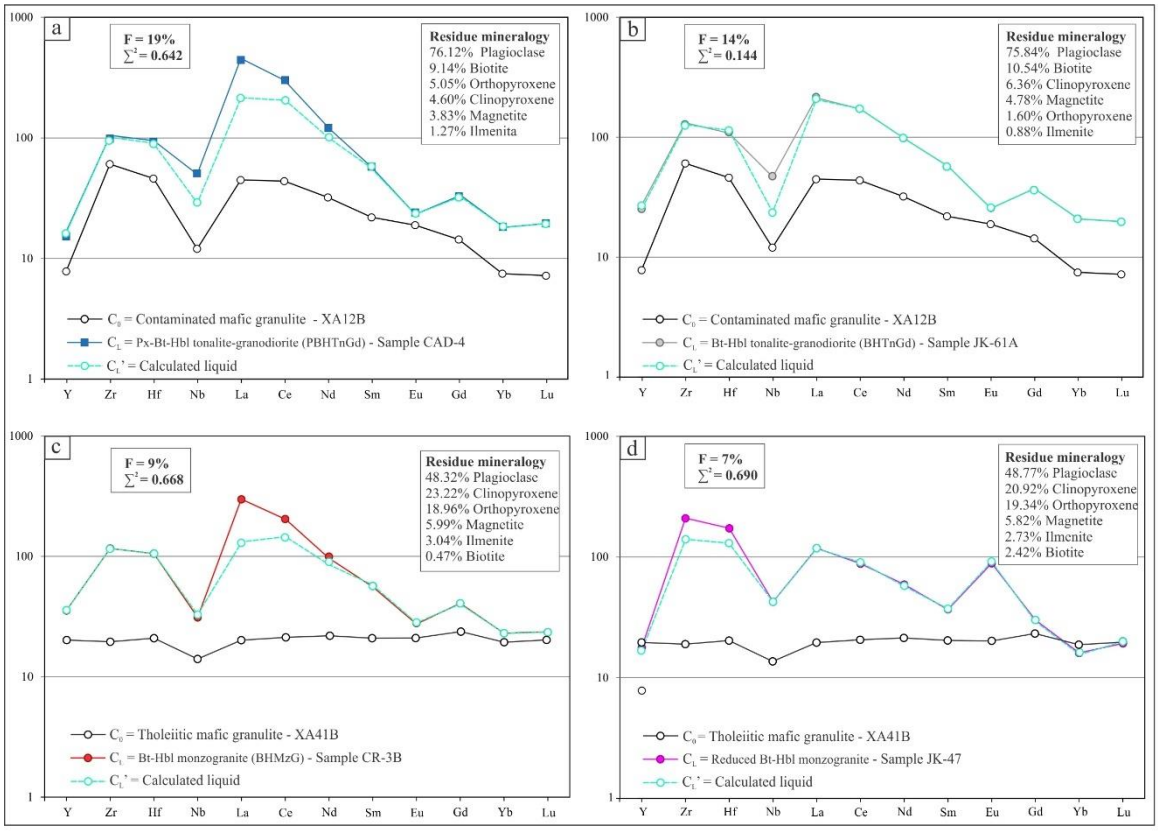

Normalization values are primitive mantle (Palme and O'Neill, 2014).

Figure 13. Modeling of trace elements for generation by partial melt of the four varieties of the Igarapé Gelado suite. a) Px-Bt-Hbl tonalite-granodiorite - sample CAD-4; b) Bt-Hbl tonalite-granodiorite - sample JK-61A; c) Bt-Hb monzogranite - sample CR-3B; d) Reduced Bt-Hbl monzogranite – sample JK-47.

Samples CAD-4 and JK-61A represent the liquid generated for the PBHTnGd (Fig. 13a) and BHTnGd (Fig. 13b) varieties respectively and showed excellent fits with 19% ($\sum R^2$ = 0.642, Table 4a) and 14% ($\sum R^2$ = 0.144, Table 4b) melting (F) of the contaminated mafic granulite (XA12B), leaving a residual assembly composed of plagioclase (76.12 or 75.84%), biotite (9.14 or 10.54%), orthopyroxene (5.05 or 1.6%), clinopyroxene (4.60 or 6.36%), magnetite (3.83 or 4.78%) and ilmenite (1.27 or 0.88%), respectively, for the PBHTnGd and BHTnGd.

Concerning the varieties BHMzG and RBHMzG, their samples plot in the diagram of Laurent et al. (2014) in the border between the evolved rocks of the high-K mafic field and the metasedimentary source field. The more accentuated reduced character of the RBHMzG (Mesquita et al., 2025) could possibly be explained by origin of its magma from low degree of melting of a tholeiitic intermediate source or from a metasedimentary source or even from a mixture of both. The BHMzG magma could be derived from a similar source but with less marked influence of a metasedimentary source.

Therefore, to model the source of these varieties, a sample with a tholeiitic character of Chicrin-Cateté mafic orthogranulite (XA41B sample, Silva et al., 2021) was modeled. This sample showed good results in the mass balance of major oxides and in the modeling of trace elements. This hypothesis is supported by the $\varepsilon_{Hf}(t)$ values of mafic granulite Chicrin-Cateté, which range from -0.7 to 0.3, and are mostly similar to those of population A from the reduced monzogranites, ranging from -1.19 to 0.1.

It was assumed that the liquids that generated the BHMzG and RBHMzG correspond to the CR-3B (Fig. 13c) and JK-47 (Fig. 13d) samples, respectively. With similar and low degrees of melt of a tholeiitic mafic granulite source, these samples showed excellent adjustments at 9% ($\sum R2 = 0.668$, Table 4c) and 7% ($\sum R2 = 0.690$, Table 4d), providing a residual assemblage composed of plagioclase (48.32 or 48.77%), orthopyroxene (18.96 or 19.34%), biotite (0.47 or 2.42%), clinopyroxene (23.22 or 20.92%), magnetite (5.99 or 5.82%) and ilmenite (3.04 or 2.73%), respectively.

Magmas forming A-type granites can derive from remelting of a same source (Creaser et al., 1991). Hence, in the initial liquids, the water content will be enhanced increasing the oxidizing character of early magmas (Feig et al., 2010). This could generate liquids with water content exceeding 4% (Dall'Agnol et al., 2017; Mesquita et al., 2025) and leads to the crystallization of magnetite and hydrated ferromagnesian minerals with a relatively low Fe/Mg ratio like the BHMzG (Mesquita et al., 2025). With the advancement of the anatexis process, the decreasing water from the source promotes the formation of reduced late melts. Experiments indicate that low water content also results in lower melt rates (Feig et al., 2006). Therefore, in the IGS, we can admit that the RBHMzG derived from late monzogranitic liquids, that were produced by lower degrees (7%, Fig. 13d) of partial melting of water depleted and more reduced sources, compared to those that originated the earlier BHMzG (Cf. Silva et al., 2025). The younger crystallization age of the reduced monzogranites (~2.68 Ga, Fig. 8), compared to the oldest rocks from the Igarapé Gelado suite (2.76 Ga, Melo et al.,

2016), reinforces the hypothesis of the origin of the RBHMzG from late anatexis during the evolution of the Igarapé Gelado batholith.

Despite geochemical data suggesting a common source for BHMzG and RBHMzG, we should interpret this with caution. The Age vs. $\varepsilon_{Nd}(t)$ plot (Fig. 12) reveals that the samples from BHMzG do not align with those from reduced monzogranites, except for one sample. This contrasts with the good alignment observed in the PBHTnGd and BHTnGd samples which suggests its cogeneticity.

Table 4. Modeled composition of major elements and trace elements and composition of residual mineralogy for generation of the varieties a) PBHTnGd, b) BHTnGd, c) BHMzG; d) RBHMzG from the partial melt of Chicrin-Cateté mafic granulite.

a)	Source rock	Residual mineralogy						Residual bulk (C_o)	Calculated magma (C_L')	Modeled sample	
	XA12B (C_o)[a]									**CAD-4[a]**	
	Contaminated	Plg[b]	Bt[c]	Opx[b]	Cpx[b]	Mt[d]	Ilm[e]	Total	**F= 19%**	Variety	
	mafic granulite [b]	76.12%	9.1%	5.05%	4.60%	3.83%	1.27%	100.0	$\sum^2$ = **0.642**	**PBHTnGd**	
Major elements (weight %)											b.dif cal
SiO_2(wt. %)	54.34							51.99	65.35	65.52	11.01
TiO_2	0.88							1.13	0.38	0.51	-0.5
Al_2O_3	20.68							22.08	15.69	15.95	-4.99
Fe_2O_{3t}	7.63							8.08	6.23	6.36	-1.4
MnO	0.09							0.08	0.05	0.03	-0.04
MgO	2.51							2.92	0.87	0.9	-1.64
CaO	6.91							7.72	3.82	3.93	-3.09
Na_2O	5.7							5.04	5.5	4.79	-0.2
K_2O	1.24							0.95	2.1	2.01	0.86
Trace Elements (ppm)											
Y	11.4								30.7	32.7	
Zr	220.0								378.0	389.0	
Hf	4.9								9.9	10.3	
Nb	3.4								7.0	14.2	
La	10.8								41.9	116.0	
Ce	27.1								109.1	194.5	
Nd	15.2								48.8	59.2	
Sm	3.4								8.7	8.9	
Eu	1.1								1.4	1.4	
Gd	3.0								7.1	6.9	
Yb	1.3								3.2	3.0	
Lu	0.2								0.5	0.5	

b)	Source rock	Residual mineralogy						Residual bulk (C_o)	Calculated magma (C_L')	**JK-61A[a]**
	XA12B (C_o)[a]									
	Contaminated	Plg[b]	Bt[c]	Cpx^C	Mt[d]	Opx[b]	Ilm[e]	Total	**F= 14%**	Variety
	mafic granulite [b]	75.84%	10.54%	6.36%	4.78%	1.60%	0.88%	100.0	$\sum^2$ = **0.144**	**BHTnGd**
Major elements (weight %)										
SiO_2(wt. %)	54.34							52.55	65.67	65.75
TiO_2	0.88							1.01	0.46	0.52
Al_2O_3	20.68							21.57	16.12	16.26
Fe_2O_{3t}	7.63							7.96	6	6.07
MnO	0.09							0.07	0.06	0.03
MgO	2.51							2.82	0.83	0.86
CaO	6.91							7.48	3.83	3.88
Na_2O	5.7							5.42	5.41	5.08
K_2O	1.24							1.13	1.61	1.56
Trace Elements (ppm)										
Y	11.4								36.7	39.6
Zr	220.0								491.2	474.0
Hf	4.9								12.5	11.8
Nb	3.4								6.7	14.2
La	10.8								51.4	56.6
Ce	27.1								110.3	107.0
Nd	15.2								46.7	47.5
Sm	3.4								9.2	9.1
Eu	1.1								1.5	1.4
Gd	3.0								7.8	8.2
Yb	1.3								3.5	3.3
Lu	0.2								0.5	0.5

c)	Source rock	Residual mineralogy						Residual bulk (C_o)	Calculated magma (C_L')	Modeled sample	
	XA41B (C_o)[a]									**CR-3B[a]**	
	Tholeiitic	Plg[b]	Cpx^b	Opx[b]	Mt[d]	Ilm[e]	Bt[c]	Total	**F= 9%**	Variety	
	mafic granulite [b]	48.32%	23.2%	18.9%	5.99%	3.04%	0.47%	100.0	$\sum^2$ = **0.668**	**BHMzG**	
Major elements (weight %)											b.dif cal
SiO_2(wt. %)	49.9							47.76	70.09	69.83	20.19
TiO_2	1.31							1.52	0.31	0.43	-1
Al_2O_3	14.58							14.88	13.46	13.66	-1.12
Fe_2O_{3t}	13.82							14.75	5.13	5.24	-8.69
MnO	0.19							0.28	-0.04	0.03	-0.23
MgO	6.83							7.45	0.45	0.47	-6.38
CaO	9.99							10.81	2.24	2.33	-7.75
Na_2O	3.29							2.44	4.37	3.62	1.08
K_2O	0.49							0.1	4.40	4.38	3.91
Trace Elements (ppm)											
Y	29.1								57.6	51.8	
Zr	70.0								437.0	422.0	
Hf	2.2								11.2	11.2	
Nb	3.9								9.4	8.8	
La	4.8								28.2	80.1	
Ce	13.0								70.1	141.0	
Nd	10.3								38.5	45.7	
Sm	3.2								9.0	8.6	
Eu	1.2								1.7	1.6	
Gd	4.9								8.2	8.4	
Yb	3.2								3.8	4.1	
Lu	0.5								0.6	0.6	

d)	Source rock	Residual mineralogy						Residual bulk (C_o)	Calculated magma (C_L')	Modeled sample
	XA41B (C_o)[a]									**JK-47[a]**
	Tholeiitic	Plg[b]	Cpx^b	Opx^b	Mt[d]	Ilm[e]	Bt[c]	Total	**F= 7%**	Variety
	mafic granulite [b]	48.77%	20.92%	19.34%	5.82%	2.73%	2.42%	100.0	$\sum^2$ = **0.690**	**RBHMzG**
Major elements (weight %)										
SiO_2(wt. %)	49.9							47.94	72.79	72.49
TiO_2	1.31							1.48	0.26	0.36
Al_2O_3	14.58							14.91	12.75	12.95
Fe_2O_{3t}	13.82							14.57	4.72	4.81
MnO	0.19							0.28	-0.04	0.04
MgO	6.83							7.35	0.1	0.13
CaO	9.99							10.65	2.02	2.1
Na_2O	3.29							2.46	4.04	3.27
K_2O	0.49							0.35	3.76	3.85
Trace Elements (ppm)										
Y	29.1								27.1	25.9
Zr	70.0								529.8	760.0
Hf	2.2								14.8	18.4
Nb	3.9								12.3	12.0
La	4.8								27.8	28.5
Ce	13.0								55.6	54.5
Nd	10.3								27.9	28.0
Sm	3.2								5.8	5.6
Eu	1.2								5.3	5.2
Gd	4.9								5.8	6.2
Yb	3.2								2.6	2.7
Lu	0.5								0.5	0.5

Abbreviations: Opx = orthopyroxene; Cpx = clinopyroxene; Bt = biotite; Plg = plagioclase; Mt = magnetite; Ilm Ilmenite.
[a]Original oxide values recalculated to 100%; [b]Mafic Granulite Chicrin Cateté From Silva (2018) ; [c]Values from Marangoanha et al. (2022); [d]Values from Moraes et al (2022);[e]Values from El-Desoky et al (2023); ∑2 = Sum of the squared residuals; All iron is reported as Fe_2O_3t

5.3 CONSIDERATIONS ABOUT HYDROTHERMAL PROCESSES ON THE IGARAPÉ GELADO SUITE EVOLUTION: FALSE A1-SUBTYPE GRANITES?

The Igarapé Gelado batholith is sectioned by the Cinzento shear zone (Pinheiro and Holdsworth, 2000), that imprinted in it mesoscopic and microstructural deformational features (Fig. 2, 3). The granitoids of IGS are spatially associated with the IOCG deposits of the Northern Cupro-Auriferous Belt of Carajás (Diniz et al., 2023; Melo et al., 2016, 2019; Toledo et al., 2019, 2023) and were affected by the hydrothermal fluids responsible for the origin of IOCG mineralization (Lacasse et al., 2020; Monteiro et al., 2008; Moreto et al., 2015; Trunfull et al., 2020; Xavier et al., 2012) (Fig. 1c).

Unlike the other Neoarchean granites from the Carajás that plot systematically in the field of A2-subtype granites, as defined by Eby (1992), some samples of the BHMzG variety are situated in the field of A1-subtype granites (Fig 7j). These samples show low Y contents and also exhibit accentuated depletion in REE (Fig. 6b). An A1-subtype geochemical signature is generally seen as evidence of mantle origin, however, the BHMzG samples, including five low Y samples (CR-1A, CR-1A1, CR-5, CR-9 and CG-22), classified as A1-subtype granites, exhibit subchondritic $\varepsilon_{Nd}(t)$ (Fig. 12; -0.65 to -2.01) and do not show evidence of participation of a mantle component in the origin of its magma.

Carneiro et al. (2023) compiled 1040 analyses of hydrothermalized rock samples from the Carajás cupro-auriferous belts and used multivariate statistical tools to assess the genetic processes and geochemical signatures of the ore deposits related to them. In the northern belt, Neoarchean IOCG deposits were found to be dominated by potassium alteration with increased REE levels in mineralized bodies. In contrast, the southern belt showed high concentrations of granitophile elements (Sn, Mo, Y), indicating the influence of evolved alkaline granites (Carneiro et al., 2023). The heat liberated by the intrusions of Paleoproterozoic A-type granites of the Serra dos Carajás suite (~1.88 Ga; Teixeira et al., 2018) facilitated the movement of magmatic-hydrothermal fluids, enhancing fluid-rock interactions and leading to significant mobilization and leaching of metals (Moreto et al., 2015; Pollard et al., 2019; Tallarico et al., 2004; Trunfull et al., 2020). Hence, it is reasonable to admit that the depletion of REE, Y, and Yb in A1-subtype BHMzG is likely due to the action of hydrothermal fluids that leached and concentrated these elements in nearby mineralized bodies (Sheard et al., 2012). In the northern belt, $^{\delta 18}O$, S, and B isotope data indicate a contribution of magmatic sources for the mineralizing fluids of the Salobo IOCG deposit (Melo et al., 2019; Melo et al., 2021). This pattern also appears in the GT-46 deposit,

where it is supported by fluid inclusion data (Toledo et al., 2019) and REE analyses in apatite (Diniz et al., 2023). The REE depletion and the marked positive anomaly of Eu in REE patterns in whole-rock of GT-46 granite (G2) approach it compositionally of the low-Y BHMzG (Fig. 6b, d). In addition, the REE signature of the apatite from G2 granite and mineralized samples from the Gt-46 and Old Salobo deposits suggest hydrothermal fluid movement during or shortly after the emplacement of these granites (Diniz et al., 2023), reinforcing the leaching hypothesis. Given the spatial proximity of the IGS to these Cu-Au deposits (Fig 1c), it is admissible that hydrothermal fluids had percolated in a heterogeneous way some portions of the IGS and leached selectively some elements, such as REE and Y, that show generally reduced mobility. This process modified the original magmatic compositions of altered granites and significantly affected their zircon crystals (Wang et al., 2024), interfering with the U-Pb system and changing REE composition as observed in their REE patterns (Fig. 5d). Yttrium normally follows geochemically REE and should be also depleted in the granites affected by these hydrothermal processes. This can explain the anomalous behavior of these samples in the Nb-Y-Zr/4 diagram (Fig. 7j). Hence, the actual compositions of the low-Y BHMzG do not correspond to original magmatic ones and it implies that they cannot be classified as A1-subtype granites.

5.4 SIGNIFICANCE OF ZIRCON U–Pb SHRIMP AGES

The concordant (Fig. 8, RBHMzG) and upper intercept (PBHTnGd and BHMzG) ages range from 2.68 to 2.60 Ga (Fig. 10) Ga, and are younger than the dominant ages of the Neoarchean granitic magmatism of Carajás (2.75 to 2.73 Ga, references in Table S1), including some rocks of the IGS (~2.74 Ga, Melo et al., 2016; Toledo et al., 2019). The mentioned younger ages are registered in the IGS and in the Lavrado suite granites (Reis, 2017; Tavares et al., 2021; Silva et al., 2023). Toledo et al. (2023) suggest that only the ages between 2.73-7.74 Ga (granodiorite gneiss, SAL-65 sample) should be considered as the crystallization ages of the IGS, while the ages between 2.68 and 2.70 Ga, would represent a deformational event (~2.70 – Cinzento Lineament, Pinheiro and Holdsworth, 2000), as recorded in the zircons of a foliated tonalite (Toledo et al., 2023) and mylonite (Melo et al., 2016). In these rocks, there was radiogenic Pb loss that would indicate zircon re-equilibration (dissolution-reprecipitation) during fluid-assisted ductile deformation, especially in metamict grains. However, the concordant ages reduced monzogranite obtained in zircons with preserved oscillatory zoning (Fig. 8b, e) and typical magmatic REE signature (Fig. 11d) are strong evidence that that rock was not intensely altered, and its ages can be attributed to

crystallization. Toledo et al. (2023) further indicates that the ages between 2.62-2.64 Ga are inconclusive, as they may represent domain mixing in zircon crystals. The high MSWD (5.4) of the population B in the JK-47 sample (2.64 Ga, Fig. 8d) may indicate a mixture. Two samples of the BHTnGd and BHMzG, located in the extreme west of the mapped area (Fig. 1c), near the Salobo deposit, showed upper intercept ages of approximately 2.55 Ga, similar to those found in the Old Salobo and Igarapé Cinzento granites (Melo et al., 2016; Toledo et al., 2023), as well as in mineralized rocks from the Salobo IOCG deposit (2555 ± 4 and 2497 ± 5 Ma U-Pb in zircon and titanite, respectively, Machado et al., 1991). These ages may be linked to the tectono-thermal reactivation of the Cinzento Lineament (~2.5 Ga), which likely reset the U-Pb system in affected rocks (Melo et al., 2016).

Mezger and Krogstad (1997) explain that if the U-Pb system of zircon is partially reset, discordant curves can appear, and the upper intercept can indicate the crystallization age of the rock. Conversely, if fully reset, the age reflects the last thermal event. The upper intercept ages (2.67-2.69 Ga) of the PBHTnGd (CR-8A sample) and BHMzG (CR-1A1 and CG-22 samples) varieties align with the concordant ages of population A in the RBHMzG variety (2.67-2.68 Ga) and they could likely represent their crystallization ages. In contrast, the IGS rocks with upper intercept ages around 2.55 Ga may result of the total system reset, as supported by the zircon crystal textures discussed below.

5.5 THE INFLUENCE OF MAGMATISM AND HYDROTHERMALISM ON THE REE AND OTHER TRACE ELEMENTS COMPOSITION IN ZIRCON.

Hydrothermal fluids can effectively dissolve and transport REE, Nb, Y, U, and Ta, leading to these elements being incorporated into metamitic zircons, which are prone to textural and compositional changes due to accumulated radiation damage (Park et al., 2016; Sheard et al., 2012; Wang et al., 2024). The modifications of zircon are based on diffusion–reaction and interface-coupled dissolution-reprecipitation (Putnis and Austrheim, 2013; Rubatto, 2017; Toledo et al., 2023). Toledo et al. (2023) described textural features in zircons of deformed rocks from IGS and similar granites. The alteration processes destroy the oscillatory zoning replacing it with homogeneous, diffuse, or convolute patterns. This alteration causes enrichment in U, Th, Y, and REE. Borba et al. (2021) show that in hydrothermally altered rocks from the southern copper belt of the Carajás Province, zircon crystals have a massive texture, rare oscillatory zoning, and a light to dark gray color. They also possess similar compositional traits, including high levels of U, Th, and REE. These features align with those of the PBHTnGd (Fig 9a) and BHMzG zircon crystals (Fig. 9b, c),

which exhibit discordant U-Pb ages (Fig. 10), and more irregular REE patterns (Fig. 11a, b, c), while zircon crystals of the RBHMzG variety display a preserved oscillatory zoning pattern, along with more uniform REE pattern, low contents of LREE and U, and high of Th (Fig. 9d, 11d). Their REE patterns resembles that of zircons from preserved igneous rocks in the Gawler Craton, Australia (Brotodewo et al., 2021, Fig. 11d), and from barren granitoids at an IOCG deposit in southern Australia (Wade et al., 2022).

In the U vs La_N (Fig. 14a) and U vs. Th+U diagrams, RBHMzG zircons are located within the magmatic zircon field or near it (Fig. 14b, fields of Borba et al., 2021). However, PBHTnGd, BHTnGd (not shown in the diagram, but with >1000 ppm of U, Table S4) and BHMzG zircons are distributed among the hydrothermally altered zircon or in the essentially hydrothermal zircon fields. The Ce/Ce* ratio was employed as an index of hydrothermal alteration in IOCG-related rocks (Wade et al., 2022). In the binary Ce/Ce* vs Sm_N/La_N (Fig. 14 c) and Sm_N/La_N vs. La (Fig. 14d) diagrams, the zircons of the PBHTnGd and BHMzG varieties fall mostly within or close to the hydrothermal zircon field (Hoskin, 2005). Finally, Toledo et al. (2023) added to these two diagrams a hydrothermal zircon field for the Neoarchean granitoids from Carajás. It can be observed that the zircons from PBHTnGd and BHMzG plot mainly in that field. In contrast, zircons of the reduced monzogranites fall within or near the magmatic zircon field in all diagrams. It is concluded that the chemical composition of zircon crystals of RBHMzG reinforces evidence of preservation of its magmatic signature and give support to the interpretation of the meaning of the concordia ages. On the other hand, the zircons crystals of PBHTnGd and BHMzG were apparently disturbed by hydrothermal processes, and this explains the more irregular behavior of the U-Pb system and the impossibility to get Concordia ages for these rocks.

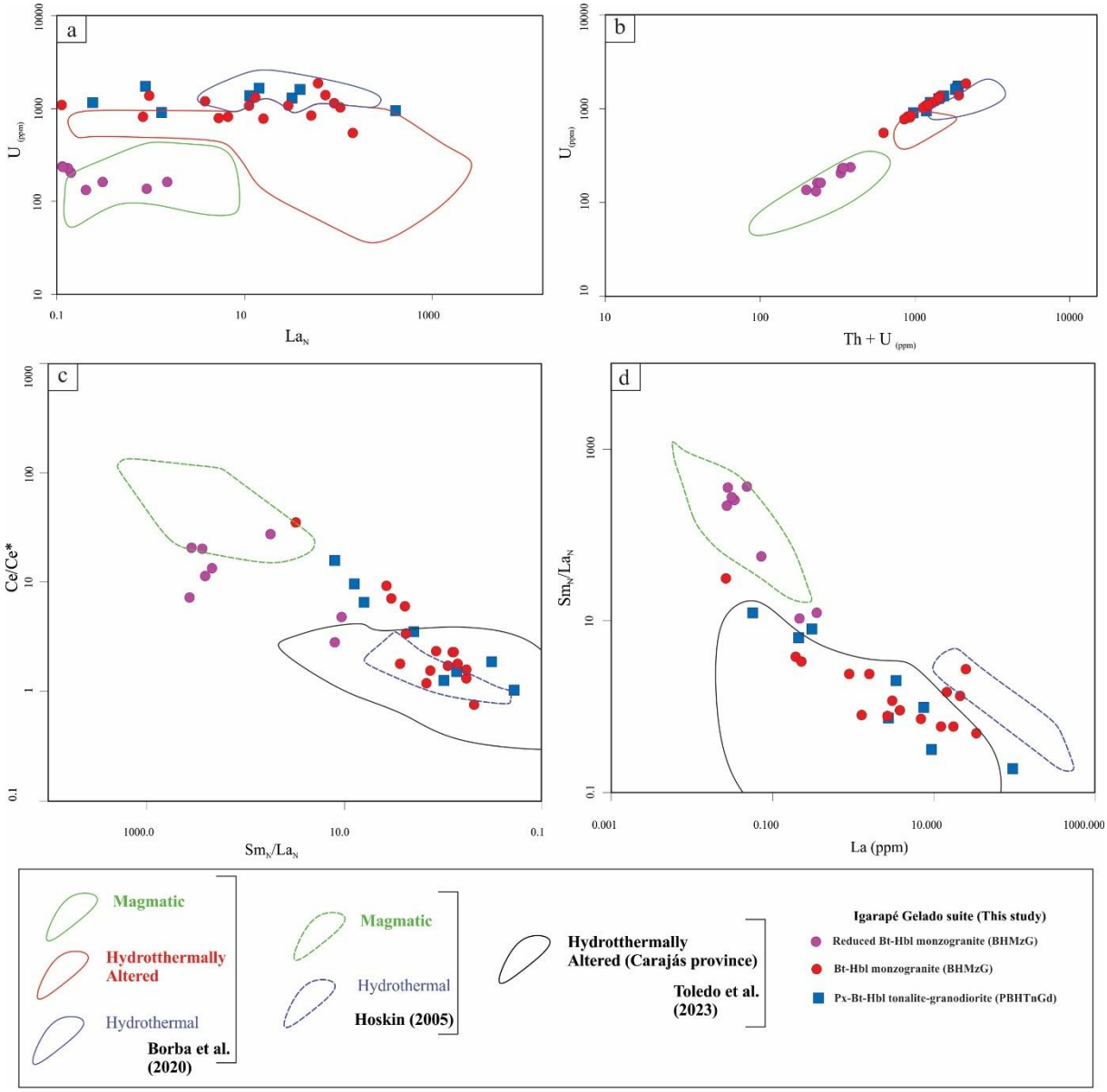

Figure 14: Evaluation of degree of hydrothermal alteration in zircon crystals of IGS : a) U vs. La_N; b) U vs. (Th + U);c) Ce/Ce* vs Sm_N/La_N e; d)Sm_N/La_N vs. La. All elements in ppm.

6 CONCLUSIONS

Rocks far from the SZ are poorly deformed and preserve primary igneous texture. In contrast, those near the SZ are more deformed and show mylonite to ultramylonite textures.

In terms of major elements, the monzogranites of IGS are similar to the reduced Neoarchean granites of the Vila Jussara, Planalto, and Vila União suites and the Estrela complex and the PBHTnGd and BHTnGd are close to the oxidized and magnesian ferroan varieties of the Vila Jussara suite, and to Café enderbite, Rio Seco chanockite, and Matok pluton granitoids. Rocks from the western sector of the IGS, associated with IOCG deposits, have higher molar values of Na and K compared to rocks from the eastern sector of the IGS

(this study). The REE patterns of the PBHTnGd and BHTnGd varieties overlap most of those of the other Neoarchean Carajás granites. In contrast, the BHMzG and RBHMzG do not display homogeneous REE patterns.

Isotope data suggest a crustal source for the IGS, with $\varepsilon_{Nd}(t)$ and $\varepsilon_{Hf}(t)$ values ranging from –2.86 to 0.18 and –3.3 to 0.1, respectively. The Nd TDM ages are Mesoarchaean (2.98 to 2.84), and Mesoarchaean to Paleoarchaean age for the RBHMzG (Hf-T_{DM}^{C} 3.27-3.12). Less negative $\varepsilon_{Nd\text{-}Hf}(t)$ values for the reduced monzogranites indicate a possible juvenile contribution to its source.

Partial melting of a modified mafic granulite was defined as a probable source of the PBHTnGd and BHTnGd varieties, with an estimated degree of melting of 19% and 14%, respectively. Meanwhile, for the BHMzG and RBHMzG varieties, partial melting of mafic granulite of tholeiitic character was defined with an estimated degree of melting of 9% and 7%, respectively.

Concordant ages have been defined for the RBHMzG variety (~2.68, ~2.65, and ~2.60 Ga) that overlap with up intercept ages from the other varieties. Although only the ~2.68 age obtained for the RBHMzG can be demonstrated as its crystallization age, it is assumed that the ages of the other varieties are similar to it. The new geochronologic data for the IGS indicate that its magmatism is younger than the dominant Neoarchean granitoids of the Carajás province (~2.74 Ga). In addition to these, the upper intercept ages of ~2.5 Ga defined for the BHMzG and BHTnGd, resembling the ages of host and mineralized rocks from the Salobo IOCG deposit, have been attributed to the effects of the thermal reactivation event of the Cinzento lineament that led to a complete reset of the U-Pb system.

In the proximity of hydrothermally altered areas, particularly the Cinzento SZ and the Northern Cupro-Auriferous belt, the composition of rocks and minerals of the IGS rocks were modified with the leaching of REE and Y, leading to the identification of false A1-subtype granites as part of the BHMzG. Hydrothermal activity has also modified original texture and composition (metamictization) of zircon crystals, resulting in massive textures and enrichment of U, Th, and LREE, except for RBHMzG zircons that retain primary characteristics. These findings enhanced our understanding of U-Pb geochronological results.

Our results highlight the significance and some particular features of the IGS extensive magmatism when compared to the Neoarchean granites of Carajás province. They also clarify how hydrothermal processes can affect the chemistry and texture of zircon in granitoid rocks

and the influence this can exert in the interpretation of geochronologic data. Careful mineralogical studies in zircon are of great importance to understanding of evolutionary aspects of granitoids and this particularly true in Archean terranes and in mineralized provinces.

7 ACKDNOWLEDGEMENTS

The authors acknowledge the Group of Research on Granitoid Petrology (GRGP), the Post-Graduate Program in Geology and Geochemistry (PPGG). We are also grateful to Kei Sato for assistance during the acquisition of the U-Pb and REE SHRIMP data at the Laboratório de Geologia de Alta Resolução (USP). Luciano Ribeiro da Silva is acknowledged for his support with geochemical modeling. We thank Geological Survey of Brazil for concessions of the samples. Geologists Sergio Huhn (VALE S.A.), Clovis Wagner Maurity and Alessandro Sabá Leite (ITV DS) are acknowledged by support in field work.This research was financed in part by the Conselho Nacional de Desenvolvimento Científico e Tecnológico (CNPq) (R. Dall'Agnol; Proc.3006767/2019–8) and by the Coordenação de Aperfeiçoamento de Pessoal de Nível Superior (CAPES) for granting a scholarship to the first author (C. J. S. Mesquita; 88882.347890/2019–01).

REFERENCES

Almeida, J.A.C, Dall'Agnol, R., de Oliveira, M.A., Macambira, M.J.B., Pimentel, M.M., Rämö, O.T., Guimarães, F.V., da Silva Leite, A.A., 2011. Zircon geochronology, geochemistry and origin of the TTG suites of the Rio Maria granite-greenstone terrane: Implications for the growth of the Archean crust of the Carajás province, Brazil. Precambrian Res. 187, 201–221.

Almeida, J.AC, Dall'Agnol, R., Leite, A., 2013. Geochemistry and zircon geochronology of the Archean granite suites of the Rio Maria granite-greenstone terrane, Carajás Province, Brazil. J. South Am. Earth Sci. 42, 103–126. https://doi.org/10.1016/j.jsames.2012.10.008

Andersen, T., Andersson, U.B., Graham, S., Åberg, G., Simonsen, S.L., 2009. Granitic magmatism by melting of juvenile continental crust: new constraints on the source of Palaeoproterozoic granitoids in Fennoscandia from Hf isotopes in zircon. J. Geol. Soc. London 166, 233–247.

Anderson, J.L., Morrison, J., 2005. Ilmenite, magnetite, and peraluminous Mesoproterozoic anorogenic granites of Laurentia and Baltica. Lithos 80, 45–60. https://doi.org/https://doi.org/10.1016/j.lithos.2004.05.008

Anderson, J.L., Bender, E.E., 1989. Nature and origin of Proterozoic A-type granitic magmatism in the southwestern United States. Lithos 23, 19–52.

Araújo, O.J.B., Maia, R.G.N., João, X.S.J., Costa, J.B.S., 1988. A megaestruturação arqueana da folha Serra dos Carajás, in: Congresso Latino-Americano de Geologia. SBG-NO Belém, pp. 324–338.

Avelar, V.G., Lafon, J.-M., Correia Jr, F.C., Macambira, E.M.B., 1999. O magmatismo arqueano da região de Tucumã Província Mineral de Carajás: novos resultados geocronológicos. Brazilian Journal of Geology 29, 453–460.

Barker, F., 1979. Chapter 1 - Trondhjemite: Definition, Environment and Hypotheses of Origin, in: BARKER, F. (Ed.), Developments in Petrology. Elsevier, pp. 1–12. https://doi.org/https://doi.org/10.1016/B978-0-444-41765-7.50006-X

Barker, F., Arth, J., 1976. Generation of trondhjemitic-tonalitic liquids and Archean bimodal trondhjemite-basalt suites. Geology 4. https://doi.org/10.1130/0091-7613(1976)4<596:GOTLAA>2.0.CO;2

Barros, C.E., Sardinha, A.S., Barbosa, J.P.O., Macambira, M.J.B., Barbey, P., Boullier, A.-M., 2009. Structure, petrology, geochemistry and zircon U/Pb and Pb/Pb geochronology of the synkinematic Archean (2.7 Ga) A-type granites from the Carajás Metallogenic Province, northern Brazil. The Canadian Mineralogist 47, 1423–1440.

Black, L., Kamo, S., Allen, C.M., Davis, D., Aleinikoff, J., Valley, J., Mundil, R., Campbell, I., Korsch, R., Williams, I., Foudoulis, C., 2004. Improved $^{206}Pb/^{238}U$ microprobe geochronology by the monitoring of trace-element-related matrix effect: SHRIMP, ID-TIMS, ELA-ICP-MS and oxygen isotope documentation for a series of zircon standards. Chem Geol 205, 115–140. https://doi.org/10.1016/j.chemgeo.2004.01.003

Black, L.P., Gulson, B.L., 1978. The age of the Mud Tank Carbonatite, Strangways Range, Northern Territory, BMR Journal of Australian Geology & Geophysics.

Bohlender, F.B.D. by, 1992. Igneous and metamorphic charnockitic rocks in the southern marginal zone of the Limpopo belt with special emphasis on the Matok enderbitic-granitic suite. PhD Thesis. University of Johannesburg. Johannesburg, November 1992

Bonin, B., 2007. A-type granites and related rocks: evolution of a concept, problems and prospects. Lithos 97, 1 e 2.

Borba, M.L., Tassinari, C.C.G., Matos, F.M. V, Sato, K., Huhn, S., Ferreira, S.N., Medeiros, C.A., 2021. Tracking hydrothermal events using zircon REE geochemistry from the Carajás Mineral Province, Brazil. J. Geochem. Explor. 221, 106679. https://doi.org/https://doi.org/10.1016/j.gexplo.2020.106679

Bouvier, A., Vervoort, J.D., Patchett, P.J., 2008. The Lu–Hf and Sm–Nd isotopic composition of CHUR: Constraints from unequilibrated chondrites and implications for the bulk composition of terrestrial planets. Earth Planet Sci. Lett. 273, 48–57. https://doi.org/https://doi.org/10.1016/j.epsl.2008.06.010

Boynton, W.V., 1984. Cosmochemistry of the rare earth elements: Meteorite studies. In: Henderson, P. (Ed.), Rare Earth Element Geochemistry. Elsevier, Sci. Publ. Co. Amsterdam, pp. 63–114.

Brotodewo, A., Tiddy, C., Zivak, D., Fabris, A., Giles, D., 2021. Geochemical discrimination of igneous zircon in the Gawler Craton, South Australia. Australian Journal of Earth Sciences 68, 557–579. https://doi.org/10.1080/08120099.2021.1825993

Brown, M., Johnson, T., Gardiner, N., 2020. Plate Tectonics and the Archean Earth. Annu Rev Earth Planet Sci. 48. https://doi.org/10.1146/annurev-earth-081619-052705

Carneiro, L. de S., Moreto, C.P.N., Monteiro, L.V.S., Xavier, R.P., 2023. Geochemical signatures of the Neoarchean and Paleoproterozoic copper systems in the Carajás Mineral Province, NW Brazil: Implications for metal endowment. J. Geochem. Explor. 254, 107306.

Chappell, B.W., White, A.J.R., 1992. I- and S-type granites in the Lachlan Fold Belt. Earth Environ Sci Trans R Soc Edinb 83, 1–26. https://doi.org/DOI: 10.1017/S0263593300007720

Chu, N.C., Taylor, R.N., Chavagnac, V., Nesbitt, R.W., Boella, R.M., Milton, J.A., German, C.R., Bayon, G., Burton, K., 2002. Hf isotope ratio analysis using multi-collector inductively coupled plasma mass spectrometry: an evaluation of isobaric interference corrections. J. Anal. At. Spectrom. 17, 1567–1574. https://doi.org/10.1039/B206707B

Clos, F., Weinberg, R.F., Zibra, I., Fenwick, M.J., 2019. Archean diapirism recorded by vertical sheath folds in the core of the Yalgoo Dome, Yilgarn Craton. Precambrian Res. 320, 391–402. https://doi.org/https://doi.org/10.1016/j.precamres.2018.11.010

Costa, F., Dos Santos, P., Serafim, I., Costa, I., Roopnarain, S., 2020. From Mesoarchean drips to modern–style tectonics in the Carajás Province, Amazonian Craton. J. South Am. Earth Sci. https://doi.org/10.1016/j.jsames.2020.102817

Creaser, R., Price, R., Wormald, R., 1991. A-type granites revisited: Assessment of a residual-source model. Geology 19, 163–166.

Cunha, I.R.V. da, Dall'Agnol, R., Feio, G.R.L., 2016. Mineral chemistry and magnetic petrology of the Archean Planalto Suite, Carajas Province–Amazonian Craton: Implications for the evolution of ferroan Archean granites. J. South. Am. Earth Sci. 67, 100–121.

Dall'Agnol, R., Cunha, I.R., Guimarães, F., Oliveira, D.C., Teixeira, M., Feio, G., Lamarão, C., 2017. Mineralogy, geochemistry, and petrology of Neoarchean ferroan to magnesian granites of Carajás Province,

Amazonian Craton: The origin of hydrated granites associated with charnockites. Lithos 277. https://doi.org/10.1016/j.lithos.2016.09.032

Dall'Agnol, R., de Oliveira, D.C., 2007. Oxidized, magnetite-series, rapakivi-type granites of Carajás, Brazil: Implications for classification and petrogenesis of A-type granites. Lithos 93, 215–233.

Dall'Agnol, R., Oliveira, D.C. de, Guimarães, F. V, Gabriel, E.O., Feio, G.R.L., Lamarão, C.N., Althoff, F.J., Santos, P.A., Teixeira, M.F.B., Silva, A.C., 2013. Geologia do Subdomínio de Transição do Domínio Carajás–implicações para a evolução arqueana da Província Carajás-pará. Simpósio de Geologia da Amazônia 13, 1082–1085.

Dall'Agnol, R., Teixeira, N.P., Rämö, O.T., Moura, C.A. V, Macambira, M.J.B., de Oliveira, D.C., 2005. Petrogenesis of the Paleoproterozoic rapakivi A-type granites of the Archean Carajás metallogenic province, Brazil. Lithos 80, 101–129.

Debon, F., Fort, P., 1983. A chemical–mineralogical classification of common plutonic rocks and associations. Trans R Soc Edinb Earth Sci. 73. https://doi.org/10.1017/S0263593300010117

Dey, S., Pandey, U., Rai, A., Chaki, A., 2012. Geochemical and Nd isotope constraints on petrogenesis of granitoids from NW part of the eastern Dharwar craton: Possible implications for late Archaean crustal accretion. Journal of Asian Earth Sciences – j. Asian. earth sci. 45. https://doi.org/10.1016/j.jseaes.2011.09.013

Dhuime, B., Hawkesworth, C., Storey, C., 2012. A Change in the Geodynamics of Continental Growth 3 Billion Years Ago. Science 335, 1334–1336. https://doi.org/10.1126/science.1216066

Dhuime, B., Wuestefeld, A., Hawkesworth, C., 2015. Emergence of modern continental crust about 3 billion years ago. Nat. Geosci. 8, 552–555. https://doi.org/10.1038/ngeo2466

Diniz, A.C., Melo, G.H.C. de, Lana, C. de C., Queiroga, G.N., Castro, M.P. de, Reis, H.L.S., 2023. Unravelling magmatic-hydrothermal processes at Salobo and GT-46 IOCG deposits, Carajás mineral province, Brazil: Constraints from whole-rock geochemistry and trace elements in apatite. J. South Am. Earth Sci. 125, 104290. https://doi.org/https://doi.org/10.1016/j.jsames.2023.104290

Eby, G.N., 1992. Chemical subdivision of the A-type granitoids: petrogenetic and tectonic implications. Geology 20, 641–644.

El-Desoky, H., Abdel-Rahman, A., Fahmy, W., Khalifa, I., Mohamed, S., Shirazi, A., Hezarkhani, A., Shirazy, A., Pour, A., 2023. Ore Genesis of the Abu Ghalaga Ferro-Ilmenite Ore Associated with Neoproterozoic Massive-Type Gabbros, South-Eastern Desert of Egypt: Evidence from Texture and Mineral Chemistry 13, 1–21. https://doi.org/10.3390/min13030307

Feig, S.T., Koepke, J., Snow, J.E., 2010. Effect of oxygen fugacity and water on phase equilibria of a hydrous tholeiitic basalt. Contributions to Mineralogy and Petrology 160, 551–568. https://doi.org/10.1007/s00410-010-0493-3

Feig, S.T., Koepke, J., Snow, J.E., 2006. Effect of water on tholeiitic basalt phase equilibria: an experimental study under oxidizing conditions. Contributions to Mineralogy and Petrology 152, 611–638. https://doi.org/10.1007/s00410-006-0123-2

Feio, G., Dall'Agnol, R., 2012. Geochemistry and petrogenesis of the Mesoarchean granites from the Canaã dos Carajás area, Carajás Province, Brazil: Implications for the origin of Archean granites. Lithos 154, 33–52. https://doi.org/10.1016/j.lithos.2012.06.022

Feio, G., Dall'Agnol, R., Dantas, E., Macambira, M., Santos, J., Althoff, F., Soares, J., 2013. Archean granitoid magmatism in the Canaã dos Carajás area: Implications for crustal evolution of the Carajás province, Amazonian craton, Brazil. Precambrian Res. 227, 157–185. https://doi.org/10.1016/j.precamres.2012.04.007

Feio, G.R.L., Dall'Agnol, R., Dantas, E.L., Macambira, M.J.B., Gomes, A.C.B., Sardinha, A.S., Oliveira, D.C., Santos, R.D., Santos, P.A., 2012. Geochemistry, geochronology, and origin of the Neoarchean Planalto Granite suite, Carajás, Amazonian craton: A-type or hydrated charnockitic granites? Lithos 151, 57–73. https://doi.org/https://doi.org/10.1016/j.lithos.2012.02.020

Felix, W., Oliveira, D., Ribeiro-Silva, L., Silva, F., 2020. Charnockites from Carajás Province, SE Amazonian Craton (Brazil): Petrogenetic constraints and intensive crystallization parameters. J. South Am. Earth Sci. 102598. https://doi.org/10.1016/j.jsames.2020.102598

Fowler A., Prokoph A., Stern R., Dupuis C. 2002. Organization of oscillatory zoning in zircon: Analysis, scaling, geochemistry, and model of a zircon from Kipawa, Quebec, Canada. Geochim Cosmochim Acta 66:311-328

Frost, B.R., Barnes, C.G., Collins, W.J., Arculus, R.J., Ellis, D.J., Frost, C.D., 2001. A geochemical classification for granitic rocks. Journal of petrology 42, 2033–2048.

Gioia, S., Pimentel, M., 2000. The Sm-Nd isotopic method in the Geochronology Laboratory of the University of Brasília. An Acadademia Brasileira de Ciências 72, 219–245. https://doi.org/10.1590/S0001-37652000000200009

Griffin, W.L., Wang, X., Jackson, S.E., Pearson, N.J., O'Reilly, S.Y., Xu, X., Zhou, X., 2002. Zircon chemistry and magma mixing, SE China: In-situ analysis of Hf isotopes, Tonglu and Pingtan igneous complexes. Lithos 61, 237–269. https://doi.org/https://doi.org/10.1016/S0024-4937(02)00082-8

Halla, J., van Hunen, J., Heilimo, E., Hölttä, P., 2009. Geochemical and numerical constraints on Neoarchean plate tectonics. Precambrian Res. 174, 155–162. https://doi.org/https://doi.org/10.1016/j.precamres.2009.07.008

Heilimo, E., Halla, J., Hölttä, P., 2010. Discrimination and origin of the sanukitoid series: Geochemical constraints from the Neoarchean western Karelian Province (Finland). Lithos 115, 27–39. https://doi.org/10.1016/j.lithos.2009.11.001

Hoskin, P.W.O., 2005. Trace-element composition of hydrothermal zircon and the alteration of Hadean zircon from the Jack Hills, Australia. Geochim. Cosmochim. Acta 69, 637–648. https://doi.org/https://doi.org/10.1016/j.gca.2004.07.006

Hoskin, P.W.O., Schaltegger, U., 2003. The composition of zircon and igneous and metamorphic petrogenesis. Rev Mineral Geochem 53, 27–62.

Huhn, S.R.B., Macambira, M.J.B., Dall'Agnol, R., 1999. Geologia e geocronologia Pb/Pb do granito alcalino arqueano Planalto, região da Serra do Rabo, Carajás-PA. Simpósio de Geologia da Amazônia 6, 463–466.

Jackson, S., Pearson, N., Griffin, W., Belousova, E., 2004. The Application of Laser Ablation-inductively Coupled Plasma-mass Spectrometry to in situ U-Pb Zircon Geochronology. Chem. Geol. 211, 47–69. https://doi.org/10.1016/j.chemgeo.2004.06.017

Janoušek, V., Farrow, C.M., Erban, V., 2006. Interpretation of Whole-rock Geochemical Data in Igneous Geochemistry: Introducing Geochemical Data Toolkit (GCDkit). Journal of Petrology 47, 1255–1259. https://doi.org/10.1093/petrology/egl013

Jayananda, M., Aadhiseshan, K.R., Kusiak, M.A., Wilde, S.A., Sekhamo, K., Guitreau, M., Santosh, M., Gireesh, R. V, 2020. Multi-stage crustal growth and Neoarchean geodynamics in the Eastern Dharwar Craton, southern India. Gondwana Research 78, 228–260. https://doi.org/https://doi.org/10.1016/j.gr.2019.09.005

Jayananda, M., Chardon, D., Peucat, J., Capdevila, R., 2006. 2.61 Ga potassic granites and crustal reworking in the western Dharwar craton, southern India: Tectonic, geochronologic and geochemical constraints. Precambrian Res. 150, 1–26. https://doi.org/10.1016/j.precamres.2006.05.004

Jorge João, X.S., Araújo, J.B., 1992. Magmatismo granítico sin-cisalhamento Itacaiúnas no SW do Estado do Pará, in: SBG, Congresso Brasileiro de Geologia. pp. 36–38.

Joshi, K.B., Singh, S.K., Halla, J., Ahmad, T., Rai, V.K., 2022. Neodymium Isotope constraints on the origin of Ttgs and high-K Granitoids in the Bundelkhand Craton, central India: Implications for Archaean Crustal evolution. Lithosphere 2022, 6956845.

Kaur, P., Zeh, A., Chaudhri, N., 2019. Archean crustal evolution of the Aravalli Banded Gneissic Complex, NW India: Constraints from zircon U-Pb ages, Lu-Hf isotope systematics, and whole-rock geochemistry of granitoids. Precambrian Res. 327, 81–102. https://doi.org/https://doi.org/10.1016/j.precamres.2019.03.004

King, P.L., White, A.J.R., Chappell, B.W., Allen, C.M., 1997. Characterization and Origin of Aluminous A-type Granites from the Lachlan Fold Belt, Southeastern Australia. Journal of Petrology 38, 371–391. https://doi.org/10.1093/petroj/38.3.371

Lacasse, C.M., Ganade, C.E., Mathieu, L., Teixeira, N.A., Lopes, L.B.L., Monteiro, C.F., 2020. Restoring original composition of hydrothermally altered Archean metavolcanic rocks of the Carajás Mineral Province

(Brazil): Geodynamic implications for the transition from lid to mobile tectonics. Lithos 372–373, 105647. https://doi.org/https://doi.org/10.1016/j.lithos.2020.105647

Laurent, O., Martin, H., Moyen, J.-F., Doucelance, R., 2014. The diversity and evolution of late-Archean granitoids: Evidence for the onset of "modern-style" plate tectonics between 3.0 and 2.5 Ga. Lithos 205. https://doi.org/10.1016/j.lithos.2014.06.012

Leake, B., 1997. Nomenclature of Amphiboles: Report of the Subcommittee on Amphiboles of the International Mineralogical Association Commission on New Minerals and Mineral Names. Mineral Mag 61, 295–321. https://doi.org/10.1180/minmag.1997.061.405.13

Leite, A.A.S., Dall'Agnol, R., Macambira, M.J.B., Althoff, F.J., 2004. Geologia e geocronologia dos granitóides arqueanos da região de Xinguara (PA) e suas implicações na evolução do Terreno Granito-Greenstone de Rio Maria. Revista Brasileira de Geociências 34, 447–458.

Leite-Santos, P.J., de Oliveira, D.C., 2016. Geologia, petrografia e geoquímica das associações leucograníticas arqueanas da área de Nova Canadá: Província Carajás. Geologia USP. Série Científica 16, 37–66.

Lenting, C., Geisler-Wierwille, T., Gerdes, A., Kooijman, E., Scherer, E., Zeh, A., 2010. The behavior of the Hf isotope system in radiation-damaged zircon during experimental hydrothermal alteration. American Mineralogist 95, 1343–1348. https://doi.org/10.2138/am.2010.3521

Ludwig, K., 2009. SQUID 2: A User's Manual. Berkeley Geochronology Center Special Publication No. 5.

Ludwig, K., 2008. User's Manual for Isoplot/Ex.

Macambira, J.M.B., Lancelot, J.R., 1996. Time constraints for the formation of the Archean Rio Maria crust, southeastern Amazonian Craton, Brazil. Int. Geol. Rev. 38, 1134–1142.

Macambira, M.J.B., Lafon, J.M., Pidgeon, R.T., 1998. Crescimento crustal arqueano registrado em zircões de sedimentos da região de Rio Maria, Província Carajás, Pará. 40th Congresso Brasileiro de Geologia, SBG, Belo Horizonte. Proceedings 55.

Machado, N., Lindenmayer, Z., Krogh, T.E., Lindenmayer, D., 1991. U-Pb geochronology of Archean magmatism and basement reactivation in the Carajás area, Amazon shield, Brazil. Precambrian Res. 49, 329–354.

Marangoanha, B., Oliveira, D.C., Oliveira, V.E.S., Galarza, M., Lamarão, C., 2019a. Neoarchean A-type granitoids from Carajás province (Brazil): New insights from geochemistry, geochronology and microstructural analysis. Precambrian Res. 324, 86–108. https://doi.org/10.1016/j.precamres.2019.01.010

Marangoanha, B., Oliveira, D.C., Dall'Agnol, R., 2019b. The Archean granulite-enderbite complex of the northern Carajás province, Amazonian craton (Brazil): Origin and implications for crustal growth and cratonization. Lithos 350–351, 105275. https://doi.org/https://doi.org/10.1016/j.lithos.2019.105275

Marangoanha, B., Oliveira, D.C., Galarza, M.A., Marques, G.T., 2020. Crustal anatexis and mantle-derived magmas forming Neoarchean A-type granitoids in Carajás Province, northern Brazil: Petrological evidence and tectonic control. Precambrian Res. 338, 105585. https://doi.org/https://doi.org/10.1016/j.precamres.2019.105585

Martin, H., 1994. The Archean grey gneisses and the genesis of continental crust, in: Developments in Precambrian Geology. Elsevier, pp. 205–259.

McDonough, W.F., Sun, S.S., 1995. The composition of the Earth. Chem. Geol. 120 (3–4), 223–253. https://doi.org/10.1016/0009-2541(94)00140-4.

Melo, G.H.C. de, Monteiro, L.V.S., Hunger, R.B., Toledo, P.I.F., Xavier, R.P., Zhao, X.-F., Su, Z.-K., Moreto, C.P.N., Jesus, S. dos S.G.P. de, 2021. Magmatic-hydrothermal fluids leaching older seafloor exhalative rocks to form the IOCG deposits of the Carajás Province, Brazil: Evidence from boron isotopes. Precambrian Res. 365, 106412. https://doi.org/https://doi.org/10.1016/j.precamres.2021.106412

Melo, G., Monteiro, L., Xavier, R., Moreto, C., Santiago, E., Dufrane, S.A., Aires, B., Santos, A., 2016. Temporal evolution of the giant Salobo IOCG deposit, Carajás Province (Brazil): constraints from paragenesis of hydrothermal alteration and U-Pb geochronology. Miner Depos 52. https://doi.org/10.1007/s00126-016-0693-5

Melo, G.H.C., Monteiro, L.V.S., Xavier, R.P., Moreto, C.P.N., Santiago, E., 2019. Tracing fluid sources for the Salobo and Igarapé Bahia deposits: implications for the genesis of the iron oxide copper-gold deposits in the Carajás Province, Brazil. Economic Geology 114, 697–718.

Mesquita, C.J.S., Dall'Agnol, R.,Silva, A.S.N., Cunha, I.R.V., Almeida, J.A.C., Oliveira, J.K.M., 2025. Crystallization parameters and thermodynamic modeling of the Igarapé Gelado suite: Implications for the Neoarchean magmatism of the Carajás province, Brazil. J South Am Earth Sci 153, 105357. https://doi.org/10.1016/j.jsames.2025.105357

Mezger, K., Krogstad, E.J., 1997. Interpretation of discordant U-Pb zircon ages: An evaluation. Journal of Metamorphic Geology 15, 127–140. https://doi.org/https://doi.org/10.1111/j.1525-1314.1997.00008.x

Milhomem Neto, J.M., Lafon, J.-M., 2019. Zircon U-Pb and Lu-Hf isotope constraints on Archean crustal evolution in Southeastern Guyana Shield. Geoscience Frontiers 10, 1477–1506. https://doi.org/https://doi.org/10.1016/j.gsf.2018.09.012

Monteiro, L.V.S., Xavier, R.P., de Carvalho, E.R., Hitzman, M.W., Johnson, C.A., de Souza Filho, C.R., Torresi, I., 2008. Spatial and temporal zoning of hydrothermal alteration and mineralization in the Sossego iron oxide–copper–gold deposit, Carajás Mineral Province, Brazil: paragenesis and stable isotope constraints. Miner Depos 43, 129–159. https://doi.org/10.1007/s00126-006-0121-3

Moraes, J., Cordeiro, P., Filho, E., Rezende, J., Rios, C.V., 2022. Metamorphic disturbances of magnetite chemistry and the Sm-Nd isotopic system of reworked Archean iron formations from NE Brazil. Geoscience Frontiers 13. https://doi.org/10.1016/j.gsf.2020.11.018

Moreto, C. P. N, Monteiro, L.V.S., Xavier, R.P., Creaser, R.A., DuFrane, S.A., Melo, G.H.C., Delinardo da Silva, M.A., Tassinari, C.C.G., Sato, K., 2015. Timing of multiple hydrothermal events in the iron oxide–copper–gold deposits of the Southern Copper Belt, Carajás Province, Brazil. Miner. Depos. 50, 517–546. https://doi.org/10.1007/s00126-014-0549-9

Moyen, J.-F., Laurent, O., Chelle-Michou, C., Couzinié, S., Vanderhaeghe, O., Zeh, A., Villaros, A., Gardien, V., 2016. Collision vs. subduction-related magmatism: Two contrasting ways of granite formation and implications for crustal growth. Lithos 277. https://doi.org/10.1016/j.lithos.2016.09.018

Moyen, J.F., Laurent, O., 2018. Archaean tectonic systems: A view from igneous rocks. Lithos 302–303, 99–125. https://doi.org/https://doi.org/10.1016/j.lithos.2017.11.038

Nardi, L.V.S., Bitencourt, M.F. 2009. A-type granitic rocks in post-collisional settings in southernmost Brazil: their classification and relationship with tectonics and magmatic series. Canadian Mineralogist, 47: 1493-1503.

Nebel, O., Capitanio, F.A., Moyen, J.-F., Weinberg, R.F., Clos, F., Nebel-Jacobsen, Y.J., Cawood, P.A., 2018. When crust comes of age: on the chemical evolution of Archaean, felsic continental crust by crustal drip tectonics. Philosophical Transactions of the Royal Society A: Mathematical, Physical and Engineering Sciences 376, 20180103. https://doi.org/10.1098/rsta.2018.0103

O'Connor, J.T., 1965. A classification for quartz-rich igneous rocks based on feldspar ratios. US geological survey professional paper B 525, 79–84.

Oliveira, D.C, Silva, L.R., Nascimento, A.C., Marangoanha, B.O., Gabriel, E.O., Santos, P.J.L., Machado, J.R.M., Felix, W.Q.,Silva, L.C.S., Santos, R.F.S. 2023. Revisão litoestratigráfica com implicações para compartimentação tectônica da Província Mineral de Carajás, sudeste do Cráton Amazônico. *In:* Anais do 17° simpósio de Geologia da Amazônia. Brazilian Geological Society, Santarém, 1, 434-441.

Oliveira, J.K.M., Tavares, F.M., Costa, I.S.L., 2018b. Mapa geológico-geofísico do lineamento Cinzento: estado do Pará. Belém: CPRM, 2018. 1 mapa, color. Escala 1:100.000.

Oliveira, M., Dall'Agnol, R., Almeida, J., 2011. Petrology of the Mesoarchean Rio Maria suite and the discrimination of sanukitoid series. Lithos 127, 192–209. https://doi.org/10.1016/j.lithos.2011.08.017

Oliveira, V.E.S., Oliveira, D.C., Marangoanha, B., Lamarão, C.N., 2018a. Geology, mineralogy and petrological affinities of the Neoarchean granitoids from the central portion of the Canaã dos Carajás domain, Amazonian craton, Brazil. J. South Am. Earth Sci. 85, 135–159. https://doi.org/https://doi.org/10.1016/j.jsames.2018.04.022

Palme, H., O'Neill, H.St.C., 2014. 3.1 - Cosmochemical Estimates of Mantle Composition, in: Holland, H.D., Turekian, K.K. (Eds.), Treatise on Geochemistry (Second Edition). Elsevier, Oxford, pp. 1–39. https://doi.org/https://doi.org/10.1016/B978-0-08-095975-7.00201-1

Park, C., Song, Y., Chung, D., Kang, I.-M., Khulganakhuu, C., Yi, K., 2016. Recrystallization and hydrothermal growth of high U–Th zircon in the Weondong deposit, Korea: Record of post-magmatic alteration. Lithos 260, 268–285. https://doi.org/https://doi.org/10.1016/j.lithos.2016.05.026

Passchier, C.W., Trouw, R.A.J., 2005. Microtectonics. Springer Science & Business Media.

Patchett, P.J., Tatsumoto, M., 1981. A routine high-precision method for Lu-Hf isotope geochemistry and chronology. Contributions to Mineralogy and Petrology 75, 263–267. https://doi.org/10.1007/BF01166766

Pearce, J., 1996. Sources and settings of granitic rocks. International Union of Geological Sciences 19, 120–125. https://doi.org/10.18814/epiiugs/1996/v19i4/005

Pearce, J., Harris, N., Tindle, A., 1984. Trace Element Discrimination Diagrams for the Tectonic Interpretation of Granitic Rocks. Journal of Petrology 25, 956–983. https://doi.org/10.1093/petrology/25.4.956

Pearce, J., Peate, D., 1995. Tectonic Implications of the Composition of Volcanic ARC Magmas. Annu Rev Earth Planet Sci 23, 251–285. https://doi.org/10.1146/annurev.ea.23.050195.001343

Pidgeon, R.T., Macambira, M.J.B., Lafon, J.-M., 2000. Th–U–Pb isotopic systems and internal structures of complex zircons from an enderbite from the Pium complex, Carajás Province, Brazil: evidence for the ages of granulite facies metamorphism and the protolith of the enderbite. Chem. Geol. 166, 159–171.

Pinheiro, R.V.L., Holdsworth, R.E., 2000. Evolução tectonoestratigráfica dos sistemas transcorrentes Carajás e Cinzento, Cinturão Itacaiúnas, na borda leste do Craton Amazônico, Pará. Brazilian Journal of Geology. 30.

Pollard, P.J., Taylor, R.G., Peters, L., Matos, F., Freitas, C., Saboia, L., Huhn, S., 2019. ^{40}Ar-^{39}Ar dating of Archean iron oxide Cu-Au and Paleoproterozoic granite-related Cu-Au deposits in the Carajás Mineral Province, Brazil: implications for genetic models. Miner. Depos. 54, 329–346. https://doi.org/10.1007/s00126-018-0809-1

Putnis, A., Austrheim, H., 2013. Mechanisms of Metasomatism and Metamorphism on the Local Mineral Scale: The Role of Dissolution-Reprecipitation During Mineral Re-equilibration, in: Harlov, D.E., Austrheim, H. (Eds.), Metasomatism and the Chemical Transformation of Rock: The Role of Fluids in Terrestrial and Extraterrestrial Processes. Springer Berlin Heidelberg, Berlin, Heidelberg, pp. 141–170. https://doi.org/10.1007/978-3-642-28394-9_5

Rämö, O.T., Haapala, I., 2005. Rapakivi granites. In: Lehtinen, M., Nurmi, P. A. & Raamo, O. T. (eds) Precambrian Geology of Finlandç. Key to the Evolution of the Fennoscandian Shield. Amsterdam: Elsevier, pp. 533-562.

Reis, P., 2017. A Sequência Meta-Vulcanossedimentar do Circular, Carajás (Pa): Geologia, Petrografia, Litogeoquímica e Geocronologia. Master dissertation. Universidade de São Paulo, São Paulo.

Ribeiro-Silva, L., Oliveira, D., Galarza, M., Nascimento, A., Marangoanha, B., Marques, G., 2023. Zircon U-Pb-Hf isotope and geochemical constraints on the petrogenesis and tectonic setting of Mesoarchean granitoids from the Carajás province, Amazonian craton, Brazil. Precambrian Res. 398, 107204. https://doi.org/10.1016/j.precamres.2023.107204

Rollinson, H., Pease, V., 2021. Using Geochemical Data: To Understand Geological Processes. https://doi.org/10.1017/9781108777834

Rubatto, D., 2017. Zircon: The Metamorphic Mineral. Rev. Mineral. Geochem. 83, 261–296. https://doi.org/10.2138/rmg.2017.83.9

Russell, W.A., Papanastassiou, D.A., Tombrello, T.A., 1978. Ca isotope fractionation on the Earth and other solar system materials. Geochim Cosmochim Acta 42, 1075–1090. https://doi.org/https://doi.org/10.1016/0016-7037(78)90105-9

Santos, J.O.S. 2003. Geotectônica do Escudo das Guianas e Brasil-Central. Brasília.

Santos, J.O.S., Hartmann, L.A., Faria, M.S.G. de, Riker, S.R., Souza, M.M. de, Almeida, M.E., McNaughton, N.J., 2006. A compartimentação do Cráton Amazonas em províncias: avanços ocorridos no período 2000-2006. Simpósio de geologia da Amazônia 9, 156–159.

Santos, P.J.L., Oliveira, D.C., Galarza, M.A., Macambira, M.J.B., 2010. Geologia, petrografia e geocronologia das rochas granitóides do Complexo Xingu da região de Nova Canadá, município de Água Azul do Norte-Província Mineral de Carajás, in: SBG, Congresso Brasileiro de Geologia.

Santos, R.D., Galarza, M.A., Oliveira, D.C., 2013. Geologia, geoquímica e geocronologia do Diopsídio-Norito Pium, Província Carajás. Boletim do Museu Paraense Emílio Goeldi-Ciências Naturais 8, 355–382.

Santos Silva, A.N., Feio, G., Silva, J.P.A., Dall'Agnol, R., Almeida, J., Gomes, A., 2020. Mineralogy, petrology, and origin of the Pedra Branca Suite: a tonalitic-trondhjemitic association with high Zr, Ti and Y, Carajás Province, Amazonian Craton. Brazilian Journal of Geology 50. https://doi.org/10.1590/2317-4889202020190093

Sardinha, A.S., Dall'Agnol, R., Gomes, A.C.B., Macambira, M.J.B., Galarza, M.A., 2004. Geocronologia Pb-Pb e U-Pb em zircão de granitóides arqueanos da região de Canaã dos Carajás, Província Mineral de Carajás, in: Congresso Brasileiro de Geologia. p. 2004.

Sardinha, A.S., Barros, C.E., Krymsky, R., 2006. Geology, geochemistry, and U–Pb geochronology of the Archean (2.74 Ga) Serra do Rabo granite stocks, Carajás Metallogenetic Province, northern Brazil. J. South Am. Earth Sci. 20, 327–339.

Sato, K., Tassinari, C., Basei, M., Júnior, O., Onoe, A., Souza, M., 2014. Sensitive High Resolution Ion Microprobe (SHRIMP IIe/MC) of the Institute of Geosciences of the University of São Paulo, Brazil: Analytical method and first results. Geologia USP. Série Científica 14, 3–18. https://doi.org/10.5327/Z1519-874X201400030001

Sato, K.T.C.B.M.O.A., S.J.O., 2016. First REE analyses in zircon by SHRIMP at Geosciences Institute of São Paulo University: REE diffusion from apatite inclusion inside Temora zircon, in: VIII International SHRIMP WorkshopVIII International SHRIMP Workshop.

Shand, S.J., 1950. Eruptive rocks their genesis, composition, classification and their relation to ore deposit, fourth ed. Murby, London, p. 488.

Sheard, E., Williams-Jones, A., Heiligmann, M., Pederson, C., Trueman, D., 2012. Controls on the Concentration of Zirconium, Niobium, and the Rare Earth Elements in the Thor Lake Rare Metal Deposit, Northwest Territories, Canada. Economic Geology 107, 81–104. https://doi.org/10.2113/econgeo.107.1.81

Silva, F.F., Oliveira, D.C., Dall'Agnol, R., Santos, J.O.S., Galarza, M.A.T., Guimarães, F.V., Souza, L.A.M., 2025. Geochemistry, SHRIMP U-Pb Zircon geochronology, and Hf-Nd isotope composition on the Neoarchean Vila Jussara granitoid complex from Carajás Province, Amazonian Craton: petrogenesis and tectonic implications.

Silva, F.F., Oliveira, D.C, Dall'Agnol, R., Ribeiro-Silva, L., Cunha, I.R., 2020. Lithological and structural controls on the emplacement of a Neoarchean plutonic complex in the Carajás province, southeastern Amazonian craton (Brazil). J. South Am. Earth Sci. 102, 102696. https://doi.org/10.1016/j.jsames.2020.102696

Silva, L., Silva, A., Silva, C., Silva, D., Rodrigues, J., 2023. Geocronologia U-Pb (Shrimp) em zircão em granitos da porção nw da província Carajás: Implicações para o magmatismo neoarqueano e metalogenia da região, in: Anais 17° Simpósio de Geologia Da Amazônia. Santatém-Pa.

Silva, M.A.D., 2018. Evolução tectono-metamórfica do embasamento mesoarqueano do Domínio Carajás, Província Carajás. Phd Thesis. Campinas. São Paulo.

Silva, M.A.D., Monteiro, L.V.S., Santos, T.J.S., Moreto, C.P.N., Sousa, S.D., Faustinoni, J.M., Melo, G.H.C., Xavier, R.P., Toledo, B.A.M., 2021. Mesoarchean migmatites of the Carajás Province: From intra-arc melting to collision. Lithos 388–389, 106078. https://doi.org/https://doi.org/10.1016/j.lithos.2021.106078

Sisson, T.W., Ratajeski, K., Hankins, W.B., Glazner, A.F., 2005. Voluminous granitic magmas from common basaltic sources. Contributions to Mineralogy and Petrology 148, 635–661. https://doi.org/10.1007/s00410-004-0632-9

Sousa, L.A.M., Dall'Agnol, R., Cunha, I.R.V., Silva, F.F. da, Oliveira, D.C., 2022. Magnetic petrology of the Neoarchean granitoids in the Vila Jussara Suite, Carajás Province, Amazonian Craton. Brazilian Journal of Geology 52, e20201071. https://doi.org/10.1590/2317-4889202220210071

Souza, S.R.B., Macambira, M.J.B., Sheller, T., 1996. Novos dados geocronológicos para os granitos deformados do Rio Itacaiúnas (Serra dos Carajás, PA); implicações estratigráficas. Proceedings of the Simpósio de Geologia da Amazônia, Belém, Brazil 380–383.

Souza, Z.S., Potrel, A., Lafon, J.M., Althoff, F.J., Pimentel, M.M., Dall'Agnol, R., Oliveira, C.G., 2001. Nd, Pb and Sr isotopes in the Identidade Belt, an Archean greenstone belt of Rio Maria region (Carajás Province, Brazil): implications for the geodynamic evolution of the Amazonian Craton. Precambrian Res. 109, 293–315.

Stern, R.A., 1998. High-resolution SIMS determination of radiogenic tracer-isotope ratios in minerals. Modern Approaches to Ore and Environmental Mineralogy.

Sylvester, P., 1989. Post-Collisional Alkaline Granites Author(s): post-collisional alkaline granites'. J. Geol. 97, 261–280.

Tallarico, F.H.B., McNaughton, N.J., Groves, D.I., Fletcher, I.R., Figueiredo, B.R., Carvalho, J.B., Rego, J.L., Nunes, A.R., 2004. Geological and SHRIMP II U-Pb constraints on the age and origin of the Breves Cu-Au-(W-Bi-Sn) deposit, Carajás, Brazil. Miner Depos 39, 68–86. https://doi.org/10.1007/s00126-003-0383-y

Tang, M., Chen, K., Rudnick, R., 2016. Archean upper crust transition from mafic to felsic marks the onset of plate tectonics. Science (1979) 351, 372–375. https://doi.org/10.1126/science.aad5513

Tassinari, C.C.G., Macambira, M.J.B., 2004. A evolução tectônica do Cráton Amazônico. Geologia do continente sul-americano: evolução da obra de Fernando Flávio Marques de Almeida.

Tavares, F., 2015. Evolução geotectônica do nordeste da Província Carajás. Phd. TheisUniversidade Federal do Rio de Janeiro, Rio de Janeiro.

Tavares, F.M., Oliveira, J.K.M. de, Lima, R.B., 2021. Áreas de relevante interesse mineral-Província mineral de Carajás, PA: controles críticos das mineralizações de cobre e ouro do lineamento Cinzento.

Tavares, F.M., Trouw, R.A.J., da Silva, C.M.G., Justo, A.P., Oliveira, J.K.M., 2018. The multistage tectonic evolution of the northeastern Carajás Province, Amazonian Craton, Brazil: Revealing complex structural patterns. J. South Am. Earth Sci. 88, 238–252. https://doi.org/https://doi.org/10.1016/j.jsames.2018.08.024

Teixeira, L.R., 2005. GENESIS 4.0—Software de Modelamento Geoquímico.

Teixeira, M.F.B., Dall'Agnol, R., Santos, J.O.S., de Oliveira, D.C., Lamarão, C.N., McNaughton, N.J., 2018. Crystallization ages of Paleoproterozoic A-type granites of Carajás province, Amazon craton: Constraints from U-Pb geochronology of zircon and titanite. J. South Am. Earth Sci. 88, 312–331.

Teixeira, M.F.B., Dall'Agnol, R., Santos, J.O.S., Kemp, A., Evans, N., 2019. Petrogenesis of the Paleoproterozoic (Orosirian) A-type granites of Carajás Province, Amazon Craton, Brazil: Combined in situ Hf-O isotopes of zircon. Lithos 332, 1–22.

Teixeira, N.P., M.C.A.V., B.J.S., 2001. Evidência da existência de crosta Arqueana de 3,68 Ga obtida em zircão de rocha gnáissica tonalítica do Complexo Xingu, no Segmento oeste da Província Mineral de Carajás, região de São Felix do Xingu, Estado do Pará, Brasil., in: VII Simpósio de Geologia Da Amazônia. Belém.

Teruiya, R.K., Paradella, W.R., Dos Santos, A.R., Dall'Agnol, R., Veneziani, P., 2008. Integrating airborne SAR, Landsat TM and airborne geophysics data for improving geological mapping in the Amazon region: the Cigano Granite, Carajás Province, Brazil. Int. J. Remote Sens. 29, 3957–3974.

Thirlwall, M.F., Anczkiewicz, R., 2004. Multidynamic isotope ratio analysis using MC–ICP–MS and the causes of secular drift in Hf, Nd and Pb isotope ratios. Int. J. Mass Spectrom. 235, 59–81. https://doi.org/https://doi.org/10.1016/j.ijms.2004.04.002

Toledo, P.I.S, Moreto, C., Monteiro, L., Melo, G., Matos, F., Xavier, R., Carvalho, J., Medeiros Filho, C.A., Navarro, M., Lana, C., 2023. Breaking up the temporal link between granitic magmatism and iron oxide-copper–gold (IOCG) deposits in the Carajás Mineral Province, NW Brazil. Miner. Depos. 59. https://doi.org/10.1007/s00126-023-01224-5

Toledo, P.I.S., Moreto, C.P, Xavier, R.P., Gao, J., da Silva Nogueira de Matos, J.H., de Melo, G.H.C., 2019. Multistage evolution of the Neoarchean (ca. 2.7 Ga) Igarapé cinzento (GT-46) iron oxide copper-gold deposit, Cinzento shear zone, Carajás Province, Brazil. Economic Geology 114, 1–34.

Topno, A., Dey, S., Liu, Y., Zong, K., 2018. Early Neoarchaean A-type granitic magmatism by crustal reworking in Singhbhum craton: Evidence from Pala Lahara area, Orissa. Journal of Earth System Science 127, 1–22. https://doi.org/10.1007/s12040-018-0947-y

Trouw, R.A.J., Passchier, C.W., Wiersma, D.J., 2009. Atlas of Mylonites-and related microstructures. Springer Science & Business Media.

Trunfull, E.F., Hagemann, S.G., Xavier, R.P., Moreto, C.P.N., 2020. Critical assessment of geochronological data from the Carajás Mineral Province, Brazil: Implications for metallogeny and tectonic evolution. Ore Geol. Rev. 121, 103556. https://doi.org/https://doi.org/10.1016/j.oregeorev.2020.103556

Turner, S., Foden, J., Morrison, R.S., 1992. Derivation of some A-type magmas by fractionation of basaltic magma: An example from the Padthaway Ridge, South Australia. Lithos 28, 151–179. https://doi.org/10.1016/0024-4937(92)90029-X

Vasquez, M.L., Rosa-Costa, L.T. da, 2008. Geologia e recursos minerais do estado do Pará. CPRM.

Vernon, R.H., 2005. A practical guide to rock microstructure. Cambridge, 594 pp. American mineralogist – Amer. Mineral. 90, 1472. https://doi.org/10.2138/am.2005.449

Wade, C.E., Payne, J.L., Barovich, K., Gilbert, S., Wade, B.P., Crowley, J.L., Reid, A., Jagodzinski, E.A., 2022. Zircon trace element geochemistry as an indicator of magma fertility in iron oxide copper-gold provinces. Economic Geology 117, 703–718. https://doi.org/10.5382/econgeo.4886

Whalen, J.B., Currie, K.L., Chappell, B.W., 1987. A-type granites: geochemical characteristics, discrimination and petrogenesis. Contributions to mineralogy and petrology 95, 407–419.

Whalen, J.B., Hildebrand, R.S., 2019. Trace element discrimination of arc, slab failure, and A-type granitic rocks. Lithos 348–349, 105179. https://doi.org/https://doi.org/10.1016/j.lithos.2019.105179

Whitney, D., Evans, B., 2010. Abbreviations for Names of Rock-Forming Minerals. American Mineralogist 95, 185–187. https://doi.org/10.2138/am.2010.3371

Wiedenbeck, M., Hanchar, J.M., Peck, W.H., Sylvester, P., Valley, J., Whitehouse, M., Kronz, A., Morishita, Y., Nasdala, L., Fiebig, J., Franchi, I., Girard, J.-P., Greenwood, R.C., Hinton, R., Kita, N., Mason, P.R.D., Norman, M., Ogasawara, M., Piccoli, P.M., Rhede, D., Satoh, H., Schulz-Dobrick, B., Skår, O., Spicuzza, M.J., Terada, K., Tindle, A., Togashi, S., Vennemann, T., Xie, Q., Zheng, Y.-F., 2004. Further Characterisation of the 91500 Zircon Crystal. Geostand. Geoanal. Res. 28, 9–39. https://doi.org/https://doi.org/10.1111/j.1751-908X.2004.tb01041.x

Williams, I.S., 1997. U-Th-Pb geochronology by ion microprobe.

Willson, M., 1989. Igneous petrogenesis. A global tectonic approach. Unwin Hyman, London, 466 p.

Wyers, G., Barton, M., 1986. Petrology and evolution of transitional alkaline - sub alkaline lavas from Patmos, Dodecanesos, Greece: evidence for fractional crystallization, magma mixing and assimilation. Contributions to Mineralogy and Petrology 93, 297–311. https://doi.org/10.1007/BF00389389

Xavier, R.P., Monteiro, L.V.S., Moreto, C.P.N., Pestilho, A.L.S., de Melo, G.H.C., da Silva, M.A.D., Aires, B., Ribeiro, C., e Silva, F.H.F., 2012. The iron oxide copper-gold systems of the Carajás mineral province, Brazil.

Wang, Zhen-Hua, Ru-Xiong Lei, Matthew J. Brzozowski, Chang-Zhi Wu., 2024. Magmatic–hydrothermal evolutionary processes in highly evolved granitic systems: Insights from zircons of the Baishitouquan pluton, NW China. GSA Bulletin 2024; 136 (11-12): 4476–4494. https://doi.org/10.1130/B37425.1

Zibra, I., Lu, Y., Clos, F., Weinberg, R., Peternell, M., Wingate, M.T.D., Prause, M., Schiller, M., Tilhac, R., 2020. Regional-scale polydiapirism predating the Neoarchean Yilgarn Orogeny. Tectonophysics 779, 228375. https://doi.org/10.1016/j.tecto.2020.228375

DADOS SUPLEMENTARES DO CAPÍTULO 3

SUPPLEMENTARY DATA 1 - ASSESSMENT OF ELEMENT MOBILITY

Due to the proximity of IGS to IOCG deposits in the Northern Copper Belt (Moreto et al., 2015), it is essential to assess elemental mobility before discussing petrogenesis. Therefore, samples with low loss on ignition values (LOI: 0.48 to 1.04) and with Ce anomalies (δCe, calculated as $Ce_N/\sqrt{(La_N \times Pr_N)}$ within the range of 0.94 to 1.07 which indicates primary chemical signature without significant changes by hydrothermal alteration and metamorphism (Polat et al., 2002; Polat and Hofmann, 2003) were selected for geochemical modeling. Furthermore, elemental mobility was tested based on correlation with Zr, the least mobile element, which is an independent index of geochemical variations (Polat et al., 2002; Sun et al., 2019; Wang et al., 2017). Moreover, Y, Hf, Nb, and REE positively correlate with Zr, also indicating low mobility (Fig. S2), and so can be used to evaluate the petrogenesis of the studied rocks. Conversely, LILEs (Rb, Ba, Sr, Th, and Ta) show greater mobility during hydrothermal alteration, as seen in the scattered data (Polat et al., 2002), and therefore, will not be used in to constrain the origin of the IGS. Additionally, BHMzG samples depleted in Y (CR-1A, CR-01A1, CR-9, CR-5, CG-22A), distinguished as possible A1-subtype granites, were excluded from modeling due to potential hydrothermal influence (See topic 5.3).

REFERENCES – SUPPLEMENTARY DATA 1

Polat, A., Hofmann, A., 2003. Alteration and geochemical patterns in the 3.7–3.8 Ga Isua greenstone belt, West Greenland. Precambrian Res. 126, 197–218. https://doi.org/10.1016/S0301-9268(03)00095-0

Polat, A., Hofmann, A., Rosing, M., 2002. Boninite-like volcanic rocks in the 3.7–3.8 Ga Isua greenstone belt, West Greenland: geochemical evidence for intra-oceanic subduction zone processes in the early Earth. Chem Geol 184, 231–254. https://doi.org/10.1016/S0009-2541(01)00363-1

Wang, W., Liu, S., Cawood, P.A., Guo, R., Bai, X., Guo, B., 2017. Late Neoarchean crust-mantle geodynamics: Evidence from Pingquan Complex of the Northern Hebei Province, North China Craton. Precambrian Res. 303, 470–493. https://doi.org/https://doi.org/10.1016/j.precamres.2017.06.007

Sun, G., Liu, S., Gao, L., Hu, Y., Guo, R., Fu, J., Wang, M., Ma, C., Hu, F., 2019. Neoarchean sanukitoids and associated rocks from the Tengzhou-Pingyi intrusive complex, North China Craton: Insights into petrogenesis and crust-mantle interactions. Gondwana Research 68, 50–68. https://doi.org/https://doi.org/10.1016/j.gr.2018.11.005

Moreto, C. P. N, Monteiro, L.V.S., Xavier, R.P., Creaser, R.A., DuFrane, S.A., Melo, G.H.C., Delinardo da Silva, M.A., Tassinari, C.C.G., Sato, K., 2015. Timing of multiple hydrothermal events in the iron oxide–copper–gold deposits of the Southern Copper Belt, Carajás Province, Brazil. Miner. Depos. 50, 517–546. https://doi.org/10.1007/s00126-014-0549-9

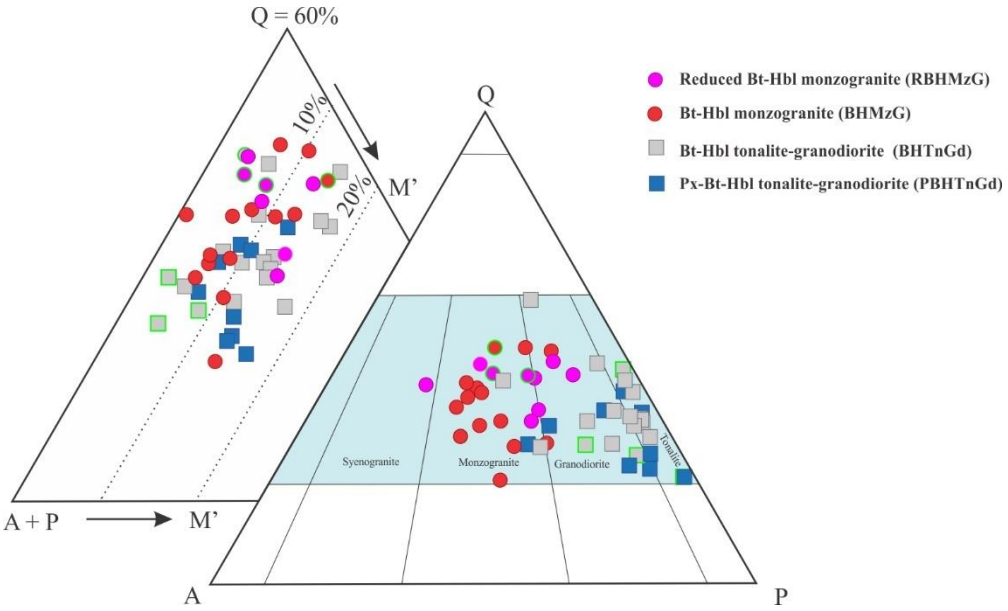

Supplementary figure 1. QAP and Q-A+P-M' diagrams (Le Maitre et al., 2020) for the varieties of the Igarapé Gelado suite. Abbreviations: A = alkali feldspar; P = Plagioclase; Q = Quartz; M'= M - (apatite + muscovite + carbonates). Symbols with a green border = hydrothermalized rocks.

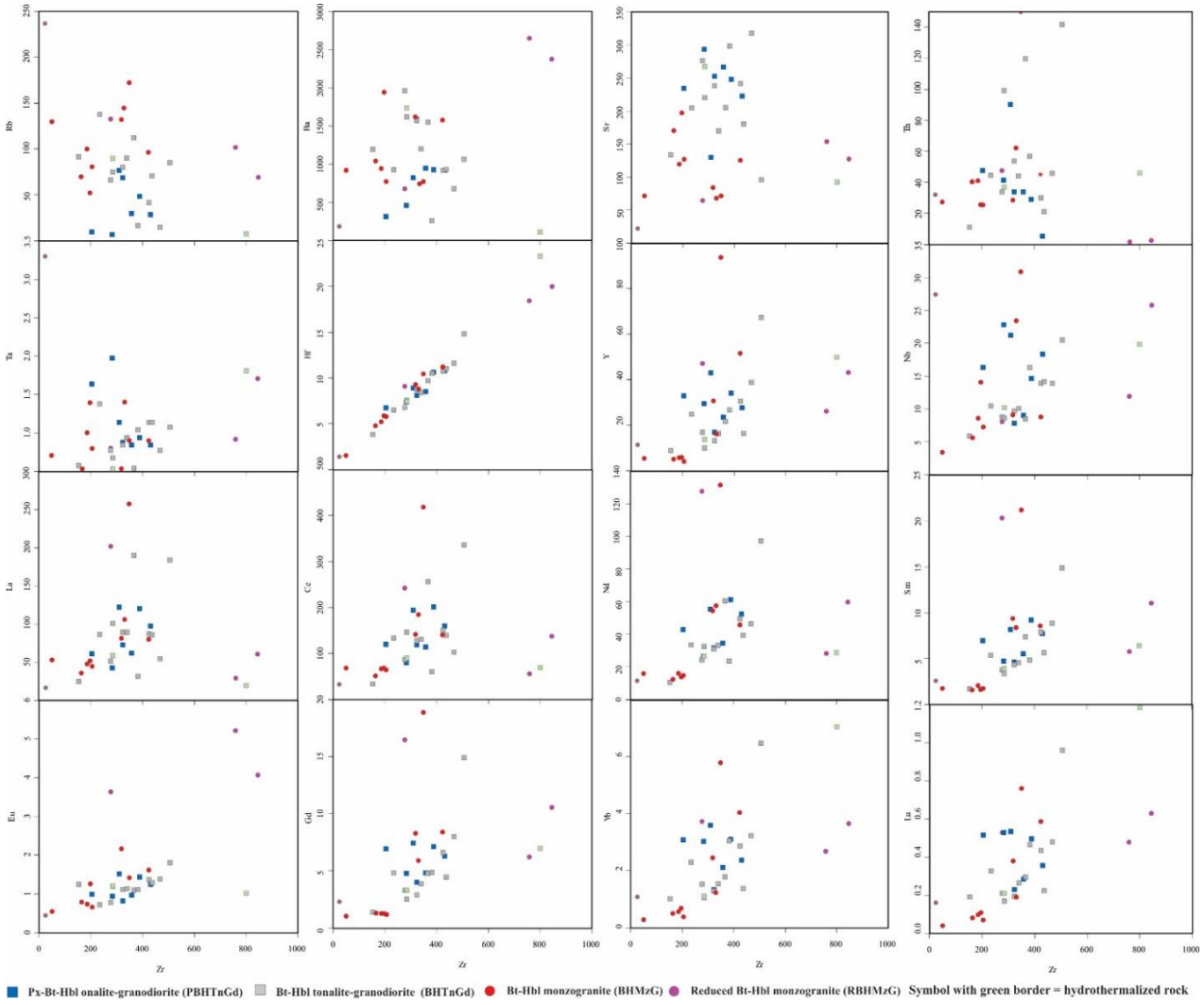

Supplementary figure 2 **.** Trace elements (ppm) vs. Zr (ppm) diagram.

Supplementary table 1. Synthesis of the geochronological data for the Neoarchean magmatism from Carajás province.

Sapucaia terrane				
Lithostratigraphic Units		**Lithology**	**Method**	**Age/Reference**
Velha Canadá leucogranite		Granodiorite	Evaporation-Pb	2733±1 Ma (1)
		Granodiorite	Evaporation-Pb	2747±2 Ma (2)
Vila Jussara suite	Magenesian	Hb-Bt monzogranite	Evaporation-Pb	2748±2 Ma (3)
		Hb-Bt monzogranite	Evaporation-Pb	2749±3 Ma (3)
		Bt-Hb Tonalite	U-Pb SHRIMP	2766±9Ma (4)
			U-Pb SHRIMP	2769±9Ma (5)
	Fe-Oxidized	Bt-Hb monzogranite	Evaporation-Pb	2754±2 Ma (6)
		Bt-Hb-Monzogranite	U-Pb SHRIMP	2743±11Ma (4)
	Fe-Reduced	Bt-Hb monzogranite	U-Pb SHRIMP	2743±9Ma (5)
		Bt-Hb-Monzogranite	U-Pb SHRIMP	2745±20Ma (4)
Canaã dos Carajás terrane				
Cristalino diorite		Diorite	Evaporation-Pb	2738±6 Ma (7)
Curral granite		Granite	U-Pb SHRIMP	2739±4M Ma (8)
Sossego granite		Granite	U–Pb LA–ICP–MS	2740±26 Ma (8)
Plaquê suite		Granitoid	Evaporation-Pb	2729±29 Ma (9)
		Granitoid	Evaporation-Pb	2736±24 Ma (9)
Vila União suite		Quartz diorite	U-Pb LA-ICP-MS	2734±9 Ma (10)
		Leucomonzogranite	U-Pb SHRIMP	2744±5 Ma (10)
		Bt-Hb monzogranite	Evaporation-Pb	2746±1.2 Ma (10)
		Bt-Hb monzogranite	U-Pb SHRIMP	2745±7.1Ma (11)
		Bt-Hb Tonalite	U-Pb SHRIMP	2745±9.9Ma (11)
Planalto suite		Granite	Evaporation-Pb	2747±2 Ma (7)
		Bt-Hb syenogranite (AMR-187B)	U-Pb LA-MC-ICP-MS	2733±2 Ma (12)
			U-Pb LA-MC-ICP-MS	2729±17 Ma (12)
			U-Pb SHRIMP	2738±3 Ma (13)
		Hb-Bt syenogranite (ARC-109)	Evaporation-Pb	2731±1 Ma (12)
			U-Pb LA-MC-ICP-MS	2710±10 Ma (12)
			U-Pb SHRIMP	2730±5 Ma (13)
		Bt syenogranite (GRD-77)	Evaporation-Pb	2736±4 Ma (12)
			U-Pb LA-MC-ICP-MS	2706±5 Ma (12)
		Bt-Hbl tonalite (AMD-01A)	Evaporation-Pb	2741±0,1 Ma (14)
		Bt-Hbl syenogranite (AMD-01B)	Evaporation-Pb	2730±0 Ma (14)
		Bt-Hbl monzogranite (AMD-02)	Evaporation-Pb	2731±0,8 Ma (14)
Café enderbite		Opx-tonalite	U–Pb LA–ICP–MS	2730±7 Ma (15)
		Opx- trondhjemite	U-Pb SHRIMP	2740±8 Ma (9)
		Opx trondhjemite	Evaporation-Pb	2754±1 Ma (15)
Pium Diopside norite		Quartzo gabbro	Evaporation-Pb	2744,2±1 Ma (16)
		Quartzo gabbro	U-Pb ICPMS	2735±5Ma (12)
		Gabbronorite	Evaporation-Pb	2744±0,8 Ma (16)
		Norite	Evaporation-Pb	2745±1,2 Ma (16)
		Associated granitoids	Evaporation-Pb	2732±1 a 2742 ±1 Ma (14)
Pedra Branca suite		Trondhjemite	Evaporation-Pb	2749±6 Ma (17)
		Trondhjemite	U-Pb TIMS	2765±39 Ma (17)
		Trondhjemite (AMR-191A)	U-Pb LA-MC-ICP-MS	2750±5 Ma (13)
Cateté suite		Gabbro	U-Pb SHRIMP	2766±6 Ma (18)

Supplementary table 1 (Cont.): Synthesis of the geochronological data for the Neoarchean magmatism from Carajás province.

Carajás basin			
Old Salobo granite	Granitoid	U-Pb	2573±3 Ma (19)
	Granitoid	U-Pb SHRIMP	2547±5 Ma (20)
	Granitoid	U-Pb SHRIMP	2551±9 Ma (20)
	Bt monzogranite	U-Pb LA-ICP_MS	2497±41Ma (21)
	granodiorite to tonalite	U-Pb LA-ICP_MS	2554 ± 3, 2549 ± 7, 2594 ± 6 Ma (22)
GT-46 deposit (Igarapé Cinzento granite)	Isotropic granite	U-Pb LA-ICP_MS	2557±26 Ma (23)
			2564 ± 4 Ma (22)
	Foliated tonalite	U-Pb LA-ICP_MS	2532±26, 2639±16 Ma (23)
			2560 ± 3, 2576 ± 4 Ma(22)
	Pegmatite		2562 ± 39 Ma (23)
Itacaiúnas granite	Granitoid	Evaporation-Pb	2560±37 Ma, 2525 ± 38 (24)
Igarapé Gelado suite	Monzogranite	Evaporation-Pb	2731±2 Ma (25)
	Foliated tonalite	U-Pb LA-ICP-MS	2680 ± 18, 2640 ± 16, 2623 ± 5 ,2579 ± 28 Ma (22)
	Ultramylonitic Monzogranite	U-Pb LA-ICP-MS	2561 ± 5 Ma (22)
	Mylonitized granitoid	U-Pb LA-ICP-MS	2701±30Ma (20)
	Granitoid	U-Pb SHRIMP	2763 ± 4Ma (20)
	Granitoid	U-Pb LA-ICP-MS	2744 ± 4, 2731 ± 7 Ma (22)
	Hb-Bt monzogranite	U-Pb SHRIMP	2682±25Ma (21)
	Monzogranite	U-Pb SHRIMP	2611±28, 2665±29 Ma (26)
	Granodiorite	U-Pb SHRIMP	2659.7±6 Ma (26)
Serra do Rabo granite	Hb-syenogranite	U-Pb-TIMS	2743±1 Ma (25)
Estrela complex	Granitoid	Evaporation-Pb	2763±7 Ma (25)
Rio Sereno granite	Foliated granodiorite	U-Pb LA-ICP-MS	2787±73Ma (27)
Lavrado suite - Aquiri	Isotropic granodiorite	U-Pb SHRIMP	2666±78Ma (28)

	Foliated granite	U-Pb SHRIMP	2651±14Ma (28)
Buritirama granite	Foliated granite	U-Pb LA-ICP-MS	2549±6Ma (29)
Luanga complex	Gabbro	U-Pb	2763±6 Ma (19)

References: (1) Santos P.J.L. et al., (2010); (2) Sousa et al., (2010); (3) Oliveira et al., (2010); (4) Silva et al., 2025 (5) F.V. Guimarães, R. Dall'Agnol e J.O.S. Santos (não publicado); (6) Silva M.L.T. et al., (2010); (7) Huhn et al., (1999); (8) Moreto et al., (2015b);(9) Avelar et al., (1999); (10) Marangonha, 2019b; (11) Marangoanha et al., (2020); (12) Feio et al., 2012; (13) Feio et al., 2013; (14) Galarza et al., (2017); (15) Marangoanha et al. (2019a); (16) Santos et al., (2013); (17) Sardinha et al., (2004); (18) Lafon et al., (2000); (19) Machado et al., (1991); (20) Melo et al., (2016); (21) Tavares et al., (2021); (22) Toledo et al., (2023); (23) Toledo et al.,(2019); (24) S.R. Souza et al., (1996); (25) Barros et al., (2009); (26) Reis, (2017); (27) Tavares e Silva, (2015); (28) Silva et al., (2023); (29) Salgado et al., (2019).

Supplementary table 2. Modal compositions of the representative samples from the Igarapé Gelado suite varieties (See Supplementary table 2 from chapter 2.).

Supplementary table 3: Representative chemical compositions of the granitoids from Igarapé Gelado suite.

Variety	PBHTnGd							BHTnGd													
Sample	CAD-4	JK-60	CR-6A	CAD-14	CR-7D	CAD-17	CR-8A	JK-61A	CR-7B	JK-86*	JK-59	CG-75	CAD-16A	CR-7A	CR-12A	CAD-5	JK-139A	CAD-3	JK-446	CAD-6B	JK-372*
SiO_2(wt. %)	64.5	65.3	67	68.2	68.7	68.7	68.7	64.5	64.9	65.8	66.1	67.2	67.9	67.9	67.9	68.5	68.6	68.3	71.2	71.6	75.7
TiO_2	0.5	0.57	0.49	0.39	0.46	0.35	0.48	0.51	0.54	0.43	0.53	0.46	0.4	0.32	0.43	0.4	0.45	0.34	0.31	0.2	0.27
Al_2O_3	15.7	15.35	15.6	13.6	15.25	14	14.95	15.95	14.65	15.25	14.7	15.55	14.25	14.2	14.55	14.7	13.5	14.4	14.15	13.8	11.35
Fe_2O_{3t}	6.26	5.67	4.08	4.87	4.93	3.9	5.64	5.95	6.07	4.65	5.57	4.36	4.97	4.18	4.01	4.3	5.02	3.7	3.75	2.92	4.07
MnO	0.03	0.03	0.03	0.03	0.02	0.02	0.03	0.03	0.03	0.02	0.02	0.03	0.02	0.02	0.02	0.02	0.03	0.02	0.01	0.02	0.02
MgO	0.89	0.91	0.71	0.44	0.73	0.62	0.77	0.84	0.86	0.65	0.81	0.8	0.71	0.49	0.57	0.63	0.55	0.51	0.47	0.36	0.33
CaO	3.87	3.54	4.88	2.64	3.08	4.51	3.7	3.81	3.84	2.78	3.45	4.29	2.66	2.59	2.63	2.82	2.3	2.23	2.03	2.3	2.33
Na_2O	4.72	4.75	5.48	3.63	4.26	4.98	4.62	4.98	4.35	4.34	3.99	5.1	3.96	3.85	4.1	4.1	3.72	3.98	4.17	3.52	4.8
K_2O	1.98	1.79	1.01	3.12	2.84	0.98	1.69	1.53	1.51	2.97	2.23	0.99	2.71	3.14	2.95	2.8	2.75	3.36	2.97	3.81	0.68
P_2O_5	0.18	0.17	0.24	0.11	0.13	0.51	0.13	0.15	0.14	0.11	0.17	0.18	0.11	0.07	0.1	0.11	0.09	0.1	0.09	0.1	0.01
LOI	1.34	1.03	0.79	0.87	0.87	1.34	0.48	0.96	1.75	2.1	1.66	1.3	1.92	1.59	0.92	1.67	1.57	1.31	1.24	1.1	0.94
Total	99.97	99.11	100.31	97.9	101.27	99.91	101.19	99.21	98.64	99.1	99.23	100.26	99.61	98.35	98.18	100.05	98.58	98.25	100.39	99.73	100.5
FeO_t	5.63	5.10	3.67	4.38	4.44	3.51	5.07	5.35	5.46	4.18	5.01	3.92	4.47	3.76	3.61	3.87	4.52	3.33	3.37	2.63	3.66
$FeO_t/(FeO_t+MgO)$	0.86	0.85	0.84	0.91	0.86	0.85	0.87	0.86	0.86	0.87	0.86	0.83	0.86	0.88	0.86	0.86	0.89	0.87	0.88	0.88	0.92
K_2O/Na_2O	0.42	0.38	0.18	0.86	0.67	0.20	0.37	0.31	0.35	0.68	0.56	0.19	0.68	0.82	0.72	0.68	0.74	0.84	0.71	1.08	0.14
A/CNK	0.93	0.95	0.82	0.96	0.97	0.80	0.93	0.95	0.93	0.99	0.96	0.90	1.00	0.98	0.99	0.99	1.02	1.01	1.03	0.98	0.88
Ba (ppm)	884	879	484	787	1610	272	908	701	882	1735	892	217	1160	1645	1985	1530	1085	1510	950	1220	113.5
Sr	243	218	296	125	255	230	262	321	237	268	175.5	294	165.5	223	279	234	98.7	201	207	136.5	91.1
Rb	45.2	25.3	8.7	73.2	70.4	6.4	26.6	17	38.1	89	67.4	13.4	86.8	77.1	68.2	76.7	87.2	109	140	93.6	6.3
Zr	389	431	290	309	330	204	357	474	425	285	437	382	339	292	285	323	513	365	241	160	800
Y	32.7	26.3	30.3	41.7	17.8	31.6	22.2	39.6	29.3	13.3	15.1	25.5	15.2	10.9	17.8	11.8	68.1	20.4	25.7	9.6	49.6
Hf	10.3	10.5	7.6	8.6	8.3	6.4	8.2	11.8	10.4	7.4	10.7	10.2	8.1	7.8	7	8.4	15	9.4	6.7	4	23.2
Nb	14.2	17.9	23.1	20.8	8.1	15.9	8.6	14.2	13.5	10.2	13.7	15.9	9.6	8.9	9.1	9.2	20.8	8	10.8	6.2	19.7
Ta	0.9	0.8	2	1.1	0.9	1.6	0.8	0.8	1.1	0.5	1.1	1	0.9	0.7	0.8	0.8	1.1	0.5	1.4	0.6	1.8
Ga	25.6	22.9	26.5	21.4	24.2	20.4	23.5	23.4	20.4	21.2	21	23	17.5	19.5	23.1	23.1	23.3	22	20.7	17	26
Th	27.2	3.45	42.6	88.2	35.1	45.8	31.9	47.1	28.3	36.6	19.4	55	42.2	100.5	35.2	51.8	143	118	45.8	12.55	45.6
U	4.36	1.34	17.9	29.4	3.77	21.9	2.53	2.54	2.55	2.57	1.69	18.4	5.85	17.55	6.87	7.24	16.05	23.6	10.85	2	6.6
V	43	48	31	19	31	24	27	38	37	34	35	77	27	26	24	25	24	21	18	15	38
La	116	93.4	44.5	118.5	75.2	57.1	57.8	56.6	83	57.6	81.5	27.3	85.4	103	54	85.1	186.5	186.5	89	26.6	18.2
Ce	194.5	153	84.2	187.5	122.5	113	107.5	107	144	89.1	133	54.1	124.5	150.5	90.8	121.5	341	250	137.5	38.1	68.8
Pr	18.85	15	7.8	17.5	10.4	11.9	10.25	12.4	14.8	8.08	12.1	5.94	10.7	12.25	8.1	10.65	30.9	21.9	11.85	3.5	7.86
Nd	59.2	50.6	27.6	53.6	32.9	41.1	32.7	47.5	47.8	26.4	37.6	21.8	31.4	33.9	25.4	29.1	98.3	58.8	34.6	11.5	28.3
Sm	8.88	7.41	4.91	7.83	4.84	6.64	5.24	9.07	7.59	3.84	5.34	4.51	4.25	3.57	3.94	4.01	15.05	7.03	5.58	1.88	6.29
Eu	1.36	1.17	0.99	1.44	0.86	0.92	0.89	1.43	1.29	1.19	1.21	1.04	1.07	1.25	0.83	1.04	1.85	1.02	0.77	1.3	1
Gd	6.88	6.07	4.98	7.2	4.17	6.69	4.57	8.15	6.37	3.34	4.2	4.62	3.62	2.7	3.5	2.67	15.1	4.54	5.02	1.57	6.97
Tb	0.96	0.97	0.82	1.27	0.52	1.09	0.66	1.31	1.03	0.54	0.63	0.79	0.57	0.44	0.51	0.37	2.46	0.6	0.81	0.24	1.37
Dy	6.4	5.32	4.68	6.88	2.94	6.11	3.88	7.75	5.48	2.77	3.2	4.83	3	1.99	3.02	2.29	14.15	3.47	4.51	1.63	8.48
Ho	1.19	1.05	0.99	1.39	0.63	1.18	0.76	1.46	1.07	0.54	0.62	0.96	0.59	0.4	0.59	0.43	2.86	0.65	0.9	0.32	1.85
Er	3.47	2.76	3.13	4.04	1.94	3.48	2.14	4.04	3.17	1.42	1.45	2.74	1.72	1.07	1.86	1.19	7.77	2.01	2.5	1.04	5.83
Tm	0.5	0.4	0.44	0.53	0.22	0.52	0.32	0.58	0.46	0.2	0.25	0.46	0.24	0.19	0.23	0.16	1.1	0.28	0.38	0.15	0.97
Yb	3	2.27	3.11	3.51	1.41	2.98	2.01	3.31	2.76	1.12	1.28	2.96	1.45	1.12	1.59	1.2	6.54	1.68	2.36	1.08	7.05
Lu	0.48	0.34	0.54	0.52	0.24	0.5	0.27	0.49	0.42	0.21	0.21	0.45	0.25	0.18	0.22	0.18	0.97	0.28	0.34	0.2	1.19
Rb/Sr	0.19	0.12	0.03	0.59	0.28	0.03	0.10	0.05	0.16	0.33	0.38	0.05	0.52	0.35	0.24	0.33	0.88	0.54	0.68	0.69	0.07
Sr/Ba	0.27	0.25	0.61	0.16	0.16	0.85	0.29	0.46	0.27	0.15	0.20	1.35	0.14	0.14	0.14	0.15	0.09	0.13	0.22	0.11	0.80
Ba/Sr	3.64	4.03	1.64	6.30	6.31	1.18	3.47	2.18	3.72	6.47	5.08	0.74	7.01	7.38	7.11	6.54	10.99	7.51	4.59	8.94	1.25
Sr/Y	7.43	8.29	9.77	3.00	14.33	7.28	11.80	8.11	8.09	20.15	11.62	11.53	10.89	20.46	15.67	19.83	1.45	9.85	8.05	14.22	1.84
La_N	374.19	301.29	143.55	382.26	242.58	184.19	186.45	182.58	267.74	185.81	262.90	88.06	275.48	332.26	174.19	274.52	601.61	601.61	287.10	85.81	58.71
Sm_N	45.54	38.00	25.18	40.15	24.82	34.05	26.87	46.51	38.92	19.69	27.38	23.13	21.79	18.31	20.21	20.56	77.18	36.05	28.62	9.64	32.26
Eu_N	18.50	15.92	13.47	19.59	11.70	12.52	12.11	19.46	17.55	16.19	16.46	14.15	14.56	17.01	11.29	14.15	25.17	13.88	10.48	17.69	13.61
Gd_N	26.56	23.44	19.23	27.80	16.10	25.83	17.64	31.47	24.59	12.90	16.22	17.84	13.98	10.42	13.51	10.31	58.30	17.53	19.38	6.06	26.91
Yb_N	14.35	10.86	14.88	16.79	6.75	14.26	9.62	15.84	13.21	5.36	6.12	14.16	6.94	5.36	7.61	5.74	31.29	8.04	11.29	5.17	33.73
$(La/Yb)_N$	26.07	27.74	9.65	22.76	35.96	12.92	19.39	11.53	20.27	34.67	42.93	6.22	39.71	62.00	22.90	47.81	19.23	74.84	25.43	16.61	1.74
Eu/Eu*	0.51	0.52	0.61	0.58	0.57	0.42	0.54	0.50	0.55	0.99	0.76	0.69	0.81	1.18	0.67	0.92	0.37	0.52	0.44	2.25	0.46
ΣREE	421.67	339.76	188.69	411.71	258.77	253.21	228.99	261.09	319.24	196.35	282.59	132.50	268.76	312.56	194.59	259.89	724.55	538.76	296.12	89.11	164.16

PBHTnGd = Px-Bt-Hb tonalite-granodiorite; BHTnGd = Bt-Hb tonalite-granodiorite; FeOt = Fe_2O_{3t}*0.8998. Eu/Eu* = Eu/((Sm*Gd)N)1/2 (Chondrite-normalized from Boynton, 1984).(*) = Hidrotermalized rock

Supplementary table 3 (cont.): Representative chemical compositions of the granitoids from Igarapé Gelado suite.

Variety	BHMzG									RBHMzG			
Sample	CR-3B	CR-01A	JK-137A	CR-3A	JK-418	CG-22A	CR-9	CR-05	CR-1A1	CR-10B	JK-47	JK-16	CR-4C*
SiO_2(% peso)	69.8	69.9	70.7	70.8	71.6	72	72.1	75.5	72.6	68.2	71.4	74.3	74.6
TiO_2	0.43	0.22	0.28	0.24	0.29	0.24	0.34	0.06	0.22	0.54	0.35	0.17	0.03
Al_2O_3	13.65	13.45	13.65	13.55	13.4	14.2	14.05	13.1	13.1	11.85	12.75	12.5	13.05
Fe_2O_{3t}	5.24	3.89	4.03	2.86	4	2.5	2.98	1.94	3.54	6.98	4.74	2.8	2.95
MnO	0.03	0.02	0.02	0.01	0.02	0.01	0.02	0.01	0.02	0.05	0.04	0.02	0.02
MgO	0.47	0.32	0.37	0.26	0.3	0.34	0.4	0.06	0.3	0.27	0.13	0.09	0.04
CaO	2.33	2.12	1.77	1.28	1.39	1.93	2.07	1.09	1.69	2.42	2.07	1.14	0.74
Na_2O	3.62	3.73	3.52	3.02	3.29	3.87	3.64	3.25	3.43	3.13	3.22	2.99	3.16
K_2O	4.38	3.48	3.89	6.11	4.71	3.57	3.57	4.72	4.36	3.57	3.79	4.8	4.97
P_2O_5	0.08	0.06	0.07	0.06	0.09	0.06	0.06	0.01	0.05	0.12	0.07	0.03	0.02
LOI	0.85	0.74	1.28	1.59	1.42	0.92	1.2	0.72	0.86	1.28	1.04	1.28	0.81
Total	100.88	97.93	99.58	99.78	100.51	99.64	100.43	100.46	100.17	98.41	99.6	100.12	100.39
FeO_t	4.71	3.50	3.63	2.57	3.60	2.25	2.68	1.75	3.19	6.28	4.27	2.52	2.65
$FeO_t/(FeO_t+MgO)$	0.91	0.92	0.91	0.91	0.92	0.87	0.87	0.97	0.91	0.96	0.97	0.97	0.99
K_2O/Na_2O	1.21	0.93	1.11	2.02	1.43	0.92	0.98	1.45	1.27	1.14	1.18	1.61	1.57
A/CNK	0.91	0.98	1.03	0.97	1.03	1.03	1.03	1.05	0.98	0.88	0.97	1.03	1.09
Ba (ppm)	1575	775	741	1620	771	1045	1940	915	941	2370	2660	679	183
Sr	125.5	127.5	68.1	83.7	71.4	170.5	197	71.3	120	127	152.5	64	22.3
Rb	96.3	80.4	145	132.5	172.5	70	52.3	130	100	68	99.8	132.5	237
Zr	422	205	331	317	348	164	195	51	186	846	760	285	23
Y	51.8	4.3	16.4	30.8	94	5.2	5.8	5.3	5.7	42.7	25.9	47	11.5
Hf	11.2	5.8	8.8	9.3	10.5	4.8	5.9	1.6	5.2	20	18.4	9.1	1.4
Nb	8.8	7.3	23.4	9.1	30.9	5.7	14.1	3.4	8.6	25.8	12	8.1	27.5
Ta	0.9	0.8	1.4	0.5	0.9	0.5	1.4	0.7	1	1.7	0.9	0.8	3.3
Ga	24.2	21	22.9	20.6	22	18.5	17.3	18.4	19.8	24.8	21.3	22.7	24.3
Th	45.4	25.7	62.1	28.6	149.5	40.5	25.7	27.5	41.1	3	1.4	47.7	32.2
U	4.52	9.9	8.92	3.73	49.9	6.57	3.38	20.3	9.26	1.17	1.13	5.45	11.1
V	17	<5	18	8	14	11	18	<5	7	<5	<5	<5	<5
La	80.1	44.7	106	81.3	257	35.6	51.8	52.6	47.3	61.2	28.5	202	16
Ce	141	65	184.5	142	419	50.9	68.8	68.2	66.7	137	54.5	242	32.3
Pr	13.55	5.32	17.8	15.2	43.1	4.33	5.1	5.88	5.49	15.05	6.86	38.3	3.42
Nd	45.7	14.8	57.4	54.4	131.5	12.8	14.1	15.8	16.1	59.4	28	127.5	11.7
Sm	8.56	1.78	8.4	9.35	21.2	1.59	1.62	1.75	2.06	11.05	5.62	20.3	2.59
Eu	1.61	0.65	1.12	2.17	1.42	0.81	1.26	0.55	0.73	4.07	5.21	3.64	0.46
Gd	8.42	1.23	5.91	8.31	18.9	1.3	1.32	1.09	1.29	10.55	6.21	16.5	2.34
Tb	1.31	0.14	0.89	1.32	3.2	0.2	0.2	0.14	0.17	1.46	0.95	2.54	0.34
Dy	8.12	0.76	3.81	6.87	17.7	1.11	1.06	0.77	1.05	8.1	5.26	13.35	1.83
Ho	1.64	0.13	0.64	1.29	3.39	0.22	0.23	0.14	0.18	1.57	1.03	2.2	0.34
Er	4.94	0.37	1.59	3.41	8.92	0.56	0.65	0.35	0.58	4.35	2.9	5.27	1.13
Tm	0.64	0.04	0.22	0.45	1.13	0.08	0.11	0.04	0.07	0.6	0.42	0.72	0.14
Yb	4.05	0.39	1.24	2.47	5.79	0.5	0.68	0.29	0.57	3.64	2.7	3.73	1.1
Lu	0.59	0.07	0.19	0.38	0.76	0.08	0.11	0.04	0.1	0.63	0.48	0.53	0.16
Rb/Sr	0.77	0.63	2.13	1.58	2.42	0.41	0.27	1.82	0.83	0.54	0.65	2.07	10.63
Sr/Ba	0.08	0.16	0.09	0.05	0.09	0.16	0.10	0.08	0.13	0.05	0.06	0.09	0.12
Ba/Sr	12.55	6.08	10.88	19.35	10.80	6.13	9.85	12.83	7.84	18.66	17.44	10.61	8.21
Sr/Y	2.42	29.65	4.15	2.72	0.76	32.79	33.97	13.45	21.05	2.97	5.89	1.36	1.94
La_N	258.39	144.19	341.94	262.26	829.03	114.84	167.10	169.68	152.58	197.42	91.94	651.61	51.61
Sm_N	43.90	9.13	43.08	47.95	108.72	8.15	8.31	8.97	10.56	56.67	28.82	104.10	13.28
Eu_N	21.90	8.84	15.24	29.52	19.32	11.02	17.14	7.48	9.93	55.37	70.88	49.52	6.26
Gd_N	32.51	4.75	22.82	32.08	72.97	5.02	5.10	4.21	4.98	40.73	23.98	63.71	9.03
Yb_N	19.38	1.87	5.93	11.82	27.70	2.39	3.25	1.39	2.73	17.42	12.92	17.85	5.26
$(La/Yb)_N$	13.33	77.27	57.63	22.19	29.93	48.00	51.36	122.28	55.95	11.34	7.12	36.51	9.81
Eu/Eu*	0.57	1.27	0.46	0.74	0.21	1.67	2.56	1.14	1.28	1.14	2.69	0.59	0.56
ΣREE	320.23	135.38	389.71	328.92	933.01	110.08	147.04	147.64	142.39	318.67	148.64	678.58	73.85

BHMzG = Bt-Hb monzogranite; SRG = Strongly Reduced granite.; FeOt = Fe_2O_{3t}*0.8998. Eu/Eu* = Eu/((Sm*Gd)N)1/2 (Chondrite-normalized from Boynton, 1984). (*) = Hidrotermalized rock

Supplementary table 4. Zircon U-Pb isotopic data obtained by SHRIMP for granitoids from Igarapé Gelado suite.

PBHTnGd

ID Spot	$^{204}Pb/^{206}Pb$ (%)	U ppm	Th ppm	Th/U	Isotopic ratios $^{207}Pb/^{235}U$	1σ	$^{206}Pb/^{238}U$	1σ	ρ	$^{207}Pb/^{206}Pb$	1σ	$^{206}Pb/^{238}U$	1σ	Age (Ma) $^{207}Pb/^{235}U$	1σ	$^{207}Pb/^{206}Pb$	1σ	Disc. (%)
CR-8A																		
9.1	0.014	1157	186	0.17	6.283	1.70	0.288	1.63	0.96	0.158	0.49	1633	24	2016	34	2435	8	+37
1.1	0.009	973	179	0.19	6.196	0.85	0.298	0.81	0.95	0.151	0.26	1682	12	2004	17	2354	4	+32
8.1	0.019	1124	149	0.14	7.190	1.25	0.322	1.17	0.93	0.162	0.46	1801	18	2135	27	2474	8	+31
4.1	0.005	1462	191	0.13	8.209	0.82	0.355	0.79	0.97	0.168	0.20	1960	13	2254	18	2533	3	+26
11.1	0.005	1073	218	0.21	8.996	0.89	0.385	0.80	0.90	0.170	0.39	2098	14	2338	21	2554	6	+21
10.1	0.006	1034	165	0.17	9.147	0.83	0.393	0.80	0.97	0.169	0.21	2136	15	2353	20	2546	3	+19
3.1	0.008	962	157	0.17	9.135	0.84	0.398	0.81	0.97	0.166	0.22	2160	15	2352	20	2522	4	+17
2.1	0.005	1802	688	0.39	10.899	0.80	0.441	0.78	0.98	0.179	0.15	2357	15	2515	20	2645	2	+13
6.1	0.004	1766	1063	0.62	11.896	0.83	0.476	0.79	0.95	0.181	0.27	2510	16	2596	22	2664	4	+7
12.1	0.003	1375	445	0.33	12.233	0.81	0.488	0.79	0.98	0.182	0.16	2563	17	2622	21	2669	3	+5
12.2	0.006	1035	168	0.17	12.538	0.89	0.507	0.82	0.92	0.179	0.35	2644	18	2646	24	2647	6	+0
5.1	0.005	1153	157	0.14	12.961	0.81	0.521	0.80	0.98	0.181	0.16	2702	18	2677	22	2658	3	-2
7.1	0.003	1249	326	0.27	14.087	1.09	0.552	1.08	0.99	0.185	0.15	2835	25	2756	30	2698	2	-6
CR-6A																		
1.1	0.016	1164	108	0.10	2.548	0.97	0.155	0.87	0.89	0.119	0.44	931	8	1286	13	1940	8	+56
7.1	0.008	1951	959	0.51	2.513	0.83	0.161	0.78	0.94	0.113	0.29	961	7	1276	11	1854	5	+52
9.1	0.006	1526	290	0.20	4.008	0.83	0.206	0.79	0.95	0.141	0.25	1209	9	1636	13	2238	4	+50
8.1	0.014	1537	139	0.09	6.023	1.01	0.285	0.95	0.94	0.153	0.35	1617	14	1979	20	2382	6	+36
10.1	0.015	2195	194	0.09	6.897	1.67	0.325	1.64	0.98	0.154	0.30	1813	26	2098	35	2391	5	+28
2.1	0.008	2282	226	0.10	8.042	1.84	0.362	1.81	0.99	0.161	0.29	1992	31	2236	41	2467	5	+22
3.1	0.005	1735	268	0.16	8.763	0.81	0.377	0.79	0.98	0.169	0.18	2062	14	2314	19	2543	3	+22
11.1	0.010	1770	566	0.33	9.217	0.81	0.385	0.79	0.98	0.174	0.18	2100	14	2360	19	2592	3	+22
5.1	0.015	1546	310	0.21	9.242	2.24	0.405	2.20	0.99	0.165	0.37	2192	41	2362	53	2513	6	+15
6.1	0.006	982	400	0.42	11.391	0.86	0.464	0.80	0.93	0.178	0.31	2459	16	2556	22	2633	5	+8
4.2	0.019	176	108	0.63	12.920	1.09	0.517	0.99	0.90	0.181	0.47	2687	22	2674	29	2664	8	-1
4.1	0.025	198	77	0.40	12.475	1.19	0.521	1.00	0.85	0.174	0.63	2704	22	2641	31	2593	11	-5
4.3	0.021	245	103	0.43	13.212	1.44	0.550	1.00	0.69	0.174	1.04	2824	23	2695	39	2600	17	-11
CAD-14																		
15.1	0.204	1933	248	0.13	1.438	2.10	0.109	1.85	0.88	0.096	1.00	667	12	905	19	1541	19	+60
14.1	1.491	1557	181	0.12	3.980	1.31	0.207	1.07	0.82	0.140	0.76	1212	12	1630	21	2221	13	+50
8.1	0.945	1611	222	0.14	6.580	1.56	0.289	1.28	0.82	0.165	0.90	1638	18	2057	32	2507	15	+39
4.1	0.137	1737	154	0.09	6.282	1.40	0.291	1.32	0.95	0.157	0.46	1647	19	2016	28	2419	8	+36
7.1	0.203	1309	1220	0.96	5.708	1.18	0.300	1.08	0.91	0.138	0.48	1690	16	1933	23	2203	8	+26
6.1	0.077	1511	184	0.13	7.342	1.18	0.332	1.06	0.90	0.161	0.52	1847	17	2154	25	2461	9	+29
5.1	0.699	1654	219	0.14	9.398	1.25	0.400	1.18	0.94	0.171	0.43	2168	22	2378	30	2563	7	+18
1.1	0.324	1368	165	0.12	9.638	1.14	0.417	1.06	0.94	0.168	0.40	2245	20	2401	27	2536	7	+14
9.1	0.149	1790	219	0.13	9.610	1.36	0.418	1.07	0.79	0.167	0.84	2250	20	2398	33	2526	14	+13
11.1	0.784	1963	136	0.07	10.130	1.25	0.428	1.19	0.95	0.172	0.37	2296	23	2447	31	2574	6	+13
13.1	0.559	1162	88	0.08	10.561	1.17	0.442	1.08	0.92	0.173	0.46	2357	21	2485	29	2592	8	+11
2.1	0.736	945	238	0.26	10.661	1.45	0.457	1.37	0.94	0.169	0.49	2426	28	2494	36	2550	8	+6
12.1	0.305	1374	106	0.08	11.382	1.15	0.475	1.07	0.93	0.174	0.42	2505	22	2555	29	2595	7	+4
10.1	0.346	908	68	0.08	13.542	1.18	0.559	1.09	0.93	0.176	0.44	2860	25	2718	32	2614	7	-12
3.1	0.180	1293	134	0.11	14.411	1.25	0.583	1.20	0.96	0.179	0.35	2961	28	2777	35	2646	6	-15

bold analysis spots = used for age calculations

BHTnGd

ID Spot	$^{204}Pb/^{206}Pb$ (%)	U ppm	Th ppm	Th/U	Isotopic ratios $^{207}Pb/^{235}U$	1σ	$^{206}Pb/^{238}U$	1σ	ρ	$^{207}Pb/^{206}Pb$	1σ	$^{206}Pb/^{238}U$	1σ	Age (Ma) $^{207}Pb/^{235}U$	1σ	$^{207}Pb/^{206}Pb$	1σ	Disc. (%)
JK-139A																		
8.1	0.000	1826	363	0.21	5.113	0.94	0.271	0.90	0.96	0.137	0.28	1548	12	1838	17	2185	5	+33
7.1	0.740	1409	176	0.13	5.659	1.01	0.288	0.98	0.97	0.143	0.22	1630	14	1925	19	2260	4	+32
11.1	0.431	1901	246	0.13	7.126	1.24	0.332	1.21	0.98	0.155	0.27	1850	20	2127	26	2407	5	+27
10.1	1.241	1857	247	0.14	7.698	1.11	0.360	1.08	0.97	0.155	0.27	1984	18	2196	24	2401	5	+20
1.1	1.507	4784	772	0.17	8.513	0.79	0.381	0.78	0.99	0.162	0.13	2081	14	2287	18	2477	2	+19
9.1	0.973	1975	284	0.15	8.852	0.80	0.391	0.78	0.98	0.164	0.16	2128	14	2323	19	2499	3	+17
4.1	0.344	1891	293	0.16	9.270	0.83	0.415	0.81	0.97	0.162	0.21	2237	15	2365	20	2477	4	+11
5.1	0.397	1822	235	0.13	9.484	1.11	0.427	1.09	0.98	0.161	0.22	2293	21	2386	26	2467	4	+8
6.1	0.542	1475	803	0.56	10.325	0.81	0.440	0.79	0.98	0.170	0.16	2351	16	2464	20	2559	3	+10
2.1	0.387	1740	245	0.15	9.974	0.82	0.439	0.80	0.97	0.165	0.20	2347	16	2432	20	2504	3	+7
12.1	0.576	1766	196	0.11	11.448	1.13	0.495	1.11	0.99	0.168	0.17	2591	24	2560	29	2536	3	-3
3.1	0.388	1614	162	0.10	13.515	0.80	0.555	0.79	0.98	0.177	0.14	2844	18	2716	22	2622	2	-10

bold analysis spots = used for age calculations

Supplementary table 4 (cont.): Zircon U-Pb isotopic data obtained by SHRIMP for granitoids from Igarapé Gelado suite.

BHMzG

ID Spot	$^{204}Pb/^{206}Pb$ (%)	U ppm	Th ppm	Th/U	Isotopic ratios $^{207}Pb/^{235}U$	1σ	$^{206}Pb/^{238}U$	1σ	ρ	$^{207}Pb/^{206}Pb$	1σ	$^{206}Pb/^{238}U$	1σ	Age (Ma) $^{207}Pb/^{235}U$	1σ	$^{207}Pb/^{206}Pb$	1σ	Disc. (%)
CR-1A																		
8.1	0.004	3523	336	0.10	2.024	1.01	0.126	0.99	0.98	0.116	0.20	768	7	1124	11	1897	4	+63
4.1	0.005	1962	167	0.09	3.178	0.85	0.173	0.78	0.92	0.133	0.34	1029	7	1452	12	2140	6	+56
12.1	0.018	1861	121	0.07	3.033	0.94	0.175	0.81	0.87	0.125	0.47	1042	8	1416	13	2034	8	+53
11.1	0.006	2999	254	0.09	3.498	0.86	0.183	0.78	0.91	0.139	0.36	1084	8	1527	13	2210	6	+55
13.1	0.012	2380	433	0.19	2.825	0.98	0.179	0.90	0.92	0.114	0.39	1063	9	1362	13	1869	7	+47
3.2	0.004	2356	221	0.10	3.735	0.99	0.191	0.98	0.98	0.142	0.19	1125	10	1579	16	2252	3	+54
2.2	0.005	2924	335	0.12	3.835	0.97	0.194	0.95	0.99	0.143	0.16	1145	10	1600	15	2266	3	+54
2.1	0.005	2256	255	0.12	3.922	0.80	0.199	0.78	0.97	0.143	0.19	1167	8	1618	13	2267	3	+53
6.1	0.006	2270	170	0.08	5.019	0.93	0.235	0.91	0.98	0.155	0.17	1359	11	1823	17	2403	3	+48
4.2	0.008	1150	637	0.57	5.028	0.90	0.239	0.80	0.89	0.152	0.41	1384	10	1824	16	2372	7	+46
3.1	0.005	2130	194	0.09	5.235	0.80	0.246	0.78	0.98	0.154	0.17	1419	10	1858	15	2393	3	+45
7.1	0.005	1959	202	0.11	5.399	0.91	0.250	0.90	0.98	0.156	0.17	1441	12	1885	17	2417	3	+45
10.1	0.004	1642	157	0.10	6.275	0.89	0.289	0.84	0.95	0.157	0.28	1638	12	2015	18	2427	5	+37
9.1	0.004	1941	159	0.08	6.837	1.13	0.300	1.12	0.99	0.165	0.15	1693	17	2090	24	2508	2	+37
5.1	0.009	2298	585	0.26	11.051	0.86	0.452	0.86	0.99	0.177	0.11	2404	17	2527	22	2628	2	+10
1.2	0.001	2055	182	0.09	12.287	0.79	0.505	0.78	0.99	0.176	0.10	2635	17	2627	21	2620	2	-1
1.1	0.001	1167	393	0.35	14.591	0.80	0.566	0.80	0.99	0.187	0.12	2891	19	2789	22	2716	2	-8
CG-22																		
2.1	0.000	997	128	0.13	2.695	1.46	0.156	1.11	0.76	0.125	0.95	935	10	1327	19	2032	17	58
4.1	0.015	1001	120	0.12	3.386	3.48	0.168	3.24	0.93	0.147	1.27	998	30	1501	52	2307	22	61
9.1	0.002	1137	557	0.51	3.261	1.31	0.172	1.07	0.82	0.138	0.76	1020	10	1472	19	2201	13	58
7.1	0.001	1391	533	0.40	3.314	1.39	0.176	1.19	0.86	0.137	0.71	1044	11	1484	21	2186	12	56
11.1	0.006	837	89	0.11	4.142	1.31	0.199	1.08	0.83	0.151	0.74	1172	12	1663	22	2354	13	55
3.1	0.000	1883	590	0.32	4.401	1.18	0.215	1.06	0.90	0.148	0.52	1255	12	1713	20	2328	9	51
6.1	0.000	1369	85	0.06	4.308	4.30	0.218	3.88	0.90	0.143	1.85	1270	45	1695	73	2270	32	48
8.1	0.000	798	107	0.14	5.588	3.06	0.263	2.18	0.71	0.154	2.15	1504	29	1914	58	2394	37	42
13.1	0.000	1304	124	0.10	5.589	1.21	0.266	1.07	0.88	0.152	0.56	1520	14	1914	23	2374	10	40
12.1	0.002	1205	165	0.14	6.480	1.23	0.279	1.08	0.87	0.168	0.60	1588	15	2043	25	2540	10	42
15.1	0.005	1044	105	0.10	8.112	1.45	0.347	1.34	0.92	0.170	0.56	1920	22	2244	33	2553	9	29
14.1	0.001	814	114	0.15	8.022	1.26	0.351	1.11	0.88	0.166	0.59	1940	19	2234	28	2515	10	26
5.1	0.002	816	82	0.10	8.153	1.29	0.352	1.10	0.86	0.168	0.67	1943	19	2248	29	2539	11	27
10.1	0.001	548	80	0.15	11.872	1.23	0.475	1.12	0.90	0.181	0.53	2504	23	2594	32	2666	9	7
1.1	0.004	795	93	0.12	11.951	1.49	0.478	1.40	0.94	0.181	0.52	2520	29	2601	39	2664	9	6
CR-09																		
15.1	0.000	1366	133	0.10	1.549	1.66	0.108	1.33	0.80	0.104	0.98	664	8	950	16	1689	18	64
12.1	0.004	1099	116	0.11	2.709	1.50	0.163	1.20	0.80	0.121	0.90	973	11	1331	20	1966	16	54
7.1	0.010	1149	126	0.11	2.802	1.51	0.165	1.22	0.81	0.123	0.88	985	11	1356	20	2001	16	55
2.1	0.007	1150	113	0.10	3.649	1.29	0.200	1.07	0.83	0.132	0.72	1175	12	1560	20	2130	13	49
13.1	0.004	1059	125	0.12	5.611	1.25	0.270	1.08	0.87	0.151	0.62	1541	15	1918	24	2354	11	39
5.1	0.009	1859	267	0.15	7.424	2.60	0.324	2.48	0.95	0.166	0.80	1809	39	2164	56	2520	13	32
14.1	0.005	1032	138	0.14	7.707	1.25	0.341	1.09	0.87	0.164	0.61	1889	18	2197	27	2499	10	28
11.1	0.001	2464	273	0.11	8.232	1.65	0.372	1.62	0.98	0.160	0.29	2041	28	2257	37	2459	5	20
10.1	0.005	1299	108	0.09	9.217	1.29	0.394	1.20	0.93	0.170	0.47	2143	22	2360	30	2553	8	19
3.1	0.004	1068	131	0.13	9.821	1.18	0.416	1.08	0.92	0.171	0.47	2242	20	2418	28	2570	8	15
8.1	0.005	1020	105	0.11	10.891	1.17	0.450	1.08	0.93	0.176	0.44	2395	22	2514	29	2612	7	10
4.1	0.002	842	98	0.12	13.159	1.20	0.529	1.10	0.92	0.180	0.48	2739	24	2691	32	2655	8	-4
9.1	0.002	1129	135	0.12	13.806	1.15	0.551	1.08	0.94	0.182	0.39	2831	25	2737	31	2668	7	-8
1.1	0.001	1075	101	0.10	16.951	1.25	0.658	1.20	0.96	0.187	0.35	3260	31	2932	37	2714	6	-26
6.1	0.002	774	77	0.10	17.035	1.16	0.662	1.09	0.95	0.187	0.37	3276	28	2937	34	2712	6	-27
JK-137A																		
6.2	0.016	2801	163	0.06	1.733	1.12	0.133	0.96	0.86	0.095	0.57	803	7	1021	11	1524	11	+50
13.1	0.037	2323	135	0.06	2.265	1.02	0.148	0.82	0.80	0.111	0.61	888	7	1201	12	1821	11	+55
12.1	0.056	3320	138	0.04	4.283	1.68	0.223	1.52	0.90	0.139	0.72	1296	18	1690	28	2221	13	+46
9.1	0.006	1781	149	0.09	4.970	1.06	0.250	1.04	0.98	0.144	0.22	1437	13	1814	19	2281	4	+41
2.1	0.038	2166	1239	0.59	5.459	0.93	0.266	0.80	0.86	0.149	0.48	1522	11	1894	18	2331	8	+39
1.1	0.041	2452	324	0.14	6.131	1.46	0.296	1.40	0.96	0.150	0.40	1670	21	1995	29	2350	7	+33
7.1	0.023	1474	177	0.12	6.326	1.64	0.313	1.61	0.98	0.147	0.33	1756	25	2022	33	2306	6	+27
3.1	0.014	2452	140	0.06	7.222	0.82	0.333	0.79	0.96	0.157	0.23	1853	13	2139	18	2426	4	+27
11.1	0.063	2460	1007	0.42	7.767	1.86	0.351	1.80	0.97	0.160	0.44	1941	30	2204	41	2460	7	+24
8.1	0.008	2478	452	0.19	7.785	1.10	0.356	1.07	0.98	0.159	0.24	1962	18	2206	24	2442	4	+23
6.1	0.005	1268	82	0.07	7.788	0.82	0.371	0.80	0.97	0.152	0.20	2035	14	2207	18	2370	3	+16
4.1	0.006	2299	170	0.08	9.105	1.17	0.408	1.14	0.98	0.162	0.23	2206	21	2349	27	2475	4	+13
5.1	0.006	1843	113	0.06	9.492	0.81	0.415	0.79	0.98	0.166	0.17	2239	15	2387	19	2516	3	+13
10.1	0.005	2061	478	0.24	12.073	1.46	0.516	1.44	0.99	0.170	0.20	2680	32	2610	38	2556	3	-6

bold analysis spots = used for age calculations

RBHMzG

ID Spot	$^{204}Pb/^{206}Pb$ (%)	U ppm	Th ppm	Th/U	Isotopic ratios $^{207}Pb/^{235}U$	1σ	$^{206}Pb/^{238}U$	1σ	ρ	$^{207}Pb/^{206}Pb$	1σ	$^{206}Pb/^{238}U$	1σ	Age (Ma) $^{207}Pb/^{235}U$	1σ	$^{207}Pb/^{206}Pb$	1σ	Disc. (%)
CR-10B																		

Population A																		
1.1	0.010	276	122	0.46	13.031	1.01	0.521	0.94	0.94	0.182	0.35	2701	21	2682	27	2667	6	-2
3.1	0.013	253	115	0.47	12.959	0.99	0.516	0.92	0.93	0.182	0.37	2682	20	2677	26	2672	6	-0
4.1	0.014	200	96	0.50	12.774	1.04	0.509	0.96	0.92	0.182	0.41	2654	21	2663	28	2670	7	+1
5.1	0.009	260	121	0.48	12.927	0.98	0.516	0.92	0.93	0.182	0.35	2683	20	2674	26	2668	6	-1
8.1	0.008	206	106	0.53	12.821	1.03	0.514	0.95	0.93	0.181	0.39	2673	21	2667	27	2662	6	-1
10.1	0.008	234	108	0.48	12.710	1.13	0.506	0.95	0.84	0.182	0.62	2640	21	2658	30	2672	10	+1
12.1	0.012	186	80	0.45	12.970	1.07	0.512	0.98	0.92	0.184	0.42	2664	21	2677	29	2688	7	+1
Population B																		
2.1	0.010	268	119	0.46	12.104	1.18	0.502	0.92	0.78	0.175	0.74	2621	20	2612	31	2606	12	-1
6.1	0.031	144	83	0.59	11.949	1.42	0.489	1.02	0.72	0.177	0.99	2565	22	2600	37	2628	16	+3
7.1	0.008	315	137	0.45	11.964	1.03	0.498	0.89	0.86	0.174	0.53	2606	19	2602	27	2598	9	-0
9.1	0.018	148	64	0.45	12.001	1.12	0.499	1.00	0.90	0.174	0.49	2610	22	2604	29	2600	8	-0
11.1	0.021	165	57	0.36	10.788	1.15	0.472	1.01	0.88	0.166	0.54	2492	21	2505	29	2515	9	+1
JK-47																		
Population A																		
4.1	0.016	162	84	0.54	13.440	1.79	0.524	1.38	0.77	0.186	1.13	2716	31	2711	48	2708	19	0
5.1	0.003	204	128	0.65	12.791	1.61	0.506	1.31	0.82	0.183	0.93	2638	28	2664	43	2684	15	2
10.1	0.012	234	111	0.49	12.847	1.61	0.508	1.29	0.80	0.183	0.96	2649	28	2669	43	2684	16	2
Population B																		
1.1	0.011	237	145	0.63	12.445	1.59	0.504	1.28	0.81	0.179	0.94	2629	28	2639	42	2646	16	1
3.1	0.012	272	82	0.31	12.501	1.57	0.501	1.25	0.80	0.181	0.94	2617	27	2643	41	2662	16	2
7.1	0.008	228	109	0.49	12.613	1.57	0.505	1.28	0.81	0.181	0.92	2635	28	2651	42	2663	15	1
2.1	0.020	163	71	0.45	12.320	1.85	0.497	1.40	0.75	0.180	1.22	2600	30	2629	49	2652	20	2
11.1	0.011	241	128	0.55	12.364	1.58	0.498	1.29	0.81	0.180	0.93	2605	28	2632	42	2654	15	2
12.1	0.000	163	84	0.53	12.680	1.75	0.510	1.39	0.80	0.180	1.05	2658	30	2656	46	2655	17	0
Population C																		
8.1	0.020	163	90	0.57	11.657	2.71	0.495	1.79	0.66	0.171	2.04	2593	38	2577	70	2565	34	-1
9.1	0.034	132	97	0.76	12.005	2.94	0.509	1.48	0.50	0.171	2.54	2653	32	2605	77	2567	42	-4
13.1	0.017	216	110	0.51	11.708	2.27	0.497	1.31	0.58	0.171	1.85	2602	28	2581	58	2566	31	-2
6.1	0.015	136	62	0.47	12.563	1.97	0.513	1.45	0.74	0.178	1.32	2669	32	2647	52	2631	22	-2

bold analysis spots = used for age calculations

CAPÍTULO 4: ASPECTOS (MICRO) ESTRUTURAIS E GEOCRONOLÓGICOS DA SUÍTE IGARAPÉ GELADO: IMPLICAÇÕES PARA COLOCAÇÃO DOS GRANITOS TIPO-A SINTECTÔNICOS DA PROVÍNCIA CARAJÁS.

Neste capítulo serão discutidos os resultados de aspectos de campo e microestruturais apresentados no capítulo 3, portanto os dados e figuras citados são referentes àquele capítulo.

4.1 ASPECTOS MICROESTRUTURAIS E COLOCAÇÃO DOS MAGMAS

Imagens de radar e dados de mapeamento geológico evidenciam a forma sigmoidal dos plutons da SIG, que são delimitados por zonas de cisalhamento regionais associadas ao lineamento Cinzento (Pinheiro & Holdsworth, 1997, Pinheiro & Holdsworth, 2000). Tais zonas exibem comportamento dúctil e direção WNW-ESE a E-W, coincidente com a das foliações presentes nas rochas da SIG. Meso-estruturas e micro-estruturas confirmam que a SIG passou por processos de deformação progressiva em diferentes intensidades, intimamente relacionadas à distância das zonas de cisalhamento (ZC) (Fig. 3).

Em campo é possível observar desde rochas pouco foliadas (Fig. 2g) até rochas intensamente deformadas como ultramilonitos (Fig. 2d), evidenciando a heterogeneidade da deformação. Os processos microdeformacionais que vão se intensifiando à medida que as ZC se aproximam se sucedem na seguinte ordem: Em primeiro lugar, mecanismos de recuperação (Blenkinsop 2000, Passchier & Trouw 2005, Fossen 2018) geram extinção ondulante em cristais de quartzo (Fig. 3d). Em seguida, feições compatíveis com o Regime 1 de Hirth & Tullis (1992) com recristalização de quartzo em baixa temperatura (200-450°C, Passchier & Trouw 2005) e baixa taxa de deformação, representados por *bulges* e subgrãos que comumente ocorrem de forma restrita em algumas rochas pouco deformadas da variedade PBHTnGd (Fig. 3b, d) e são ausentes nos monzogranitos mais deformados.

Mais próximo às ZC e preferencialmente nos monzogranitos, com o aumento contínuo da deformação, esta evolui para processos de maior temperatura e mais intensa recristalização que incluem os processos descritos por Passchier & Trouw, (2005) como rotacão de subgrãos (> 10°) refletindo na textura núcleo manto em quartzo e feldspatos (Fig. 3i, m, n) e a migração dos limites de grãos de alta temperatura evidenciada pelas bordas suturadas e/ou ameboidais (Fig. 3k). De acordo com Hirth & Tullis (1992), em quartzo estes processos se desenvolvem em sistemas hidratados a 500°C e a rotação de subgrão em feldspatos em T>600°C (Tullis & Yund 1989). Já para Trouw *et al.* (2009) estas características descritas, incluindo, quartzo *ribbons* recristalizados por rotação de subgrão, podem ser encontradas em ultramilonitos (Fig. 3l), e se desenvolvem em temperaturas de deformação >650°C. Por fim, com a diminuição

dos esforços diferenciais em um estágio pós deformacional, se desenvolvem cristais com contatos poligonais (Fig. 3j) (Nédélc & Bouchez 2015), pois, na ausência de deformação, os processos podem prosseguir em direção a um nível interno com baixa energia do cristal (deformação estática, Passchier & Trouw 2005). As temperaturas neste estágio seriam próximas das T do *solidus* em ~ 660 ° C estimadas por Mesquita *et al.* (2025), através da aplicação de geotermômetros e modelamento termodinâmico. A aceitação desta premissa implica que estas rochas tenham sido deformadas no final do estágio magmático ou logo após o final da sua cristalização em condições *subsolidus*.

Neste sentido, existem microestruturas que podem evidenciar que os mecanismos de deformação atuaram antes do magma cristalizar completamente, ainda na presença de fluidos magmáticos (Pawley & Collins 2002, Bitencourt *et al.* 2009, Felix *et al.* 2020; Ludovic *et al.* 2021, Silva *et al.* 2022, Silva *et al.* 2020, Silva-Silva *et al.* 2020, Zibra *et al.* 2024). Rutter & Neumann (1995) mostraram em estudos experimentais que microfraturas preenchidas por material quartzo-feldspático similar à matriz (Bouchez *et al.* 1992, Passchier & Trouw 2005) podem se formar com presença de até ~15% de líquido, portanto no estágio tardi-magmático (Fig. 3n). Estas feições, tal como a textura núcleo-manto, comumente encontrada nas variedades mais deformadas da SIG, são típicas de recristalização sintectônica (Blenkinsop 2000, Nedelec & Bouchez 2015). Por fim, a presença de uma meso-estrutura rúptil-dúctil caracterizada por fraturas que propiciaram pequenas movimentações dúcteis na foliação (Fig. 2e), indicam que processos rúpteis iniciaram quando a rocha ainda estava em estado plástico, possivelmente em condições *subsolidus.*

4.2 CARÁTER TECTÔNICO E COLOCAÇÃO

A porção norte da PC é marcada pela geração da Bacia Carajás em ~2.76 Ga (Docegeo 1988, Tavares *et al.* 2018, Araújo Filho *et al.* 2020). A gênese dos granitos neoarqueanos possui íntima relação com a evolução desta bacia e duas hipóteses têm sido amplamente discutidas na literatura. A primeira sugere que estes granitos são sintectônicos e deformados concomitantemente à sua colocação, que seria controlada por zonas de cisalhamento geradas durante o fechamento da Bacia Carajás entre ~2.75 e ~2.73 Ga (Barros *et al.* 2001, Barros *et al.* 2009, Cunha *et al.* 2016, Dall'Agnol *et al.* 2017; Marangoanha *et al.* 2019a, Oliveira *et al.* 2018a, Silva *et al.* 2020). A segunda hipótese considera que estes granitos são extensionais formados entre 2.76 e 2.70 Ga durante a abertura do rifte onde se instalou a Bacia Carajás e posteriormente deformados durante sua inversão em uma suposta colisão intracratônica entre

os domínios Carajás e Rio Maria que teria ocorrido entre ~2.68 e ~2.63 Ga (Tavares 2015; Tavares *et al.* 2018).

As similaridades geológicas e (micro) estruturais com os demais granitos neoarqueanos de Carajás, bem como com o Pluton Matok (2,67 Ga), colocado sintectonicamente no Cinturão Limpopo, situado no limite dos crátons Zimbabwe e Kaapvaal (Laurent *et al.* 2014, Rapopo 2011), sugerem que a SIG foi formada de acordo com a primeira hipótese apresentada. Dentre os critérios estruturais em escala de afloramento, estabelecidos por Silva *et al.* (2020) e Barros *et al.* (2009) para demonstrar que as rochas da Suíte Vila Jussara e do Complexo Estrela, respectivamente, ascenderam e se colocaram sintectonicamente ao longo de zonas de cisalhamento, foram observadas na SIG os seguintes: paralelismo da foliação em relação à estruturação regional WNW-ESE; forma elipsoidal ou alongada dos plutons (Figs. 1c, 2a); distribuição das rochas controladas por zonas de cisalhamento (Fig. 1c); e presença de estruturas dúcteis-rúpteis (Fig. 2ei). Tais evidências corroboram a hipótese de colocação sintectônica. As demais feições mesoscópicas descritas pelos autores supracitados não foram observadas, talvez ofuscadas pela espessa capa intempérica no extremo norte da Bacia Carajás, que limita a ocorrência de afloramentos na região. No entanto, os aspectos microestruturais presentes na SIG (Fig. 3) são similares aqueles descritos nos demais granitoides sintectônicos do Sul e Norte do Domínio Carajás e de outros crátons (Barros *et al.* 2001, 2009, Pawley & Collins, 2002, Rapopo 2011, Feio *et al.* 2012, Cunha *et al.* 2016, Dall'Agnol *et al.* 2017, Oliveira *et al.* 2018, Ribeiro-da Silva *et al.* 2018, Felix *et al.* 2020, Silva *et al.* 2020, Ludovic *et al.* 2021, Zibra *et al.* 2024) e dão sustentação à hipótese assumida: São eles: i) deformação progressiva que inicia a temperatura acima do *solidus* e se estende com a diminuição da temperatura no *subsolidus*; ii) fraturas preenchidas por material quartzo-feldspático similar a matriz; iii) extinção ondulante e textura núcleo-manto em quartzo. Além disso, recentemente, Cunha *et al.* (2021) concluíram por meio de estudo de dissolução de cristais de epidoto, que a ascenção do magma que originou os granitos da Suíte Vila Jussara foi rápida (~8210 m/ano), compatível com modelo de ascensão e colocação de magmas graníticos através de diques, falhas ou zonas de cisalhamento (Clemens & Mawer 1992, Petford *et al.* 2000, Cruden & Weinberg 2018). Embora não tenha sido identificado epidoto magmático na SIG, as demais características que apresenta em comum com a Suíte Vila Jussara permitem estender tal interpretação para os granitoides estudados neste trabalho. É válido destacar que foram estimadas pressões de colocação relativamente baixas para os granitoides neoarqueanos de Carajás (300-500 MPa, Cunha *et al.*, 2016, Dall'Agnol *et al.* 2017, Oliveira et al 2018a), no entanto, para SIG foram

obtidas pressões ligeiramente mais elevadas (≥550 MPa, Mesquita *et al.* 2025). Independente das diferenças mencionadas na pressão de colocação, os valores indicados são compatíveis com processo de migração dos magmas para porções mais rasas da crosta controlado por zonas de cisalhamento (Félix *at al*. 2020, Silva *at al.* 2020, Marangoanha *at al.* 2022).

4.3 IMPLICAÇÕES TECTÔNICAS DAS NOVAS IDADES U-Pb SHRIMP (2,68 Ga)

O ambiente tectônico da Bacia Carajás ainda não está totalmente definido e foram propostas para explicá-lo hipóteses divergentes. A primeira considera ambiente extensional com magmatismo bimodal associado à contaminação crustal em ambiente de rifte continental (Gibbs et. al. 1986, Wirth et. al. 1986, Olszewski et. al. 1989, Machado et. al. 1991, Macambira et. al. 1996, Trendall et. al. 1998, Martins *et al.* 2017). A segunda, sustentada por padrões ETR e afinidades geoquímicas cálcio-calcalinas/shoshoníticas de parte dos litotipos do Supergrupo Itacaiúnas, sugere ambiente de arco magmático, com instalação de bacias retro-arco (Meirelles & Dardenne, 1991, Teixeira & Eggler 1994, Lindenmayer *et al.* 2005, Lobato *et al.* 2005, Zucchetti 2007, Silva 2009).

O vulcanismo e as rochas mais antigas da granitogênese neoarqueana da Bacia Carajás forneceram idades similares (2,76 a 2,73 Ga), sugerindo ambiente extensional para geração dos granitos (Tavares *et al.* 2018). Embora ainda não exista um consenso sobre a relação entre o magmatismo granítico e o vulcanismo do Domínio Carajás, os dados (micro) estruturais indicam uma natureza compressiva/transpressional para os granitos neoarqueanos de Carajás e isto fortalece a interpretação de seu caráter sintectônico (Barros *et al.* 2001, Barros *et al.* 2009, Cunha *et al.* 2016, Dall'Agnol *et al.* 2017, Marangoanha *et al.* 2019a, Oliveira *et al.* 2018a, Silva *et al.* 2020), sendo adotada no presente estudo.

Neste trabalho foram obtidas idades de cristalização U-Pb SHRIMP (~2.68 Ga, Mesquita *et al.* subm.) menores que as registradas na maioria dos granitos neoarqueanos da Província Carajás (cf. Tabela Suplementar 1 no capítulo 3), e também inferiores àquelas divulgadas em trabalhos anteriores para a SIG (~2.76 Ga, Barbosa 2004, Melo *et al.* 2016). Portanto, a geração destes granitos mais tardios da SIG é síncrona a gênese dos depósitos IOCGs dos cinturões norte (|Lineamento Cinzento) e sul (Cinturão Itacaiúnas) do cobre da Província Carajás, que se instalaram em zonas de cisalhamento dúcteis (2,68 a 2,72 Ga, Silva *et al*. 2005, Monteiro *et al*. 2008, Moreto *et al.* 2015a, 2015b, Toledo *et al*. 2019). De acordo com Trunfull *et al.* (2020) estas idades obtidas para as mineralizações balizam o evento transpressional em ambos os cinturões do cobre de Carajás.

Desta forma, assumir as novas idades obtidas neste trabalho implica importantes mudanças na duração e configuração tectônica do magmatismo neoarqueano da PC. Neste caso, ao considerar a hipótese de caráter sintectônico para a SIG, o evento transpressional do lineamento Cinzento, responsável pelo fechamento da Bacia Carajás (~2.7 Ga, Pinheiro & Holdsworth 2000), teria durado mais que o admitido anteriormente, de maneira que os diferentes intervalos para inversão da Bacia Carajás disponíveis na literatura se sobreporiam, tendo se dado, face às novas idades obtidas, entre 2,76 e 2,68 Ga (Barros *et al.* 2009, Tavares 2015, este estudo). Seguindo este raciocínio, acredita-se que os magmas que originaram a SIG começaram a cristalizar aproximadamente no mesmo período que os demais granitoides neoarqueanos em ~2.76 Ga, conforme a idade apresentada por Melo *et al.* (2016), porém fusões mais tardias da fonte se estenderam no tempo até ~2.68 Ga (Mesquita *et al.* subm.), dentro do limite mínimo para inversão da Bacia proposto por Tavares 2015, e geraram os granitos mais tardios da SIG.

CAPÍTULO 5: CONCLUSÕES E CONSIDERAÇÕES FINAIS

O mapeamento geológico associado a estudos petrográficos, geoquímicos e químico-mineralógicos da porção centro-leste da Suíte Igarapé Gelado permitiu individualizar quatro variedades que consistem em: tonalitos e granodioritos com quantidades variáveis de biotita e anfibólio com ou sem clinopiroxênio e/ou ortopiroxênio associados; monzogranitos com biotita e anfibólio, classificados como rochas moderada ou fortemente reduzidas. A variedade com piroxênios inclui ortopiroxênio (ferrosilita) e clinopiroxênios, representados por augita com hedenbergita subordinada. Os anfibólios das quatro variedades são classificados como K-hastingsita e, subordinadamente, Fe-Tschermakita. As biotitas são predominantemente magmáticas primárias, ferrosas e as dos monzogranitos fortemente reduzidos têm #Fe > 0,9. Os tonalitos e granodioritos com piroxênios têm biotitas alcalinas e aqueles sem piroxênios biotitas subalcalinas. As biotitas dos monzogranitos fortemente reduzidos são principalmente alcalinas, enquanto as dos outros monzogranitos são subalcalinas. O plagioclásio das diferentes variedades é oligoclásio (An_{16-24}).

A integração da termobarometria e modelagem termodinâmica, aliada à paragênese modal das rochas, permitiu refinar os parâmetros de cristalização do magma. As rochas com piroxênio cristalizaram entre 1000±50°C e ~660°C. O BHTnGd e o BHMzG tiveram temperaturas de cristalização semelhantes às rochas com piroxênio, enquanto os monzogranitos reduzidos apresentaram temperaturas *liquidus* mais baixas (≤900°C). A pressão de colocação foi estimada em ~5,5 Kbar para diferentes variedades, valores estes ligeiramente superiores aos de outros granitos neoarqueanos de Carajás (Barros *et al*. 2009, Cunha *et al.* 2016, Dall'Agnol *et al*. 2017). O BHMzG evoluiu sob baixa fugacidade de oxigênio, próximo ao tampão FMQ, enquanto as variedades tonalíticas e granodioríticas teriam se formado em condições de FMQ+0,5. O BHMzGR cristalizou sob condições mais reduzidas (FMQ-0,5 a FMQ-1). Os magmas monzograníticos possuíam altos teores de H_2O (>4%, chegando a 7% no BHMzGR), comparáveis ou superiores aos estimados para os demais granitos neoarqueanos da região. Além disso, a variedade com piroxênio tem um teor de H_2O estimado em ~4%, próximo ao atribuído aos charnoquitos da Suíte Pium e Pluton Matok (Rapopo 2011, Félix *et al.* 2020 Marangoanha *et al.* 2022).

A geoquímica em rocha total demonstrou que os monzogranitos da SIG são semelhantes aos granitos neoarqueanos reduzidos da Supersuíte Planalto (Felix *et al*. 2023), enquanto os tonalitos e granodioritos se aproximam composicionalmente das variedades

ferrosas oxidadas e magnesianas da Suíte Vila Jussara, e das rochas charnoquíticas da Suíte Pium e do Pluton Matok.

A assinatura hidrotermal das rochas do setor oeste da SIG associadas aos depósitos IOCG é marcada por valores molares mais elevados de Na e K em comparação com as rochas do setor leste do IGS (este estudo). Os padrões de ETR das variedades PBHTnGd e BHTnGd se sobrepõem à maioria dos demais granitos neoarqueanos de Carajás. Em contraste, o BHMzG e o RBHMzG não apresentam padrões homogêneos de ETR, o que foi atribuído à influência de processos heterogêneos de alteração hidrotermal nessas rochas.

Os novos dados geocronológicos para a SIG mostram que suas rochas são mais jovens do que os granitoides neoarqueanos dominantes da província de Carajás (~2,74 Ga). Entretanto, apenas a idade ~2,68 Ga obtida para o BHMzGR foi assumida como representativa da cristalização. As demais idades concordantes definidas para a variedade BHMzGR (~ 2,65 e ~ 2,60 Ga), se sobrepõem às idades de intercepto superior das outras variedades, e sugerem mistura de zonas em cristais de zircão ou *reset* parcial do sistema U-Pb ocasionados pela intensa circulação de fluídos hidrotermais que percolaram por fraturas geradas pelas zonas de cisalhamento. Além dessas, as idades de intercepto superior de ~ 2,5 Ga obtidas para BHMzG e BHTnGd, semelhantes às idades das rochas hospedeiras e mineralizadas do depósito Salobo IOCG, foram atribuídas aos efeitos do evento de reativação do lineamento Cinzento que levou a uma reinicialização completa do sistema U-Pb.

A deformação das rochas da SIG foi condicionada por zonas de cisalhamento associadas ao lineamento do Cinzento, que moldaram corpos alongados sigmoidais com foliação incipiente a fortemente penetrativa com direções preferenciais de WNW-ESE a E-W. Através destas zonas os magmas provavelmente migraram e sofreram deformação progressiva até que ocorresse o resfriamento total, o que permite assumir caráter sintectônico para estas rochas. Além disso, o sintectonismo está intimamente relacionado ao processo de inversão da Bacia Carajás, portanto, a idade de cristalização mais jovem que as atribuídas anteriormente para os demais granitoides neoarqueanos da Bacia Carajás, permite estender o intervalo em que se deu a inversão para até 2,68 Ga, sendo assim mais longo que o proposto anteriormente (2,76 – 2,73 Ga).

Os dados isotópicos Lu-Hf e Sm-Nd indicam uma fonte dos magmas geradores da SIG essencialmente crustal [$\varepsilon_{Nd}(t)$ –2.86 a 0.18 e $\varepsilon_{Hf}(t)$ –3.3 a 0.1] com extração de crosta a partir do manto no Mesoarqueano (Nd-T_{DM} 2.98 a 2.84). Em particular para os monzogranitos

reduzidos esta extração ocorreu no Mesoarqueano-Paleoarqueano (Hf-T_{DM}^{C} 3.27-3.12). Além disso, estas rochas também exibem valores de εNd-Hf(t) menos negativos, sugerindo uma possível contribuição juvenil para sua fonte.

O modelo de geração adotado para as rochas da SIG foi baseado em similaridades geológicas com os demais granitoides e rochas charnoquíticas neoarqueanas da Província Carajás, bem como em dados isotópicos que indicam fusão parcial de diferentes porções de uma crosta granulítica máfica da região Chicrim-Cateté (Silva *et al*. 2021). Desta forma, o processo formador das variedades PBHTnGd e BHTnGd é a fusão parcial de um granulito máfico modificado a um grau de fusão estimado de 19% e 14%, respectivamente. Enquanto isso, para as variedades BHMzG e BHMzGR, foi definida a fusão parcial do granulito máfico, porém, de caráter toleítico, com um grau de fusão estimado de 9% e 7%, respectivamente.

Na proximidade de áreas hidrotermalizadas, particularmente a zona de cisalhamento Cinzento e o cinturão Cupro-Aurífero Setentrional, a composição das rochas e minerais da SIG foi modificada com a lixiviação de ETR e Y, levando à identificação de falsos granitos do subtipo A1 como parte do BHMzG. A atividade hidrotermal também modificou a textura e composição originais (metamictização) dos cristais de zircão, resultando em texturas maciças e enriquecimento de U, Th e LREE, exceto para zircões do BHMzGR que retêm características primárias. Essas observações permitiram melhor compreensão dos resultados geocronológicos U-Pb.

Por fim, nossos resultados destacam a importância e algumas características particulares do extenso magmatismo do SIG quando comparado aos granitos neoarqueanos da Província Carajás, bem como reforça a presença da relação deles com os charnoquitos. Eles também esclarecem como a deformação e os processos hidrotermais podem afetar a estrutura, textura e química de rochas e minerais e influenciar na interpretação petrogenética desses granitoides da Província Carajás e de outros crátons arqueanos.

REFERÊNCIAS

Almeida J.A.C, Dall'Agnol R., Oliveira M.A., Macambira M.J.B., Pimentel M.M., Rämö O.T., Guimarães F.V., da Silva Leite A.A. 2011. Zircon geochronology, geochemistry and origin of the TTG suites of the Rio Maria granite-greenstone terrane: Implications for the growth of the Archean crust of the Carajás province, Brazil. *Precambrian Research,* **187**: 201–221. https://doi.org/10.1016/j.precamres.2011.03.004

Almeida J., Dall'Agnol R., Leite A. 2013. Geochemistry and zircon geochronology of the Archean granite suites of the Rio Maria granite-greenstone terrane, Carajás Province, Brazil. *Journal of South American Earth Sciences*, **42**: 103–126. https://doi.org/10.1016/j.jsames.2012.10.008

Althoff F.J., Barbey P., Boullier A.M. 2000. 2.8–3.0 Ga plutonism and deformation in the SE Amazonian craton: the Archean granitoids of Marajoara (Carajás Mineral Province, Brazil). *Precambrian Research*, **104**: 187–206. https://doi.org/10.1016/S0301-9268(00)00103-0

Althoff A.M.R., Villas R.N.N., Giuliani G.A. 1994. Mineralização cuprífera da área Bahia, Serra dos Carajás, PA: evolução dos fluidos hidrotermais e modelo metalogenético. *Geochimica Brasiliensis*, **8**(2):135–155.

Althoff F.J., Barbey P., Macambira M.J.B., Scheller T., Leterrier J., Dall'agnol R., Lafon J.M. 1998. La croissance du craton sud-amazonien (région de Rio Maria, Brésil). *In*: Réunion des Sciences de la Terre. Brest, Societé Géologique de France, *Resumés*, p. 62.

Andersen T., Andersson U.B., Graham S., Aberg G., Simonsen S.L. 2009. Granitic Magmatism by melting of juvenile continental crust: new constraints on the source of Paleoproterozoic granitoids in Fennoscandia from Hf isotopes in zircon. *Journal of the Geological Society*, **166**:233–247.

Araújo O.J.B. & Maia R.G.N. 1991. Serra dos Carajás, Folha SB.22-Z-A, Estado do Pará, escala 1:250.000. Brasília, DF, CPRM- Programa Levantamentos Geológicos Básicos do Brasil (PLGB), Projeto Especial Mapas de Recursos Minerais, de Solos e de Vegetação para a Área do Programa Grande Carajás, 135 p.

Araújo R. & Nogueira A.C.R. 2019. Serra Sul diamictite of the Carajás Basin (Brazil): A Paleoproterozoic glaciation on the Amazonian Craton. *Geology*, **47**:1166–1170.

Araújo R.N. & Sousa M.J. 2018. Geologia, Estratigrafia e análise do minério dos depósitos de manganês de Carajás: regiões do Azul, Sereno, Buritirama e Antônio Vicente. *In:* Araújo Raphael Neto & Sousa Marcelo Januário de. *Área de relevante interesse mineral, Província Mineral de Carajás, PA*: estratigrafia e análise do minério de Mn de Carajás, áreas Azul, Sereno Buritirama & Vicente Antônio. Belém, CPRM, 198p. (Relatório técnico). (Províncias Mineral do Brasil, 16).

Araújo-Filho R.C., Nogueira A.C.R., Araújo R.N. 2020. New stratigraphic proposal of a Paleoproterozoic siliciclastic sucession: implications for the Evolution of the Carajás Basin, Amazonian Craton, Brazil. *Journal of South American Earth Sciences*, **102**:102665.

Avelar V.G. 1996. *Geocronologia Pb-Pb por evaporação em monocristal de zircão do magmatismo da região de Tucumã, SE do estado do Pará, Amazônia Oriental.* MS Dissertation. Instituto de Geociências, Universidade Federal do Pará, Belém, 149 p.

Avelar V.G., Lafon J.M., Correia JR, F.C., Macambira E.M.B. 1999. O Magmatismo Arqueano da região de Tucumã – Província Mineral de Carajás: novos resultados geocronológicos. *Revista Brasileira de Geociências*, **29**(4):453–460.

Barbosa O., Ramos J. R.de Andrade, Gomes F.A., Helmbold R. (eds). 1966. Geologia estratigráfica, estrutural e econômica da área do Projeto Araguaia. *Divisão de Geologia e Mineralogia*, Rio de Janeiro, **19**: 1-94.

Barbosa J.P.O. 2004. *Geologia estrutural, geoquímica, petrografia e geocronologia de granitoides da região do Igarapé Gelado, Norte da Província Mineral de Carajás*. MS Dissertation, Instituto de Geociências, Universidade Federal do Pará, Belém, 96 p.

Barros C.E., Barbey P., Boullier A.-M. 2001. Role of magma pressure, tectonic stress and crystallization progress in the emplacement of syntectonic granites. The A-type Estrela Granite Complex (Carajás Mineral Province, Brazil). *Tectonophysics* **343**:93–109. https://doi.org/10.1016/S0040-1951(01)00260-8

Barros C.E., Dall'Agnol R., Barbey P., Boullier A.-M. 1997. Geochemistry of the Estrela Granite Complex, Carajás region, Brazil: An example of an Archaean A-type granitoid. *Journal of South American Earth Sciences* **10**: 321–330. https://doi.org/10.1016/S0895-9811(97)00017-5

Barros C.E., Sardinha A.S., Barbosa J.P.O., Macambira M.J.B., Barbey P., Boullier A.-M. 2009. Structure, petrology, geochemistry and zircon U/Pb and Pb/Pb geochronology of the synkinematic Archean (2.7 Ga) A-type granites from the Carajás Metallogenic Province, northern Brazil. *The Canadian Mineralogist,* **47:**1423–1440. https://doi.org/10.3749/canmin.47.6.1423

Batuk Joshi, K., Bhattacharjee J., Rai, G., Halla J., Ahmad T., Kurhila M., Heilimo E., Choudhary A.K. 2017. The diversification of granitoids and plate tectonic implications at the Archaean–Proterozoic boundary in the Bundelkhand Craton, Central India. *Geological Society*, London, Special Publications, **449**: 123–157.

Bitencourt M. de F., Kruhl J., Peternell M. 2009. Syntectonic flow and crystallization processes investigated by qualitative and quantitative fabric analysis: the Piquiri Syenite Massif (Southern Brazil). *AGU Spring Meeting Abstracts*.

Black L., Kamo S., Allen C.M., Davis, D., Aleinikoff J., Valley, J., Mundil R., Campbell I., Korsch R., Williams I., Foudoulis C. 2004. Improved $^{206}Pb/^{238}U$ microprobe geochronology by the monitoring of trace-element-related matrix effect: SHRIMP, ID-TIMS, ELA-ICP-MS and oxygen isotope documentation for a series of zircon standards. *Chemical Geology,* **205**: 115–140. https://doi.org/10.1016/j.chemgeo.2004.01.003

Black L.P. & Gulson B.L. 1978. The age of the mud tank carbonatite, strangways range, Northern territory. *BMR Journal of Australian Geology & Geophysics,* **3** (3): 227-232.

Blenkinsop T.G. 2000. *Deformation microstructures and mechanisms in minerals and rocks*. Springer Science & Business Media, 150 p.

Bouchez J. L., Delas C., Gleizes G., Nédélec A., Cuney M. 1992. Submagmatic microfractures in granites. *Geology*, **20**(1): 35–38.

Bouvier A., Vervoort J.D., Patchett P.J. 2008. The Lu-Hf and Sm-Nd isotopic composition of CHUR: constraints from unequilibrated chondrites and implications for the bulk composition of terrestrial planets. *Earth and Planetary Sciences Letters*, **273**:48–57. https://doi.org/https://doi.org/10.1016/j.epsl.2008.06.010

Brown M., Johnson, T., Gardiner N. 2020. Plate Tectonics and the Archean Earth. *Annual Review of Earth and Planetary Sciences,* **48:** 291-320. https://doi.org/10.1146/annurev-earth-081619-052705

Chappell B.W. & White A.J.R. 1974. Two contrasting granite types. *Pacific Geology*, **8**:173-174.

Chu N.C., Taylor R.N., Chavagnac V., Nesbitt R.W., Boella R.M., Milton J.A., German C.R., Bayon G., Burton K. 2002. Hf isotope ratio analysis using multi-collector inductively coupled plasma mass spectrometry: an evaluation of isobaric interference corrections. *Journal of Analytical Atomic Spectrometry,* **17:**1567–1574. https://doi.org/10.1039/B206707B

Clemens J. D. & Mawer C. K. 1992. Granitic magma transport by fracture propagation. *Tectonophysics*, **204**(3):339–360. https://doi.org/https://doi.org/10.1016/0040-1951(92)90316-X

Costa I.S.L., Serafim, I.C.C. O., Tavares, F.M., Polo, H.J.O. 2020a. Uranium anomalies detection through Random Forest regression. *Exploration Geophysics* **51**:555–569. https://doi.org/10.1080/08123985.2020.1725387.

Costa U.A.P., Paula R.R., Silva D.P.B., Tavares F.M., Oliveira J.K.M., Justo A.P. 2016. *Mapa geológico-geofísico ARIM Carajás*. Belém, CPRM. (Programa Geologia do Brasil-PGB) – Projeto Evolução Crustal e Metalogenia da Província Mineral de Carajás – ARIM Carajás. Escala 1:250.000.

Costa J.B.S, Araújo O.J.B., Jorge João X.S., Maia R., Macambira E.M.B., Vale A.G., Santos A., Pena Filho J.I.C., Neves A.P. 1994. Panorama tectono-estrutural da região sudeste do estado do Pará. *In:* SBG, 4° Simpósio geologia da Amazônia, Belém. *Resumos*[...], p.314–317.

Costa J.B.S., Araújo O.J.B., Santos A., Jorge João X.S., Macambira M.J.B. Lafon J.M. 1995. A Província Mineral de Carajás: aspectos tectono-estruturais, estratigráficos e geocronológicos. *Boletim do Museu Paraense Emilio Goeldi,* **7**:199–235.

Costa F.G., Santos, P.A., Serafim I.C.C.O., Costa I.S.L., Roopnarain S. 2020b. From Mesoarchean drips to modern–style tectonics in the Carajás Province, Amazonian *Craton. Journal of South American Earth Sciences*, **104**: 102817.

Cruden A. R. & Weinberg R. F. 2018. Chapter 2 - Mechanisms of Magma Transport and Storage in the Lower and Middle Crust—Magma Segregation, Ascent and Emplacement. *In* S. Burchardt (Ed.), *Volcanic and Igneous Plumbing Systems* (pp. 13–53). Elsevier. https://doi.org/10.1016/B978-0-12-809749-6.00002-9

Cunha B.C.C., Santos D.B., Prado P. 1984. Contribuição ao estudo da estratigrafia da região dos Gradaús, com ênfase no Grupo Rio Fresco. *In*: SBG, 33º Congresso Brasileiro de Geologia, *Anais*[...], Rio de Janeiro, p. **2**:873–885.

Cunha I.R.V., Dall'Agnol R., Feio G.R.L. 2016. Mineral chemistry and magnetic petrology of the Archean Planalto Suite, Carajas Province–Amazonian Craton: Implications for the evolution of ferroan Archean granites. J*ournal of South American Earth Sciences,* **67**: 100–121.

Cunha I. R. V., Dall'Agnol R., Scaillet B., Souza L.A.M. (2021). Magmatic epidote in Archean granitoids of the Carajás Province, Amazonian craton, and its stability during magma rise and emplacement. *Journal of South American Earth Sciences*, **112**. https://doi.org/10.1016/j.jsames.2021.103570

Dall´Agnol R., Vieira E.A.P., SÁ C.A.S., Medeiros H., Gastal M.C.P., Texeira N.P. 1986. Estado atual do conhecimento sobre as rochas granitoides da porção sul da Amazônia Oriental. *Revista Brasileira de Geociências*, **16**(1):11–23.

Dall'Agnol R., Cunha I.R., Guimarães F., Oliveira D., Teixeira M., Feio, G., Lamarão C. 2017. Mineralogy, geochemistry, and petrology of Neoarchean ferroan to magnesian granites of Carajás Province, Amazonian Craton: The origin of hydrated granites associated with charnockites. *Lithos* **277**:3-32. https://doi.org/10.1016/j.lithos.2016.09.032

Dall'Agnol R. & Oliveira D.C. 2007. Oxidized, magnetite-series, rapakivi-type granites of Carajás, Brazil: Implications for classification and petrogenesis of A-type granites. *Lithos* **93**: 215–233.

Dall'Agnol R., Teixeira N.P., Rämö O.T., Moura C.A. V, Macambira M.J.B., Oliveira D.C. 2005. Petrogenesis of the Paleoproterozoic rapakivi A-type granites of the Archean Carajás metallogenic province, Brazil. *Lithos*, **80**:101–129.

Dall'Agnol R., Oliveira M.A., Almeida J.A.C., Althoff F.J., Leite A.A.S., Oliveira D.C., Barros C.E.M. 2006. Archean and Paleoproterozoic granitoids of the Carajás metallogenic province, eastern Amazonian craton. *In*: Dall'Agnol R., Rosa-Costa L.T., Klein E.L. (eds.). Symposium on Magmatism, Crustal Evolution, and Metallogenesis of the Amazonian Craton. Belém, Abstracts Volume and Field Trips Guide, p. 150.

Dall'Agnol R., Oliveira D.C., Guimarães F.V., Gabriel E.O., Feio G.R.L., Lamarão C.N., Althoff F.J., Santos P.A., Teixeira M.F.B., Silva A.C., Rodrigues D.S., Santos M.J.P., Silva C.R.P., Santos R.D., Santos P.J.L. 2013. Geologia do Subdomínio de Transição do Domínio Carajás – Implicações para a Evolução Arqueana da Província Carajás – Pará. *In*: SBG, 13° Simpósio de Geologia da Amazônia, Belém, Anais[...], CD-rom.

Depaolo D. 1981. A Neodymium and Strontium Isotopic Study of the Mesozoic Calc-Alkaline Granitic Batholiths of the Sierra Nevada and Peninsular Ranges, California. *Journal of Geophysical Research,* **86:**10470–10488. https://doi.org/10.1029/JB086iB11p10470

Dey S., Pandey U., Rai A., Chaki A. 2012. Geochemical and Nd isotope constraints on petrogenesis of granitoids from NW part of the eastern Dharwar craton: Possible implications for late Archaean crustal accretion. *Journal of Asian Earth Sciences* **45**:40-56 https://doi.org/10.1016/j.jseaes.2011.09.013

Dhuime B., Hawkesworth C., Cawood P. 2011. When Continents Formed. *Science,* **331**:154–155. https://doi.org/10.1126/science.1201245

Dhuime B., Hawkesworth C., Delavault H., Cawood P. 2017. Continental growth seen through the sedimentary record. *Sedimentary Geolology*, **357**:16-32 https://doi.org/10.1016/j.sedgeo.2017.06.001

Dhuime B., Hawkesworth C., Storey C. 2012. A Change in the Geodynamics of Continental Growth 3 Billion Years Ago. *Science*, **335**:1334–1336. https://doi.org/10.1126/science.1216066

Dhuime B., Wuestefeld A., Hawkesworth C. 2015. Emergence of modern continental crust about 3 billion years ago. *Nature Geoscience* **8**:552–555. https://doi.org/10.1038/ngeo246

Dias S.B. 2009. *Caracterização geológica, petrográfica e geoquímica de granitos arqueanos da Folha Marajoara, terreno granito–greenstone de Rio Maria, sudeste do Pará*. MS Dissertation. Instituto de Geociências, Programa de Pós-Graduação em Geologia e Geoquímica, Universidade Federal do Pará, Belém, 129 p.

Docegeo E.D.A. 1988. Revisão litoestratigráfica da Província Mineral de Carajás. *In*: CVRD, 35º Congresso Brasileiro de Geologia, Belém, Anais [...], p.10–54.

Eby G.N. 1992. Chemical subdivision of the A-type granitoids: petrogenetic and tectonic implications. *Geology*, **20**:641–644.

Fabre S., Nédélec A., Poitrasson F., Strauss H., Thomazo C., Nogueira A. 2011. Iron and sulphur isotopes from the Carajás mining province (Pará, Brazil): implications for the oxidation of the ocean and the atmosphere across the Archaean-Proterozoic transition. *Chemical Geololgy*, **289**:124–139.

Feio G. & Dall'Agnol R. 2012. Geochemistry and petrogenesis of the Mesoarchean granites from the Canaã dos Carajás area, Carajás Province, Brazil: Implications for the origin of Archean granites. *Lithos,* **154**: 33–52. https://doi.org/10.1016/j.lithos.2012.06.022

Feio G., Dall'Agnol R., Dantas E., Macambira M., Santos J., Althoff F., Soares J. 2013. Archean granitoid magmatism in the Canaã dos Carajás area: Implications for crustal evolution of the Carajás province, Amazonian craton, Brazil. *Precambrian Research,* **227**:157–185. https://doi.org/10.1016/j.precamres.2012.04.007

Feio G.R.L., Dall'Agnol R., Dantas E.L., Macambira M.J.B., Gomes A.C.B., Sardinha A.S., Oliveira D.C., Santos R.D., Santos P.A. 2012. Geochemistry, geochronology, and origin of the Neoarchean Planalto Granite suite, Carajás, Amazonian craton: A-type or hydrated charnockitic granites? *Lithos,* **151**:57–73. https://doi.org/https://doi.org/10.1016/j.lithos.2012.02.020

Felix W., Oliveira, D., Ribeiro-Silva L., Silva F. 2020. Charnockites from Carajás Province, SE Amazonian Craton (Brazil): Petrogenetic constraints and intensive crystallization parameters. *Journal South American Earth Science* **101:**102598. https://doi.org/10.1016/j.jsames.2020.102598

Felix W. Q., Oliveira D. C., Silva L. R., Nascimento A. C., Marangoanha B, Silva F. F. 2023a. Supersuíte plutônica Planalto: uma proposta estratigráfica para o magmatismo Neoarqueano subalcalino da Província Carajás. *In*: SBG, 17° Simpósio de Geologia da Amazônia, Santarém. *Anais,* 394-399.

Felix W. Q., Oliveira D. C., Silva L. R., Nascimento A. C., Marangoanha B., Silva F. F. 2023b. Suíte Charnoquítica Pium: uma proposta litoestratigráfica para o magmatismo charnoquítico da Província Carajás. *In*: SBG, 17° Simpósio de Geologia da Amazônia, Santarém. *Anais,* 400-405.

Fossen H. 2012. *Geologia estrutural*. Tradução de Andrade R.D.F. São Paulo, Editora Oficina de Textos. 584p.

Fraga L.M., Silva C.M.G., Silva D.P.B., Corrêa L.W.C., da Silva L.C., Costa U.A.P., Barbosa J.S.P.O., Paula, R.R. 2020. *Mapa Geológico e de Recursos Minerais do Setor Aquiri – ARIM Carajás. Estado do Pará.* Serviço Geológico do Brasil - CPRM, Belém, 1 mapa colorido. Escala 1:50.000.

Frost B.R., Barnes C.G., Collins W.J., Arculus R.J., Ellis D.J., Frost C.D. 2001. A geochemical classification for granitic rocks. *Journal of Petrology*, **42**:2033–2048.

Gabriel E.O. & Oliveira D.C. 2014. Geologia, petrografia e geoquímica dos granitoides arqueanos de alto magnésio da região de Água Azul do Norte, porção sul do Domínio Carajás, Pará. *Boletim do Museu Paraense Emílio Goeldi-Ciências Naturais*, **9**(3):533–564.

Galarza M.A. 2002. *Geocronologia e geoquímica isotópica dos depósitos de Cu-Au Igarapé Bahia e Gameleira, Província Mineral de Carajás, Brasil*. PhD Thesis, Centro de Geociências, Universidade Federal do Pará, Belém.

Galarza M.A., Macambira M.J.B., Villas R.N. 2008. Dating and isotopic characteristics (Pb and S) of the Fe oxide–Cu–Au–U–REE Igarapé Bahia ore deposit, Carajás mineral province, Pará state, Brazil. *Journal of South American Earth Sciences*, **25**:377–397.

Galarza M.A., Oliveira D.C., Rodrigues E.A., Santos A.N., Martins A.C., Marangoanha B. 2017. Neoarchean granitoids (2.73–2.74 Ga) intrusive and associated with the Pium Diopside-Norite, Canaã dos Carajás, Carajás Province (PA). *Contribuições à geologia da Amazônia*, **10**: 225–246.

Gibbs A.K., Wirth K.R., Hirata W.K., Olszewski Jr W.J. 1986. Age and composition of the Grão Pará Group volcanics, Serra dos Carajás. *Revista Brasileira de Geociências*, **16**:201–211.

Gioia S. & Pimentel M. 2000. The Sm-Nd isotopic method in the Geochronology Laboratory of the University of Brasília. *An Academia Brasileira de Ciências,* **72**:219–245. https://doi.org/10.1590/S0001-37652000000200009

Gomes A.C.B. 2003. *Geologia, petrografia e geoquímica dos granitoides de Canaã dos Carajás, SE do estado do Pará*. MS Dissertation. Programa de Pós-Graduação em Geologia e Geoquímica, Instituto de Geociências, Universidade Federal do Pará, Belém, 160 p.

Gonçalez M.G.B., Dall'Agnol R., Vieira E.A.P., Macambira M.J.B., Della Senta N. 1988. Geologia do maciço anorogênico Cigano, Vale do Rio Parauapebas-PA, *In*: SBG, 35° Congresso Brasileiro de Geologia. Belém, p. 1132-1146.

Griffin W.L., Wang X., Jackson S.E., Pearson N.J., O'Reilly S.Y. 2002. Zircon geochemistry and magma mixing, SE China: in-situ analysis of Hf isotopes, Tonglu and Pingtan igneous complexes. *Lithos*, **61**: 237–269.

Guimarães F.V.G., Dall'Agnol R., Almeida J.A.C., Oliveira M.A. 2010. Caracterização geológica, petrográfica e geoquímica do trondhjemito Mogno e Tonalito Mariazinha, Terreno Granito-Greenstone de Rio Maria, SE do Pará. *Revista Brasileira de Geociências*, **40**(2):196–211.

Halla J., van Hunen J., Heilimo E., Hölttä P. 2009. Geochemical and numerical constraints on Neoarchean plate tectonics. *Precambrian Research*, **174**:155–162. https://doi.org/https://doi.org/10.1016/j.precamres.2009.07.008

Harris N., Pearce J., Tindle, A. 1986. Geochemical characteristics of collision zone magmatism. *Geological Society London Special Publications* **19**, 67–81. https://doi.org/10.1144/GSL.SP.1986.019.01.04

Heilimo E., Halla J., Hölttä P. 2010. Discrimination and origin of the sanukitoid series: Geochemical constraints from the Neoarchean western Karelian Province (Finland). *Lithos* **115**:27–39. https://doi.org/10.1016/j.lithos.2009.11.001

Hirata W.K., Rigon J.C., Kadekaru K., Cordeiro A.A.C., Meireles E.M. 1982. Geologia regional da Província Mineral de Carajás. *In*: 1º Simpósio de Geologia da Amazônia, Belém, *Anais*[…]*,* **1**:100–110.

Hirth G. & Tullis J. 1992. Dislocation creep regimes in quartz. *Journal of Structural Geology*, ***14***:145–159. https://doi.org/10.1016/0191-8141(92)90053-Y

Holland T.J.B., Green E.C.R., Powell R. 2018. Melting of peridotites through to granites: a simple thermodynamic model in the system KNCFMASHTOCr. *Journal of Petrology* **59**: 881–900. https://doi.org/10.1093/petrology/egy048

Horstwood M., Košler J., Gehrels G., Jackson S., McLean N., Paton C., Pearson N., Sircombe K., Sylvester P., Vermeesch P., Bowring J., Condon D., Schoene B. 2016. Community-Derived Standards for LA-ICP-MS U-Th-Pb Geochronology - Uncertainty Propagation, Age Interpretation and Data Reporting. *Geostandards and Geoanalytical Research* **40**. https://doi.org/10.1111/j.1751-908X.2016.00379.x

Huhn S.R.B., Macambira M.J.B., Dall'Agnol R. 1999. Geologia e geocronologia Pb/Pb do granito alcalino arqueano Planalto, região da Serra do Rabo, Carajás-PA. *In*: Simpósio de Geologia da Amazônia **6**:463–466.

Jackson S., Pearson N., Griffin W., Belousova E. 2004. The Application of Laser Ablation-inductively Coupled Plasma-mass Spectrometry to in situ U-Pb Zircon Geochronology. *Chemical Geololy,* **211**:47–69. https://doi.org/10.1016/j.chemgeo.2004.06.017

Janoušek V., Farrow C.M., Erban,V. 2006. Interpretation of Whole-rock Geochemical Data in Igneous Geochemistry: Introducing Geochemical Data Toolkit (GCDkit). *Journal of Petrology* **47**: 1255–1259. https://doi.org/10.1093/petrology/egl013

Javier Rios F., Villas R.N.N., Fuzikawa K. 1994a. Estudo preliminar de Inclusões Fluidas (IF) em veios hidrotermais do Granito Cigano, Serra dos Carajás, PA. *In*: SBG, 38° Congresso Brasileiro de Geologia. Camboriú, *Boletim de resumos expandidos*, p. 639-640.

Javier Rios F., Villas R.N.N., Pimenta M.A. 1994b. Fluidos relacionados com o hidrotermalismo do Granito Musa (PA): indicações das Inclusões Fluidas (IF) em quartzo de

veios mineralizados da Jazida de W de Pedra Preta. *In:* SBG, 38° Congresso Brasileiro de Geologia. Camboriú, *Boletim de resumos expandidos*, p. 644-645.

Jayananda M., Aadhiseshan, K.R., Kusiak M.A., Wilde S.A., Sekhamo K., Guitreau M., Santosh M., Gireesh R. V. 2020. Multi-stage crustal growth and Neoarchean geodynamics in the Eastern Dharwar Craton, southern India. *Gondwana Research*, **78**:228–260. https://doi.org/https://doi.org/10.1016/j.gr.2019.09.005

Jayananda M., Chardon D., Peucat J., Capdevila R. 2006. 2.61 Ga potassic granites and crustal reworking in the western Dharwar craton, southern India: Tectonic, geochronologic and geochemical constraints. *Precambrian Research,* **150**:1–26. https://doi.org/10.1016/j.precamres.2006.05.004

Joshi K.B., Singh S.K., Halla J., Ahmad T., Rai V.K. 2022. Neodymium Isotope constraints on the origin of TTGs and high-K Granitoids in the Bundelkhand Craton, central India: Implications for Archaean Crustal evolution. *Lithosphere*, 2022, 6956845.

Kaur P., Zeh A., Chaudhri N. 2019. Archean crustal evolution of the Aravalli Banded Gneissic Complex, NW India: Constraints from zircon U-Pb ages, Lu-Hf isotope systematics, and whole-rock geochemistry of granitoids. *Precambrian Research*, **327**:81–102. https://doi.org/https://doi.org/10.1016/j.precamres.2019.03.004

King P.L., White A.J.R., Chappell B.W., Allen C.M., 1997. Characterization and Origin of Aluminous A-type Granites from the Lachlan Fold Belt, Southeastern Australia. *Journal of Petrology,* **38**: 371–391. https://doi.org/10.1093/petroj/38.3.371

Krymsky R.S., Macambira J.B., Macambira M.B.J. 2002. Geocronologia U-Pb em zircão de rochas vulcânicas da Formação Carajás, estado do Pará. *In*: 2º Simpósio sobre vulcanismo e ambientes associados, SBG–Núcleo Norte, Belém, *Anais*[...], 41 p.

Lafon J.M., Rodrigues E., Duarte K.D. 1994. Le granite Mata Surrão: un magmatisme monzogranitique contemporain des associations tonalitiques trondhjemitiques-granodioritiques archéennes de la région de Rio Maria (Amazonie Orientale, Brésil). *Comptes Rendus de la Academie de Sciences de Paris*, **318**(5):643–649.

Lafon J.M. & Scheller T. 1994. Geocronologia Pb/Pb em zircão do Granodiorito Cumaru, Serrados Gradaús, PA. In: 4º Simpósio de Geologia da Amazônia, SBG–Núcleo Norte, Belém, *Resumos expandidos*[...], p. 321–323.

Lafon J.M., Macambira M.J.B., Pidgeon R.T. 2000. Zircon U-Pb SHRIMP dating of Neoarchean magmatism in the southwestern part of the Carajás Province (Eastern Amazonian Craton, Brazil). *In*: 31º International Geological Congress. Rio de Janeiro, *Abstracts*, 1 CDrom

Laurent O., Martin H., Moyen J.-F., Doucelance R. 2014. The diversity and evolution of late-Archean granitoids: Evidence for the onset of "modern-style" plate tectonics between 3.0 and 2.5 Ga. *Lithos* **205:** 208-235. https://doi.org/10.1016/j.lithos.2014.06.012

Leite A.A.S., Dall'Agnol R., Macambira M.J.B., Althoff F.J. 2004. Geologia e geocronologia dos granitóides arqueanos da região de Xinguara (PA) e suas implicações na evolução do Terreno Granito-Greenstone de Rio Maria. *Revista Brasileira de Geociências*, **34**:447–458.

Leite-Santos P.J. & Oliveira D.C. 2014. Trondhjemitos da área de Nova Canadá: novas ocorrências de associações magmáticas tipo TTG no Domínio Carajás. *Boletim do Museu Paraense Emílio Goeldi- Ciências Naturais*, **9**(3):635–659.

Leite-Santos P.J. & Oliveira D.C., 2016. Geologia, petrografia e geoquímica das associações leucograníticas arqueanas da área de Nova Canadá: Província Carajás. *Geologia USP. Série Científica **16***:37–66.

Leite-Santos P.J., Oliveira D.C., Galarza M.A., Macambira M.J.B. 2010. Geologia, Petrografia e Geocronologia das rochas granitoides do Complexo Xingu da região de Nova Canadá, município de Água Azul do Norte – Província Mineral de Carajás. *In:* SBG, 45° Congresso Brasileiro de Geologia. Belém, *Anais*, CDrom.

Leite-Santos P.J. 2016. *Petrologia e geocronologia das associações leucograníticas arqueanas da região de Água Azul do Norte (PA): implicações para a evolução crustal da Província Carajás*. Qualificação de Doutorado. Instituto de Geociências, Universidade Federal do Pará, 83 p.

Leite-Santos P.J., Nascimento A.C., Oliveira D.C., Silva L.R., Gabriel O.G. 2023 Granodiorito Pantanal, Granodiorito Nova Canadá e Granito Velha Canadá: dados isotópicos de U–Pb–Hf–Nd–Sr e implicações para os processos de crescimento e retrabalhamento crustal do Terreno Sapucaia, Província Carajás. *In*: SBG, 17° Simpósio de Geologia da Amazônia, Santarém. *Anais* [...]. p. 377-382.

Lima P.H.A., Lamarão C.N., Santos M.J.P. 2014. Petrografia, geoquímica e suscetibilidade magnética do Granito Paleoproterozoico São João, sudeste do Cráton Amazônico, Província Carajás. *Boletim do Museu Paraense Emílio Goeldi,* Ciências Naturais. **9**: 47-72.

Lindenmayer Z.G. Fleck A., Gomes C.H., Santos A.B.S., Caron R., Paula F.C., Laux J.H., Pimentel. M.M., Sardinha A.S. 2005. Caracterização geológica do Alvo Estrela (Cu-Au), Serra dos Carajás, Pará. *In*: Marini O.J., Queiroz E.T., Ramos B.W. (ed.). *Caracterização de depósitos minerais em distritos mineiros da Amazônia.* Brasília, DNPM-CT/Mineral-ADIMB, p. 157–226.

Lobato L.M., Rosière C.A., Silva R.C.F., Zucchetti M., Baars F.J., Seoane J.C.S., Rios F.J.,Pimentel M., Mendes G.E., Monteiro A. M. 2005. A mineralização hidrotermal de ferro da Província Mineral de Carajás: controle estrutural e contexto na evolução metalogenética da província. *In*: Marini O.J., Queiroz E.T., Ramos B.W. (eds.). *Caracterização de depósitos minerais em distritos mineiros da Amazônia.* Brasília, DNPM-CT/Mineral-ADIMB, 25–92.

Ludovic A., Kwékam M., Eric Martial F., Kouemo J., Efon Awoum J., Styve Cliff C., Robinson Belmien S. Y., Blandine K., Lauraine, A. 2021. Field observations and microstructural evidences of syntectonic emplacement of the Ngwi granitic plutons (central Cameroon domain). *Arabian Journal of Geosciences*, **14**. https://doi.org/10.1007/s12517-021-07778-w

Ludwig K. 2009. *Squid 2*: a user's manual. Berkeley Geochronology Center Special Publication No. 5.

Ludwig K. 2008. *User's manual for isoplot/Ex*. [*S.l.*, *s.n.*].

Macambira J.B. 1986. Estratigrafia e mineralizações primárias de ouro da aba sul do sinclinório de Gradaús – sul do Pará. *In*: 34º Congresso Brasileiro de Geologia, SBG, Goiânia, *Anais* [...], **5**:1956–1968.

Macambira M.J.B. & Lafon J.M. 1995. Geocronologia da Província Mineral de Carajás; síntese dos dados e novos desafios. *Boletim do Museu Paraense Emílio Goeldi*, **7**:263 288.

Macambira E.M.B. & Vale A.G. 1997. *São Félix do Xingu*: folha SB.22-Y-B - estado do Pará. Brasília,DF, CPRM, 344 p.(Programa Levantamentos Geológicos Básicos do Brasil).

Macambira M.J.B. & Lancelot J. 1991. Em busca do embasamento arqueano da região de Rio Maria, sudeste do estado do Pará. *In*: SBG, 3º Simpósio de geologia da Amazônia. Belém, *Resumos Expandidos* [...], p. 49–58.

Macambira M.J.B. & Lancelot J. 1996. Time constraints for the formation of the Archean Rio Maria crust, southeastern Amazonian Craton, Brazil. *International Geology Review*, **38** (12):1134–1142.

Macambira J.B., Macambira M.J.B., Scheller T., Gomes A.C.B. 1996. Geocronologia Pb/Pb e tipologia de zircões de rochas vulcânicas da Formação Carajás-Pará: indicador da idade dos BIFs. *In*: SBG, 39° Congresso Brasileiro de Geologia, Salvador, *Anais*... Salvador, **6**: 516-519.

Macambira M.J.B., Costa J.B.S., Althoff F.J., Lafon J.M., Melo J.C.V., Santos A. 2000. New geochronological data for the Rio Maria TTG terrane: implications for the time constraints of the crustal formation of the Carajas Province, Brazil. *In*: 31º International Geological Congress, *Abstracts* […], 1 CDrom.

Macambira J.B. 2003. *O ambiente deposicional da Formação Carajás e uma proposta de modelo evolutivo para a Bacia Grão-Pará*. PhD Thesis, Instituto de Geociências, Universidade Estadual de Campinas, 200 p.

Machado N., Lindenmayer Z., Krogh T.E., Lindenmayer D. 1991. U/Pb geochronology of Archean magmatism and basement reactivation in the Carajás Área, Amazon Shield, Brazil. *Precambrian Research*, **49**:329–354.

Machado J.R.M., Oliveira D.C., Almeida J.A.C. 2021. Geologia, geoquímica e afinidades tectonomagmáticas dos granitoides de Bannach do Domínio Rio Maria, Província Carajás, Brasil. *Geologia USP-Série cientifica*, **21**(2):5–90.

Maitre R., Streckeisen A., Zanettin B., Le Bas M., Bonin B., 2020. *Igneous rocks: a classification and glossary of terms.* 256 p.

Marangoanha B. & Oliveira D.C. 2014. Diabásios e anfibolitos da área de Nova Canadá: natureza e implicações tectônicas para a Província Carajás. *Boletim do Museu Paraense Emílio Goeldi-Ciências Naturais*, **9**(3):565–596.

Marangoanha B., Oliveira D., Oliveira V.E.S., Galarza M., Lamarão C., 2019a. Neoarchean A-type granitoids from Carajás province (Brazil): New insights from geochemistry, geochronology and microstructural analysis. *Precambrian Research* **324**:86–108. https://doi.org/10.1016/j.precamres.2019.01.010

Marangoanha B., Oliveira D., Lamarão C., Marques G., Ribeiro-Silva L., 2022. Geothermobarometry and geochemical modeling of Archean charnockites from Carajás Province, Amazonian craton, Brazil. *Brazilian Journal of Geology* **52**(4). https://doi.org/10.1590/2317-4889202220210092

Marangoanha B., Oliveira D.C., Dall'Agnol R. 2019b. The Archean granulite-enderbite complex of the northern Carajás province, Amazonian craton (Brazil): Origin and implications for crustal growth and cratonization. *Lithos* **350–351**, 105275. https://doi.org/https://doi.org/10.1016/j.lithos.2019.105275

Marangoanha B., Oliveira D.C., Galarza M.A., Marques G.T., 2020. Crustal anatexis and mantle-derived magmas forming Neoarchean A-type granitoids in Carajás Province, northern Brazil: Petrological evidence and tectonic control. *Precambrian Research* **338**, 105585. https://doi.org/https://doi.org/10.1016/j.precamres.2019.105585

Marinho P.A.C. 1977. *Projeto carvão no Rio Fresco*: relatório final. Belém, CPRM, **1**:126.

Martins P.L.G., Toledo C.L.B., Silva A.M., Chemale Jr F., Santos J.O.S., Assis L.M. 2017. Neoarchean magmatism in the southeastern Amazonian Craton, Brazil: Petrography, geochemistry and tectonic significance of basalts from the Carajás Basin. *Precambrian Research*, **302**:340–357.

Medeiros Filho C.A. & Meireles E.M. 1985. Dados preliminares sobre a ocorrência de cromita na área de Luanga. *In*: SBG, 2° Simpósio de Geologia da Amazônia, Belém. *Atas*, **3**:1488-1499.

Meireles E.M., Teixeira J.T., Medeiros Filho C.A. 1982. Geologia preliminar do depósito de ouro de Serra Pelada. *In*: Simpósio de Geologia da Amazônia, Belém. *Anais*... Belém: SBG, **2**:74–84.

Meirelles M.R. & Dardenne M.A. 1991. Vulcanismo basáltico de afinidade shoshonítica e ambiente de arco arqueano, Grupo Grão-Pará, Serra dos Carajás, Pará. *Revista Brasileira de Geociências*, **21**(1):41–50.

Melo G.H.C., Monteiro L.V.S., Xavier R.P., Moreto C.P.N., Arquaz R.M., Silva M.A.D. 2019. Evolution of the Igarapé Bahia Cu-Au deposit, Carajás Province (Brazil): Early syngenetic chalcopyrite overprinted by IOCG mineralization. *Ore Geology Reviews* **111**:102993. https://doi.org/https://doi.org/10.1016/j.oregeorev.2019.102993

Melo G.H.C., L.V.S., Xavier R.P., Moreto CP.N., Santiago E., Dufrane S.A., Aires B., Santos A. 2016. Temporal evolution of the giant Salobo IOCG deposit, Carajás Province (Brazil): constraints from paragenesis of hydrothermal alteration and U-Pb geochronology. *Mineralium Deposita,* **52**: 709-732. https://doi.org/10.1007/s00126-016-0693-5

Melo G.H.C., Monteiro L.V.S., Xavier R.P., Moreto C.P.N., Santiago E.S.B., Dufrane S.A., Aires B., Santos A.F.F. 2016. Temporal evolution of the giant Salobo IOCG deposit, Carajás Province (Brazil): constraints from paragenesis of hydrothermal alteration and U-Pb geochronology. *Mineralium Deposita,* **52**:709–732. https://doi.org/10.1007/s00126-016-0693-5

Mesquita C.J.S., Dall'Agnol R., Silva A.S.N., Cunha I.R.V., Almeida J.A.C., Oliveira J.K.M. 2025. Crystallization parameters and thermodynamic modeling of the Igarapé Gelado suite: Implications for the Neoarchean magmatism of the Carajás province, Brazil. Journal South American Earth Science **153:** 105357. https://doi.org/10.1016/j.jsames.2025.105357

Milhomem Neto, J.M., Lafon, J.-M. 2019. Zircon U-Pb and Lu-Hf isotope constraints on Archean crustal evolution in Southeastern Guyana Shield. *Geoscience Frontiers* **10**:1477–1506. https://doi.org/https://doi.org/10.1016/j.gsf.2018.09.012

Monteiro L. V. S., Xavier R. P., Carvalho E. R., Hitzman M. W., Johnson C. A., Souza Filho C. R., Torresi I. 2008. Spatial and temporal zoning of hydrothermal alteration and mineralization in the Sossego iron oxide–copper–gold deposit, Carajás Mineral Province, Brazil: paragenesis and stable isotope constraints. *Mineralium Deposita,* **43**:129-159.

Moreto C.P.N., Monteiro L.V.S., Xavier R.P., Amaral W.S., Santos T.J.S., Juliani C., Souza Filho C.R. 2011. Mesoarchean (3.0 and 2.86 Ga) host rocks of the iron oxide-Cu-Au Bacaba deposit, Carajás Mineral Province: U-Pb geochronology and metallogenetic implications. *Mineralium Deposita,* **46**:789-811.

Moreto C.P.N., Monteiro, L.V.S., Xavier, R.P., Creaser R.A., DuFrane S.A., Melo, G.H.C., Silva, D.M.A., Tassinari C.C.G., Sato K. 2015a. Timing of multiple hydrothermal events in the iron oxide–copper–gold deposits of the Southern Copper Belt, Carajás Province, Brazil. *Mineralium Deposita*, **50**, 517–546. https://doi.org/10.1007/s00126-014-0549-9

Moreto C. P. N., Monteiro L. V. S., Xavier R. P., Creaser R. A., DuFrane S. A., Tassinari C. C. G., Sato K., Kemp A. I. S., Amaral W. S. 2015b. Neoarchean and Paleoproterozoic Iron Oxide-Copper-Gold Events at the Sossego Deposit, Carajás Province, Brazil: Re-Os and U-Pb Geochronological Evidence. *Economic Geology,* **110**:809-835.

Moyen J.-F., Laurent, O., Chelle-Michou C., Couzinié, S., Vanderhaeghe O., Zeh, A., Villaros A., Gardien V. 2016. Collision vs. subduction-related magmatism: Two contrasting ways of granite formation and implications for crustal growth. *Lithos* **277**:154-177. https://doi.org/10.1016/j.lithos.2016.09.018

Moyen J.F. & Laurent O. 2018. Archaean tectonic systems: a view from igneous rocks. *Lithos,* **302–303**: 99–125. https://doi.org/https://doi.org/10.1016/j.lithos.2017.11.038

Nascimento A. C., Oliveira D. C., Gabriel E. O., Silva L. R., Dall'Agnol R., Santos P. J. L., Santos, J. O. S., Machado, J. R. M., Toro, M. A. G., Guimarães, F. V. 2023. Suíte gnássico-migmatítica Caracol: novos dados isotópicos (U-Pb–Hf–Nd–Sr) e implicações para o significado tectono-metamórfico do embasamento mesoarqueano do terreno Sapucaia, Província Carajás.*In:* SBG, 17° Simpósio de Geologia da Amazônia, Santarém, Pa. *Anais* 200-204.

Nedelec A. & Bouchez J.L. 2015. *Granites:* petrology, structure, geological setting, and metallogeny. 335 p. https://doi.org/10.1093/acprof:oso/9780198705611.001.0001.

Oliveira D.C., Santos P.J.L., Gabriel E.O., Rodrigues D.S., Faresin A.C., Silva M.L.T., Sousa S.D., Santos R.V., Silva A.C., Souza M.C., Santos R.D., Macambira M.J.B. 2010. Aspectos geológicos e geocronológicos das rochas magmáticas e metamórficas da região entre os municípios de Água Azul do Norte e Canaã dos Carajás – Província Mineral de Carajás, *In*: SBG, 45° Congresso Brasileiro de Geologia. Belém, *Anais*, CDrom.

Oliveira D.C, Silva L.R., Nascimento A.C., Marangoanha B.O., Gabriel E.O., Santos P.J.L., Machado J.R.M., Felix W.Q., Silva L.C.S., Santos R.F.S. 2023. Revisão litoestratigráfica com implicações para compartimentação tectônica da Província Mineral de Carajás, sudeste do Cráton Amazônico. *In*: SBG, 17° Simpósio de Geologia da Amazônia, Santarém. *Anais* [...]. p. 434-441.

Oliveira E.P., Winter C., Sachs L.L.B., Batista J.J., Figueiredo B.R., Foster R. 1993. Limiting factors in applying geochemistry to tectonic settings identification in continental áreas: implications to the Carajás basic metavolcanics, Brazil. *In*: 4º Congresso Brasileiro de Geoquímica, SBGq, Brasília, *Resumos expandidos*[...], p. 20–22.

Oliveira J.R., Silva Neto C.S., Costa E.J.S. 1994. *Serra Pelada; folha SB.22.X.C. Estado do Pará*. Brasília, CPRM, p 220. (Programa Levantamentos Geológicos Básicos do Brasil – PLGB). Escala 1:250.000.

Oliveira J.K.M., Tavares F.M., Costa I.S.L., 2018b. *Mapa geológico-geofísico do lineamento Cinzento: estado do Pará.* Belém: CPRM. 1 mapa, color. Escala 1:100.000.

Oliveira M.A., Dall'Agnol R., Althoff F.J., Leite A.A.S. 2009. Mesoarchean sanukitoid rocks of the Rio Maria Granite Greenstone Terrane, Amazonian craton, Brazil. *Journal of South American Earth Sciences*, **27**(2–3):146–160. https://doi.org/10.1016/j.jsames.2008.07.003

Oliveira M.A., Dall'Agnol R., Scaillet B. 2010. Petrological constraints on crystallization conditions of Mesoarchean sanukitoid rocks, southeastern Amazonian Craton, Brazil. *Journal of Petrology*, **51**(10):2121–2148. https://doi.org/10.1093/petrology/egq051

Oliveira M.A., Dall'Agnol R., Almeida J. 2011. Petrology of the Mesoarchean Rio Maria suite and the discrimination of sanukitoid series. *Lithos* **127**:192–209. https://doi.org/10.1016/j.lithos.2011.08.017

Oliveira R.G. 2018c. Insights on the framework of the Carajás Province, Amazonian Craton, Brazil, and on the three–dimensional shape of the Carajás Basin, based on gravity data. *Journal of the Geological Survey of Brazil*, **1**(3): 101–112.

Oliveira V.E.S., Oliveira D.C., Marangoanha B., Lamarão C.N. 2018a. Geology, mineralogy and petrological affinities of the Neoarchean granitoids from the central portion of the Canaã dos Carajás domain, Amazonian craton, Brazil. *Journal South American Earth Sciences* **85**:135–159. https://doi.org/https://doi.org/10.1016/j.jsames.2018.04.022

Olszewski W.J., Wirth K.R., Gibbs A.K., Gaudette H.E. 1989. The age, origin, and tectonics of the Grão Pará Group and associated rocks, Serra dos Carajás, Brazil: Archean continental volcanism and rifting. *Precambrian Research*, **42**:229–254.

Paiva-Júnior A.L., Lamarão C.N., Araújo Lima P.H. 2011. Geologia, Petrografia e Geoquímica do Batólito Seringa, Província Carajás, SSE do Pará. *Revista Brasileira de Geociências*, **41**(2):185–202.

Passchier C.W. & Trouw R.A.J. 2005. *Microtectonics*. Springer Science & Business Media. 366 p.

Patchett P.J. & Tatsumoto M. 1981. A routine high-precision method for Lu-Hf isotope geochemistry and chronology. *Contributions to Mineralogy and Petrology* **75**:263–267. https://doi.org/10.1007/BF01166766

Pawley M. J. & Collins W. J. 2002. The development of contrasting structures during the cooling and crystallisation of a syn-kinematic pluton. *Journal of Structural Geology*, **24**(3):469–483. https://doi.org/https://doi.org/10.1016/S0191-8141(01)00069-4

Pearce J. 1996. Sources and settings of granitic rocks. *International Union of Geological Sciences* **19**:120–125. https://doi.org/10.18814/epiiugs/1996/v19i4/005

Pearce J., Harris N., Tindle A. 1984. Trace Element Discrimination Diagrams for the Tectonic Interpretation of Granitic Rocks. *Journal of Petrology* **25**:956–983. https://doi.org/10.1093/petrology/25.4.956

Pereira R.M.P., Rosière C.A., Santos J.O.S., Lobato L.M., Silva R.C.F. e, McNaughton N.J. 2009. Unidade Caninana: sequência clástica paleoproterozoica revelada por datação U-Pb em zircões detríticos da Província Mineral Carajás. *In*: SBG, 11º Simpósio de Geologia da Amazônia, Manaus, p 376–379.

Petford N., Cruden A. R., McCaffrey K. J. W., Vigneresse J.L. 2000. Granite magma formation, transport and emplacement in the Earth's crust. *Nature*, ***408***(6813):669–673.

Pidgeon R.T., Macambira M.J.B., Lafon J.M. 2000. Th-U-Pb isotopic systems and internal structures of complex zircons from an enderbite from the Pium Complex, Carajás Province, Brazil: evidence for the ages of granulites facies metamorphism and the protolith of the enderbite. *Chemical Geology*, **166**:159–171.

Pimentel M.M. & Machado N. 1994. Geocronologia U-Pb do Terrenos Granito-Greenstone de Rio Maria, Pará. *In*: 38º Congresso Brasileiro de Geologia. Camboriú, *Resumos Expandidos*, p. 390–391.

Pimentel M.M., Lindenmayer Z.G., Laux J.H., Armstrong R., Araújo J.C. 2003. Geochronology and Nd isotope geochemistry of the Gameleira Cu-Au deposit, Serra dos Carajás, Brazil: 1.8-1.7 Ga hydrothermal alteration and mineralization. *Journal of South American Earth Sciences*, **15**(7):803–813.

Pinheiro R.V.L., Kadekaru K., Soares A. V., Freitas C., Ferreira S.N., Matos F.M. V. 2013. Carajás, Brazil—a short tectonic review. *In*: SBG,13th Simpósio de Geologia da Amazônia, Belém (Proceedings).

Pinheiro R. & Holdsworth R. 1997. Reactivation of Archaean strike-slip fault systems, Amazon region, Brazil. *Journal of The Geological Society,* **154:**99–103. https://doi.org/10.1144/gsjgs.154.1.0099

Pinheiro R. V. L. & Holdsworth R. E. 2000. Evolução tectonoestratigráfica dos sistemas transcorrentes Carajás e Cinzento, Cinturão Itacaiúnas, na borda leste do Craton Amazônico, Pará. *Brazilian Journal of Geology*, **30**(4):597-606.

Ramos J.F.F., Moura C.A.V., Melo C. F.,Pereira J. l., Serique J.S.B., Rodrigues R. M.,P. 1984. Uma discussão sobre seqüências sedimentares tidas como formação Rio Fresco, Sudeste do

Pará. *In*: *FADESP,* 33º Congresso Brasileiro de Geologia, SBG, Rio de Janeiro, *Anais*[...], **2**:862–872.

Rapopo M. 2011. *Petrogenesis of the syntectonic Matok pluton in the Limpopo Belt (South Africa) and its implications on the geodynamic environment.* MS Dissertation. Faculty of Science, Stellenbosch University, South Africa197 p. http://scholar.sun.ac.za

Reis P. 2017. *A sequência meta-vulcanossedimentar do circular, Carajás (Pa):* geologia, petrografia, litogeoquímica e geocronologia. MS Dissertation. Universidade de São Paulo, São Paulo. 129 p.

Ricci P.S.F. 2006. Rocks of the Pium-Area, Carajás Block, Brazil – a deep-seated high-T gabbroic pluton (charnockitoid like) with xenoliths of enderbitic gneisses dated at 3002 Ma – the basement problem revisited. *In*: SBG, 9º Simpósio de Geologia da Amazônia, Belém, *Resumos expandidos*[...], 1 CDrom.

Ribeiro-Silva L., Oliveira D., Galarza M., Nascimento A., Marangoanha B., Marques G. 2023. Zircon U-Pb-Hf isotope and geochemical constraints on the petrogenesis and tectonic setting of Mesoarchean granitoids from the Carajás province, Amazonian craton, Brazil. *Precambrian Research*, **398**:107204. https://doi.org/10.1016/j.precamres.2023.107204

Ribeiro-Silva L., Oliveira D., Nascimento A., Lamarão C., Almeida J. 2022. The Mesoarchean plutonic complex from the Carajás province, Amazonian craton: Petrogenesis, zircon U Pb SHRIMP geochronology and tectonic implications. *Lithos*, **432–433**, 106901. https://doi.org/10.1016/j.lithos.2022.106901

Ribeiro-Silva L., Oliveira D. C., Santos, M. N. S. 2018. Diversity, origin and tectonic significance of the Mesoarchean granitoids of Ourilândia do Norte, Carajás province (Brazil). *Journal of South American Earth Sciences*, ***82*:**33–61. https://doi.org/https://doi.org/10.1016/j.jsames.2017.12.004

Rivalenti G., Mazzucchelli M., Girardi V.A.V., Cavazzini G., Finatti C., Barbieri M.A., Teixeira W. 1998. Petrogenesis of the paleoproterozoic basalt-andesite-rhyolite dyke association in the Carajas region, Amazonian craton. *Lithos*, **43**:235-265.

Rodrigues D.S., Oliveira D.C., Macambira M.J.B. 2014. Geologia, geoquímica e geocronologia do granito mesoarqueano Boa Sorte, município de Água Azul do Norte, Pará–Província Carajás. *Boletim Do Museu Paraense Emílio Goeldi-Ciências Naturais* **9**:597–633.

Rolando A.P., Macambira M.J.B. 2003. Archean crust formation in Inajá range area, SSE of Amazonian Craton, Brazil, based on zircon ages and Nd isotopes. *In*: South American Symposium on Isotope Geology. Salvador, *Expanded Abstracts*[…], 1 CDrom.

Rollinson H. & Pease V. 2021. *Using Geochemical Data: To Understand Geological Processes*. 346 p. https://doi.org/10.1017/9781108777834

Russell W.A., Papanastassiou D.A., Tombrello T.A. 1978. Ca isotope fractionation on the Earth and other solar system materials. *Geochimica et Cosmochimica Acta* **42**:1075–1090. https://doi.org/https://doi.org/10.1016/0016-7037(78)901059

Rutter E. H. & Neumann D. H. K. (1995). Experimental deformation of partially molten Westerly granite under fluid-absent conditions, with implications for the extraction of granitic magmas. *Journal of Geophysical Research: Solid Earth*, **100**(B8):15697–15715.

Salgado S., Caxito F., Castro M. 2019a. Stratigraphy, petrography and tectonics of the manganese-bearing Buritirama Formation, Northern Carajás Domain, Amazon Craton. *Brazilian Journal of Geology*, **49**:1–15. https://doi.org/10.1590/2317-4889201920180106

Salgado S., Caxito F., Figueiredo R., Uhlein G., Nogueira L., Nalini Jr H., Aranda R. 2021. Metallogenetic Mn-model of the Rhyacian-aged Buritirama Formation, Carajás Domain (Amazon Craton). *Ore Geology Reviews*, **138,** 104396. https://doi.org/10.1016/j.oregeorev.2021.104396

Salgado S., Caxito F., Novais B. 2023. Síntese da geologia da Formação Buritirama e suas mineralizações manganesíferas: limite norte do Domínio Carajás, Pará. SBG, *Contribuições a Geologia da Amazônia*, **12:**173-185.

Salgado S. S., Caxito F.A., Figueiredo R.C.S., Lana C. 2019b. Provenance of the Buritirama Formation reveals the Paleoproterozoic assembly of the Bacajá and Carajás blocks (Amazon Craton) and the chronocorrelation of Mn-deposits in the Transamazonian/Birimian system of northern Brazil/West Africa. *Journal of South American Earth Sciences*, **96**: 102364. https://doi.org/https://doi.org/10.1016/j.jsames.2019.102364

Santos A. & Pena Filho J.I.C. 2000. *Xinguara:* folha SB.22-Z-C. Estado do Pará, Brasília, CPRM, 1 CDrom. (Programa Levantamentos Geológicos Básicos do Brasil - PLGB). Escala 1:250.000.

Santos J.O.S. 2003. Geotectônica do Escudo das Guianas e Brasil-Central. *In*: Bizzi L.A. *et al.* (eds.). *Geologia, tectônica e recursos minerais do Brasil:* texto, mapas e SIG. Brasília, DF, CPRM - Serviço Geológico do Brasil, 169–226 p.

Santos J.O.S., Hartmann L.A., Faria M.S.G., Riker S.R., Souza M.M., Almeida M.E., McNaughton N.J., 2006. A compartimentação do Cráton Amazonas em províncias: avanços ocorridos no período 2000-2006. *In*: SBG, 9º Simpósio de Geologia da Amazônia, *Anais*[...] p.156–159.

Santos P.A., Teixeira M.F.B., Dall'Agnol R., Guimarães A.V. 2013a. Geologia, petrografia e geoquímica da associação Tonalito-Trondhjemito-Granodiorito (TTG) do extremo leste do Subdomínio de Transição, Província Carajás, Pará. *Boletim do Museu Paraense Emílio Goeldi-Ciências Naturais*, **8**(3):257–290

Santos R.D., Galarza M.A., Oliveira D.C. 2013b. Geologia, geoquímica e geocronologia do Norito Pium, Província Carajás. *Boletim do Museu Paraense Emílio Goeldi-Ciências Naturais*, **8**(3):355–382.

Santos M.N.S. & Oliveira D.C. 2016. Rio Maria granodiorite and associated rocks of Ourilândia do Norte - Carajás province: petrography, geochemistry and implications for sanukitoid petrogenesis. *Journal of South American Earth Sciences*, **72**:279–301.

Santos M.S., Oliveira D.C., Gabriel E.O. 2018. Granitoides TTG de Água Azul do Norte (PA): implicações tectônicas para a Província Carajás. *Geologia USP-Série cientifica*, **18**:119–148.

Santos-Silva R.C., Sabóia A.M., Oliveira H.J. 2021. *Projeto integração geológica-geofísica metalogenética das sequências de Greenstone Belts do Domínio Rio Maria – Novas Fronteiras Rio Maria*. Belém, CPRM. pp. 274. Escalas: 1.250.000–1:100.000.

Santos-Silva A.N., Feio, G.R.L., Silva, J.P.A., Dall'Agnol, R., Almeida, J.A.C., Gomes, A., 2020. Mineralogy, petrology, and origin of the Pedra Branca Suite: a tonalitic-trondhjemitic association with high Zr, Ti and Y, Carajás province, Amazonian Craton. *Brazilian Journal of Geology*, **50**. https://doi.org/10.1590/2317-4889202020190093

Santos-Silva R. C., Costa F. G., Silva C. M. G., Ricci P.S. F., Rodrigues J. B. 2023. Idade U-Pb SHRIMP em zircão da intrusão ultramáfica Fafá, Província Carajás: cristalização em 2,76 Ga seguido de metamorfismo/hidrotermalismo em 2,73 Ga? *In*: SBG, 17° Simpósio de Geologia da Amazônia, Santarém, PA. *Anais*[...].

Santos R. F. S., Oliveira D. C., Marangoanha B., Galarza M. A., Santos, M. R. 2023. Geochemistry, zircon U-Pb geochronology and Lu-Hf isotopes of the Manda Saia granite: Petrological affinity and magma source of evolved A-type granites from the Carajás province, southeastern Amazonian craton, Brazil. *Lithos*, **462–463**: e 107412. https://doi.org/https://doi.org/10.1016/j.lithos.2023.107412

Sardinha A.S., Dall'Agnol R., Gomes A.C.B., Macambira M.J.B., Galarza M.A. 2004. Geocronologia Pb-Pb e U-Pb em zircão de granitoides arqueanos da região de Canaã dos Carajás, Província Mineral de Carajás. *In*: 42º Congresso Brasileiro de Geologia, SBG, Araxá, *Anais*[...], 1 CD-ROM.

Sardinha A.S., Barros, C.E.M., Krymsky R. 2006. Geology, geochemistry, and U–Pb geochronology of the Archean (2.74 Ga) Serra do Rabo granite stocks, Carajás Metallogenetic Province, northern Brazil. *Journal South American Earth Sciences*, **20**:327–339.

Sato K., Basei M.A.S., Siga Júnior O., Sproesser W.M., Passarelli C.R. 2008. Novas técnicas aplicadas ao método U-Pb no CPGeo-IGc/USP: avanços na digestão química, espectrometria de massa (TIMS) e exemplos de aplicação integrada com SHRIMP. *Geologia USP. Série Científica*, **8**:76–99.

Sato K., Tassinari C., Basei M., Siga Júnior O., Onoe A., Souza M. 2014. Sensitive High Resolution Ion Microprobe (SHRIMP IIe/MC) of the Institute of Geosciences of the University of São Paulo, Brazil: Analytical method and first results. *Geologia USP. Série Científica* **14**:3–18. https://doi.org/10.5327/Z1519-874X201400030001

Sato K., Tassinari C.C.G., Basei M.A.S., Onoe A.T., Siga Junior O. 2016. First REE analyses in zircon by SHRIMP at Geosciences Institute of São Paulo University: REE diffusion from apatite inclusion inside Temora zircon. *In*: VIII International SHRIMP Workshop

Silva A.C., Dall'Agnol R., Guimarães F.V., Oliveira D.C. 2014. Geologia, petrografia e geoquímica de Associações Tonalíticas e Trondhjemíticas Arqueanas de Vila Jussara, Província Carajás, Pará. *Boletim do Museu Paraense Emílio Goeldi-Ciências Naturais*, **9**(1):13–46.

Silva C.R.P. & Oliveira D.C. 2013. Geologia, petrografia e geoquímica das associações TTGs e leucogranodioritos do extremo norte do Domínio Rio Maria, Província Carajás. *Boletim do Museu Paraense Emílio Goeldi*, **8**(3):383–415.

Silva F.F., Oliveira D.C., Antonio P.Y.J., D'Agrella M.S.F., Lamarão C.N. 2016. Bimodal magmatism of the Tucumã area, Carajás province: U-Pb geochronology, classification and processes. *Journal of South American Earth Sciences*,**72:**95–114.

Silva F., Oliveira D., Dall'Agnol R., Ribeiro-Silva L., Cunha I.R. 2020. Lithological and structural controls on the emplacement of a Neoarchean plutonic complex in the Carajás province, southeastern Amazonian craton (Brazil). *Journal South American Earth Scienses* **102**: e102696. https://doi.org/10.1016/j.jsames.2020.102696

Silva F.F., Oliveira D.C., Dall'Agnol R., Santos J.O.S., Galarza M.A.T., Guimarães F.V., Souza L.A.M. 2025. Geochemistry, SHRIMP U-Pb Zircon geochronology, and Hf-Nd isotope composition on the Neoarchean Vila Jussara granitoid complex from Carajás Province, Amazonian Craton: petrogenesis and tectonic implications. *Journal of the Geological Society,***182**(2): jgs2024-109. https://doi.org/10.1144/jgs2024-109

Silva R.C.F.e 2009. *Evolução e gênese do minério de ferro hidrotermal nos depósitos da Serra Norte, Província Mineral de Carajás*. PhD Thesis, Instituto de Geociências, Universidade Federal de Minas Gerais, 236p.

Silva-Silva L.C., Oliveira D.C., Souza D.B. 2020. Geology and geochemical constraints on the origin of the Mesoarchean granitoids from Carajás province, Amazonian craton. *Journal of South American Earth Sciences*, **100**:102–568.

Silva-Silva L.C. (em preparação). *Petrologia e tectônica dos granitoides mesoarqueanos da Folha Rio Branco (SB-22-Y-B-VI), porção centro-oeste da Província Carajás – SE do Cráton Amazônico*. PhD Thesis. Instituto de Geociências, Universidade Federal do Pará, Belém, Brasil.

Silva L., Silva A., Silva C., Silva D., Rodrigues J. 2023. Geocronologia U-Pb (SHRIMP) em zircão em granitos da porção NW da Província Carajás: Implicações para o magmatismo neoarqueano e metalogenia da região, *In*: SBG, 17° Simpósio de Geologia Da Amazônia. Santatém-Pa. *Anais* 591-595.

Silva M.A.D., Monteiro L.V.S., Santos T.J.S., Moreto C.P.N., Sousa S.D., Faustinoni J.M., Melo G.H.C., Xavier R.P., Toledo. B.A.M. 2021. Mesoarchean migmatites of the Carajás Province: From intra-arc melting to collision. *Lithos*, **388–389**: e106078.

Silva M. G., Teixeira J. B. G., Pimentel M. M., Vasconcelos P. M., Arielo A., Rocha W. J. S. F. 2005. Geologia e mineralizações de Fe-Cu-Au do Alvo GT46 (Igarapé Cinzento), Carajás. *In:* Marini O. J., Queiroz E. T., Ramos B. W., eds., *Caracterização de Depósitos Minerais em Distritos Mineiros da Amazônia: Brasília, Brazil, DNPMCT/Mineral-ADIMB*, República das Letras: 94-151.

Söderlund U., Patchett P.J., Vervoort J.D., Isachsen C.E. 2004. The 176Lu decay constant determined by Lu-Hf and U-Pb isotope systematics of Precambrian mafic intrusions. Earth and Planetary Science Letter, 219:311–324.

Sousa S.D., Oliveira D.C., Gabriel E.O., Macambira M.J.B. 2010. Geologia, Petrografia e Geocronologia das rochas granitoides do Complexo Xingu da porção a leste da cidade de Água Azul do Norte (PA) - PMC. *In*: 45º Congresso Brasileiro de Geologia. Belém, *Anais*[...], CDrom.

Sousa S.D., Monteiro L.V.S., Oliveira D.C., Delinardo M.A.S., Moreto C.P.N., Juliani C. 2013. O greenstone belts Sapucaia na região de Água Azul do Norte, Província Mineral de Carajás: Contexto geológico e caracterização petrográfica. In: 47º Congresso Brasileiro de Geologia. Salvador, Anais[...], CDrom.

Sousa L.A.M., Dall'Agnol R., Cunha I.R.V., Silva F.F., Oliveira D.C. 2022. Magnetic petrology of the Neoarchean granitoids in the Vila Jussara Suite, Carajás Province, Amazonian Craton. *Brazilian Journal of Geology,* **52**: e20201071. https://doi.org/10.1590/2317-4889202220210071

Sousa S.D., Monteiro L.V.S., Oliveira D.C., Delinardo M.A.S., Moreto C.P.N., Juliani C. 2013. O greenstone belts Sapucaia na região de Água Azul do Norte, Província Mineral de Carajás: Contexto geológico e caracterização petrográfica. *In*: 47º Congresso Brasileiro de Geologia. Salvador, Anais[...], CDrom.

Souza S.R.V.B., Macambira M.J.B., Sheller T. 1996b. Novos dados geocronológicos para os granitos deformados do Rio Itacaiúnas (Serra dos Carajás, PA); implicações estratigráficas. *In*: 5th Simpósio de Geologia da Amazônia, Belém. (Proceedings).

Souza Z.S., Dall'Agnol R., Althoff F.J., Leite A.A.S., Barros C.E.M. 1996a. Carajás Mineral Province: geological, geochronological and tectonic contrasts on the Archean evolution of the Rio Maria granite – greenstone terranes and the Carajás Block. *In:* SBG, Symposium Archaean terranes of the South American Platform, Brasília. *Extended Abstracts*. p. 31–32

Souza Z.S., Potrel H., Lafon J.M., Althoff F.J., Pimentel M.M., Dall'Agnol R., Oliveira C.G. 2001. Nd, Pb and Sr isotopes of the Identidade Belt, an Archaean greenstone belt of the Rio Maria region (Carajas province, Brazil): implicationsfor the Archaean geodynamic evolution of the Amazonian Craton. *Precambrian Research,* **109**:293-315.

Souza D.B., Oliveira D.C., Monteiro L.V.S., Gabriel E.O. Marangoanha B. 2017. Colocação, metamorfismo e natureza dos anfibolitos de Água Azul do Norte, Província Carajás. *Geologia USP-Série Cientifica*, **17**:98–123.

Souza D.B. 2018. Geologia e Petrologia dos Granitoides Arqueanos da Área de Tucumã: Implicações Para a Evolução Crustal da Província Carajás. *Exame de qualificação*. Instituto de Geociências, Universidade Federal do Pará, Belém, 84 p

Stern R.A. 1998. High resolution SIMS determination of radiogenic trace isotope ratios in minerals. *In*: Cabri L.J., Vaughan D.J. *Modern approaches to ore and environmental mineralogy*. Mineralogical Association of Canada, Canada Short Course Series, **27**:241-268.

Sylvester P. 1989. Post-Collisional Alkaline Granites Author(s): Post-Collisional Alkaline Granites'. *Journal of Geology*, **97**:261–280.

Tallarico F.H.B., Figueiredo B.R., Groves D.I., Kositcin N., MCNaughton N.J., Fletcher I.R., Rego J.L. 2005. Geology and Shrimp U-Pb geochronology of the Igarapé Bahia deposit, Carajás Copper-Gold belt, Brazil: an Archean (2.57 Ga) example of iron-oxide Cu-Au-(U-REE) mineralization. *Economic Geology*. **100**:7–28.

Tang M., Chen K., Rudnick R. 2016. Archean upper crust transition from mafic to felsic marks the onset of plate tectonics. *Science* (1979) **351**: 372–375. https://doi.org/10.1126/science.aad5513

Tassinari C.C.G. & Macambira M.J.B. 2004. A evolução tectônica do Cráton Amazônico. *Geologia do continente sul-americano: evolução da obra de Fernando Flávio Marques de Almeida.* 613 p.

Tavares F.M. 2014. *Programa Geologia do Brasil – PGB, Rio Verde – SB.22-Z-A-III*, Estado do Pará – Carta Geológica. Belém: CPRM, Escala1:100.000.

Tavares F.M. 2015. *Evolução geotectônica do nordeste da Província Carajás.* Phd Thesis. Universidade Federal do Rio de Janeiro, Rio de Janeiro, 115 p.

Tavares F.M., Trouw R.A.J., Silva C.M.G., Justo A.P., Oliveira J.K.M. 2018. The multistage tectonic evolution of the northeastern Carajás Province, Amazonian Craton, Brazil: Revealing complex structural patterns. Journal South American Earth Sciences, **88**:238–252. https://doi.org/https://doi.org/10.1016/j.jsames.2018.08.024

Tavares F.M., Oliveira J.K.M., Lima R.B. 2021. *Áreas de relevante interesse mineral-Província mineral de Carajás, PA: controles críticos das mineralizações de cobre e ouro do lineamento Cinzento.* CPRM, Belém. 154 p.

Teixeira J.B.G. & Eggler D.H. 1994. Petrology, geochemistry, and tectonic setting of Archean basaltic and dioritic rocks from the N4 iron deposit, Serra dos Carajás, Pará, Brazil. *Acta Geologica Leopoldensia*. **17**:71-114.

Teixeira N.P., Bettencourt J. S., Moura C. A., Dall'Agnol R., Macambira E. M. 2002. Archean crustal sources for paleoproterozoic tin-mineralized granites in the Carajás Province, SSE Pará, Brazil: Pb-Pb geochronology and Nd isotope geochemistry. *Precambrian Research*, **119**:257–275.

Teixeira L.R. 2005. *Genesis 4.0*—software de modelamento geoquímico.

Teixeira M.F.B., Dall'Agnol R., Silva A.C., Santos P.A. 2013. Geologia, petrografia e geoquímica do Leucogranodiorito Pantanal e dos leucogranitos arqueanos da área a norte de Sapucaia, Província Carajás, Pará: implicações petrogenéticas. *Boletim do Museu Paraense Emílio Goeldi-Ciências Naturais*, **8**(3):291–323.

Teixeira M.F.B., Dall'Agnol R., Santos J.O.S., Sousa L.A.M., Lafon J.M. 2017. Geochemistry, geochronology and Nd isotopes of the Gogó da Onça Granite: A new Paleoproterozoic A-type granite of Carajás Province, Brazil. *Journal of South American Earth Sciences*, **80**:47–65.

Teixeira M.F.B., Dall'Agnol R., Santos J.O.S., Oliveira D.C., Lamarão C.N., McNaughton N.J. 2018. Crystallization ages of Paleoproterozoic A-type granites of Carajás province, Amazon craton: Constraints from U-Pb geochronology of zircon and titanite. *Journal of South American Earth Sciences*, **88**:312–331.

Teixeira J.B.G. 1994. *Geochemistry, petrology, and tectonic setting of archean basaltic and dioritic rocks from the N4 Iron deposit, Serra dos Carajás, Pará, Brazil*. PhD Thesis, Department of Geosciences, Penn State University, 161 p.

Teruiya R.K., Paradella W.R., Santos A.R, Dall'Agnol R., Veneziani P. 2008. Integrating airborne SAR, Landsat TM and airborne geophysics data for improving geological mapping

in the Amazon region: the Cigano Granite, Carajás Province, Brazil. International Journal of Remote Sensing, **29**:3957-3974.

Thirlwall M.F. & Anczkiewicz R. 2004. Multidynamic isotope ratio analysis using MC–ICP–MS and the causes of secular drift in Hf, Nd and Pb isotope ratios. *International Journal of Mass Spectrometry,* **235**:59–81. https://doi.org/https://doi.org/10.1016/j.ijms.2004.04.002

Trendall L.A.F. Basei M.A.S., De Laeter J.R., Nelson D.R. 1998. SHRIMP zircon U-Pb constraints on the age of the Carajás formation, Grão-Pará Group, Amazon Craton. *Journal of South American Earth Sciences*, **11**(3):265–277. https://doi.org/10.1016/S0895-9811(98)00015-7

Trouw R. A. J., Passchier C. W., Wiersma, D. J. 2009. *Atlas of Mylonites-and related microstructures*. Springer Science & Business Media.

Toledo P., Moreto C., Monteiro L., Melo G., Matos F., Xavier R., Carvalho J., Medeiros Filho C.A., Navarro M., Lana C., 2023. Breaking up the temporal link between granitic magmatism and iron oxide-copper–gold (IOCG) deposits in the Carajás Mineral Province, NW Brazil. *Mineralium Deposita,* **59:** 601-625. https://doi.org/10.1007/s00126-023-01224-5

Toledo P.I.S., Moreto C.P.N., Xavier R.P., Gao J., Matos J.H., Melo, G.H.C. 2019. Multistage evolution of the Neoarchean (ca. 2.7 Ga) Igarapé cinzento (GT-46) iron oxide copper-gold deposit, Cinzento shear zone, Carajás Province, Brazil. *Economic Geology* **114**:1–34.

Topno A., Dey S., Liu Y., Zong K. 2018. Early Neoarchaean A-type granitic magmatism by crustal reworking in Singhbhum craton: Evidence from Pala Lahara area, Orissa. *Journal of Earth System Science* **127**:1–22. https://doi.org/10.1007/s12040-018-0947-y

Trouw R.A.J., Passchier C.W., Wiersma D.J. 2009. *Atlas of Mylonites-and related microstructures*. Springer Science & Business Media. 322 p.

Trunfull E.F., Hagemann S.G., Xavier R.P., Moreto C.P.N. 2020. Critical assessment of geochronological data from the Carajás Mineral Province, Brazil: Implications for metallogeny and tectonic evolution. *Ore Geology Reviews,***121**:103556. https://doi.org/https://doi.org/10.1016/j.oregeorev.2020.103556

Tullis J. & Yund R. A. 1989. Hydrolytic weakening of quartz aggregates: The effects of water and pressure on recovery. *Geophysical Research Letters*, **16**(11):1343–1346. https://doi.org/https://doi.org/10.1029/GL016i011p01343

Vasquez M.L. & Rosa-Costa L.T. (orgs.). 2008. *Geologia e recursos minerais do Estado do Pará: Sistema de Informações Geográficas – SIG: texto explicativo dos mapas Geológico e Tectônico e de Recursos Minerais do Estado do Pará*. Escala 1:1.000.000. Belém, CPRM. 329p.

Vernon R.H. 2005. *A Practical Guide To Rock Microstructure. Cambridge*. American Mineralogist **90**,1472. 594 p. https://doi.org/10.2138/am.2005.449

Whalen J.W., Currie K.L., Chappel B.W. 1987. A-type granites: geochemical characteristics, discrimination and petrogenesis. *Contributions to Mineralogy and Petrology,* **95**: 407-419.

Whalen J.B. & Hildebrand R.S. 2019. Trace element discrimination of arc, slab failure, and A-type granitic rocks. *Lithos*, **348–349**, 105179. https://doi.org/https://doi.org/10.1016/j.lithos.2019.105179

Wiedenbeck M., Hanchar J.M., Peck W.H., Sylvester P., Valley J., Whitehouse M., Kronz A., Morishita Y., Nasdala L., Fiebig J., Franchi I., Girard J.-P., Greenwood R.C., Hinton R., Kita N., Mason P.R.D., Norman M., Ogasawara M., Piccoli P.M., Rhede D., Satoh H., Schulz-Dobrick B., Skår O., Spicuzza M.J., Terada K., Tindle A., Togashi S., Vennemann T., Xie Q., Zheng Y.-F. 2004. Further Characterisation of the 91500 Zircon Crystal. *Geostandards and Geoanalytical Research,* **28**:9–39. https://doi.org/https://doi.org/10.1111/j.1751-908X.2004.tb01041.x

Wirth K. R., Gibbs A. K., Olszewski Jr. W.J. 1986. U-Pb zircon ages of the Grão Pará group and Serra dos Carajás granite, Pará, Brazil. *Revista Brasileira de Geociências*, **16** (2):195-200.

Williams I.S. 1997. *U-Th-Pb Geochronology by Ion Microprobe, Applications of Microanalytical Techniques to Understanding Mineralizing Processes*. Michael A. McKibben, W.C. Shanks, III, W. Ian Ridley.

Willson M. 1989. *Igneous petrogenesis a global tectonic approach*. London, Unwin Hyman, 466 p.

Wyers G. & Barton M. 1986. Petrology and evolution of transitional alkaline - sub alkaline lavas from Patmos, Dodecanesos, Greece: evidence for fractional crystallization, magma mixing and assimilation. *Contributions to Mineralogy and Petrology*, **93**:297–311. https://doi.org/10.1007/BF00389389

Xiang H. & Connolly J.A.D. 2022. GeoPS: An interactive visual computing tool for thermodynamic modelling of phase equilibria. *Journal of Metamorphic Geology,* **40**: 243–255.

Yavuz F. 2013. WinPyrox: A Windows program for pyroxene calculation classification and thermobarometry. *American Mineralogist,* **98**: 1338–1359. https://doi.org/10.2138/am.2013.4292

Yavuz F. & Doner Z. 2017. WinAmptb: A Windows program for calcic amphibole thermobarometry. *Periodico di Mineralogia* **86**: 135–167. https://doi.org/10.2451/2017PM710

Zibra I., Smithies R., Weinberg R., Peternell M., Prause M., Mcfarlane. 2024. The importance of being molten: 100 Myr of synmagmatic shearing in the Yilgarn Craton (Western Australia). Implications for mineral systems. *Precambrian Research*, **406:**107393. https://doi.org/10.1016/j.precamres.2024.107393

Zucchetti M. 2007. *Rochas máficas do Grupo Grão Pará e sua relação com a mineralização dos depósitos de ferro N4 e N5, Carajás, PA*. PhD Thesis, Instituto de Geociências, Universidade Federal de Minas Gerais, Belo Horizonte.

UNIVERSIDADE FEDERAL DO PARÁ
INSTITUTO DE GEOCIÊNCIAS
PROGRAMA DE PÓS-GRADUAÇÃO EM GEOLOGIA E GEOQUÍMICA

PARECER

Sobre a Defesa Pública da Tese de Doutorado de CAIO JOSÉ SOARES MESQUITA

A banca examinadora da Tese de Doutorado de **CAIO JOSÉ SOARES MESQUITA** orientando do Prof. Dr. Roberto Dall'Agnol (UFPA), e composta pelos professores doutores Valdecir de Assis Janasi (Membro-USP), Carlos Eduardo de Mesquita Barros (Membro-UFPR), Fernando Fernandes da Silva (Membro-UNIFESSPA), Jean Michel Lafon (Membro-UFPA) após apresentação da sua tese intitulada "**PETROGÊNESE DA SUÍTE IGARAPÉ GELADO: IMPLICAÇÕES PARA O MAGMATISMO NEOARQUEANO DA PROVÍNCIA CARAJÁS, CRÁTON AMAZÔNICO**", emite seguinte parecer:

O candidato realizou sua apresentação de forma clara, bem organizada e segura, no tempo estipulado. Na arguição mostrou domínio da temática abordada e respondeu às perguntas formuladas pela banca. O trabalho escrito foi apresentado na forma de dois artigos em periódicos de impacto internacional, sendo um publicado e outro submetido. Dessa forma, o documento atende às exigências para uma tese de doutorado.

Por cumprir com todas as exigências, a banca examinadora decidiu por unanimidade **aprovar a tese de doutorado.**

Belém, 30 de abril de 2025

Prof. Dr. Roberto Dall'Agnol (Orientador – UFPA)

Documento assinado digitalmente
gov.br
VALDECIR DE ASSIS JANASI
Data: 05/05/2025 09:28:30-0300
Verifique em https://validar.iti.gov.br

Prof. Dr. Valdecir de Assis Janasi (Membro-USP)

Documento assinado digitalmente
gov.br
CARLOS EDUARDO DE MESQUITA BARROS
Data: 06/05/2025 13:32:00-0300
Verifique em https://validar.iti.gov.br

Prof. Dr. Carlos Eduardo de Mesquita Barros (Membro-UFPR)

Documento assinado digitalmente
gov.br
FERNANDO FERNANDES DA SILVA
Data: 02/05/2025 11:26:37-0300
Verifique em https://validar.iti.gov.br

Prof. Dr. Fernando Fernandes da Silva (Membro-UNIFESSPA)

Documento assinado digitalmente
gov.br
JEAN MICHEL LAFON
Data: 01/05/2025 13:36:48-0300
Verifique em https://validar.iti.gov.br

Prof. Dr. Jean Michel Lafon (Membro-UFPA)